A search for functional connectivity rules in the visual thalamus and hippocampus

Martin Hans Peter Fernholz

München 2022

A search for functional connectivity rules in the visual thalamus and hippocampus

Martin Hans Peter Fernholz

Dissertation
zur Erlangung des Doktorgrades der
Naturwissenschaften Doctor rerum naturalium
(Dr. rer. nat.)
an der Fakultät für Biologie der
Ludwig–Maximilians–Universität München

vorgelegt von
Martin Hans Peter Fernholz
aus Starnberg

München, den 19. Oktober 2022

Erstgutachter: Prof. Dr. Tobias Bonhoeffer
Zweitgutachter: Prof. Dr. Laura Busse
Eingereicht am: 19. Oktober 2022
Tag der mündlichen Prüfung: 14. Februar 2023

Table of contents

List of figures

List of tables

Abstract

Computations in the brain arise from the functional connectivity of individual neurons, brain regions and circuits. Understanding the fundamental connectivity rules in the brain is an important step to better understand the brain itself. In this dissertation, a suite of methods and approaches were employed to investigate such rules at the synaptic and circuit level.

The first part of this dissertation dealt with the conflicting results of recent structural (Rompani et al., 2017) and functional (Howarth, Walmsley, & Brown, 2014; Jaepel et al., 2017; Sommeijer et al., 2017) reports regarding the degree of functional binocular convergence in the dorsal lateral geniculate nucleus (dLGN). To address this, a novel dual-color optogenetic assay was developed to map functional connectivity between RGCs and individual dLGN cells *in vitro*. While structural convergence is large, with > 60 % of dLGN cells receiving binocular input, the dLGN is functionally monocular: not only did the dominant eye provide > 95 % of a dLGN cell's retinogeniculate input, but the non-dominant eye was unable to elicit the firing of action potentials under resting conditions. Analysis of dLGN cell morphology in relation to the axonal input pattern of RGC afferents in the dLGN revealed axo-dendritic overlap could not explain the levels of functional monocularity observed in the *in vitro* assay. Instead, the dominant and non-dominant eye differed with regards to the expression of AMPA and NMDA receptors, seemingly favoring the dominant eye: fine-scale input selection and refinement were found to limit the functional convergence in the retinogeniculate pathway, resulting in a winner-takes-all wiring rule in this part of the visual circuit.

In the second part of this dissertation a deep learning tool for the detection of dendrites and dendritic spines, termed DeepD3, was developed. DeepD3

directly addresses the current need for automated methods of spine detection. Unlike other areas of neuroscience, where data collection and analysis throughput has improved considerably in the last years, most studies to date still only investigate dozens of dendritic spines per neuron. The analysis - such as identification or segmentation of dendritic spines in image data - represents the main bottleneck in current analysis efforts. DeepD3 was tested against a number of *in vitro* and *in vivo* datasets with varying image properties to ensure that this method performs well in a large range of data qualities. DeepD3 performed as well as human in both *in vivo* and *in vitro* data. Importantly, DeepD3 fully processes large datasets within hours, a procedure which would take months if done via the current gold standard, human annotation. DeepD3 can be flexibly employed for counting dendritic spines or to measure 2D, 3D or time-series fluorescence values of spines and dendrites.

The third part of this dissertation aims towards understanding the functional connectivity rules of LTP-induced dendritic spines. Dendritic spines grow in neurons undergoing LTP (Engert & Bonhoeffer, 1999; Toni et al., 1999) and rapidly form functional synapses (Nägerl et al., 2007). However, it remains unclear which presynaptic neurons are chosen to establish functional connectivity, and hence whether there is a fundamental wiring rule followed by the brain. To address this, improvements to an existing assay to map functional synaptogenesis following LTP *in vitro* (Coneva, 2015) were made. By modifying the timeline of the assay and introducing high-throughput volumetric calcium imaging methods, the throughput of the assay was improved several-fold. Moreover, a molecular approach was devised to combat a potential confounding variable, the lack of spine maturity in nascent spines, when determining functional connectivity rules of LTP-induced dendritic spines. Lastly, several pharmacological and computational means were tested in their ability to assess functional connectivity on a single-spine level despite the occurrence of dendritic calcium events, which otherwise prevent such assessments. Neither the pharmacological, nor the computational methods applied proved effective in this undertaking. As a consequence, determining functional connectivity rules of nascent, LTP-induced dendritic spines remains outstanding. This dissertation paved the way for attempts of this undertaking in the future.

Abbreviations

2D	two dimensional
2p	two-photon
3D	three dimensional
4-AP	4-aminopyridine
AAV	adeno-associated virus
AMPA	aminomethylphosphonic acid
AP	action potential
ACSF	artificial cerebrospinal fluid
AP5	(2R)-amino-5-phosphonovaleric-acid
A.U.	arbitrary units
bV1	binocular primary visual cortex
CA1	cornu ammonis 1
CA2	cornu ammonis 2
CA3	cornu ammonis 3
CAG	CMV early enhancer/chicken β actin
cAMP	cyclic adenosine monophosphate
ChR2	channelrhodopsin 2
CMV	cytomegalovirus
CNN	convolutional neural network
CRACM	channelrhodopsin-assisted circuit mapping
DeepD3	deep-learning framework for the detection of dendrites and dendritic spines
DG	dentate gyrus
DIV	days in vitro
DMSO	dimethyl sulfoxide
DNN	deep neural network
EC	entorhinal cortex

EGTA	ethylene glycol-bis(β-aminoethyl ether)-N,N,N',N'-tetraacetic acid
EM	electron microscopy
EPSC	excitatory postsynaptic current
EPSP	excitatory postsynaptic potential
fEPSP	field excitatory postsynaptic potential
FOV	field of view
GABA	γ-aminobutyric acid
GB	gigabyte
GBSS	Gey's balanced salt solution
GECI	genetically encoded calcium indicator
GFP	green fluorescent protein
GPU	graphical processing unit
h	hour
HBSS	Hank's balanced salt solution
HEPES	4-(2-hydroxyethyl)-1-piperazineethanesulfonic acid
ISI	inter-stimulus interval
LTP	long-term potentiation
MEM	minimum essential medium
MSE	mean squared error
NBQX	6-nitro-2,3-dioxo-1,4-dihydrobenzo[f]quinoxaline-7-sulfonamide
NMDA	N-methyl-D-aspartic acid
n.s.	not significant
OD	optical density
OHSC	organotypic hippocampal slice culture
PCA	principal component analysis
PMT	photomultiplier tube
PSD	postsynaptic density
PVP	polyvinylpyrollidone
RELU	rectifier linear unit
RGC	retinal ganglion cell
ROI	region of interest
RSDR	ratiometric spine-to-dendrite ratio
RT	room temperature
SCE	single-cell electroporation

sCRACM	subcellular channelrhodopsin-assisted circuit mapping
SD	standard deviation
SEM	standard error of the mean
STDP	spike-timing-dependent plasticity
SV40	simian vacuolating virus 40
SV	synaptic vesicle
TC	thalamic cell
tdTomato	tandem-dimer Tomato
Trolox	6-Hydroxy-2,5,7,8-tetramethylchromane-2-carboxylic acid
TTX	tetrodotoxin
V1	primary visual cortex
VGCC	voltage-gated calcium channel
VGSC	voltage-gated sodium channel
VGPC	voltage-gated potassium channel
WPRE	Woodchuck hepatitis virus post-transcriptional regulatory element

Chapter 1

Introduction

1.1 General

The brain is one of the most complex structures in the known universe (Kuhl, 2013). As such, the brain has intrigued countless scientists over time, as they sought to ultimately understand basic, yet abstract features of our everyday lives, such as emotion, sleep, or learning and memory. The brain's building blocks, neurons, were first brought into man focus by Santiago Ramón y Cajal, who published a famous collection containing precise drawings of neurons in 1888 (Ramón y Cajal, 1888). Cajal studied neuronal morphology with the help of Camillo Golgi's silver chromate staining technique (Golgi, 1873; Golgi, 1885). This enabled him to visualize the detailed structures of individual brain cells, such as their dendrites, axons and cell bodies. Cajal rang in the modern era of neuroscience by supplying critical evidence for the later termed Neuron doctrine, the concept that individual nerve cells, neurons, communicate with each other and jointly make up the nervous system.

But how is such communication between neurons achieved? Already prior to Cajal's influential discoveries, the role of electricity in the nervous system had been studied (Galvani & Aldini, 1797; Boulogne, 1876): after the discovery that cell membranes carried a voltage across them (Matteucci, 1841) the first action potential (AP) was recorded in 1843 (Du Bois-Reymond, 1884; Finkelstein, 2013). It soon became clear that neurons must transmit electrical information (i.e. action potentials) between them to communicate. However, where and how this happens remained elusive. Using Golgi staining,

Cajal had persistently observed small bulbous protrusions from the dendrite, so-called dendritic spines ("espinas"; Ramón y Cajal, 1891). In complete disagreement with the dominant doctrine of that time, Cajal correctly postulated that dendritic spines receive input from other neurons' axons, and therefore represent the physical connection points between neurons. However, this connection point, the synapse, could, due to its small size, not be visualized until the mid-late 1950s. With the emergence of electron microscopy, initially individual synapses (De Robertis & Bennett, 1955), and later synapses that contained dendritic spines (Gray, 1959b, 1959a) could be resolved. This discovery, among other things, sparked a large interest in dendritic spines, synapses and their wiring in the field of neuroscience all the way to the present (Yuste, 2015; Ofer et al., 2021b).

The human brain hosts an estimated 100 billion neurons, connected via ∼1.000 trillion synapses (Zhang, 2019). Given the scale of this massively complex structure, one can only wonder about its organization: what are the rules, allowing the brain to function the way it does? And in particular, which fundamental rules of synaptic wiring are in place to aid in the organization of one of the most complex structures we know of? This dissertation attempts to shed light on the influence of synaptic wiring on two scales in two widely studied circuits: at the level of the retinogeniculate synapse and in the Schaffer collateral pathway of the hippocampus.

1.2 The synapse

Synapses are the connection elements between two cells that allow the passing on of electrical or chemical signals. This process, also called synaptic transmission, is essential to the brain's ability to perform computations. Synaptic transmission is realized between two compartments in neurons, typically called presynaptic and postsynaptic compartment, indicating the direction of transmission. A large diversity of synapses exists, which are generally grouped into two categories, electrical and chemical synapses. In the former, electric current is propagated from one neuron to another via a site of direct membrane contact that is equipped with gap-junction proteins. Voltage changes in the presynaptic cell affect these proteins such that electrical current is transmitted to the postsynaptic compartment.

At chemical synapses, signals are transmitted from the presynaptic to the postsynaptic cell in several key steps. First, an action potential arrives at the presynaptic terminal, where it causes the opening of voltage-gated calcium channels (VGCC), which in turn trigger the influx of calcium into the presynaptic compartment. This rise in calcium is detected by synaptotagmin, which causes synaptic vesicles (SVs) to fuse with the presynaptic membrane. Since SVs contain neurotransmitters, this causes the release of neurotransmitters from the presynaptic compartment into the synaptic cleft. The synaptic cleft is a morphological feature that distinguishes chemical from electrical synapses. In contrast to the latter, the former do not share a common membrane but instead are separated via a small crevice in between, the synaptic cleft (De Robertis & Bennett, 1955; Gray, 1959b, 1959a). After presynaptic neurotransmitter release, receptors at the postsynaptic site bind the neurotransmitter and change conformation to allow the passing of ions across the postsynaptic membrane. Neurotransmission at chemical synapses strongly depends on the composition of receptors available postsynaptically and the neurotransmitter type released presynaptically. As such, neurotransmission can be excitatory or inhibitory, via de- or hyperpolarization of a postsynaptic compartment, respectively.

This work focuses on the most common form of excitatory chemical neurotransmission, which relies on the amino acid glutamate as its neurotransmitter. Postsynaptically, such neurotransmission is detected by glutamate-sensitive receptors, of which the two most prominent types are called AMPA (α-amino-3-hydroxy-5-methyl-4-isoxazolepropionic acid) and NMDA (N-methyl-D-aspartic acid) receptors (Watkins & Evans, 1981). Both are expressed in all brain regions (Goebel & Poosch, 1999; Shen & Limon, 2021) and are heavily involved in regulating the brains' excitatory processing. Mutations in their respective genes have been implicated in many disorders (Dingledine et al., 1999; Burnashev & Szepetowski, 2015; Lee, Choi, & Kim, 2015; Henley & Wilkinson, 2016; Salpietro et al., 2019; Hanada, 2020). Most AMPARs are fast, conduct only single-charged cations (such as potassium and sodium), and are responsible for the initial postsynaptic depolarization after neurotransmission (Henley & Wilkinson, 2016; Platt, 2007). NMDARs, on the other hand, are a more complicated family of receptors, which have historically been described as a coincidence detector (Seeburg et al., 1995). While NMDARs, like AMPARs, also bind glutamate, they require two ad-

ditional factors to generate ion flow across a membrane: first, besides glutamate, NMDARs require either glycine or D-serine as a co-agonist to trigger the receptor conformational change. Second, and in contrast to AMPARs, NMDARs require an additional, concurrent depolarization to achieve channel opening (Dingledine et al., 1999). A magnesium ion sits in the channel pore of the NMDA receptor and prevents ions to pass, when a cell's membrane is at resting potential or in a hyperpolarized state. However, sufficient depolarization removes the magnesium, allowing ion flow through the channel pore and across the membrane (Nowak et al., 1984; Mayer, Westbrook, & Guthrie, 1984; Hansen et al., 2018). Hence, NMDAR opening depends on two factors being coincident, A) the availability of both agonists, glutamate and glycine/D-serine, and B) the depolarization of the postsynaptic membrane. Once these conditions are met, NMDARs conduct large currents, and unlike most AMPARs, are also conductive to calcium (Dingledine et al., 1999; Hansen et al., 2018). Once a postsynaptic site is sufficiently depolarized, another action potential can be triggered there, which can then travel along the postsynaptic cell to reach its axonal terminals, where the process of synaptic transmission can restart.

1.3 Dendritic spines

The postsynaptic part of most excitatory synapses is found on dendritic spines. These small protrusions along the parent dendrite act as the brain's fundamental units of neuronal integration (Yuste & Denk, 1995; Losonczy, Makara, & Magee, 2008). Morphologically, dendritic spines (from here on also simply referred to as spines) are characterized by a bulbous head, which is connected to the dendrite via a thin spine neck (Fig. 1A). Historically dendritic spines have been categorized into distinct sub-classes, based on their morphological characteristics of the spine head and neck (Fig. 1.1A; Peters & Kaiserman-Abramof, 1970; Rodriguez et al., 2008). However, recent evidence suggests that spine morphologies are rather distributed along a continuum (Ofer et al., 2021a; Ofer et al., 2022), arguing against categorization of dendritic spines based on the morphological characteristics. Nonetheless, large differences in morphologies exist: smaller spines have a spine length of 0.1-1 μm and spine volume of $\sim$0.01-0.1 μm^3. However, spines can also reach much

greater lengths (>3 μm) and sizes (> 0.25 μm^3). A spine's morphology plays a large role in the function of the synapse it harbors. For example, synaptic strength typically scales with spine size (Holler et al., 2021). Moreover, the morphology of the spine neck dictates how well synaptic inputs are propagated and allowed to participate in dendritic or cellular signaling (Cornejo, Ofer, & Yuste, 2021). Lastly, the size of spines has been associated with their structural stability, with larger spines seemingly being more stable (Trachtenberg et al., 2002; Kasai et al., 2003), whereas smaller spines are more prone to be pruned (O'Donnell, Nolan, & Rossum, 2011).

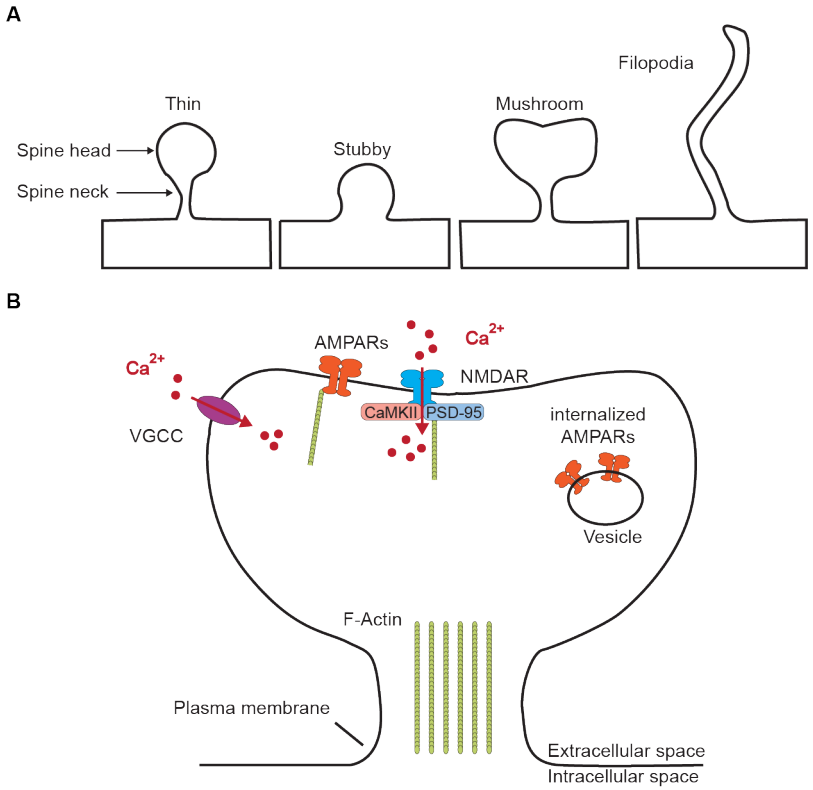

Figure 1.1 Dendritic spines and postsynaptic molecular players
A Morphological types of dendritic protrusions. From top to bottom and left to right: filopodia are characterized by an elongated shape without a visible bulbous head. Stubby spines do not show a thin spine neck other spine types show. Thin spines are characterized by a normal-sized spine head and a thin spine neck.

Mushroom spines have a bulbous spine head and thin spine neck. **B** A dendritic spine and its main molecular players in synaptic calcium signaling. Calcium entry from the extracellular space into the spine head is mediated by VGCCs, AMPARs, and NMDARs. Figure redesigned after Rochefort and Konnerth (2012).

Receptors sensitive to neurotransmitters are typically located in apposition to the presynaptic release zones (active zones; Hruska et al., 2018; Hruska, Cain, & Dalva, 2022). At glutamatergic synapses, most receptors, such as AMPARs or NMDARs, are anchored by proteins within the postsynaptic density. This area, eventually named after its electron-dense appearance in early electron microscopy images (Gray, 1959b, 1959a), harbors many proteins that are critical for synaptic function (Dosemeci et al., 2016). One particularly important protein is PSD-95, which anchors AMPAR and NMDARs in the synapse (Fig. 1.1B; Chen et al., 2015). The abundance of PSD-95 at a spine is correlated with the size of a spine and has been implicated with its stability (Cane et al., 2014). Moreover, since key postsynaptic receptors required for glutamatergic synaptic transmission require PSD-95, this protein has been prominently featured as a marker for spine maturity (El-Husseini et al., 2000; Béıque et al., 2006; Lambert et al., 2017).

1.4 Synaptic plasticity

Synaptic transmission is a highly plastic process that can undergo lasting changes, a phenomenon called synaptic plasticity. The first evidence of this was reported in 1973 in a seminal publication by Bliss and Lømo: they showed that synaptic transmission between pre- and postsynaptic neurons could be increased (potentiated) long-lastingly by specific patterns of presynaptic activity (Bliss & Lømo, 1973). They termed this phenomenon long-term potentiation, LTP for short. This was seen as the first evidence in favor of a long-standing postulate formulated by Donald Hebb in 1949, which reads in its long form: "When an axon of cell A is near enough to excite a cell B and repeatedly or persistently takes part in firing it, some growth process or metabolic change takes place in one or both cells such that A's efficiency, as one of the cells firing B, is increased" (p. 62, Hebb, 1949). Several aspects of

the report by Bliss and Lømo and Hebb's postulate matched: for example, presynaptic activity was driven by electrical stimulation in the experiment, in agreement with the temporal specificity put forward by the postulate (activity in cell A precedes firing in cell B). Hebb's postulate also highlights the need for consistency in presynaptic activity of cell A ("persistently takes part in firing it"), which is reflected in the repetitive stimulation pattern used in the experiment by Bliss and Lømo. Two other aspects are implied in Hebb's postulate, namely (1) the causality of potentiation, as the efficiency of synaptic transmission is improved only after repeated involvement of cell A in cell B's activity, and (2) input-specificity, as it is assumed that changes in synaptic transmission selectively occur at active synapses between cells A and B.

The true validation of Hebb's postulate came more than a decade later, when another form of LTP induction, spike-timing-dependent plasticity (STDP), was discovered. It was shown that the precise timing of pre- and postsynaptic action potentials determines the direction of synaptic plasticity (Levy & Steward, 1983; Gustafsson & Wigstrom, 1986; Dan & Poo, 1992; Markram et al., 1997; Bi & Poo, 1998): if the presynaptic AP precedes the postsynaptic AP by 5-20ms, connecting synapses are strengthened. Instead, if the order is inverted, they are weakend (Bi & Poo, 1998). The temporal sequence of the action potentials, the need for consistency, and the causal nature of the cellular activity fulfilled the fundamental aspects of Hebb's postulate.

Over the years, multiple forms of LTP have been described. However, three fundamental properties of LTP remain the same (Baltaci, Mogulkoc, & Baltaci, 2019): first, only those synapses that were involved in the induction of LTP are potentiated, while others remain unchanged (input-specificity). Second, a joint effort of multiple synapses is required to induce LTP, as unitary connections or weak stimulation typically fail to elicit LTP. This property of LTP is called cooperativity. Third, a weak stimulus can also lead to LTP if it is presented simultaneously with a strong stimulus. Via such an associativity of inputs, LTP can be induced by a stimulus that would typically fall short of triggering LTP (Rogan, Stäubli, & LeDoux, 1997). However, the precise activity patterns required to induce LTP, as well as other aspects seem to vary between brain areas (for a review, see Malenka & Bear, 2004). Nevertheless, one molecular underpinning seems to be conserved among the various forms of LTP and their induction protocols: the induction of LTP

almost always depends on an increase in postsynaptic calcium (Lynch et al., 1983; Madison, Malenka, & Nicoll, 1991) (but see also: Mellor & Nicoll, 2001). Hence, postsynaptic NMDA receptors were identified as critical players in the initiation and maintenance of many forms of LTP, due to their calcium-conducting properties (Collingridge, Kehl, & McLennan, 1983; Harris, Ganong, & Cotman, 1984). Intracellular calcium, when available postsynaptically in sufficient amounts, triggers two chain events responsible for the two phases of LTP, respectively.

First, calcium binds to calmodulin, which in turn binds to Ca^{2+}/calmodulin-dependent protein kinase 2 (CaMKII). CaMKII itself potentiates transmission via binding to membrane-bound AMPA receptors, leading to increases in channel conductance (Derkach, Barria, & Soderling, 1999) and open probability (Banke et al., 2001; Andrásfalvy & Magee, 2004). Moreover CaMKII directly (Opazo & Choquet, 2011) and indirectly (Zhu et al., 2002) causes a redistribution of extrasynaptic AMPARs closer to the synaptic cleft (Opazo & Choquet, 2011) or insertion of internalized AMPARs in the PSD (Lu et al., 2001b). This increase in postsynaptic AMPA receptor number is one of the main underpinnings of a synapse's potentiation during LTP (Terashima, Suh, & Isaac, 2019; Choquet & Opazo, 2022). This initial phase of AMPAR potentiation and insertion is also called early LTP (E-LTP; Abraham & Williams, 2003).

The second phase, called late LTP (L-LTP), consists of the synthesis and trafficking of new proteins, such as AMPA receptors or its anchoring proteins (e.g. PSD-95), to the postsynaptic site (Frey et al., 1988; Nguyen, Abel, & Kandel, 1994). This depends critically on several messenger pathways, in which cyclic adenosine monophosphate (cAMP) and its downstream targets play an important role (Frey, Huang, & Kandel, 1993; Nayak et al., 1998). The synthesis of new proteins, such as glutamate-sensitive receptors, improve the efficiency of synaptic transmission, thereby achieving potentiation thereof.

Over time, it became clear that LTP can also be induced by players other than NMDARs, such as calcium-permeable AMPARs (Gu et al., 1996; Jia et al., 1996), or voltage-gated calcium channels (VGCCs; Bauer, Schafe, & LeDoux, 2002). Moreover, expression of LTP is also frequently seen presynaptically (Zalutsky & Nicoll, 1990; Salin, Malenka, & Nicoll, 1996; Enoki et

al., 2009), and LTP properties can vary from brain area to brain area (Citri & Malenka, 2008). Additionally, besides LTP, other forms of synaptic plasticity that can shape the landscape of synaptic strength have been discovered, such as homeostatic plasticity (Turrigiano & Nelson, 2004), metaplasticity (Abraham & Bear, 1996), and long-term depression (LTD; Ito, Sakurai, & Tongroach, 1982; Mulkey & Malenka, 1992). Hence, in the living brain, many mechanisms are at work in parallel, continuously changing synaptic transmission efficacy over time.

1.5 Structural plasticity

Electrophysiological changes in synaptic transmission, as seen during LTP, are frequently accompanied by structural changes at the spine level. Fluctuations in spine structure happen naturally (Woolley et al., 1990) and with the emergence of chronic structural imaging it was evident that dendritic spines emerge and disappear frequently, a process also called spine turnover, or more generally, spine dynamics (Holtmaat et al., 2005; Bhatt, Zhang, & Gan, 2009; Pfeiffer et al., 2018). However, it became clear that LTP and LTD cause more systematic changes, unlike those observed during naturally occurring spine turnover: while LTD is typically associated with spine shrinkage (Zhou, Homma, & Poo, 2004) and later on with spine loss (Wiegert & Oertner, 2013), LTP manifests itself structurally in two ways. First, the spines of potentiated synapses increase in size in an activity-dependent manner (Hosokawa et al., 1995; Matsuzaki et al., 2004; Kopec et al., 2006). This process happens in the span of minutes and is carried out by CaMKII-mediated polymerization of actin (Fifková & Van Harreveld, 1977; Okamoto et al., 2007). Spines grow rapidly initially and then shrink again towards a new stable spine size that is larger than its pre-LTP state (Okamoto et al., 2004). Critically, enlargement of dendritic spines also stabilizes them and therefore extends their lifetime (De Roo, Klauser, & Muller, 2008; Wiegert et al., 2018). Following LTP, the spine neck decreases in length but increases in width, leading to an overall decrease of its compartmentalizing effect on synaptic input (Fifková & Anderson, 1981), thereby increasing a spine's ability to influence dendritic or somatic signaling (Tsay & Yuste, 2004; Araya, Vogels, & Yuste, 2014). The postsynaptic density size increases proportionally to the spine head size after LTP to maintain a similar relationship between PSD and spine size (Desmond & Levy, 1986; Ostroff et al., 2002; Meyer, Bonhoeffer, & Scheuss,

2014). These changes jointly enable the accommodation of more receptors at a potentiated dendritic spine (Opazo, Sainlos, & Choquet, 2012) and allow the spine to contribute more strongly to somatic and dendritic signaling.

The second structural manifestation of LTP is the activity-dependent emergence of new dendritic spines (Engert & Bonhoeffer, 1999; Toni et al., 1999; Maletic-Savatic, Malinow, & Svoboda, 1999). Some of these nascent spines remain stable after hours and form functional synapses (Nägerl et al., 2007). Critically, activity-dependent spinogenesis has also been observed *in vivo* after events of somatosensory (Zuo et al., 2005; Holtmaat et al., 2006) or visual deprivation (Keck et al., 2008; Hofer et al., 2009). Moreover, growth of dendritic spines can be triggered by certain learning events (Roberts et al., 2010; Fu et al., 2012; Briones et al., 2018) or the consolidation of memories (Restivo et al., 2009; Vetere et al., 2011). Besides experience-dependent changes, other factors, such as the hormones ghrelin or estradiol, have been found to modulate the process of activity-dependent spinogenesis (Diano et al., 2006; Murakami et al., 2006; Sellers et al., 2015). While the electrophysiological consequences of structural plasticity in pre-existing spines after LTP are relatively well established (for a review, see Baltaci, Mogulkoc, & Baltaci, 2019), much less is known about the functional consequences of LTP-induced spinogenesis. Critically, it is entirely unknown with which presynaptic neurons new synaptic connections are formed. Whether or not synaptogenesis via the growth of LTP-induced dendritic spines follows the same activity-dependent and input-specific rules LTP itself does remains unclear. Some evidence is provided by an electron microscopy study, which found that following LTP, many axonal boutons had established functional synapses with two previously active dendritic spines that shared the same dendritic branch (Toni et al., 1999). This suggests that at least some newly-grown dendritic spines form functional synapses with axons that induce LTP. However, due to several technical limitations, the report could account for only a small number of LTP-induced dendritic spines and their functional wiring preferences. These preferences could have far-ranging consequences. For example, LTP-induced synaptogenesis could follow a single wiring rule, shaping circuits throughout the brain in the same manner. Alternatively, several wiring rules could be at work, varying between cell types and brain areas, similarly to how LTP can depend on different molecular players and stimulation patterns in different brain regions.

Interestingly, in the past many of the structural hallmarks of LTP are also observed during learning or experience-dependent plasticity paradigms (Holtmaat et al., 2006; Hofer et al., 2009). Consequently, it is generally believed that LTP underlies memory formation and consolidation, as well as other experience-dependent behavioral changes. In fact, it has been reported that a previously consolidated memory that had been dormant could be reactivated using LTP of a particular sensory input (Nabavi et al., 2014). In another study, new memories could be generated via LTP induction (Jeong et al., 2021), indicating that LTP may at least in part underlie memory formation/consolidation. Hence, it is possible that the structural changes accompanying LTP, such as spine remodeling and the emergence of new dendritic spines, are critical to many forms of experience-dependent plasticity *in vivo*. As a consequence, identifying the precise wiring rules that LTP-induced dendritic spines follow will be pivotal to better understand how learning and memory are implemented and represented in the brain.

1.6 The hippocampus

The hippocampus is one of the most studied brain structures, and is located bilaterally in the medial temporal lobes of mammalian brains. Named after its uncanny resemblance to the sea horse (subfamily of *Hippocampinae*; Greek: 'hippocampus'), its popularity in research was sparked by research on a patient named H.M. (Henry Molaison; Scoville & Milner, 1957): H.M. suffered from epilepsy, and following the medical and scientific trends at the time, underwent a bilateral medial temporal lobectomy in an attempt to cure his epileptic seizures. This surgery removed both hippocampi (amongst other brain structures). Hippocampal loss following surgery caused anterograde amnesia, a condition in which the patient is unable to recall newly formed memories for longer than a few minutes (Scoville & Milner, 1957). The causal role the hippocampus seemingly played in the formation of memories motivated researchers to more systematically study its structure and function. Although it was later found that patient H.M. had extensive damage outside of the mediotemporal lobe as well (Corkin et al., 1997; Annese et al., 2014), the hippocampus has been identified as a critical brain area for the formation of memories (Lacruz et al., 2010; Robinson et al., 2020).

The structure of the hippocampus has since been well documented, and con-

sists of the dentate gyrus and the *cornu ammonis* region, which can be further divided into subparts (CA1-CA3; Fig. 1.2). The main source of hippocampal input arrives via the perforant path from the entorhinal cortex to granule cells in the dentate gyrus (DG; Witter & Amaral, 1991). The DG in turn projects via the mossy fiber pathway to the CA3 region. Mossy fibers preferentially target proximal apical dendrites of CA3 pyramidal neurons. The CA3 region gives input to the CA1 region via the Schaffer collaterals, which target apical dendrites of CA1 pyramidal cells, completing the so-called trisynaptic circuit (Andersen, Bliss, & Skrede, 1971). However, given that the CA3 region shows high levels of recurrency, this name is not entirely justified. The CA1 region is the main output region of the hippocampal formation, mainly via the subiculum and the EC, and to a lesser degree via projections to regions such as the nucleus accumbens, the contralateral hippocampus, the prefrontal cortex and olfactory areas via the fimbria (Cenquizca & Swanson, 2007). Apart from its highly organized synaptic architecture, the hippocampus has a highly preserved cytoarchitectonic organization (Fig. 1.2; Andersen et al., 2006): the DG has three layers the molecular layer, granule cell layer and a polymorphic layer, which is sometimes also referred to as the hilus of the dentate gyrus. Granule cell dendrites are oriented towards the molecular layer, with the granule cellbodies lying in the granule cell layer, while the mossy fibers cross the polymorphic layer towards CA3. The regions of the cornu ammonis follow a similar organization to that of the DG, with cell bodies lying closely packed in the *stratum pyramidale*. From there, basal dendrites grow outwards, into the *stratum oriens*. The organization of their inner layers of CA1-3 is as follows: *stratum radiatum* and *stratum lacunosum-moleculare* (in order towards the pial surface) can be found in all three *cornu ammonis* regions, while the CA3 region contains an additional, innermost layer, the *stratum lucidum* (Andersen et al., 2006; Amaral, Scharfman, & Lavenex, 2007).

Findings about the hippocampus' structural innerworkings have brought forward influential computational models, aiming to explain the role of the hippocampus in memory and recall (Marr, 1971; Treves & Rolls, 1994). Notably, the hippocampus has also been involved in a multitude of fundamental behavioral processes besides memory encoding. It is a critical structure for spatial memory and navigation: not only do single cells in the hippocampus code for the spatial position of an animal (O'Keefe & Dostrovsky, 1971; Ranck Jr,

1973; O'Keefe, 1976; Leutgeb et al., 2004) but ablation or modulation of activity in the hippocampus strongly disrupts spatial learning (Morris et al., 1982; Morris et al., 1986; Robinson et al., 2020). Additionally, a wide array of cell-types relevant to spatial mapping and navigation have been identified in the hippocampus or areas directly associated to it (such as EC or the subiculum): grid cells (Hafting et al., 2005; Doeller, Barry, & Burgess, 2010; Yartsev, Witter, & Ulanovsky, 2011), boundary cells (Solstad et al., 2008; Boccara et al., 2010), time cells (MacDonald et al., 2011), head direction selective cells (Ranck Jr, 1984), or cells that are tuned to the position of social conspecifics (Omer et al., 2018)

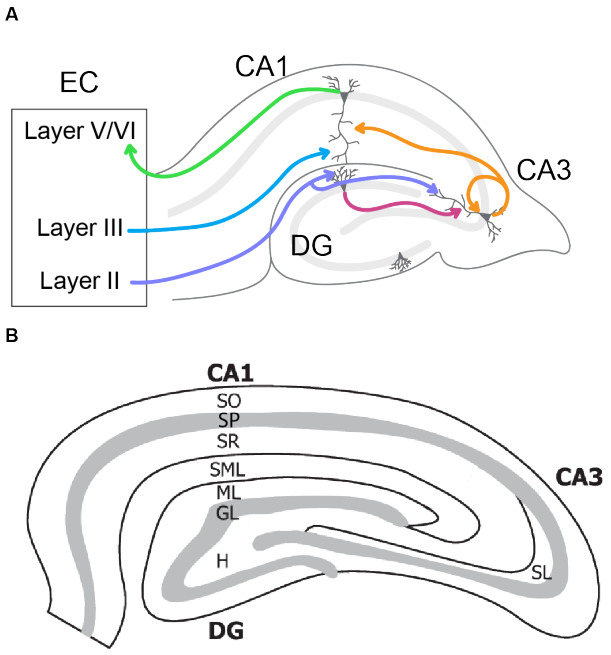

Figure 1.2 The hippocampal circuit and structure
A The hippocampal circuit. Input to the hippocampus arrives via the entorhinal cortex (EC) to the dentate gyrus (DG, purple arrow) and the CA1 region (blue arrow). The dentate gyrus projects to the CA3 region (pink arrow), which exhibits strong recurrent activity (loop-shaped yellow arrow). The CA3 region feeds information forward via the Schaffer collateral pathway to the CA1 region (yellow arrow), which constitutes the main output region of the hippocampus (here visualized via a green arrow back to the EC). Figure panel designed after

Ludkiewicz et al. (2002). **B** The structure of the hippocampus. SO: *stratum oriens*, SP: *stratum pyramidale*, SR: *stratum radiatum*, SML: *stratum lacunosum-moleculare*, SL: *stratum lucidum*, ML: molecular layer, GL: granule cell layer, H: hilus of dentate gyrus. Figure panel modified from Petrantonakis and Poirazi (2014) with permission.

Aside from research in the intact animal, the hippocampal structure has emerged as one of the most frequently used means of investigating basic neuronal function *in vitro*. Dissociated primary hippocampal cell cultures disrupt its stereotypical wiring, yet constitute a great model to explore fundamental neuronal properties by physiological and molecular means (Banker & Cowan, 1977; Kaech & Banker, 2006). Alternatively, the trisynaptic circuit is maintained in two other preparations, the acute slice (Schwartzkroin, 1975) and the organotypic hippocampal slice culture (Gähwiler, 1981; Stoppini, Buchs, & Muller, 1991b). Particularly, the latter emerged as a mean to investigate the well-studied hippocampal circuit with a high degree of experimental control over the course of several weeks (Gähwiler, 1988; Gähwiler et al., 1997; Engert & Bonhoeffer, 1999; Wiegert & Oertner, 2013). For this reason, many of the fundamental properties of dendritic spines, such as changes during events of structural plasticity and their response properties to synaptic input have been determined in experiments using organotypic hippocampal slice cultures (Engert & Bonhoeffer, 1997, 1999; Lu et al., 2001a; Roo et al., 2007; De Roo et al., 2008; Wiegert & Oertner, 2013; Wiegert et al., 2018). In the third part of dissertation, this preparation will be utilized to attempt to investigate the functional connectivity rules of LTP-induced dendritic spines (Results 3.3).

1.7 The visual system

While the hippocampus lends itself to study synaptic wiring rules at the spine and cellular level, it is also essential to investigate these rules at a circuit and systems level. In this dissertation, such an investigation was performed in the visual system, and in particular in the visual thalamus, where inputs from the two eyes terminate (Results 3.1).

Vision shapes our everyday perception of the environment more than any other sense. Hence, understanding how the brain computes its physical environment visually has been a long-standing goal of neuroscience. Traditionally, a number of model systems have been used in vision research. However, in the last two decades, the mouse has been the dominant model organism in visual neuroscience, due to the flexibility afforded by modern genetic manipulation tools, the improved ability to control cellular activity, the increased throughput of data acquisition methodologies, as well as relatively low maintenance costs and convenience in terms of size and handling (Seabrook et al., 2017; Farris, 2020). Undeniably, there are several differences between the mouse and human visual systems, such as the fact that the mouse is a crepuscular animal with relatively low visual acuity, which makes it rely on other sensory systems more than vision when exploring its surroundings. Nonetheless, the overall architecture of the mouse and human visual systems is very similar, with visual processing steps occurring at similar places in both systems.

1.7.1 The retina

In the mouse visual system, light is captured by the optical apparatus in the eye and projected onto the retina. The retina is organized into five layers, three of which are nuclear and two of which are synaptic (Wassle & Boycott, 1991; Baden, Euler, & Berens, 2020). Initially, light is detected by rod- and cone photoreceptors, located in the photoreceptor layer. Here phototransduction occurs, a process in which light-sensitive proteins called opsins convert incoming photons into neuronal signals. Via the first synaptic layer, the outer plexiform layer, the information of the photoreceptors is passed onto horizontal and bipolar cells (Kolb, 1977). The former, inhibitory horizontal cells, provide feedback to the photoreceptors and feedforward information to bipolar cells, while the latter feed information forward to retinal ganglion cells (RGCs) and amacrine cells via the inner plexiform layer (Wassle & Boycott, 1991). Here again, inhibitory amacrine cells provide feedback to bipolar cells and feedforward information to RGCs. RGCs themselves form the output layer of the retina, and project to dozens of subcortical regions via the optic nerve (Morin & Studholme, 2014).

Of key importance in retinal, and visual processing in general, is the extraction of spatial features in the visual scene. To achieve this, retinal cells

typically react to changes in a confined region of visual space, their receptive fields. Across the visual system, many neurons exhibit sensitivity to certain characteristics within the receptive field. For example, some RGCs prefer a bright center and a dark surround within their receptive fields, while others prefer the opposite (ON-center and OFF-center RGCs, respectively; Kuffler, 1953; Hartline, 1969; Werblin & Dowling, 1969). Moreover, some RGCs are sensitive to motion within their receptive field, while others are not (Lettvin et al., 1959; Barlow, Hill, & Levick, 1964; Baden et al., 2016). Overall, at least 32 distinct RGC celltypes have been identified in the mouse retina, generating a large combinatorial diversity for downstream processing (Baden et al., 2016).

1.7.2 Retinal projections

In the mouse, RGC axons are bundled in the optic nerve, and the vast majority of such projections cross over to the contralateral hemisphere at the optic chiasm, with only 5% of RGC axons projecting ipsilaterally (Fig. 1.3; Williams et al., 2003). Visual input is provided via the optic nerve to several retinorecipient areas. Most RGC axons project to either the superior colliculus or the dorsal lateral geniculate nucleus (dLGN; Martersteck et al., 2017b), providing input for the image-forming pathways. However, in total, over 50 (Martersteck et al., 2017b) brain regions receive direct retinal inputs, contributing to functions of non-image-forming circuits such as the pupillary light reflex or the maintenance of the circadian rhythm (Osterhout et al., 2011; Sweeney, Tierney, & Feldheim, 2014; Fernandez et al., 2016).

A key feature of the image-forming pathways is their retinotopic organization: visual space is mapped in these particular brain regions such that it parallels the topological organization of receptive fields in the retina. Hence, neighboring features in the visual scene are also represented by neighboring neurons in the retina and some subsequent areas in the image-forming pathways. The precise arrangement of RGC projections aids in propagating the retinotopic map across the image-forming retinorecipient areas.

1.7.3 Dorsal lateral geniculate nucleus (dLGN)

The dorsal lateral geniculate nucleus, is a nucleus located in the posterior-lateral part of the thalamus. Other thalamic nuclei, involved in visual pro-

cessing are located in close proximity to the dLGN, such as the intergeniculate leaflet of the lateral geniculate complex (IGL), the ventral lateral geniculate nucleus (vLGN), and the lateral posterior nucleus of the thalamus (LP; Lein et al., 2007).

Biochemically, the mouse dLGN can be subdivided into two regions: (1) the shell region, neighboring the optic tract on the dorsolateral surface of the dLGN and (2) the core region, which, in contrast to the shell region, does not contain calbindin positive cells (Grubb & Thompson, 2004). Besides this separation, neurons in the dLGN can also be split into categories based on their mode of neurotransmission: excitatory thalamic relay cells (TRCs, ∼85 % of neuronal dLGN cells) and inhibitory interneurons (∼15 %, Arcelli et al., 1997), both of which receive retinogeniculate input. Morphologically, TRCs exhibit large variability, with conflicting reports on distinct morphological categories (Krahe et al., 2011; Morgan et al., 2016). Interneurons in the dLGN are different to TRCs in that they innervate other TRCs and have larger dendritic reach (Morgan et al., 2016).

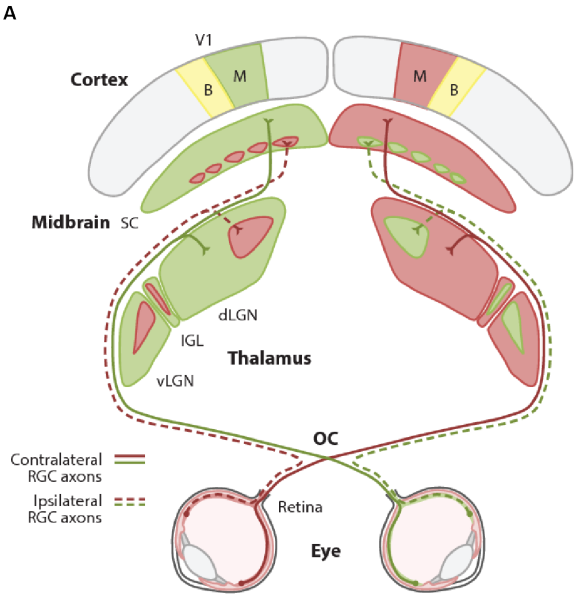

Figure 1.3: The canonical view of the mouse visual system in the adult animal
A RGCs from both retinae project via the optic chiasm to the visual thalamus and SC. From the former, information is forwarded to the primary visual cortex. V1: primary visual cortex, SC: superior colliculus, B: binocular region, M: monocular region, dLGN: dorsolateral geniculate nucleus, vLGN: ventrolateral geniculate nucleus, IGL: intergeniculate leaflet, OC: optic chiasm, RGC: retinal ganglion cell. Figure modified from Seabrook et al. (2017) with permission.

Functionally, the dLGN has been historically viewed as a relay station, passing on information from the retina to visual cortex without large modifications. This notion is supported by several processes occurring during the development of the mouse dLGN: Innervation of RGC axons into the dLGN occurs around E16-E18 (Godement, Salaün, & Imbert, 1984). In the first postnatal weeks, retinogeniculate projections separate diffusely into eye-specific projection zones without clear borders (Stevens et al., 2007). Distinctly segregated eye-specific RGC axon terminal projection zones are established around p12-p14 (Jaubert-Miazza et al., 2005; Pfeiffenberger et al., 2005). During this process, retinogeniculate projections are pruned in an activity-dependent process that is mediated via proteins in the complement family and local microglia (Stevens et al., 2007; Schafer et al., 2012). The developmental segregation of eye-specific input zones is accompanied by the developmental switch of AMPA over NMDA receptor expression in the retinogeniculate synapse (Hooks & Chen, 2006), further favoring inputs of one eye. Functionally, binocular connectivity reportedly fades in the dLGN after P18 (Ziburkus & Guido, 2006). As a consequence, dLGN cells in the adult animal have been historically viewed as functionally monocular, relaying information between the retina and the visual cortex.

Recently however, this view has been challenged on structural and functional grounds. Utilizing monosynaptic rabies tracing, it was found that dLGN cells receive input from up to 91 individual RGCs. Critically, almost half (40 %) of TRCs were found to be structurally connected to both retinae (Rompani et al., 2017), indicating that binocularity could be abundant in the dLGN. Further evidence came from *in vivo* calcium imaging studies, targeting dLGN TRC afferent boutons at the level of visual cortex. Here, it was shown that some, albeit relatively few (6-14 %), of these boutons are responsive to stimulation of either eye (Jaepel et al., 2017; Huh et al., 2020). In contrast, electrophysiological recordings performed directly in the dLGN, suggest that binocularity might be much more ubiquitous in the dLGN, with up to 33 % of cells responding to stimulation of either eye (Howarth, Walmsley, &

Brown, 2014; Sommeijer et al., 2017). While these reports are in line with the results of Rompani et al. (2017), it remains unclear to what extent the dLGN functionally integrates information of both eyes. *In vitro* studies have shown that input to dLGN cells is dominated by 1-3 RGC neurons, which determine the response properties of a given TRC (Ziburkus & Guido, 2006; Litvina & Chen, 2017; Rosón et al., 2019). Moreover, in addition to retinogeniculate input, dLGN neurons receive a multitude of smaller, modulatory input from thalamic, cortical and tectal areas (Roth et al., 2016; Born et al., 2021). Therefore, there is a need for a thorough investigation mapping functional binocularity in the dLGN and assessing how much binocular integration occurs at the retinogeniculate synapse.

1.7.4 Visual Cortex and higher order areas

Visual cortex is the main recipient of dLGN afferents, and as such, an important part of the image-forming pathway of the mouse (Fig. 1.3). Visual cortex is subdivided into primary visual cortex (V1) and many higher-order visual areas, which are extensively and reciprocally connected with the former. V1's input-output connectivity is manifested in its multi-layered architecture: while all layers (L1-6) receive thalamocortical input, input is strongest in layer 4 (Harris & Shepherd, 2015). From L4, information is distributed to all other cortical layers, with L2/3 receiving more input than the other layers (Niell, 2015). L2/3 in turn projects most strongly to L5, with some input also projecting to other cortical areas and the contralateral hemisphere. From L2/3, information is sent to L5 but also to other cortical areas as well as the contralateral hemisphere. Within L5, information is forwarded to regions within the cortex (e.g. L6 and the contralateral hemisphere) or to subcerebral targets (Niell & Scanziani, 2021). L5 and L6 are host to excitatory cells called corticocortical and corticothalamic neurons, which project to other cortical and thalamic regions, respectively (Vries et al., 2020). These cells mainly receive input from L2/3, and constitute the main output layers of the visual cortex. The most superficial of cortical layer, L1, contains mostly dendrites of excitatory neurons of deeper levels and very few neuronal cell bodies. Here, cortical and subcortical input converges onto the apical dendrites of neurons of the deeper layers (e.g. L5).

Functionally, the mouse visual cortex displays a number of features that are critical for visual processing, which have also been found in other species (Hubel & Wiesel, 1959, 1962, 1968). First, retinotopy is maintained throughout V1 and many higher-order visual areas (for review, see Glickfeld and Olsen, 2017). Additionally, receptive fields show distinctly more complex patterns in V1 compared to lower-level visual areas (e.g. dLGN). As such, cells in V1 have response properties strongly tuned to the orientation and direction of stimuli, as well as to the spatial and temporal patterns within (Metin, Godement, & Imbert, 1988; Andermann et al., 2011).

1.8 Methodological considerations

1.8.1 Advances in light microscopy

The light microscope has been a foundational tool of neuroscience since its infancy: Santiago Ramón y Cajal used it in conjunction with the Golgi staining method to visualize the structure of individual neurons in the late 1800s (Ramón y Cajal, 1888). In the past 40 years, light microscopy has been further developed and refined, and as a consequence it is featured as a prominent technique in many neuroscience research endeavours (White, Amos, & Fordham, 1987; Denk, Strickler, & Webb, 1990; Sheppard & Shotton, 1997; Nguyen et al., 2001; Helmchen & Denk, 2005; Nikolenko, 2008; Kazemipour et al., 2019). Nowadays, light microscopy typically involves the use of fluorophores, substances that emit light after absorption of photons. Fluorophores are sensitive to photons of a certain range of wavelengths, comprising their excitation spectrum, and emit photons of another range of wavelengths, forming their emission spectrum. At the quantum level, absorption of a single photon moves a fluorophore to a higher energy level, which can trigger a radiative transition, resulting in the emission of a photon. The excitation and emission spectra, i.e. the wavelength with which a fluorophore can be excited, and the wavelength of the emitted photons following excitation, vary between fluorophores.

In confocal microscopy, the excitation light beam is focused to a small area, the so-called focal point of the microscope, in which the majority of flu-

orophore excitation occurs. However, since some emission also originates from areas outside of the focal point, photons must be spatially filtered during photodetection, i.e. by using a pinhole to allow passing of only those photons that originate from the focal point. While pinholes reliably block out-of-focus photons during photodetection, the excitation of fluorophores outside the focal point in confocal microscopy can lead to undesired side effects, such as phototoxicity and photobleaching of tissue. To obtain an image of a region of interest, the focal point is guided throughout the sample with the help of scan mirrors. Raster-scanning the focal point in this manner can generate a digital 2D fluorescence image of the sample in the focal plane. To visualize objects in the sample in 3D, the focal plane is typically moved up- or downwards, generating multiple image planes, comprising an image stack, which contains the object of interest in 3D.

Notably, fluorophores can also be excited by the simultaneous absorption of two instead of one photon. In this case, the two photons each carry approximately half the energy required to transition the fluorophore to a higher energy level before emission. This process is called two-photon absorption, and it offers several advantages over one-photon fluorescence measurements regarding certain aspects of light microscopy. For example, since photons used for excitation in two-photon microscopy require half the energy than those in one-photon microscopy, and since photons of higher wavelength carry less energy, near-infrared or infrared lasers are frequently employed in 2p imaging. The use of light at these wavelengths permits the excitation beam to penetrate tissue much more effectively with less light scattering along the distance traveled than light sources in the visible spectrum. This effectively allows for imaging of deep brain regions that are impossible to reach using conventional fluorescence microscopy (Helmchen & Denk, 2005). Ti:sapphire lasers are commonly used in two-photon microscopy to generate a laser beam in the infrared spectrum. Importantly, instead of providing a steady supply of photons, these lasers pack photons together closely in time with intervals of no light emission in between. This aids in achieving the required simultaneous absorption of two photons by fluorophores in the sample, a process that would rarely happen otherwise.

Similar to confocal microscopes, two-photon microscopes focus light via objective lenses to a focal point. Outside of this small area, effective excitation of fluorophores rarely happens, eliminating most out-of-focus excitation

(Denk, Strickler, & Webb, 1990). As a consequence, the vast majority of photons emitted from the sample can be regarded as coming from the target point in the sample, what is known as "signal" (principle of optical sectioning). As a consequence, compared to confocal microscopy, phototoxicity and photobleaching are usually more manageable in two-photon microscopy, given there is almost no out-of-focus excitation. In both of these imaging techniques, emitting photons are typically measured employing sensitive photodetection methods, such as photomultiplier tubes (PMTs).

Over time, countless improvements in two-photon microscopy have been developed, such as increased scanning speed (resonant scanning, Nguyen et al., 2001; two-photon tomography, Kazemipour et al., 2019; reverberation two-photon microscopy, Beaulieu et al., 2020; light beads microscopy, Demas et al., 2021a) spatial resolution (adaptive optics, 2012, 2012, 2017, Ji; two-photon super-resolution imaging, Moneron and Hell, 2009, Ding, Takasaki, and Sabatini, 2009), or efficiency of photon detection (Wu, Hawkins, & Bowers, 1997; Becker et al., 2010; Ching-Roa et al., 2021). Moreover, attempts were made to improve how the focal point is moved through the sample, in order to obtain images faster or with higher sampling from certain areas of interest. These operational degrees of freedom are made available through methods such as temporal focusing (Oron, Tal, & Silberberg, 2005; Zhu et al., 2005), remote focusing (Botcherby et al., 2008) or random-access imaging (Nadella et al., 2016). Some of these techniques require spatial light modulators (SLMs), devices that enable pixel-wise phase modulation of the excitation beam with high temporal resolution. Such precise and flexible manipulation of beam wavefronts has allowed for other novel two-photon imaging methods that have further improved operational degrees of freedom when imaging, such as holographic 3D imaging (Nikolenko, 2008), mesoscope imaging (Sofroniew et al., 2016; Yu et al., 2021), or volumetric imaging (Lu et al., 2017). Leveraging these advances in optical imaging allows for faster recording and/or acquisition of larger amounts of tissue. This has enabled researchers to advance the frontier of possible experiments and perform whole-brain imaging experiments *in vivo* (Hoffmann et al., 2022) or sample from brain areas with unprecedented temporal resolution (Kazemipour et al., 2019).

1.8.2 Genetically-encoded indicators

Alongside the development of two-photon microscopy came the advent of genetically encoded fluorophores, such as green fluorescent protein (GFP; Prasher et al., 1992; Chalfie et al., 1994; Inouye & Tsuji, 1994; Heim, 1995; Cormack, Valdivia, & Falkow, 1996). Critically, the cloning and directed expression of such fluorophores allowed scientists to label cells with much improved precision via genetic methods. Moreover, spectral variants, such as cyan fluorescent protein (CFP) were generated soon after the characterization of GFP (Heim, Prasher, & Tsien, 1994). Nowadays, several fluorophores can be expressed with minimal spectral overlap to visualize specific proteins, cell types, or cellular compartments in the same field of view simultaneously (Depry, Mehta, & Zhang, 2013; Falkner et al., 2016; Bauer et al., 2021).

Genetically encoded fluorophores are also utilized as reporter proteins of locally occurring molecular changes. For example, GFP fused to the calcium-binding protein calbindin can be utilized as a genetically encoded calcium indicator (GECIs; Nakai, Ohkura, & Imoto, 2001). In particular, the fluorescence of GECIs is quenched when little or no calcium can be bound by the calcium-sensitive part of the protein. On the other hand, when calcium is bound to calbindin, the fluorophore can emit without obstruction. Hence, local availability of calcium is reported as increases in GECI fluorescence. Since action potentials, and even many types of sub-threshold inputs, trigger the influx of calcium into a neuron, quantifying the fluctuations of intracellular calcium concentrations via GECIs serves as an indirect but close proxy of neuronal activity (Yuste et al., 1999; Lütcke et al., 2013).

Originally, the only fluorescent reporters of biological processes were chemically based. Such synthetic dyes were either introduced to cells in bulk or to single cells via dialysis (e.g. patch-clamp). However, such labeling is not permanent, making chronic imaging experiments challenging. Moreover, filling single cells with a dye can alter the way these cells undergo plastic events (Malinow & Tsien, 1990), rendering this type of labeling unsuited for certain experiments.

GECIs, on the other hand, can be expressed in genetically defined subpopulations of cells with high specificity. This allows for chronic imaging of cells or subcellular structures over long periods of time. However, chronic

overexpression of any protein should be done with care, as many fluorophores, though not cytotoxic themselves (Shemiakina et al., 2012), can lead to severe issues in cellular signaling and eventual cell death if expression is too high. Since expression can effectively be controlled by choice of promoter and posttranscriptional regulatory elements, overexpression artifacts can nowadays typically be avoided. These advantages of genetically-encoded reporter proteins over synthetic dyes underlie the popularity GECIs have gained in recent years (Holtmaat et al., 2009). Over the years, GECIs have also improved in terms of photostability and brightness (Goedhart et al., 2012; Akerboom et al., 2012; Chen et al., 2013; Dana et al., 2019; Zhang et al., 2020), rivaling the optical properties of formerly popular synthetic calcium indicators. Nowadays, GECIs are flexibly utilized to record from large neuronal populations *in vivo* (Rose et al., 2016; Smith et al., 2018; Yu et al., 2021), track calcium dynamics in dendritic spines (Chen et al., 2012; Wilson et al., 2016; Dana et al., 2019; Ali et al., 2020; Scholl et al., 2021) or dendrites (Roome & Kuhn, 2018; Kerlin et al., 2019), or visualize calcium processing in organelles (Suzuki, Kanemaru, & Iino, 2016; Gökerküçük, Tramier, & Bertolin, 2020) among others.

In this dissertation, modern GECIs were utilized to measure synaptic connectivity between genetically defined populations of pre- and postsynaptic cells over long periods of time. Reliable and time-locked calcium influx into postsynaptic compartments, such as dendritic spines, following stimulation of presynaptic terminals indicates functional synaptic connectivity between such cell populations. This powerful method enables large-scale investigations into the functional connectivity of neurons and their changes in living tissue. Detecting functionally connected spines is aided by the morphological characteristics of the spine neck, which can aid in confining the area of calcium influx to the spine head and prevent calcium signaling to spill into the dendritic arbor. However, coincident synaptic input at multiple postsynaptic sites in close proximity can trigger dendritic calcium spikes, which flood the dendritic arbor and its dendritic spines with calcium. Such a regenerative dendritic calcium event can mask which spines showed increases in calcium due to synaptic transmission, complicating quantification of synaptic connectivity via GECIs. To address this problem, computational (Coneva, 2015; Wilson et al., 2016; Kerlin et al., 2019), electrophysiological (Chen et al., 2011) and pharmacological methods (Chalifoux & Carter, 2011; Grienberger, Chen, & Konnerth, 2014; Kovalchuk et al., 2000) have been tested in

the past, to enable mapping functional connectivity on a single-spine basis in spite of dendritic calcium events. However, while some advances could be made, regenerative dendritic calcium events remain problematic for the extraction of synaptic connectivity on a single-spine basis in some experimental settings (see Results 3.3.3-3.3.6).

1.8.3 Deep neural networks for automated image segmentation

The size of imaging datasets has increased rapidly in the last years (Landhuis, 2017). This has brought forward a need for automated, unsupervised data processing and analyses. However, many endeavours in neuroscience still rely on manual annotation, or the need for manual intervention, during data processing. For example, until recently, behavioral phenotypes were typically classified by blinded researchers via visual inspection of videographic data. Recently, software packages have been developed to automatically estimate the pose of an animal with minimal time investment of the researchers (Mathis et al., 2018; Pereira et al., 2019; Graving et al., 2019; Liu et al., 2020; Lauer et al., 2021). Using changes in animals' poses, behavioral phenotypes can then be classified automatically without the need of human involvement (Vyas et al., 2019; Fang et al., 2021).

These software packages utilize modern methods of artificial intelligence, in particular deep learning. Deep learning is a subfield of machine learning, in which artificial neural networks (ANNs) are trained to learn features of the data (representation learning). ANNs consist of interconnected artificial neurons that are organized in multiple layers (Ivakhnenko & Lapa, 1965). An artificial neuron or node is an integrating mathematical operator that transmits activity based on a built-in activation function. Activation functions determine the output of a node by summing incoming input and integrating it via a mathematical function, such as a rectified linear unit for example (ReLU; Krizhevsky, Sutskever, & Hinton, 2012). In ANNs, the individual artificial neurons are connected by edges, which have adjustable weights associated with them, much like synaptic strength is plastic in biological neuronal connections, hence the name "neural network". The individual neurons are

organized in layers, such as the input, output, or any number of intermediate layers. These intermediate layers, which due to their 'depth' in the network give deep learning its name, are used to improve the capacity of the network.

Networks are trained to annotated sample data (training data), such that the networks' outputs match the target output, a process during which the networks' weights are altered. Afterwards, the network is evaluated on novel data (test data). In a landmark early application, LeCun et al. (1989) successfully trained ANNs to recognize handwritten zip codes in pictures and translate them into printed digits, ushering an era of ANN research and applications.

The ANNs trained by LeCun et al. performed image segmentation, a process in which shapes or objects in an image are classified on a pixel-wise scale (LeCun et al., 1989). Convolutional neural networks (CNNs), a particular type of ANNs, have been found to be particularly suited for this task. Neurons in CNNs are organized into layers, with individual neurons of one layer only being connected certain other neuron in the next layer. Each layer "convolves" the input image(s) with a kernel, and subsequently decreases its spatial size by pooling (e.g. max pooling; Yamaguchi & Matsumoto, 1990). These operations extract the dominant features of the image(s) at each level, aiming to preserve spatial and temporal aspects as much as possible, while minimizing the required computational power. This is achieved via a reduction in number of required operations as the layers get smaller through the dimensionality reduction induced by the convolution and max pooling functions. After the last layer, the image is flattened and fed into a classifier, which ultimately determines the networks' output, i.e. the segmented image. Particularly, the U-Net - named after the shape of its layers - has since risen to popularity for image segmentation in recent years (Ronneberger, Fischer, & Brox, 2015; Falk et al., 2019).

Therefore, CNNs have been widely utilized for image segmentation in recent years, particularly in studies involving biomedical and neuroscience imaging (Ronneberger, Fischer, & Brox, 2015; Shen, Wu, & Suk, 2017; Gómez et al., 2020; Tyson et al., 2021). Nowadays, tasks such as identifying or counting cells (Al-Kofahi et al., 2018; Falk et al., 2019; Stringer et al., 2021; Greenwald et al., 2022) or tracing the neurites of a neuron (Li et al., 2017; Zhou et al., 2018; Saberi-Bosari, Flores, & San-Miguel, 2020) are frequently per-

formed in an automated fashion using CNN-based tools. These automated methods are typically much faster than human annotations. Moreover, a well-trained network can perform more reliably than manual annotation, as inter-human variability is eliminated. However, particular care should be taken to generate unbiased and represenative training data, as any such biases will subsequently be 'learned' by the network and become the rule. Lastly, deep learning-based tools make certain big data experiments possible, as the amount of data required to obtain reliable answers can dictate the feasibility of an experiment.

While cell bodies and neurites can be segmented relatively reliably, other features of a neuron's morphology, such as dendritic spines, proved to be more challenging. Nevertheless, efforts were made to automate spine identification (Zhang et al., 2010), segmentation (Koh & Lindquist, 2001; Rodriguez et al., 2008) and classification (Rodriguez et al., 2008; Shi, Huang, & Hong, 2014). However, despite the employment of CNNs for this task (Rodriguez et al., 2008; Vidaurre-Gallart et al., 2022), these automated tools typically do not perform well across different types of microscopy data. The signal-to-noise ratio and pixel size, i.e. how many pixels are contained in a typical neuronal compartment, strongly influence the performance of current tools (Basu et al., 2018). Hence, flexible segmentation of dendritic spines in different types of microscopy data remains to date a manual task. As mentioned above, this limits the questions that can be addressed experimentally, such as the one featured in section 3.3 of the Results in this dissertation, namely: which wiring rules nascent dendritic spines follow after LTP induction. To answer such questions, hundreds or thousands of dendritic spines need to be recorded repeatedly and dynamics captured reliably, generating a dataset that would require years to analyze via manual annotations. Hence, there is a strong need for an automated tool that performs quick and reliable segmentation of spines and dendrites in image data, which will be presented in section 3.2 of the Results.

1.8.4 Optogenetics

In order to establish causal relationships between molecular or cellular processes and physiological or behavioral changes, scientists sought to develop novel tools of selectively manipulating some of the relevant players during an experiment. In neuroscience, over the last decade and a half the rise of

optogenetics - the ability to control cellular function via light-sensitive genetically encoded constructs - has been one of the most prominent and popular new ways of manipulation (Häusser, 2014). Nowadays, optogenetics can be applied in a multitude of ways, but its origins can be traced back to the early 2000s. At this time, the performance of phototaxis, a long-studied feature of some green algae such as *Chlamydomonas reinhardtii*, was found to critically depend on the photosensitive proteins channelrhodopsin-1 and -2. (Stavis & Hirschberg, 1973; Nagel et al., 2002; Nagel et al., 2003). Phototaxis is the movement of an organism towards or away from a stimulus of light. In the search for the driving force behind this light-dependent behavior, it was found that channelrhodopsins respond to blue light by opening a channel pore and thereby becoming non-selective cation channels. Via the opening of the channel, cations can flow into a cell and depolarize it, triggering cellular signaling cascades, which eventually cause a behavioural response - phototaxis.

In the same time frame, two alternative means of optogenetically controlling cellular activity were developed. First, co-expression of a threesome of constructs (arrestin-2, rhodopsin, and the G protein α subunit, called chARGe) for the first time rendered neurons of choice light-responsive (Zemelman et al., 2002), a major breakthrough. However, due to the limited achievable temporal control, and the fact that multiple proteins were required, this approach did not find broad applications. Second, endogenously existing ion channels were mutated such that a synthetic photoresponsive ligand could be permanently linked to the ion channel. The result was a photoswitchable, gated ion channel that could be expressed in neurons of choice (Banghart et al., 2004). Over the years, a multitude of endogenous ion channels/receptors, such as potassium channel, kainate, metabotropic glutamate (mGluR), GABA, NMDA, and dopamine receptors amongst others, have been engineered to generate photoswitchable counterparts (Banghart et al., 2004; Volgraf et al., 2005; Szobota et al., 2007; Levitz et al., 2013; Lin et al., 2014; Berlin et al., 2016; Donthamsetti et al., 2021). This method is temporally much more precise than the chARGe and provided the advantage to precisely control endogenous receptors - with all downstream signaling - of choice with light. This is in contrast to both chARGe and ChR2, which ultimately just control cellular membrane potentials. However, the need to overexpress engineered receptors/channels or create knock-in animals hampered widespread applications. Moreover, due to protein turnover, labeling channels/receptors with the synthetic ligand limited the duration in which experiments could be per-

formed, unless receptors/channels were labeled repeatedly. Ultimately, ChR2 proved to be the more applicable method. ChR2's co-factor, all-*trans*-retinal, is present in sufficient amounts in cells, omitting the need for supplements (unlike the light-activated endogenous ion channels). Although it took until 2005 to employ ChR2 in neuronal cells (Boyden et al., 2005), soon user-optimized variants were developed (Nagel et al., 2005; Berndt et al., 2011), aided by the characterization of its protein structure (Kato et al., 2012) and the details of its photocycle (Hegemann, Ehlenbeck, & Gradmann, 2005). Recently, ChR2 variants have been engineered to be sensitive to light of different wavelengths, offering orthogonal control over distinct neuronal populations (Klapoetke et al., 2014; Hooks et al., 2015). These variants also proved critical to selectively induce neuronal activity in distinct ensembles of neurons in the living brain (Dal Maschio et al., 2017; Carrillo-Reid et al., 2019; Adesnik & Abdeladim, 2021).

Since its early beginnings, channelrhodopsins have found broad application in circuit neuroscience (Petreanu et al., 2007; Petreanu et al., 2009), cardiology (Boyle et al., 2013), memory research (Ryan et al., 2015), and vision science (Sahel et al., 2021). In this dissertation, optogenetics are employed to map functional connectivity in the retinogeniculate and Schaffer collateral pathways. In both circuits, the fact that neurotransmitter release from opsin-expressing boutons can be triggered optically is exploited. This enables flexible readouts of input strength, as measured electrophysiologically from the postsynaptic neuron (Petreanu et al., 2007), or single-synapse connectivity via calcium imaging of dendritic spines (Wiegert & Oertner, 2013; Wiegert et al., 2018). In the first application, two opsins with distinct excitation spectra are employed to disentangle the input two sources provide (Klapoetke et al., 2014; Bauer et al., 2021). To aid in the latter application, excitation of channelrhodopsins can be spatially confined to $\sim$30 μm using optical (Schoenenberger et al., 2008) and/or pharmacological means, such as the blocking of voltage-gated sodium and -potassium channels (Petreanu et al., 2009). Hence, channelrhodopsins can be utilized in a highly spatially and temporally confined manner, offering sensitive and flexible control over neuronal signaling. This has been leveraged to dissect circuits (Huang et al., 2018; Shelton et al., 2022) or investigate the consequences of synaptic plasticity on a single-synapse basis (Wiegert & Oertner, 2013; Wiegert et al., 2018). Consequently, optogenetics constitute a powerful tool to investigate causal relationships in circuits and synapses in modern neuroscience.

1.9 Objectives of this study

This dissertation attempts to shed light on the rules of functional connectivity that govern the brain. As such, this dissertation is split into three parts, in which functional connectivity in the retinogeniculate pathway, an automated method of spine identification, and the wiring rules of LTP-induced synaptogenesis are presented.

The first objective of this dissertation was to map functional binocular convergence in the retinogeniculate pathway. Recent structural and functional studies have varied in the amount of binocular convergence reported in the dLGN, with estimates ranging from 6 to 40 % of dLGN cells being binocular (Jaepel et al., 2017; Sommeijer et al., 2017; Rompani et al., 2017; Huh et al., 2020). Widespread binocular convergence found by some reports is unexpected, as it contradicts the classical view of the mouse visual circuit, in which eye-specific information is strictly segregated at the level of the dLGN. To precisely assess binocular convergence in the dLGN, a dual-color optogenetic approach was devised. This method was then utilized to assess the eye-specific input strength across the dLGN with single-cell precision. Moreover, the underlying mechanisms of binocular convergence were investigated by visualizing the morphology of dLGN cells as well the projection pattern of RGC axons in the visual thalamus.

The second objective was to address the need for a tool to perform automated segmentation of dendrites and dendritic spines in image data. Current methods lack broad applicability across a range of image qualities, complicating analyses involving large and/or diverse image data sets. Hence, a deep-learning tool was devised that rapidly identifies and segments dendrites and dendritic spines in microscopy data with high accuracy. Additionally, as part of this endeavour, a diverse and fully annotated dataset was obtained, that can be utilized to benchmark this and future automated efforts for segmenting dendritic spines.

The third objective of this dissertation was to work towards understanding the functional connectivity rules of LTP-induced dendritic spines. Dendritic spines grow in neurons undergoing LTP (Engert & Bonhoeffer, 1999; Toni et al., 1999) and rapidly form functional synapses (Nägerl et al., 2007). However, it remains unclear which presynaptic neurons are chosen to establish

functional connectivity, and hence whether there is a fundamental wiring rule followed by the brain. To address this, improvements to an existing assay to map functional synaptogenesis following LTP *in vitro* (Coneva, 2015) were made. In particular, pharmacological and computational means to map synaptic connectivity despite the occurrence of dendritic calcium events were explored. Moreover, a molecular approach was devised to combat a potential confounding variable, the lack of spine maturity in nascent spines, when determining functional connectivity rules of LTP-induced dendritic spines.

This dissertation presents a suite of methods and approaches to assess functional wiring rules at different levels, paving the way for further analysis in this direction.

Chapter 2

Materials and methods

2.1 General

In the results section of this dissertation, three projects are outlined. To clarify which methodologies were employed for which project, the relevant paragraphs of this section were indicated with the corresponding results section as follows. Descriptions pertaining to the investigation into the functional connectivity in the retinogeniculate pathway (Results 3.1), an automated method of spine identification (Results 3.2), and the wiring rules of LTP-induced synaptogenesis (Results 3.3).

2.2 Animals

All experiments were carried out in compliance with the institutional guidelines of the Max Planck Society and of the local government (Regierung von Oberbayern). For the experiments in Results 3.2 and 3.3, Wistar rats were housed under a 12 hour light-dark cycle with water and food available *ad libitum*. Pups were weaned at postnatal days 4-9 (P4-9) and organotypic hippocampal slice cultures were prepared the same day.

For the experiments in Results 3.1, female wild-type C57bl/6 mice were housed under a 12 hour light-dark cycle with water and food available *ad libitum*. Intravitreal eye injections were performed between P30-48, and *in vitro* acute brain slice experiments were performed between P67-108. For the experiments in Results 3.2, craniotomies and intracortical viral injec-

tions were performed P35-P40, and *in vivo* structural imaging of dendrites and spines in L2/3 of bV1 was performed between P61-74.

For the experiments in Results 3.2, female Thy1-GFP mice were housed under a 12 hour light-dark cycle with water and food available *ad libitum*. One mouse was sacrificed at age P100 to extract the brain.

2.3 Genetic tools

2.3.1 DNA

For the experiments in Results 3.2 and 3.3, a number of genetic constructs were generated. To visualize spine maturity in CA1 neurons, an exchange of mNeonGreen to mTurquoise2 in the PSD-95-binding nanobody construct (pCAG_Xph15-mNeonGreen-CCR5TC, Addgene 135533; Rimbault et al., 2021) was performed via Gibson assembly and verified via PCR sequencing, resulting in the final construct pCAG_Xph15-mTurquoise2 -CCR5TC. For full sequence, see Appendix.

For the experiments in Results 3.2 and 3.3, pENN.AAV.CAG.tdTomato.-WPRE.SV40 was obtained via Addgene (15554; Wilson lab, unpublished), and utilized as a structural marker in single CA1 neurons.

For the experiments in Results 3.2 and 3.3, DNA for a recombinant adeno-associated virus (AAV) encoding the humanized channelrhodopsin 2 (hChR2) with the H134R mutation was created to optically control neuronal activity in a subpopulation of CA3 neurons. The viral construct was generated by subcloning the hChR2(H134R) coding sequence from pAAV-hSyn-hChR2(H134R)-EYFP (Addgene, 26973) into pENN.AAV.CAG.tdTomato.-WPRE.SV40 (Addene, 15554) by replacing tdTomato using Gibson assembly. Correct insertion was verified via PCR and subsequent sequencing. The final construct was pAAV-CAG-hChR2(H134R)-WPRE-SV40.

For the experiments in Results 3.2 and 3.3, pGP-AAV-syn-jGCaMP7b-WPRE was obtained via Addgene (104489; Dana et al., 2019), and utilized as a calcium indicator in single CA1 neurons.

2.3.2 Viruses

Two adeno-associated viruses (AAVs) were used for mapping binocularity in the dLGN. DNA constructs for Syn-Chronos-EGFP (Addgene 59170) and Syn-ChrimsonR.tdT (Addgene 59171; Klapoetke et al., 2014) were obtained, and purified virus of AAV serotype 2/2 was produced via the Gene Therapy Center Vector Core at the University of North Carolina at Chapel Hill (titer $2.1\times10e^{12}$, $3.7\times10e^{12}$ GC/ml for Chronos-EGFP and ChrimsonR-tdT, respectively). pAAV-CAG-hChR2(H134R)-WPRE-SV40 was used for optical control of CA3 neurons. DNA was generated (see above) and purified virus of AAV serotype 2/1 produced via VectorBuilder (Santa Clara, CA, USA, titer: 1.05 $\times e^{13}$ GC/ml).

To obtain structural images of dendrites and dendritic spines in bV1 *in vivo*, two viruses were utilized: AAV2/1.1CamKII0.4.Cre.SV40 and AAV2/1.Syn.Flex.mRuby2.GSG.P2A.GCaMP6s.WPRE.SV40 were produced at the Penn Vector Core, Gene Therapy Program, Department of Pathology and Laboratory Medicine, Perelman School of Medicine at the University of Pennsylvania (titer: 1.81 $\times e^{13}$, and 2.2 $\times e^{13}$ for Cre and mRuby2-GCaMP6s double construct, respectively). All viruses were aliquoted (3 μl per aliquot) and stored at -80°C.

2.4 Equipment

2.4.1 Tools

Equipment	**Supplier**
Preparation of organotypic hippocampal slice cultures	
2x scissors	Fine Science Tools, cat. no. 14090-09 (Germany)
Scissors	Fine Science Tools, cat. no. 14001-14 (Germany)
2x Forceps Dumont #5	Fine Science Tools, cat. no. 11251-20 (Germany)
2x sharpened spatulas 3mm width	VWR, cat. no. 231-2231 (Germany)
Sharpened spatulas 5mm width	VWR, cat. no. 231-0466 (Germany)

Sharpened spatula with rounded end 5mm width	VWR, cat. no. 231-1045 (Germany)
Razor blade	Fine Science Tools, cat. no. 10050-00 (Germany)
Tissue membrane Millipore Biopore ™ Membrane	Millipore, cat. no. BGCM00010 (USA)
Syringe filter Millex-GP	Millipore, cat. no. SLGP033BS (USA)
Millicell cell culture inserts	Millipore, cat. no. PICMORG50 (USA)
McIlwain tissue chopper	The Mickle Laboratory Engineering, cat. no. 10180 (UK)
Dissection microscope	Nikon, cat. no. SMZ645 (Germany)
Syringe 50 ml BD Plastipak	VWR, cat.no. BD309653 (Germany)
6-well plates	TPP, cat. no. Z707767-72EA (Switzerland)
Incubator Hera cell 150	Thermo Fisher, cat no. 51025153 (Germany)
Virus injection and single-cell electroporation setup	
Micropipette puller for virus injection pipettes, P-97	Sutter Instruments (USA)
borosilicate glass capillaries (1.2 mm outer diameter, 1.12 mm inner diameter	World Precision Instruments, cat. no. TW150F-4 (USA)
Upright microscope BX51WIF	Olympus (USA)
Axoporator 800A	Axon Instruments (USA)
Glass capillaries for electroporation pipettes (Ø: 1.5 mm, thickness: 0.3 mm)	World Precision Instruments, cat. no. TW150F-3 (USA)
Millicell cell culture inserts	Millipore, cat. no. PICMORG50 (USA)
Pneumatic Pico Pump PV 820	World Precision Instruments (USA)
Vertical micropipette puller PC10	Narashige (Japan)
0.22 μM Ultrafree MC Centrifugal Filter	Merck, cat. no. UFC30GC0S (Germany)
40x "Achroplan" IR 40x/0.8 W objective	Zeiss (Germany)

4x air objective RMS4X-PF	Olympus (USA)
Biolistic transfection	
Tubing prep station	Bio-Rad, cat. no. 1652420 (USA)
Helios gene gun	Bio-Rad (part of cat. no. 1652432) (USA)
Helium hose Assembly	Bio-Rad, cat. no.1652412 (USA)
Helium regulator	Bio-Rad, cat. no. 1652413 (USA)
Tubing cutter	Bio-Rad, cat. no.1652422 (USA)
Barrel liner	Bio-Rad, cat. no. 1652417 (USA)
Polyamid mesh 100μm (gene gun filter)	Klein Königswinter (Germany)
Cartridge holder	Bio-Rad, cat. no. 1652426 (USA)
Cartridge extractor Tool	Bio-Rad, cat. no. 1652435 (USA)
Tefzel tubing	Bio-Rad, cat. no. 1652441 (USA)
1.6 μm gold particles	Bio-Rad, cat. no. 1652244 (USA)
Helium gas (4.6) cartridge 10 l	Westfalen (Germany)
Surgeries	
26G virus loading needle	World Precision Instruments, cat. no. NF26BV-2 (USA)
34G injection needle	World Precision Instruments, cat. no. NF34BV-2 (USA)
Biopsy punch (4 mm)	Pfm Medical, cat. no. 48401 (USA)
Dental drill (Presto II)	NSK (USA)
Dissecting microscope SOM-62	Karl Kaps GmbH (Germany)
Dumont #5/45 cover slip forceps	Fine Science Tools GmbH, cat. no. 11251-33 (Germany)
Dumont #5 forceps-assorted styles straight	Fine Science Tools GmbH, cat. no. 11251-10 (Germany)
Dumont #7 forceps-standard	Fine Science Tools GmbH, cat. no. 11251-30 (Germany)
Drill bits HM1 005	Meisinger (Germany)
Pulse generator/trigger Master-8	A.M.P.I. (Israel)
Glass coverslips, round, Ø: 4 and 10 mm, thickness: 0. 13 mm	Menzel GmbH (Germany)
Hamilton syringe (NANOFIL)	World Precision Instruments (USA)

Hamilton syringe (Model 75 RN SYR)	Hamilton, cat. no. 7634-01 (USA)
32G blunt needle (Small hub RN needle)	Hamilton, cat. no. 7803-14 (USA)
Micromanipulators	World Precision Instruments, cat. no. M3301R (USA)
Headbar	MPI Neurobiology (Germany)
Heating blanket	MPI Neurobiology (Germany)
Micropipette puller for virus injection pipettes, P-97	Sutter Instruments (USA)
Pressure micro-injection system	Toohey Company (USA)
Rapid-Filtermax, 0.22μm Pore Size, Nr. 99505	TPP Rapid (Switzerland)
Scalpel blades # 11	Fine Science Tools GmbH, cat. no. 10011-00 (Germany)
Stereotaxic apparatus	MPI Neurobiology (Germany)
Student Iris Scissor, 11.5 cm, straight	Fine Science Tools GmbH, cat. no. 91460-11 (Germany)
Acute slice preparation	
2x light-shielded slice incubation chambers	Custom made, MPI Neurobiology
525-555 nm emission filter	BLS Biological Laboratory Equipment (Hungary)
590-660 nm emission filter	BLS Biological Laboratory Equipment (Hungary)
Dumont #5 Forceps-Assorted Styles straight	Fine Science Tools GmbH, cat. no. 11251-10 (Germany)
Filter paper, round, Ø: 110 mm	Whatman (UK)
Fine scissors	Fine Science Tools GmbH, cat. no. 14090-09 (Germany)
Glass coverslips, round, Ø: 12 mm, thickness: 0.13 mm	Menzel GmbH (Germany)
Miners lamp with light source	BLS Biological Laboratory Equipment (Hungary)
excitation filter: 525–555 nm	BLS Biological Laboratory Equipment (Hungary)

emission filter: 590–660 nm	BLS Biological Laboratory Equipment (Hungary)
Razor blade	Martor (Germany)
Small spatula	VWR, cat. no. 231-2151 (Germany)
Standard pattern forceps	Fine Science Tools GmbH, cat. no. 11000-12 (Germany)
Thin razor blade Razolution for vibratome	Simbatec (Germany)
Tissue Flotation Bath	Medite (USA)
Vibratome (VT1200S)	Leica (Germany)

Table 1 Tools

2.4.2 Setup equipment

Equipment	**Supplier**
Main setup (*In vitro* multiphoton setup)	
Multiphoton imaging system	Thorlabs, cat. no. MPM200-2 (USA)
Mai Tai HP Ti:Sapphire laser	Spectra-Physics/Newport (USA)
Upright microscope	Nikon, model Eclipse FN1 (Japan)
Pockels Cell	Conoptics, Model 350-80 Electro-optic modulator (USA)
Pockels Cell mount	Conoptics, Model M102 (USA)
Pockels Cell amplifier	Conoptics, Model 302RM (USA)
4x GaASp photomultiplier modules	Hamamatsu, H7422-40 (Germany)
2x PMT amplifiers	Thorlabs, model ECU 1 (USA)
1.4 NA oil Condenser	Thorlabs, cat. no. CSC1003 (Germany)
Lens: f=500	Thorlabs, cat. no. AC508-500-B-ML (Germany)

Broadband dielectric mirrors	Thorlabs, cat. no. BB1-E03 (Germany)
Lens: f = 30	Thorlabs, cat. no. AC254-030-B-ML (Germany)
Lens: f = 60	Thorlabs cat. no. AC254-060-B-ML (Germany)
Precision Pinhole	Thorlabs, cat. no. P50S (Germany)
720 nm shortpass filter	Semrock (USA)
Notched dichroic filter TLAB033 transmission: 398-408 nm, 470-490 nm, and 561-568 nm (all >90%), 710-1600 nm (>93%)) reflection: 350-386 nm (>90%) 421-455 nm, 503-545 nm, and 586-680 nm (all >98%))	Semrock (USA) via Thorlabs (Germany)
mechanical shutter (VMM-D1)	Uniblitz Vincent Associates (USA)
3x mechanical Optical Shutter (VS25 25 mm)	Uniblitz Vincent Associates (USA)
510-84 nm bandpass filter	Semrock (USA)
560nm dichroic beam splitter	Semrock (USA)
525-50 nm bandpass filter	Semrock (USA)
607-70 nm bandpass filter	Semrock (USA)
CFI75 LWD x16, 0.8 NA, water immersion objective	Nikon (Japan)
LUMPlan x40, 0.8 NA water immersion objective	Olympus (Japan)
UPlanFLN x4, 0.13 NA air objective	Olympus (Japan)
20X-PFH 20x 0.95 NA water immersion objective	Olympus (Japan)
LUMFI 60x 1.1 NA water immersion objective	Olympus (Japan)
Bessel module	
Motorized flip mirrors, ±2° accuracy	Newport, cat. no. 8892-K-M (Germany)

Spatial light modulator (SLM)	Meadowlark Optics, Spatial Light Modulator XY series (512 x 512) (USA)
Lens 1: f = 400	Thorlabs, cat. no. AC508-400-B-ML (Germany)
Lenses 2 and 3: f = 500	Thorlabs, cat. no. AC508-500-B-ML (Germany)
Lens: f = 30	Thorlabs, cat. no. AC254-030-B-ML (Germany)
Lens: f = 75	Thorlabs, cat. no. AC254-075-B-ML (Germany)
Precision Pinhole, 50 $\pm$3 μm pinhole diameter	Thorlabs, cat. no. P50S (Germany)
Custom-made Al-coated mask	Photo Sciences Inc (USA)
Auxilliary equipment	
Multiclamp 700 B amplifier	Axon Instruments, Molecular Devices
Recording electrode headstage CV-7B	Axon Instruments (USA)
HumBug Noise Eliminator	Quest Scientific Instruments Inc. (USA)
Controller for x-y-motorized stage	Lang GmbH, Lang MCL-2
B.Braun Perfusor F	B.Braun Melsungen AG, Germany
LVPZT-Amplifier piezo objective mount	Physik Instrumente, cat. no. E-665K007 (Germany)
PIFOC P-725 high-load piezoelectric z stepper	Physik Instrumente (Germany)
Peristaltic minipump	Gilson (USA)
Digital indicating controller	CHINO Corporation, cat. no. DB1060B000-G0A (Japan)
Micromanipulators LN Mini25	Luigs and Neumann (Germany)
Controller SM-5	Luigs and Neumann (Germany)
Photostimulation	
Fabry-Perot Benchtop Laser Source, 473 nm, 5.0 mW	Thorlabs, cat. no. S3FC473 (Germany)
Fabry-Perot Benchtop Laser Source, 637 nm, 70 mW	Thorlabs, cat. no. S4FC637 (Germany)

2-color combining fiber	Thorlabs, cat. no. RB42F1 (Germany)
Fiber port and collimator	Thorlabs, cat. no. PAF-X-15-A (Germany)
Ø600 μm, 0.39 NA optic fiber	Thorlabs, cat. no. FT600EMT (Germany)
LED light source	pE2 CoolLED, cat. no. 244-1400 (UK)
10x beam expander	Thorlabs, GBE10-E3 (Germany)
Secondary *in vitro* multiphoton imaging setup	
Multiphoton imaging system	Thorlabs, cat. no. MPM200-2 (USA)
MaiTai HP DeepSee Ti:Sapphire laser	Spectra-Physics/Newport (USA)
Upright microscope	Nikon, model Eclipse FN1 (Japan)
Pockels Cell	Conoptics, Model 350-80 Electro-optic modulator (USA)
Pockels Cell mount	Conoptics, Model M102 (USA)
Pockels Cell amplifier	Conoptics, Model 302RM (USA)
2x GaASp photomultiplier modules	Hamamatsu, H7422-40 (Germany)
PMT amplifiers	Thorlabs, model ECU 1 (USA)
1.4 NA oil Condenser	Thorlabs, cat. no. CSC1003 (Germany)
2-color combining fiber	Thorlabs, cat. no. RB42F1 (Germany)
CCD camera Retiga-EXi	QImaging (Canada)
CFI75 LWD x16, 0.8 NA, water immersion objective	Nikon (Japan)
LUMPlan x40, 0.8 NA water immersion objective	Olympus (Japan)
UPlanFLN x4, 0.13 NA air objective	Olympus (Japan)
Fabry-Perot Benchtop Laser Source, 473 nm, 5.0 mW	Thorlabs, cat. no. S3FC473 (Germany)
Fabry-Perot Benchtop Laser Source, 637 nm, 70 mW	Thorlabs, cat. no. S4FC637 (Germany)

Fiber port and collimator	Thorlabs, cat. no. F230FC-A (Germany)
Image acquisition software: ScanImage 4.2	Vidrio Technology (USA)
Image processing software	ImageJ (USA) (Schindelin et al., 2012)
Electrophysiological data acquisition software: Ephus	Vidrio Technology (USA)
2x mechanical shutter (VMM-D1)	Uniblitz Vincent Associates (USA)
Multiclamp 700 B amplifier	Axon Instruments, Molecular Devices
PCI Digitizers, 125 MS/s	Alazartech (Canada)
B.Braun Perfusor F	B.Braun Melsungen AG, Germany
Peristaltic minipump	Gilson (USA)
2x Photodiode	Thorlabs, cat. no. PDA100A-EC (Germany)
HumBug Noise Eliminator	Quest Scientific Instruments Inc. (USA)
LVPZT-Amplifier piezo objective mount	Physik Instrumente, cat. no. E-665K007 (Germany)
PIFOC P-725 high-load piezoelectric z stepper	Physik Instrumente (Germany)
Micromanipulators LN Mini25	Luigs and Neumann (Germany)
Controller SM-5	Luigs and Neumann (Germany)
In vivo multiphoton imaging setup	
In vivo benchtop 2-photon setup, Bergamo ® II Series	Thorlabs (Germany)
CFI75 LWD x16, 0.8 NA, water immersion objective	Nikon (Japan)
Pockels Cell	Conoptics, Model 350-80 Electro-optic modulator (USA)
Pockels Cell mount	Conoptics, Model M102 (USA)
Pockels Cell amplifier	Conoptics, Model 302RM (USA)
Dichroic beam splitter, 560 nm	Semrock (USA)
Emission filter 525/50-25 nm bandpass filter	Semrock (USA)
Emission filter 607/70-25 nm bandpass filter	Semrock (USA)

Emission filter 720/25 nm short pass filter	Semrock (USA)
Epifluorescence microscope Lumar.V12 Stereo	Zeiss (Germany)
2x GaASp photomultiplier modules	Hamamatsu, H7422-40 (Germany)
Image acquisition software: ScanImage 4.2	Vidrio Technology (USA)
Image processing software	ImageJ (USA) (Schindelin et al., 2012)
MaiTai HP DeepSee Ti:Sapphire laser	Spectra-Physics/Newport (USA)
P-726 PIFOC® high load objective scanner	Physik Instrumente (Germany)
PCI Digitizers, 125 MS/s	Alazartech (Canada)
Photodiode	Thorlabs, cat. no. PDA100A-EC (Germany)
N25X-APO-MP 25x 1.1 NA water immersion objective	Nikon (USA)
Confocal microscope	
Leica TCS SP8 scanning confocal microscope	Leica Microsystems (USA)
HX PL APO L 20x/0.75 IMM CORR CS2 objective	Leica Microsystems (USA)

Table 2 Equipment

2.4.3 Other equipment

Reagent	**Supplier**
Glass capillaries for patch pipettes (Ø: 1.5 mm, thickness: 0.3 mm)	World Precision Instruments, cat. no. TW150F-3 (USA)

FluoSpheres™ Carboxylate-Modified Microspheres, 0.1 μm, yellow-green fluorescent (505/515), 2 % solids	Thermo Fisher, cat. no F8803 (USA)

Table 3 Other equipment

2.4.4 Software

Software	Use	Supplier/source
MATLAB 2019b, 2008a, 2013b	Data analysis	Mathworks (USA)
Python 3.8	DeepD3	Van Rossum and Drake, 2009
ImageJ	3D watershed segmentation, cell morphology reconstruction, manual spine annotation, manual image registration	Schindelin et al., 2012
Adobe Illustrator	Figure editing	Adobe Inc. (USA)
Scanimage r4.2	2p-image acquisition	Mathworks (USA Pologruto, Sabatini, & Svoboda, 2003)
Ephus	Electrophysiological recordings	Mathworks (USA Suter et al., 2010)
LASX	Confocal image acquisition	Leica (Germany)
SnapGene	DNA construct engineering	GSL Biotech (USA)
NeuTube	Pixel-wise dendrite annotation	Feng, Zhao, and Kim, 2015

PiPra	Pixel-wise spine annotation	Gómez et al., 2020
CMTK	Affine registration	NeuroImaging Tools & Resources Collaboratory

Table 4 Software

2.4.5 Reagents and solutions

Reagent	Supplier
70% (vol/vol) Ethanol	VWR, cat. no. 97064-768 (Germany)
100% (vol/vol) Ethanol	Sigma Aldrich cat. no. 1.00983 (Germany
Alexa 594	Thermo Fisher, cat. no. A10438 (Germany)
$CaCl_2$	Sigma, cat. no. 21115 (USA)
Carbogen (95% (vol/vol) O_2, 5% (vol/vol) CO_2)	
$CsMeSO_4$	Merck, cat. no. C1426 (USA)
EGTA	Sigma, cat. no. E3889 (USA)
Glucose	Carl Roth, cat. no. X997.2 (Germany)
HEPES	Carl Roth, cat. no. HN77.2 (Germany)
KCl	Sigma, cat. no. 60135 (USA)
K-gluconate	Sigma, cat. no. G4500 (USA)
KH_2PO_4	Merck, cat. no. 104873 (USA)
$MgCl_2$	Sigma, cat. no. 63069 (USA)
$MgSO_4$	Merck, cat. no. 105886 (USA)
Na-ATP	Sigma, cat. no. A2383 (USA)
NaCl	VWR, cat. no. 470302-522 (Germany)

Na-GTP	Sigma, cat. no. 51120 (USA)
NaH_2PO_4	Merck, cat. no. 1063460 (USA)
$NaHCO_3$	Merck, cat. no. 1063290 (USA)
Na-L-ascorbate	Sigma, cat. no. A7631 (USA)
NaOH	VWR, cat. no. SS0580 (Germany)
Na-phosphocreatine	Sigma, cat. no. P7936 (USA)
Poly-D-Lysine hydrobromid	Sigma, cat. no. P6407 (USA)
Sterile saline 0.9% (wt/vol) NaCl	B. Braun Melsungen AG (Germany)
Sucrose	Merck, cat. no. 107687 (USA)
UHU® super glue liquid	UHU (Germany)
Spermidine	Sigma-Aldrich, cat. no. S2626 (Germany)
PVP	Bio-Rad, part of cat. no. 1652440 (USA)
4-AP	Sigma, cat. no. T5648 (USA)
Bicuculline	Sigma, cat. no. 14340 (USA)
QX-314 chloride	Alomone labs, cat. no. Q-150 (Israel)
TTX	Tocris, cat. no. 1078 (UK)
Mibefradil dihydrochloride	Bio-Techne GmbH, cat. no. 2198 (Germany)
D890 chloride (quaternary, permanently charged analog of N-methyl-verapamil)	ChiroBlock GmbH (Germany)
Nifedipine	Bio-Techne GmbH, cat. no. 1075 (Germany)
Muscimol	Bio-Techne GmbH, cat. no. 0289 (Germany)
Trolox	Sigma-Aldrich, cat. no. 238813 (USA)
Magnesium adenosine triphosphate (MgATP)	Sigma Aldrich, cat. no. A9187 (USA)
MEM	Invitrogen/Gibco, cat. no. 21575-022 (USA)
HBSS	Invitrogen/Gibco, cat. no. 24020-091 (USA)
Horse serum	Invitrogen/Gibco, cat. no. 26050-088 (USA)
Kynurenic acid	Sigma-Aldrich, cat. no. K3375 (USA)
D-Serine	Tocris, cat. no. 0226 (USA)

D-AP5	Bio-Techne GmbH, cat. no. 0106 (Germany)
NBQX disodium salt	Bio Techne GmbH, cat. no. 1044 (Germany)
DMSO	Sigma/Aldrich, cat. no. D2650 (USA)

Table 5 Reagents and solutions

2.4.6 Media and solutions

Sterile cortex buffer for *in vivo* surgeries and single-cell electroporations contained (in mM): 125 NaCl, 5 KCl, 10 glucose, 10 HEPES, 2 $CaCl_2$ and 2 $MgSO_4$. The buffer was sterilized and maintained at pH 7.4.

Sterile phosphate buffered saline (PBS) contained (in mM): 137 NaCl, 2.7 KCl, 8 NaH_2PO_4 and 1.5 KH_2PO_4, with the pH was adjusted to 7.4 using NaOH.

4% (wt/vol) Paraformaldehyde (PFA): 40 g PFA were dissolved in 800 ml distilled H_2O and 10 ml 1 M NaOH was added over low heat (max. 60 °C) until the solution clears. The solution was cooled down, 100 ml 10x PBS were added and the pH was adjusted to 7.4 with 1 M HCl. The solution was brought to 1000 ml with distilled H_2O and then filtered through a sterilization filter.

The cutting solution for in vitro experiments contained (in mM): 85 NaCl, 75 sucrose, 2.5 KCl, 25 glucose, 1.25 NaH_2PO_4, 4 $MgCl_2$, 0.5 $CaCl_2$ and 24 $NaHCO_3$, 310-325 mOsm, bubbled with 95% (vol/vol) O_2, 5% (vol/vol) CO_2.

Artificial cerebrospinal fluid (ACSF) contained (in mM): 127 NaCl, 2.5 KCl, 26 $NaHCO_3$, 2 $CaCl_2$, 2 $MgCl_2$, 1.25 NaH_2PO_4 and 10 glucose, 305-315 mOsm, bubbled with 95% (vol/vol) O_2, 5% (vol/vol) CO_2.

High-calcium ACSF contained (in mM): 127 NaCl, 26 $NaHCO_3$, 10 D-Glucose,

3.7 $CaCl_2$, 2.5 KCl, 1.25 NaH_2PO_4, 0.15 $MgCl_2$, 305-315 mOsm, bubbled with 95% (vol/vol) O_2, 5% (vol/vol) CO_2.

Magnesium-free ACSF contained (in mM): 127 NaCl, 26 $NaHCO_3$, 10 D-Glucose, 4 $CaCl_2$, 2.5 KCl, 1.25 NaH_2PO_4, 0 $MgCl_2$, 305-315 mOsm, bubbled with 95% (vol/vol) O_2, 5% (vol/vol) CO_2.

Cesium-based internal solution contained (in mM): 122 $CsMeSO_4$, 4 $MgCl_2$, 10 HEPES, 4 Na-ATP, 0.4 Na-GTP, 3 Na-L-ascorbate, 10 Na-phosphocreatine, 0.2 EGTA, 5 QX-314, and 0.03 Alexa 594, pH 7.25, 295-300 mOsm.

K-gluconate-based intracellular recording solution contained (in mM): 126 K-gluconate, 4 KCl, 10 HEPES, 4 Mg-ATP, 0.3 Na-GTP, 10 Na-phosphocreatine, 0.3-0.5% (wt/vol) Neurobiotin tracer and 0.03 mM Alexa 594, pH 7.25, 295-300 mOsm. The same solution, omitting Alexa 594 was mixed with target DNA (see methods) to electroporate single neurons in organotypic hippocampal slice cultures.

For brain slice clearing and immunostaining, the blocking buffer contained: 10% Normal Goat Serum, 2% Triton X-100, 0.2% Sodium Azide in PBS. The antibody buffer contained: 1% Normal Goat Serum, 0.2% Triton X-100, 0.2% Sodium Azide in PBS. The washing buffer contained: 3% NaCl, 0.2% Triton X-100 in PBS. The permeabilization buffer contained: 2% Triton X-100 in PBS. Brain slice clearing was performed using RapiClear © 1.47, according to the manufacturing protocol.

200 ml culture medium for organotypic hippocampal slice cultures contained 50 ml heat inactivated horse serum, 50 ml HBSS, 95.5 ml minimum essential medium (MEM), 2.5 ml Hepes (1 M) and 2 ml D(+)-Glucose stock solution (1 M). Occasionally, the culture medium was supplemented with the antibiotics penicillin (0.7 mM) and streptomycin (0.343 mM) to prevent bacterial and fungal infections after SCE or experiments.

Gey's balanced salt solution (GBSS) contained (in mM): 1.5 $CaCl_2$, 4.96 KCl, 0.22 KH_2PO_4, 1.03 $MgCl_2$, 0.28 $MgSO_4$, 136.89 NaCl, 2.7 $NaHCO_3$, 0.87 Na_2HPO_4, 5.55 D(+)-Glucose.

OHSC preparation solution contained: 99% GBSS, 1% ddH_2O, 9.5 mM

kynurenic acid, and 0.5% (wt/wt) D(+)-Glucose.

2.4.7 Pharmacology

Pharmacological applications during *in vitro* experiments

In experiments in acute slices containing dLGN, regular ACSF was used and supplemented with bicuculline (20μM). In experiments in OHSCs, high-calcium or magnesium-free ACSF was used and supplemented with TTX (1 μM), 4-AP (100 μM), D-serine (10 μM) and trolox (1 mM). In some experiments, muscimol (1 μM) or mibefradil (15 μM) and nifedipine (30 μM) were washed in to prevent dendritic calcium spikes from occurring. In some experiments in OHSCs, patch-clamp recordings of CA1 pyramidal neurons were performed using a Cs-based internal solution that also contained D-890 (1-2.5 mM) to block VGCCs postsynaptically (Grienberger, Chen, & Konnerth, 2014), as well as a synthetic structural marker (Alexa 594, 50 μM) and a calcium indicator (Fluo-4, 150 μM).

Anesthesia and analgesia for surgeries

To induce anesthesia in mice, sleep mix (MMF mix) was administered, containing fentanyl: 0.05 mg/kg, midazolam: 5 mg/kg, and medetomidine: 0.5 mg/kg. To counteract sleep-mix-induced anesthesia, wake mix was administered containing naloxone: 1.2 mg/kg, flumazenil: 0.5 mg/kg, and atipamezol: 2.5 mg/kg.

To prevent skin infections, povidone-iodine was administered (7.5% in 70% EtOH).
Analgesic care was provided via topical application of lidocaine (10%) and subcutaneous injection of carprofen (5 mg/kg per day for three days, starting with the day of surgery).

2.5 Procedures

2.5.1 Organotypic Hippocampal Slice Culture Preparation

Organotypic hippocampal slice cultures (OHSCs) were prepared from Wistar rats on postnatal days 4 - 9 (P4-9) as previously described (Stoppini, Buchs, & Muller, 1991a). In short: after decapitation of the rat pups, the scalp was cut along the midline. This exposed the skull, which was subsequently cut along the midline to release the brain into OHSC preparation solution. Hippocampi were isolated bilaterally and cut in 400 μm transverse sections using a McIlwain tissue chopper. Sections were incubated at 4°C for 45 minutes and subsequently placed on a membrane patch, which in turn was placed onto a cell culture membrane insert (0.4 μm pore size). Inserts were placed in wells of a 6-well plate, containing 1ml of pre-warmed culture medium and subsequently kept in an incubator at 35°C with 5 % CO_2 enriched atmosphere. Medium (50 % volume of each well) was exchanged twice a week.

2.5.2 Virus Injection

In some organotypic cell cultures, injection of adeno-associated viruses (AAVs) was performed to densely transduce the CA3 region of the hippocampus. In short: Borosilicate glass capillaries (1.5 mm outer diameter, 0.86 mm inner diameter) were pulled using a horizontal puller (Model P-97, Heat = 740, Ramp = 760, Pull = 170, Velocity = 120, Time = 120, all arbitrary units (A.U.)). The backs were fire-polished and the tips were subsequently broken using sterile forceps such that an outer tip diameter of $\sim$10 μm was achieved. OHSCs, which had been 1-4 days in vitro (DIV) were placed in a previously sterilized recording chamber of a microscope that was filled with pre-warmed (37°C) culture medium. The glass capillary was back-filled with virus (AAV2/1.CAG.hChR2(H134R).WPRE) and connected to a pneumatic pump, which was set to produce pulses at 20 psi for 100 ms in order to inject the AAVs into the slice culture. The CA3 region was located visually using a 4x objective and the tip of the capillary was placed just above the stratum pyramidale of CA3. The tip was then carefully inserted into the culture tissue and 3-6 pressure pulses were applied to inject a viral load into two regions in CA3. After injection, slices were returned to the incubator (35 °C,

5% CO_2) for 10 - 18 days before further treatment.

2.5.3 Single-Cell Electroporation

To express DNA constructs in single hippocampal neurons (DIV 10-18), single-cell electroporation (SCE) was performed, similar to Judkewitz et al. (2009): in short, borosilicate glass capillaries were pulled using a vertical puller (Model PC-10, T1 = 72.6, T2 =61.2, both A.U.) to produce tips with a resistance of 12-14 MΩ. The backs were fire-polished. SCE solution was prepared using filtered (0.22 μm) K-gluconate-based intracellular solution and DNA (100 ng/ml final concentration, constructs: pENN-AAV-CAG-tdTomato-WPRE-SV40, in combination with either pGP-AAV-syn-jGCaMP7b-WPRE, or pCAG_Xph15-mTurquoise2 -CCR5TC, as pairs, see results). Most experiments used tdTomato as a structural indicator, along with either GCaMP7b or Xph-15 as calcium/spine maturity indicators in a ratio of 1:9. Using acoustic output coupling of the electrode tip resistance and a 40x water immersion objective, a cell was targeted and approached applying positive pressure to prevent clogging of the tip. After positioning of the tip just next to the cell body, the positive pressure was alleviated and resistance usually increased to 25-40 MOhm. Subsequently, a train of pulses (-12 V, 0.5 ms width, 50 Hz for 1 second) was applied (Axoporator 800A). The tip was gently retracted after the pulse protocol and positive pressure was re-applied. After electroporation of 1-5 cells, slices were returned to the incubator (35 °C, 5 % CO_2) for a DNA expression time-window of 2-8 days.

2.5.4 Biolistic Transfection

In some experiments, as an alternative to SCE, single-cell transfection was achieved biolistically, as described previously (Jiao et al., 1993; Lo, McAllister, & Katz, 1994). In short: 1.6 μm gold particles were coated with DNA (constructs: pENN-AAV-CAG-tdTomato-WPRE-SV40, pGP-AAV-syn-jGCaMP7b-

WPRE, pCAG_Xph15-mTurquoise2-CCR5TC) using spermidine. Then, tefzel tubing was inner-coated with these gold particles using polyvinylpyrrolidone (PVP), subsequently dried by passing N_2 gas for 10 minutes, and finally cut into small cylindrical parts. These parts were "loaded" into a Helios Gene Gun System, and gold particles were "shot" at OHSCs (DIV 10-18) by briefly passing helium through the gun system (pressure ≈ 200 psi).

2.5.5 Surgeries

Head bar mounting, IOS imaging, craniotomy, intracortical virus injection and cranial window implantation

To obtain high quality images of dendrites and dendritic spines of L2/3 pyramidal cells of bV1, surgeries were performed on C57bl/6 mice (similar to Weiler et al., 2018): first, a head bar was mounted onto the skull of the animal to enable head-fixed in vivo imaging. Second, bV1 was localized using intrinsic optical signal (IOS) imaging and intracortical virus injections were performed. Last, a craniotomy was performed, replacing part of the skull with a cranial window to provide optimal optical access to the cortex. In this procedure, mice were anesthetized intraperitoneally with FMM mix (see 2.3.6 Pharmacology) and subsequently placed into a sterotaxic frame. Body temperature was maintained using a closed-loop rectal temperature probe and heat mat. Eye cream was applied to prevent corneal drying. After desinfecting the scalp (70 % EtOH, 7.5 % iodopovidine) and topical application of an analgesic (lidocaine: 10 %), the skull of the right hemisphere was exposed. Next, a custom-made metal head bar was placed over bV1 and mounted using super glue and dental cement.

Subsequently, IOS imaging (Grinvald et al., 1986; Bonhoeffer, 1996; Bonhoeffer, 1999; Weiler et al., 2018) was performed to localize the binocular zone of V1 for subsequent intracranial virus injection. Using a 4x air objective and a CCD camera, the blood vessel pattern and bV1 were visualized/localized using 530 nm and 735nm light, respectively. Matlab custom software was utilized to acquire and analyze images. Visual stimulation was given in two patches, to map visuotopic areas, as described earlier (see Bauer et al., 2021). The localized area of interest (bV1) was marked and a craniotomy was performed, removing a round segment of the skull (4 mm diameter). Gelfoam was utilized to prevent drying-induced cortical tissue damage. Subsequently, AAVs (AAV2/1.1CamKII0.4.Cre.SV40 and AAV2/1.Syn.Flex.mRuby2.GSG.-
P2A.GCaMP6s.WPRE.SV40 at titers of $\sim 1 \times e^8$ and $1 \times e^{13}$ GC/ml, respectively) were injected in layer 2/3 of bV1 (200-500 μm below the pial surface) at a rate of $\sim$10 nl/min. Last, the exposed cortical surface was covered with a glass cover slip, using histoacryl to fixate and seal the window. Further application of dental cement stabilized both the head bar and the glass

window. After surgery, the anesthesia was counteracted with wake mix (see 2.3.6 Pharmacology). Viruses were given at least three weeks time to express before *in vivo* imaging.

Intravitreal injections

To express two opsins (Chronos, ChrimsonR) in RGCs of the two retinae, intravitreal eye injections were performed, as described earlier (Bauer et al., 2021). Mice were anesthetized intraperitoneally via FMM mix (see 2.3.6 pharmacology). Separate 5 μl Hamilton syringes were loaded with AAVs expressing the two opsins (AAV2/2.Syn-Chronos.EGFP and AAV2/2.Syn-ChrimsonR.tdT, respectively). The procedure was identical for the two eyes. Using a sharp syringe tip, a small hole was generated in the stereotaxically fixed animal's eye. The virus-loaded syringe was then inserted intravitreally via the hole, avoiding the lens. In total, 1-2 μl of virus were introduced and allowed to disperse. Subsequently, the syringe was removed and eye cream was applied. Pre- and postoperative analgesic (carprofen: 5 mg/kg) was administered on the day of injection and the two days following. Viruses were given five to nine weeks time to express. Some animals were checked for cataracts (lens damage), which was not observed using this procedure. Estimated RGC transduction efficiency of the two opsins was >90 % (Bauer et al., 2021).

2.5.6 Acute slice preparation

To map binocular retinogeniculate input in the dLGN, acute brain slices of mice were obtained as previously described (Weiler et al., 2018; Bauer et al., 2021). In a sealed container, mice were deeply anesthetized (∼2 % isoflurane) and subsequently rapidly decapitated. The brain was then cut into coronal sections (320 μm), that contained the dLGN using ice cold carbogenated cutting solution and a vibratome. After incubation in ACSF (34 °C) for at least 45 minutes, slices were transferred to room temperature (RT) ACSF until used for experiments. Expression of both opsins was checked via fluorescence detection goggles (see 2.3 Equipment) before recordings. Slices with visible EGFP and tdTomato expression were considered for recordings. Of the 37 animals with performed intravitreal injections, 7 were excluded at this stage based on insufficient transduction. Before use at the experimental setups (see below), slices were carefully transferred to poly-D-lysine-coated

coverslips (12 mm diameter). Brain slices were used for experiments for 6-12 hours after acute slice preparation.

2.5.7 Immunohistochemistry

Coronal brain slices containing dLGN, in which in vitro electrophysiological recordings were obtained, were kept in 4 % PFA at 4 °C. Subsequently, immunohistochemistry and brain clearing were performed as described earlier (Bauer et al., 2021). In brief, after washing (3x10 min in PBS at RT) and permeabilization (overnight in permeabilization buffer at 4 °C), slices were blocked (8 h in blocking buffer at RT). Then slices were incubated with the primary antibody (initially overnight in Rabbit Anti-Calbindin D28k, 1:2,000 in antibody buffer at 4 °C and subsequently for 3 days in the same buffer at RT) and washed (overnight, PBS at RT). Subsequently, slices were incubated with the secondary antibody (2 days, Anti-Rabbit Alexa 647 (1:200 in antibody buffer at 4 °C), then washed (washing buffer overnight at 4 °C, 10 min PBS at RT) before clearing. Brain slice clearing was performed using RapiClear 1.47 for ∼3 h, after which slices were embedded in RapiClear solution and placed on a coverslip with a 300 µm spacer to prevent squeezing of the slice.

A Thy1-GFP mouse brain was sliced into 300 μm thick coronal brain slices, which were subsequently brain cleared 3.5 months after extraction. Brain slice clearing was performed using RapiClear 1.47 for ∼3 h, after which slices were embedded in RapiClear solution and placed on a coverslip with a 300 µm spacer to prevent squeezing of the slice.

2.6 Main setup

With the exception of a proportion of the thalamic cell *in vitro* imaging, all *in vitro* two-photon imaging was performed on a custom built Thorlabs multiphoton system (MPM200), capable of two-photon laser scanning imaging, dual-color one-photon optogenetic stimulation, epifluorescence microscopy, and electrophysiology (see Fig. 2.1).

2.6.1 Electrophysiological capabilities

The setup was equipped with a set of three micromanipulators to guide a recording electrode with three degrees of freedom. A chloride-coated silver wire (recording electrode) was connected to a head stage. Data were acquired with Multiclamp 700 B amplifiers. This configuration allowed for whole-cell patch clamp recordings in voltage and current clamp configuration, as well as extracellular recordings, such as local field potentials (LFP). Infrared differential interference contrast optics (iDIC) were utilized for visualization of the specimen, navigation and visual guidance in electrode placement.

2.6.2 Epifluorescence

The setup was equipped with a LED system (470 nm, 525 nm), standard GFP and mCherry filtercube sets, and a trinocular eyepiece for standard epifluorescence microscopy. The pathway consisted of the following elements: 1) a collimation lens to collimate the incoming LED signal. 2) a tube and "scan" lens to reduce the diameter of the beam profile according to the pathway. 3) three neutral density (ND) filters (NDs of 4, 8, and 16) for additional control over light intensity. 4) two diaphragms (field, aperture) for confinement of the illumination spot size.

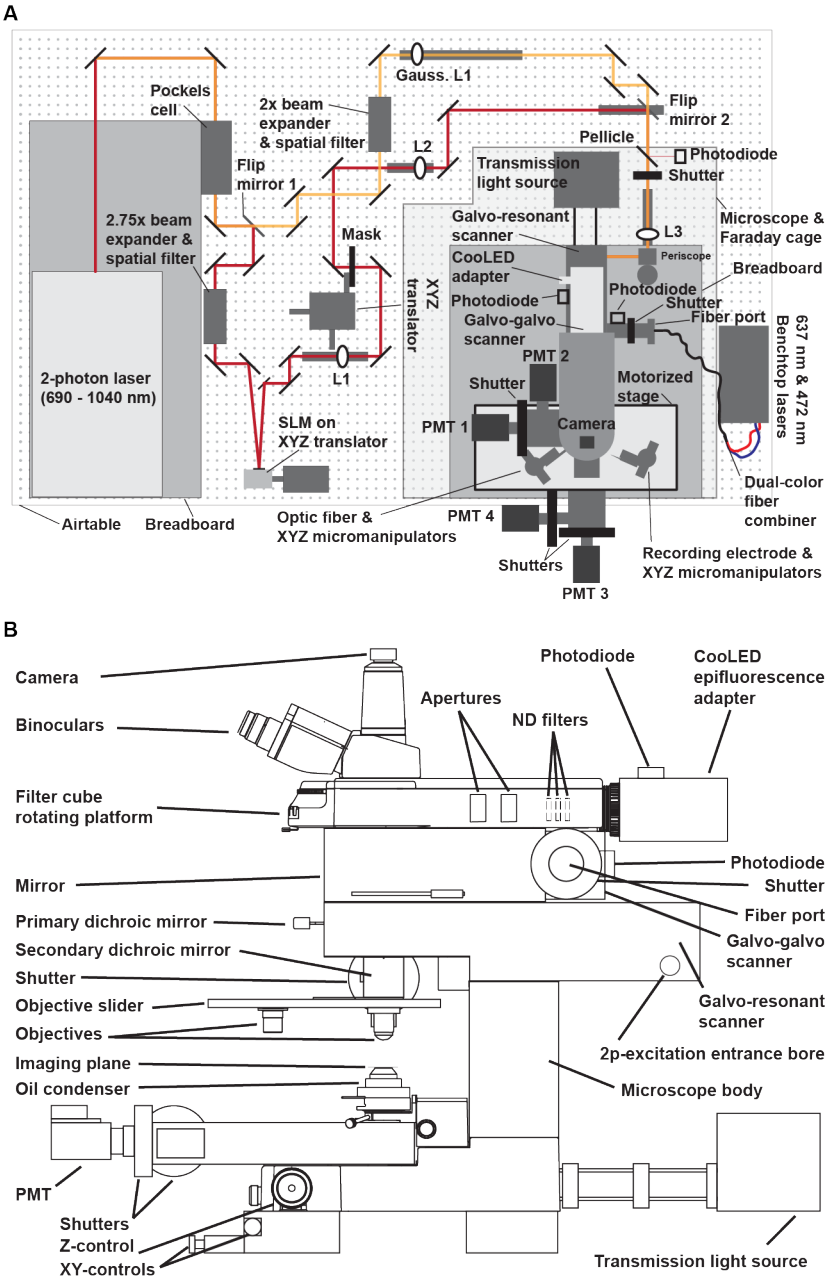

Figure 2.1 Design of the main setup

A Main *in vitro* setup from top. 2-photon laser on left. "Bessel path" in dark red (via flip mirror1, 2.75x beam expander, SLM, L1, mask, L2, flip mirror 2 and

L3. 'Regular path" in light orange. Light path that is shared in dark orange. The setup is also equipped with 4 PMTs (2 for epi- and 2 for transdetection), electrophysiological capabilities, as well as multiple optogenetic stimulation paths (red and blue benchtop lasers connecting to either a fiber port or an optic fiber on right, LED epifluorescence lamp in the rear of the setup). **B** Main *in vitro* setup from the side (right side in A). Epifluorescence path is on top, followed by the dual-color optogenetic stimulation path (via galvo-galvo scanners), followed by the 2-photon path (via galvo-resonant scanners). Transmission light is provided from the bottom via the oil condenser. Recording electrode and optic fiber are left out for simplicity.

2.6.3 Optogenetic stimulation

Two independent pathways for stimulating spectral optogenetic variants were built (Fig. S2.1, S2.2, S2.3). 1) The above mentioned epifluorescence path allowed for simulation of blue-responsive opsin variants (e.g. ChR2, Chronos) in a spatially confined and temporally precise manner. Stimulation of this pathway reached the specimen via the objective. This path (1) was used in most of the experiments that were performed in OHSCs. 2) A pair of benchtop laser sources for blue (473 nm) and red (637 nm), combined using a 2-color fiber combiner provided input for more spectrally diverse stimulation patterns. This input was utilized in two manners. 2A) Via a fiber-collimator, a set of Galvanic scan-mirrors, and a scan-tube-lens system, the beam could be guided into the specimen. This manner of optogenetic stimulation offered the option of performing subcellular channelrhodopsin-assisted circuit mapping (sCRACM) by minimizing the diameter of the beam profile to $\sim$70 μm in the focal plane. Alternatively, a larger diameter could be generated via a second beam expander in the scan-tube-lens system, such that a much larger diameter could be achieved in the focal plane ($\sim$2.3 mm). The former was not utilized in experiments described in this thesis. The latter was used for dual-color photostimulation to map binocular retinogeniculate inputs. 2B) The 2-color fiber combiner could feed an optic fiber (600 μm diameter), that could be placed in close proximity to the specimen, providing an input that is independent of the imaging microscope. This is a critical feature of the setup to move forward in identifying input-specific wiring rules of LTP-induced dendritic spines. Decoupling of imaging location and stimulation area is essential

to obtain sufficient quantities of data in diverse areas following LTP. This path (2B) was used in electrophysiological recordings of CA1 pyramidal cells in OHSCs before and after wash-in of muscimol (Fig. 3.3.8A-C).

2.6.4 Two-photon laser-scanning imaging

An 80 MHz pulsed femtosecond Ti:sapphire laser (MaiTai eHP, Spectra-Physics) was used as excitation source (690-1040 nm) for two-photon (2p) imaging. The 2p-laser intensity was controlled via an electro-optical modulator (Pockels cell). The latter was also used for turnaround blanking. A spatial filter (50 μm), that included a 2x beam expander, blocked higher spatial frequencies in the incoming excitation beam, achieving an approximation of a collimated Gaussian beam. Another 1x beam expander was implemented just before the periscope, which in turn directed the light towards a galvo-resonant (8 KHz) scanning system. The scanners guided the beam through a pair of lenses (scan and tube lens, f = 40 and f = 200, respectively), placed in 4f configuration between the scanning mirrors and the back pupil plane of the objective. After passing through the tube lens, the light was reflected downward via a dichroic mirror (720 nm short-pass filter), towards the objective. Subsequently, the 2p excitation beam passed the primary dichroic - either a 680-1600 nm long pass filter or a triple-notched dichroic mirror, depending on use - prior to hitting the objective. The notched dichroic mirror effectively allowed for optogenetic activation and simultaneous 2p imaging in green and red spectral regions. The long-pass filter was employed when no photostimulation was needed during 2p imaging. The above mentioned configuration of lenses ensured appropriate overfilling of the objective and thus a tightly focused point-spread function in the sample (Fig. 2.2B).

Depending on scan settings (mainly the number of line scans in the y-axis of the image, and to a lesser degree on zoom settings), frame rates of upward of 300 Hz could be achieved. However, such images only contained 8-16 line scans in the y axis of the resulting images, and hence constitute a specialized case of image acquisition, which was utilized in Fig. 3.3.4. For most applications this was not a suitable setting, and consequently a trade-off between temporal and spatial frequency had to be made: most calcium-imaging and structural image acquisitions, usually were obtained with framerates of $\sim$58.3 and $\sim$7.5 Hz, respectively (for more details, see methods, 2.7.2).

To collect emitting photons from the imaging plane, a total of 4 photomultiplier tube detection modules (PMTs) across two photodetection arms were employed (Fig. 2.1A, 2.2A). Two PMTs were used per arm, capturing photons epidirectionally (via the objective) and transdirectionally to the objective (via a 1.4 NA oil immersion condenser). Emitting photons from the specimen were filtered according to use and wavelength (i.e. fluorophore of interest, see below) prior to reaching the PMTs. Per color of interest, two PMTs (one per detection arm) were paired to capture emitting photons of the same wavelength spectrum. PMTs of the transdirectional detection arm contributed ∼60 % of the signal. A set of three mechanical shutters were placed just in front of the three of the four PMT modules, such that they could be light-shielded for brief periods of time. This allowed for continuous imaging, even during episodes of optogenetic light stimulation (see below). Due to spatial constraints of the setup, the last PMT could not be equipped with a shutter and was consequently turned off during calcium imaging involving photo-stimulation.

To image fluorophores with different emission spectra, two sets of filters (placed before the PMTs) were employed (Fig. S2.1, S2.2, S2.3): For red/green imaging, a 560nm dichroic beam splitter and 525-50 nm and 607-70 nm bandpass filters were used to detect photons in the green and red spectra, respectively. This configuration was utilized for ratiometric calcium imaging and structural imaging in OHSCs, as well as to obtain images of the retinogeniculate axonal surroundings of dLGN cells. In the alternative configuration, to capture photons in the blue-green spectrum, a broader filter (510-84 nm bandpass filter) was placed in front of one pair of PMTs, while a 6.0 neutral density filter prevented photons from reaching the other pair of PMTs. This configuration was utilized for calcium imaging or imaging of spine maturity (in which a blue-shifted fluorophore such as mTurquoise2 was utilized) in OHSCs. Switching between imaging modes was achieved by manual exchange of filter sets in the both detection arms.

For overview images, either a 16x 0.8 NA water immersion or 20x 0.95 NA water immersion objective were used. For all other imaging in OHSCs, a 60x 1.1 NA water immersion objective was used. For all other imaging in acute slices, a 40x 0.8 NA water immersion objective was used. Finally, a 4x air objective was used for orienting in OHSCs and slices, and for photostimulation in slices.

2.6.5 Volumetric two-photon laser-scanning imaging

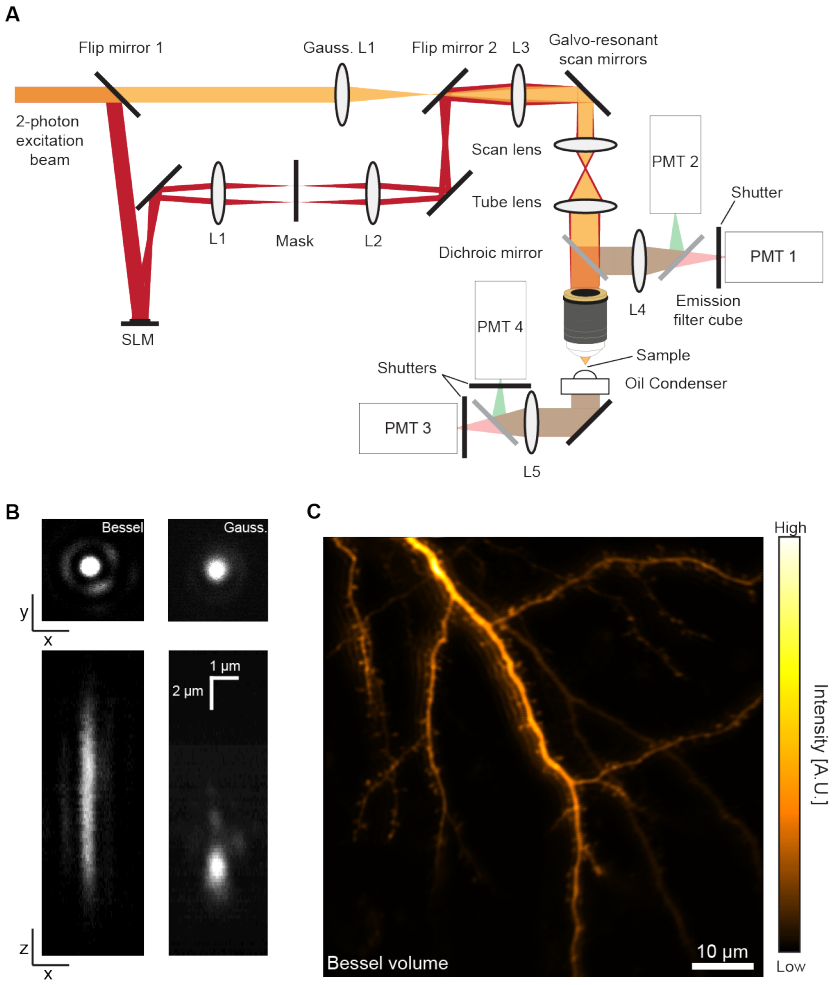

Figure 2.2 Engineering a setup with flexible volumetric Bessel-beam imaging capabilities

A Schematic of the light paths. "Bessel path" in red, "regular path" in yellow, common path in orange. For volumetric Bessel-beam imaging, the 2p excitation beam is directed towards an SLM via flip mirror 1, generating a light pattern of concentric rings. L1 and the annular mask cut out an annular light pattern, which is projected onto the galvo-resonant scanners via L2, flip mirror 2 and L3. Scan and tube lenses project this pattern onto the back pupil of the objective, producing an approximation of a Bessel beam in the sample. Emitting photons

(red, green, brown) are captured by four PMTs, each two epi- and two trans-directional to the objective. PMTs are equipped with filters and/or shutters. **B** Point spread functions of the two pathways. Left: Bessel-beam PSF. Right: Regular (Gaussian) beam path. Top: Maximum intensity Z projections of PSFs. Bottom: Average intensity Y projection of PSFs. The Bessel path produces a in PSF in the sample that is elongated in z, which lends itself for volumetric imaging. **C** Dendrites and spines of a pyramidal CA1 neuron of a OHSC shown as an average intensity projection of a time series (254 frames) captured using volumetric Bessel-beam imaging.

Functional characterization of dendritic spines requires high throughput approaches due to the high demands in temporal and spatial resolutions. To this end, the 2p imaging setup was equipped with a "Bessel module" to enable volumetric imaging via extended depth-of-field 2p Bessel beam imaging (as described in Lu et al., 2017). Rapid switching between the "Bessel light path" (i.e. volumetric imaging) and the "regular light path" during an experiment was achieved by using a pair of motorized flip mirrors. In the "Bessel light path" first an approximation of a Gaussian light distribution was achieved using a spatial filter (50 μm) that included a 2.5x beam expander. Subsequently, an annular, Bessel-like illumination pattern was generated using a 512 x 512 pixel spatial light modulator (SLM) displaying concentric ring patterns at a phase of 81.65. This pattern was produced, as described earlier (see Supplementary Technical Notes in Lu et al., 2017). The Fourier transform of the SLM-generated phase pattern was then projected onto a custom-made aluminium-coated annular mask by placing a lens (L1) with f = 400 equi-distantly between the SLM and the mask. The annular mask let the first-order Bessel pattern pass, while blocking zero- (undiffracted light) and higher-order patterns, as well as unwanted impurities. To achieve a Bessel focus in the sample, this mask-generated ring pattern was imaged onto the resonant scanner (using L2 and L3 (both f = 500) in 4f configuration, see Fig. 2.2A) and then onto the back pupil plane of the objective (using the same path as the "regular light path", i.e. via scan and tube lenses, also in 4f configuration). This configuration produced a z-elongated point spread function, which allowed for effective stimulation of a volume (Fig. 2.2B, C). As a consequence, roughly 5 times as many dendritic spines could be captured during calcium imaging without compromising temporal frequency (Fig. 2.3A-E).

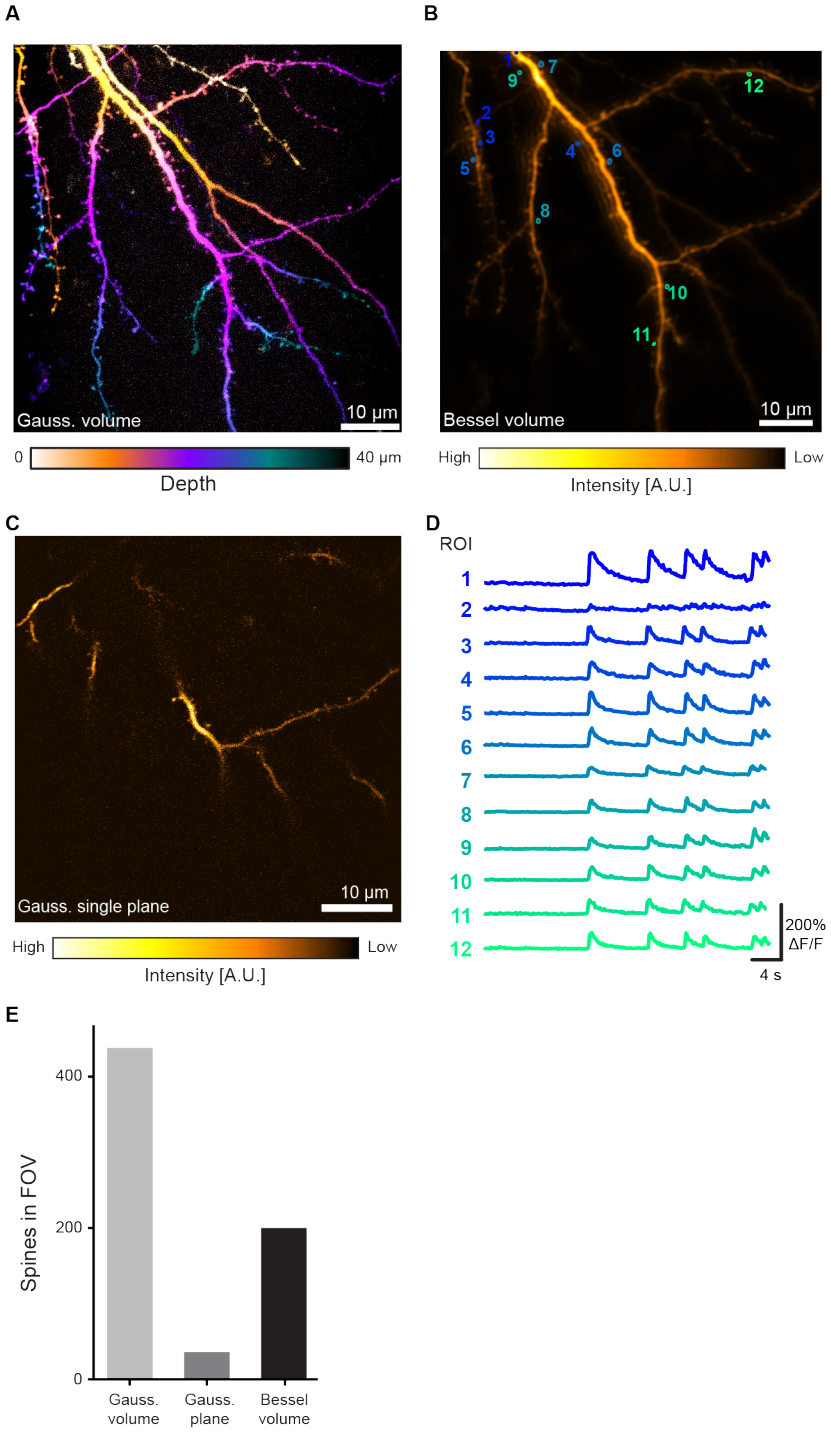
A
Gauss. volume
10 µm
0
40 µm
Depth
B
Bessel volume
10 µm
High
Low
Intensity [A.U.]
C
Gauss. single plane
10 µm
High
Low
Intensity [A.U.]
D
ROI
1
2
3
4
5
6
7
8
9
10
11
12
200%
ΔF/F
4 s
E
Spines in FOV
400
200
0
Gauss. volume
Gauss. plane
Bessel volume

Figure 2.3 Volumetric Bessel-beam imaging improves functional spine imaging throughput
A Maximum intensity projection of a dendritic stretch of a CA1 pyramidal cell in an OHSC, acquired using regular ("Gaussian") beam imaging. The image is color-coded for depth (see scale bar on bottom). **B** The same dendritic stretch shown in A imaged using volumetric ("Bessel-beam") imaging. Shown is an average intensity projection of a time series (254 frames) captured using volumetric Bessel-beam imaging. Note that most of the image shown in A could be captured using volumetric imaging. Individual dendritic spines are outlined in color (blue-green). **C** The same dendritic stretch shown in A imaged using regular ("Gaussian") imaging. Shown is an average intensity projection of 3 frames in a single plane. The difference in coverage between volumetric imaging (D) and regular imaging is apparent. **D** Calcium traces of spine outlines shown in D. To aid in generating events of synaptic transmission, the GABA-A-antagonist bicuculline (20 μM) was added. Hence, rhythmic activity can be seen. **E** Quantification of the number of spines seen in C (light gray), D (black) and E (dark gray). For imaging modalities that require high temporal resolution (e.g. calcium imaging), volumetric Bessel beam imaging offers approximately 5x higher throughput.

2.7 Other setups

2.7.1 Second *in vitro* setup

A proportion of the *in vitro* thalamic cell imaging was performed at another *in vitro* 2p setup. This setup was identical to the main setup (see above) in terms of electrophysiological, regular line-scan 2-photon imaging, and two-color optogenetic stimulation capabilities, but lacked the hardware for volumetric Bessel-beam imaging, photostimulation-induced calcium imaging (i.e. shutters) and the transdirectional detection pathway. Nevertheless, retinogeniculate mapping experiments were performed at this setup in a near-identical manner as the main setup.

2.7.2 *In vivo* two-photon laser-scanning microscopy

In vivo two-photon imaging was performed on a separate multiphoton imaging setup (see Rose et al., 2016; Jaepel et al., 2017; Bauer et al., 2021). An 80 MHz pulsed femtosecond Ti:sapphire laser (720-1040 nm) powered a custom-built multiphoton system, equipped with a 8 KHz resonant scanner, a Pockels cell for beam turnaround blanking and power control. For imaging of green or red-shifted fluorophores, a 560nm dichroic beam splitter and 525-550 nm and 607-670 nm bandpass filters were used to detect photons in the green and red spectrum, respectively. GaAsP photomultiplier tubes were utilized for photodetection (employing short-pass filters at 720 nm). Structural images (mRuby2) of L2/3 pyramidal neurons in mouse V1 were acquired with a 25x 1.1 NA water immersion objective. Image acquisition was performed at a resolution of 1024 × 1024 pixel (15.2 Hz), a step size of 0.5 μm, acquiring 30 images per step. In total 1000 frames were obtained with an effective voxel size of 73 × 73 × 500 nm. Imaging wavelength was set to 1040 nm. Average laser power under the objective was kept below 50 mW. Images were acquired using Scanimage r4.2 (Pologruto, Sabatini, & Svoboda, 2003) and custom-written hardware drivers.

2.7.3 Confocal microscope

To precisely quantify axonal innervation of RGC afferents in the dLGN, imaging of cleared brain slices was performed using a commercial confocal microscope (Sp8, Leica), equipped with an argon-ion laser (used at 488 nm), as well as a diode pumped solid-state (DPSS) laser (561 nm) and a Helium-Neon laser (633 nm). Photodetection was performed by PMTs and hybrid detectors (HyDs, Leica). The same microscope was utilized to image cleared coronal brain slices of a Thy1-GFP mouse as part of the DeepD3 training data acquisition (see below).

2.8 Data acquisition

2.8.1 Electrophysiological recordings

Whole-cell recordings

Whole-cell voltage- and current-clamp recordings of thalamic neurons in acute slices and CA1 neurons in OHSCs were performed at room temperature with borosilicate glass patch pipettes (tip resistance of 4-5 MΩ) filled with Cs- and K-gluconate-based internal solution, respectively. Series resistance was usually below 30 MΩ. Data were acquired with Multiclamp 700 B amplifiers and subsequently marshalled into cell-specific folders for subsequent analysis. Voltage clamp recordings were filtered at 8 kHz and digitized at 20 kHz at the main setup, and filtered at 4 kHz and digitized at 10 kHz at the secondary *in vitro* setup. Experiments in thalamic neurons were performed in standard ACSF and in the presence of the GABA-A receptor antagonist bicuculline (20 μM) to block inhibitory di-synaptic connections. Experiments in CA1 neurons of OHSCs were performed in high-calcium or magnesium-free ACSF and in the presence of TTX (1 μM), 4-AP (100 μM) and D-serine (10 μM). In some experiments in OHSCs, muscimol (1 μM) was washed in to activate GABA-A receptors (Fig. 3.3.8A-D). In other experiments, the internal solution contained D-890 (1-2.5 mM) to prevent VGCC opening in patch-clamped CA1 neurons (Fig. 3.3.9C, D).

2.8.2 *In vitro* two-photon imaging

In vitro two-photon imaging in CA1 neurons and most dLGN neurons was performed on the main setup. Images were acquired using Scanimage r4.2 (Mathworks Pologruto, Sabatini, & Svoboda, 2003).

Structural imaging

Overview images of CA1 neuromorphologies in OHSCs were acquired to navigate throughout the experiment. Image stacks were acquired at a resolution of 1024 × 1024 pixels in x and y with a step size of 1-2 μm in z, using a high (60x, 1.1 NA) or lower (20x, 0.95 NA) magnification objective. Some overview images were further processed and subsequently utilized as part of the DeepD3 training dataset (see Table 7). High-resolution structural images (tdTomato) of CA1 neuromorphologies in OHSCs were acquired at different

zoom levels, usually with a resolution of 2048 × 2048 pixels (7.3 Hz), a step size of 0.5 μm (using a piezoelectric z-scanner), while frame averaging 50 frames online. A typical structural image stack spanned ∼193, ∼193 and 60 μm in x, y and z, with a voxel size of 0.0944 by 0.0944 by 0.5 μm. For structural imaging, the excitation wavelength was tuned to 1040 (tdTomato) or 810 nm (Alexa 594). Average laser power under the objective was kept below 15 mW.

Spine maturity imaging

To determine the maturity level of dendritic spines of CA1 neurons in OHSCs, the mTurquoise2-fused nanobody Xph-15 was imaged at 860 nm. Spine-maturity imaging was performed after high-resolution structural imaging, matching the image acquisition settings of the just acquired structural images (except for laser intensity and excitation wavelength; see above). Due to the lack of spectral overlap between the two fluorophores employed in structural (tdTomato) and spine maturity (mTurquoise2) imaging, two separate image stacks had to be acquired. Image registration (see below) was performed to create two-colored images of structure and maturity. To quantify the localization optimum of Xph-15, regions of interest were chronically imaged once per day over the course of four days, starting with day 2 post SCE. Regions were re-found visually. Spines were not matched across experimental days. Per region of interest, laser powers remained identical across imaging days for both structural and spine maturity imaging.

Calcium imaging

To visualize functional responsiveness of single spines and their neighboring dendritic segments to optogenetic stimulation, 2p calcium imaging of GCaMP7b was performed at the main setup. Imaging regions were visually inspected during the experiment to maximize the number of dendritic spines in the field of view. Imaging was performed using 940 nm excitation and typically with a framerate of ∼58.3 Hz, using a high-magnification (60x, 1.1 NA) objective. Movies spanned 93.87 × 24.05 μm in x and y, with a pixel size of 0.091 × 0.093 μm and captured ∼6 seconds (250 frames). Optogenetic stimulation (5 ms, 473 nm) of presynaptic boutons (ChR2-positive Schaffer collaterals) was delivered after 0.5 or 1 second, splitting the movie into baseline and response time windows. The majority of calcium imaging

was performed in the ”regular line scan mode” and not using the "Bessel module". However, volumetric imaging was performed similarly as described above, with the trade-off of sacrificing effective spatial resolution (NA) for volumetric image acquisition (z, depth).

To quantify responsiveness before and after wash-in of muscimol or VGCC blockers (mibefradil & nifedipine), optogenetic stimulation was set such that no dendritic calcium spikes were initiated. Next, ten repeats of optogenetic stimulation were performed with an inter-stimulus interval (ISI) of 120 seconds. This was repeated after wash-in of pharmacological agents.

To generate a data set containing movies of single-spine responses (data A) and dendritic calcium events (data B), regions of interest were imaged with varying blue-light stimulation intensities to evoke calcium responses in single spines or dendritic calcium spikes. Typically the latter required higher stimulation intensities.

To assess the effectiveness of the subtype-unspecific VGCC blocker D890, calcium imaging of the synthetic calcium indicator Fluo-4 (150 μM, intracellularly introduced via whole-cell patch clamp) was performed in dendritic stretches of CA1 pyramidal neurons. Here, blue-light stimulation intensities were again varied to evoke calcium responses in single spines or dendritic calcium spikes. As a control, identical experiments omitting D890 were performed.

To assess the spread of calcium spikes throughout the cell, lower spatial resolution calcium imaging was performed in regular line scan mode, using a 20x 0.95 NA objective (Fig. 3.3.4A-C). To this end, the y-axis of the images was decreased to a minimum (16-32 pixel) to maximize temporal resolution (280-330 Hz). Movies typically spanned close to 5 seconds ($\sim$1300-1500 frames). Here, optogenetic stimulation was administered after $\sim$750 ms.

In vitro two-photon imaging of thalamic cells

Before electrophysiological recordings, overview images of the dLGN were obtained using low-magnification objectives (20x, 0.95 NA or 16x, 0.8 NA). These served as orientation tools for targeting cells for patch-clamp recordings. During electrophysiological recordings, cells were filled with Alexa 594

and subsequently imaged to obtain a detailed image stack of the cell's morphology (excitation wavelength: 810 nm, 40x 0.8 NA objective, emission filter 607/70-25, 1024 × 1024 pixels, 0.3-0.8 μm pixel size, step size 1.2 μm). Moreover, another image stack was obtained to later identify the location of the cell in the dLGN within the retinogeniculate axonal fibers expressing td-Tomato and EGFP (excitation wavelength = 940 nm, 40x 0.8 NA objective, emission filters 607/70-25, 525-50, 1024 × 1024 pixels, 0.3-0.8 μm pixel size, step size 1.2 μm).

Point spread functions

To obtain point spread functions of the two imaging pathways at the main setup ("regular pathway", "Bessel pathway"), 100 nm sized beads embedded in 5 % agarose, were imaged at 940 nm with a step size of 200 nm and 50 frame averaging per step using a 60x 1.1 NA water immersion objective.

2.8.3 *In vivo* two-photon imaging

Structural image stacks (mRuby2) of apical and basal dendrites of pyramidal L2/3 neurons of bV1 were acquired using the *in vivo* two-photon laser-scanning microscope. Regions were selected heuristically, based on dendrite outgrowth and image clarity. Images were obtained using a 25x 1.1 NA objective (N25X-APO-MP, Nikon, USA), at a resolution of 1024 × 1024 pixels in x and y with a voxel size of 73 × 73 × 500 nm in x, y and z. Excitation wavelength was set to 1040 nm , 30 frames were obtained per z-level and post-hoc averaged (see image processing). Typically the imaged volume spanned 50 μm (100 planes) in z.

2.8.4 Confocal imaging

To quantify RGC axonal convergence in the dLGN, three-color images were obtained at a voxel size of 1.614 × 1.614 × 4.0 μm using an argon-ion laser (used at 488 nm), as well as a diode pumped solid-state (DPPS) laser (561 nm) and a Helium-Neon laser (633 nm). The three channels were acquired sequentially through a 20x 0.75 NA objective (HX PL APO L 20x/0.75 IMM CORR CS2). Spectral detection windows were set to capture EGFP (493-555 nm) and Alexa-647 (staining against calbindin, 638-750 nm) - imaged simultaneously -, and tdTomato (565-628 nm) - imaged sequentially. Scan

speed was set to 600 Hz (bidirectional). Online averaging of three line scans resulted in the individual images, which were mosaic merged (10 % overlap, LAS X, Leica) to create the final, tiled image of the entire part of the LGN that the slice contained.

Confocal images of cortical dendrites and dendritic spines were obtained from cleared coronal slices of a Thy1-GFP mouse at a voxel size of 61-117 × 61-117 × 500 nm using an argon-ion laser (used at 476 nm) to excite GFP. Emitting photons were captured using a PMT (488 - 738 nm). Scan speed was set to 600 Hz (bidirectional). Frames were online-averaged 10 times.

2.9 Externally obtained datasets

To validate DeepD3 on externally generated and annotated data, a publicly available dataset was obtained (Smirnov, Garrett, & Yasuda, 2018). In short, OHSCs were prepared from C57BL/6J mice, biolistically transfected with GFP and subsequently two-photon imaged (60x objective, pixel size: 66.7 × 66.7 nm).

2.10 Data analysis

2.10.1 Electrophysiological data processing

Whole-cell recordings of thalamic neurons

Light-evoked PSCs were quantified as described earlier (Bauer et al., 2021). In short: Recordings of inward and outward currents (-70mV, AMPAR-mediated; +40mV, NMDAR-mediated, respectively) were treated differentially, due to the slow NMDAR decay, which caused responses of the first stimulation (red) to override the responses to the second laser stimulation (blue). Hence, an exponential fit (one or two parameters, depending on df-adjusted R^2) was utilized to subtract the decay of the first response from the second in +40 mV recordings. Subsequently, mean peak responses for each channel (red, blue stimulation) were calculated from baseline-adjusted traces (100ms window prior to stimulation). Significant light-evoked PSCs were determined using a non-parametric signed-rank test (last 6 steps of the 11 step protocol, $p < 0.05$). Using NMDAR PSC peaks, input types were defined

as follows: contralateral/ipsilateral-only, binocular, contralateral/ipsilateral-silent (only NMDAR-response from the contralateral/ipsilateral input, respectively), other (e.g. cells that received input from both eyes at -70mV but not at +40mV).

The ocular dominance index (ODI) determined relative input strength from both eyes, separately for AMPAR and NMDAR-mediated responses:

$$ODI = \frac{\overline{PSCpeak}_{contra} - \overline{PSCpeak}_{ipsi}}{\overline{PSCpeak}_{contra} + \overline{PSCpeak}_{ipsi}} \tag{2.1}$$

where PSCpeak was defined as follows: If both inputs were significant, PSCpeak was equal to the maximum response current across all 11 steps. If only the blue input was significant, instead of using the peak, the mean of the last 6 steps of the protocol was taken, as it proved to be a more reliable measure. PSCpeak was set to zero for non-significantly responsive cells.

To quantify crosstalk-suppression between opsins, the crosstalk suppression index (Fig. S3.1.1) was calculated as:

$$Crosstalk\ suppresion\ index = \frac{\overline{PSCpeak}_{red} - \overline{PSCpeak}_{blue}}{\overline{PSCpeak}_{red} + \overline{PSCpeak}_{blue}} \tag{2.2}$$

where the PSCpeak for red and blue deflections exceeded 3 standard deviations above baseline. Baseline was determined as 100 ms prior to stimulation for red responses and 100, 2, and 1 ms for blue stimulation (depending on the length of the red stimulation of 250, 10 and 1 ms).

Whole-cell recordings of CA1 neurons

Whole-cell patch-clamp recordings of CA1 neurons in OHSCs (Fig. 3.3.8, 3.3.9) were low-pass filtered (4^{th} order Butterworth at 1000 Hz). Traces were subsequently baseline subtracted (average inward current of the first 300 ms or 990 ms, depending on the timing of the blue-light stimulation) and the peak response in the stimulation time window (350-370 ms, 1000-1020 ms) was determined.

The effect of the the GABA-A receptor agonist muscimol on maximal inward current in the Schaffer collaterals was quantified. To this end, the peak

inward current in the stimulation time window was computed. Using an 11-step protocol increasing photstimulation in steps of 10 % from 0 to 100 %, photo-dose-response curves before and after wash-in of muscimol were obtained (Fig. 3.3.8B). The maximal inward current of this protocol was then compared before and after wash-in (Fig. 3.3.8C).

To quantify the effect of D890, a subtype-unspecific VGCC blocker, on the generation of dendritic calcium spikes, whole-cell recordings in voltage-clamp and calcium imaging was performed (n = 5 cells). As a control, similar recordings were done without the inclusion of D890 in the internal solution (n = 2 cells). To this end, the maximal inward current after photostimulation was determined as outlined above. Next, using two-photon calcium imaging, it was determined whether a dendritic calcium spike had occurred or not (see below for details on criteria). Then, the average maximal inward currents per condition (D890, control) were determined, averaging across all recordings in all cells (Fig. 3.3.9F).

2.10.2 Image processing

Reconstruction and analysis of thalamic cell morphology

Cell morphologies were reconstructed manually using the Simple Neurite Tracer plugin of ImageJ (Longair, Baker, & Armstrong, 2011; Schneider, Rasband, & Eliceiri, 2012). Reconstructions were subsequently analyzed using custom-written MATLAB code and the TREES toolbox (Cuntz et al., 2011). Dendritic length was defined as the sum of all dendritic internode sections, while dendritic reach was set to the maximum Euclidean distance of dendritic nodes from the cell soma position. Sholl analysis was performed as previously described (Bauer et al., 2021), with 20 μm distance increments. Dendritic orientation was calculated via its index (DOi), and as previously described (Krahe et al., 2011; Bauer et al., 2021).

Axo-dendritic overlap analyses were performed using a 3D interpolated morphology. Manual alignment of dLGN slice overview images to confocal image stacks (10° increments), together with precise location of the somata of the patched cells in the confocal image stacks allowed calculations of morphology-based fluorescence differences (mFD; see below). Furthermore, confocal image stacks were manually aligned to the dLGN of the right hemisphere of

the Allen common coordinate framework (ACCF; Wang et al., 2020). These series of alignments effectively set all imaging data - morphology, 2p overview stacks, confocal images - of all cells into the same common coordinate framework. Dendritic asymmetry direction (Asymdir) and orientation ($\mathrm{Asym_{ori}}$) were defined as:

$$Asym_{dir} = \arctan 2(\overline{y}_m, \overline{x}_m) \tag{2.3}$$

$$Asym_{ori} = \arctan(\frac{\overline{y}_m}{\overline{x}_m}) \tag{2.4}$$

Where $\mathrm{\overline{x}_m}$ and $\mathrm{\overline{y}_m}$ are the means of all interpolated (see above) nodes in the medio-lateral and ventro-dorsal axes, respectively. The magnitude of assymmetry ($\mathrm{Asym_{mag}}$) was defined as follows: drawing a line orthogonal to the asymmetry orientation and also intersecting the soma split the number of nodes per cell into two groups. The absolute normalized difference between the groups was defined as $\mathrm{Asym_{mag}}$, ranging from 0 to 1:

$$Asym_{mag} = |\frac{2 \cdot \sum_{p=1}^{n}(x_p - (\frac{y_p}{\tan(-1 \cdot Asym_{ori})}) > 0) - n}{n}| \tag{2.5}$$

Where n is the number of nodes and $\mathrm{x_p}$ and $\mathrm{y_p}$ are the node coordinates.

Principal component analysis (PCA) of the x and y coordinates of the dendritic morphology (interpolated maps) revealed two further morphological parameters, elongation orientation ($\mathrm{Elong_{ori}}$) and elongation magnitude ($\mathrm{Elong_{mag}}$):

$$Elong_{ori} = \arctan(\frac{v_{(pc1,y)}}{v_{(pc1,x)}}) \tag{2.6}$$

$$Elong_{mag} = 1 - (\frac{expvar_{pc2}}{expvar_{pc1}}) \tag{2.7}$$

Where $\mathrm{v_{(pc1,y)}}$ and $\mathrm{v_{(pc1,x)}}$ are the first principal components (PC) eigenvector x and y coefficients. And where $\mathrm{expvar_{pc1}}$ and $\mathrm{expvar_{pc2}}$ are the explained variances of the first and second principal components, respectively.

PCA was performed on all six morphological measures (maximum Sholl crossing, dendritic reach, DOi, total dendritic length, asymmetry magnitude and

elongation magnitude). To assess if distinct morphological types exist, multimodality was assessed using Hartigan's dip test (Hartigan & Hartigan, 1985) of the first two PCs.

Re-identification of dLGN cells and normalized fluorescence difference stack generation

Cell body positions of patch-clamped neurons were identified manually in confocal image stacks as described before (Bauer et al., 2021). dLGN outlines were generated manually at different z positions to produce a convex hull of the dLGN. Background was subtracted and a normalized fluorescence difference (FD) stack was generated for each slice (see Bauer et al., 2021). Subsequently, the normalized difference between both fluorescence markers was calculated, producing a FD stack, which ranges from -1 to 1 (ipsi to contra) of each slice:

$$FD(pix) = \frac{F_{contra}(pix) - F_{ipsi}(pix)}{F_{contra}(pix) + F_{ipsi}(pix)} \tag{2.8}$$

Where F is the fluorescence intensity at a given pixel (pix) of a the fluorphore matched to that particular eye (contra, ipsi). Binarized FD stacks were generated using a 3D 64 μm standard deviation Gaussian filter per channel prior to FD computation and binarization (FD threshold = 0).

Alignment of patch-clamp data to ACCF and visuotopic data

The Allen common coordinate framework (ACCF) was downloaded from http://data.cortexlab.net/allenCCF/ (10 μm voxel resolution). This framework contained pixel-wise annotations of the dLGN, the dLGN shell and the dLGN ispilateral projection zone. Confocal images were manually aligned to the ACCF by comparing dLGN shape and ipsilateral projection zone via custom-written MATLAB code (Bauer et al., 2021). Average eye preference was mapped onto the ACCF using an inter-/extrapolated 3D map of ODI values per cell location, as described earlier (Bauer et al., 2021). Visuotopy was mapped onto the ACCF by manually registering a previously generated *in vivo* electrophysiological dataset onto the ACCF using custom-written MATLAB code (Bauer et al., 2021). Inter- and extrapolation were performed similarly as described above. The two maps could then be used

to generate an ACCF-registered map of average eye preference across visuotopy (in 10° azimuth and elevation bins). To produce a map of average eye preference across visuotopy, the mean eye preference of voxels was calculated across elevation and azimuth bins of 10°, as described earlier (Bauer et al., 2021).

Calculation and comparison of mFD and rFD

After cell re-identification (see above), a 600 μm × 600 μm (x × y) column, centered around the re-identified soma position was extracted from the generated FD stack. To calculate the morphology based fluorescence differences (mFDs), voxel size was adjusted to 14.6 μm. Then, the interpolated and aligned morphology served as a voxel-wise morphology template to extract FD values for each cell. This extraction process was repeated at various rotational steps of the morphology template to obtain mFD values at rotational angles. Radial-mask-based binarized FD (rFD) values were calculated similarly. Rather than using a cell's own morphology, the mean 3D dendritic density of all cells was used to extract FD values. Binarization was done at a threshold of 0 to simulate conditions of perfect projection segregation. During rFD and mFD calculation, the voxel containing the soma was excluded due to spectral overlap in the red channel between Alexa 594 and tdTomato.

To simulate rFD distributions across a slice, sampling points were seeded in a grid (40 μm spacing, at a depth of the average z position of all patched cells in the slice of interest) with rFD values being calculated based on seeded sampling points.

To determine the decoding accuracy of the mFD measure, d' was calculated as follows. First, the fraction of cells that had the same sign of ODI and mFD was calculated (initial decoding accuracy). Second, cell ODI was subsequently shuffled (10.000 ×) and decoding accuracy was re-determined to test if the initial decoding accuracy data was above chance (initial decoding accuracy $\leq$ 5th percentile of shuffles). Third, d' was calculated to compare performance of contra- and ipsilaterally dominated cells, based on mFD, as well as mFD when morphology masks were rotated by 180°:

$$d'(bsh) = \frac{meanFD_c(bsh) - meanFD_i(bsh)}{\sqrt{\frac{((n_c-1)\cdot\sigma FD_c(bsh)^2+(n_i-1)\cdot\sigma FD_i(bsh)^2)}{(n_c+n_i-2)}}} \tag{2.9}$$

Where i and c are ipsi- and contralaterally dominated cells, respectively. bsh is the bootstrapped shuffle iteration, n is the number of cells, meanFD is the average of the FD measure (e.g. mFD), σFD is the standard deviation of the FD measure. The obtained distribution of shuffles subsequently served to compute the two-sided p-value of (bootstrapped) differences of d':

$$p = min(\frac{1}{10000} \cdot \sum_{bsh=1}^{10000} \Delta d'(bsh) \geq 0, \frac{1}{10000} \cdot \sum_{bsh=1}^{10000} \Delta d'(bsh) \leq 0) \cdot 2 \tag{2.10}$$

Where Δd'(bsh) is the difference in d' of the two FD measures per bootstrap iteration (bsh).

Calculating background FD gradient

Fluorescence difference (FD) gradients were calculated per cell extracting a 600 μm × 600 μm (x × y) column around the soma and applying a spherical mask within (radius = 150 μm). Extracted FD values were subsequently used to perform linear regression on the displacement in x and y from cell soma of each pixel as the regressors. The magnitude of the background gradient was set to the length of the vector, while x and y were set to the regression coefficients. The orientation of the background gradient was set to values between -90° and +90°.

Processing of structural and spine maturity data

Structural (tdTomato) and spine maturity (mTurquoise2) images of dendrites and spines of CA1 neurons were processed as follows. When possible, a uniform background signal was obtained before the start of the experiment (100+ frames of PMT dark-noise) and subsequently used for baseline correction. Images were subsequently de-interlaced to correct for minor scan-phase misalignments using custom-written MATLAB code.

Next, image-to-image registration was performed. This applies to registration of different structural image stacks across structural imaging time points,

as well as registration of spine maturity image stacks to their respective structural image stacks. Registration was performed in two steps. First, using custom written MATLAB code, images were manually aligned. This initial approximation was then utilized in a second, affine registration step. Blank frames from the prior manual alignment step were omitted and the image was subsequently smoothed using a Gaussian blur (sigma = 2 pixels). Affine registration of these smoothed and cropped images was performed using the Computational Morphometry Toolkit (CMTK, https://www.nitrc.org/projects/cmtk/) , using the structural stack as a reference. Warping was performed on the non-smoothed spine maturity data. After registration, frames which were affected by warping artifacts (usually 3-5 frames from both ends of the image volume) were excluded from analysis.

Structural image stacks were subsequently processed by DeepD3 (see methods, 2.10), providing outlines of dendritic spines and dendrites in 3D. Dendrite ROI outlines were determined by the DeepD3-assigned probability (>70 %), and excluded if the minimal dendritic length was insufficient (100 connected pixels in 2D). Spine ROIs were excluded base on distance to dendrite (centroid of spine ROI distance to dendrite < 15 pixels), size (minimum size = 10 pixel in 3D). Spine ROI outlines were determined by the DeepD3-generated probability (>50 %). These outlines were subsequently utilized to extract average raw fluorescence values of dendrites and spines from the two registered image stacks (structural, spine maturity). To quantify the localization preference of Xph-15, a ratiometric measure was utilized, comparing the maturity level of each spine to the maturity level of the entire dendritic arbor in the image. This measure, the ratiometric spine-to-dendrite ratio, was computed as follows:

$$StD_{ratio} = \frac{\frac{Maturity_{spine}}{Structure_{spine}}}{\frac{Maturity_{dendrite}}{Structure_{dendrite}}} \tag{2.11}$$

Where $\text{Maturity}_{\text{spine}}$ and $\text{Structure}_{\text{spine}}$ are the average raw fluorescence values of all voxels within a given spine ROI of the maturity and structural images, respectively. $\text{Maturity}_{\text{dendrite}}$ and $\text{Structure}_{\text{dendrite}}$ are in turn the mean raw fluorescence values of all voxels that had been labeled/outlined as dendrite, extracted from the maturity and structural images, respectively.

Processing of calcium imaging

High-resolution image series of calcium dynamics of dendrites and dendritic spines were processed as follows: when possible, a uniform background signal was obtained before the start of the experiment (100+ frames of PMT dark noise) and used for correction. When ratiometric imaging was performed, images were split into their respective channels (green/functional and red/structural). Images were then de-interlaced to correct for minor scan-phase misalignment. To correct for lateral motion, images were then translationally registered via frame-wise phase correlation (using the mean of the first 100 signal frames as a template). These internally registered images were subsequently registered to one another (across-movie-registration), using the same method used for lateral motion correction. An average projection (across frames; using the structural channel when ratiometric imaging was performed, and using the functional channel otherwise) was then used as a template for automated outlining of dendrites and dendritic spines via DeepD3 (see methods, 2.10). Dendrite ROIs outlines were determined based on the DeepD3-extracted probability (>70 %), and excluded if the minimal dendritic length was insufficient (100 connected pixels). Spine ROIs were excluded base on distance to dendrite (centroid of spine ROI distance to dendrite <30 pixels), size (minimum size: 20 pixels). Spine ROI outlines were also determined by thresholding on the DeepD3 output probability (>40 %). A 2D watershed segmentation was applied to separate touching or overlapping spine ROIs.

A typical image contained several tens of spines, and one to two dendritic stretches (see e.g. Fig. 3.3.3C). DeepD3-generated dendritic ROIs were further subdivided into 30 pixel (∼3 um) long stretches, termed dendritic subROIs. Each spine was paired with one dendritic subROI for further analysis using a k-means nearest neighbor search (MATLAB, knnsearch.m). This was used to test several approaches, attempting to computationally disentangle spine-localized transmission-induced calcium events from dendritic calcium spike-generated calcium events in the spine (see below, Fig. 3.3.3, 3.3.5, 3.3.6).

Spine ROIs were matched across time points based on x-y overlap (minimal overlap = 15 pixels), using the first time point as a reference. Non-matched spine ROIs were omitted from analysis. The matching of spines was per-

formed to assess their responsiveness across time and treatments (e.g. before and after wash-in of a pharmacological agent). After automatic ROIing and ROI matching, matched spine and dendrite ROI outlines were utilized to extract average raw fluorescence values of dendrites and spines per frame. This resulted in one fluorescence time series for each ROI (dendrite or spine) per movie per channel (functional and/or structural). Using these time series, normalized fluorescence fluctuations were computed:

$$\Delta F/F_0(t) = \frac{F(t) - F_0}{F_0} \tag{2.12}$$

Where F is the mean fluorescence of a given channel from a given ROI at time point t, and F_0 is the mean raw fluorescence of that same channel prior to photostimulation (baseline). Typically ∼45 frames were taken as baseline frames (before photostimulation). However, the exact number depended on the imaging frame-rate and experiment.

In a similar fashion, ratiometric normalized fluorescence fluctuations were computed for some analyses:

$$\Delta F/R_0(t) = \frac{F(t) - F_0}{R_0} \tag{2.13}$$

Where F is the mean fluorescence of the green (functional) channel of a given ROI at time point t, F_0 is the mean raw fluoresecence of that same channel prior to photostimulation (baseline), and R_0 is the mean raw fluorescence of the red (structural) channel prior to photostimulation.

To identify fitting criteria for the automated detection of dendritic calcium spikes, 64 movies across 9 imaging regions (n = 6 cells) were visually inspected and human-annotated for the presence or absence of a dendritic calcium spike prior to any analysis (blind). $\Delta F/F_0$ and $\Delta F/R_0$, as well as their smoothed versions (using a 9-point moving average) were computed to identify the measure of choice for quantifying calcium dynamics. The criteria for those measures were tested and compared to the human-annotated data in three steps. First, responsiveness of each dendritic subROI was determined:

$$Response(Mo, dR) = \begin{cases} 1 & \text{if } M_{resp}(Mo, dR) > \overline{M_{bsl}}(Mo, dR) + X \cdot \sigma(M_{bsl}(Mo, dR)) \\ 0 & \text{if } M_{resp}(Mo, dR) < \overline{M_{bsl}}(Mo, dR) + X \cdot \sigma(M_{bsl}(Mo, dR)) \end{cases}$$

Where Response is the binary responsiveness of a dendritic subROI dR in a movie of interest Mo. M_{resp} is the value of the measure of choice in the response window, $\overline{M_{bsl}}$ is the average of the measure of choice in the baseline window, and $\sigma(M_{bsl})$ is the standard deviation of the measure of choice in the baseline window. X is the stringency of responsiveness tested (ranging from 1 to 10 in increments of 1). In total, nine measures were tested (see Table 6) in this manner.

Criterion	$\mathbf{M_{resp}}$	$\overline{\mathbf{M_{bsl}}}$	$\sigma(\mathbf{M_{bsl}})$
1	peak $\Delta F/F_0$	$\Delta F/F_0$	$\Delta F/F_0$
2	peak $\Delta F/F_0$ (smoothed)	$\Delta F/F_0$ (smoothed)	$\Delta F/F_0$ (smoothed)
3	peak $\Delta F/F_0$ (smoothed)	$\Delta F/F_0$	$\Delta F/F_0$
4	avg. $\Delta F/F_0$	$\Delta F/F_0$	$\Delta F/F_0$
5	avg. $\Delta F/F_0$ (smoothed)	$\Delta F/F_0$ (smoothed)	$\Delta F/F_0$ (smoothed)
6	peak $\Delta F/R_0$	$\Delta F/R_0$	$\Delta F/R_0$
7	mean $\Delta F/R_0$	$\Delta F/R_0$	$\Delta F/R_0$
8	peak $\Delta F/R_0$ (smoothed)	$\Delta F/R_0$ (smoothed)	$\Delta F/R_0$ (smoothed)
9	mean $\Delta F/R_0$ (smoothed)	$\Delta F/R_0$ (smoothed)	$\Delta F/R_0$ (smoothed)

Table 6 Response measures

In addition to the 9 measures outlined in Table 6, Wilcoxon rank-sum tests were performed between values in the baseline and response windows, as an alternative to using $X \times \sigma(M_{bsl})$ as a responsiveness threshold. Here, only $\Delta F/F_0$ and $\Delta F/F_0$ (smoothed) were utilized. Instead of using X as a stringency measure, the significance threshold was set to $\alpha = 0.05$, 0.01, 0.001, 0.0001, and 0.00001.

Second, after determining responsivenesses of each dendritic subROI, the

occurrence of a dendritic calcium spike was tested as follows:

$$DendriticSpike(Mo) = \begin{cases} 1 & \text{if } \frac{\sum_{dR} Response(Mo)}{N_{dR}(Mo)} > Thresh_{dROIs} \\ 0 & \text{if } \frac{\sum_{dR} Response(Mo)}{N_{dR}(Mo)} < Thresh_{dROIs} \end{cases}$$

Where DendriticSpike is the presence/absence of a dendritic calcium spike in movie Mo, N_{dR} is the total number of dendritic subROIs in the movie and $Thresh_{dROIs}$ is the threshold of the dendritic calcium spike detection (stringency), ranging from 0.1 to 1 in increments of 0.1.

Third, using the above mentioned measures (n = 9 & 2), responsiveness criteria (k = 10 & 5) and $Thresh_{dROIs}$ (j = 10), a dendritic calcium spike detection table was obtained, indicating whether or not a dendritic calcium spike was found in a given movie with a given set of criteria and thresholds. This array was subsequently compared to the visually inspected and human-annotated data. Consequently, a parameter matrix, similar to a confusion matrix, was computed, quantifying "true positives" (TP), "false positives" (FP), "true negatives" (TN), and "false negatives" (FN). Quotation marks are used here, since the comparison was performed on visually inspected data and not ground truth data in the common sense. Precision, recall and F1 score were computed using the parameter matrix.

$$Precision = \frac{TP}{TP + FP} \tag{2.14}$$

$$Recall = \frac{TP}{TP + FN} \tag{2.15}$$

$$F1Score = \frac{2 \cdot TP}{(2 \cdot TP) + FP + FN} \tag{2.16}$$

The responsiveness of single dendritic spines was determined in a similar fashion: To identify fitting criteria for the automated detection of spines showing responses to photostimulation, 161 movies across 15 dendritic regions in n = 4 neurons (>950 dendritic spines) were visually inspected and human-annotated for the presence or absence of such single-spine dendritic

events. This was done prior to analysis, effectively blinding the annotator. $\Delta F/F_0$ and $\Delta F/R_0$, as well as their smoothed versions (using a 9-point moving average) were computed to identify the measure of choice for quantifying calcium dynamics. Criteria on those measures were tested and compared to the human-annotated data in three steps. First, the responsiveness of each spine ROI was determined:

$$Response(Mo, sR) = \begin{cases} 1 & \text{if } M_{resp}(Mo, sR) > \overline{M_{bsl}}(Mo, sR) + X \cdot \sigma(M_{bsl}(Mo, sR)) \\ 0 & \text{if } M_{peak}(Mo, sR) < \overline{M_{bsl}}(Mo, sR) + X \cdot \sigma(M_{bsl}(Mo, sR)) \end{cases}$$

Where Response is the binary responsiveness of a spine ROI sR in a movie of interest Mo. $\text{Measure}_{\text{resp}}$ is the value of the measure of choice in the response window, $\overline{\text{Resp}_{\text{bsl}}}$ is the average of the measure of choice in the baseline window, and σ(Resp(bsl)) is the standard deviation of the measure of choice in the baseline window. X is the stringency of responsiveness tested (ranging from 1 to 10 in increments of 1). In addition to the measures of choice (Table 6) used in this approach, three additional responsiveness tests were done. As in the detection of dendritic calcium spikes, here, too, Wilcoxon rank-sum tests were performed (between values of the baseline and response windows) as an alternative to using X $\times$ σ($\text{Measure}_{\text{bsl}}$ as a responsiveness threshold. αs of 0.05, 0.01, 0.001, 0.0001, and 0.00001 were used on $\Delta F/F_0$ and $\Delta F/F_0$ (smoothed) data, constituting two additional responsiveness tests. Third and last, instead of testing whether a peak or mean value surpassed a response threshold (X), it was tested whether consecutive frames of the response window fell below a response threshold (X) for a time period of Y. First, at each frame, the response window was tested against a responsiveness criterion:

$$Above(F, Mo, sR) = \begin{cases} 1 & \text{if } M_{resp}(F, Mo, sR) > \overline{M_{bsl}}(Mo, sR) + X \cdot \sigma(M_{bsl}(Mo, sR)) \\ 0 & \text{if } M_{resp}(F, Mo, sR) < \overline{M_{bsl}}(Mo, sR) + X \cdot \sigma(M_{bsl}(Mo, sR)) \end{cases}$$

Where Above is the binary responsiveness of a spine ROI sR in movie Mo at frame F, $\text{Measure}_{\text{resp}}$ is the value of sR of the measure of choice in movie Mo at frame F, and $\overline{\text{Resp}_{\text{bsl}}}$ and σ(Resp(bsl)) are the mean and standard deviation of the measure of choice of spine ROI sR in movie Mo, respectively.

Second, it was tested whether Above(F,Mo,sR) was 1 in consecutive frames

of the response window for a time period of Y (from F to F+Y), if so, this meant the spine ROI sR was treated as responsive (Response(Mo,sR) = 1).

Third, the responsiveness of all spine ROIs of the various measures were compared with the visually inspected and human-annotated data. Again, a parameter matrix and its accompanying measures (TP, FP, TN, FN) were computed (see above).

Using matched spine ROI responsiveness data, release probability for a given spine was computed as follows:

$$P_r(sR) = \frac{\sum\limits_{M} Response(Mo, sR)}{n_M o} \tag{2.17}$$

Where P_r(sR) is the release probability of spine ROI sR, Mo is movie and n_{Mo} is the total number of movies.

To analyze the spread of dendritic calcium spikes, high-temporal resolution (280-330 Hz), low spatial resolution movies were utilized. Images were background-subtracted and subdivided into square ROIs of equal size, spanning the entire length of the image (see Fig. 3.3.4F). Fluorescence changes were computed (ΔF) and subsequently normalized:

$$\Delta F(t) = F(t) - F_0 \tag{2.18}$$

Where F is the mean fluorescence of the green (functional) channel of a given ROI at time point t, and F_0 is the mean raw fluorescence of that same channel prior to photostimulation (baseline).

$$\Delta F_{norm}(t) = \frac{\Delta F(t) - \Delta F_{min}}{\Delta F_{max} - \Delta F_{min}} \tag{2.19}$$

Where ΔF_{norm}(t) is the normalized flurescence change at time point t, and ΔF_{min} and ΔF_{max} are the minimal and maximal ΔF values of all time points t. ΔF_{norm} was subsequently smoothed using a 9-point moving average. The smoothed ΔF_{norm} was then truncated, keeping only the 200th to 500th frame. To determine the half-max value of, the dendritic calcium spike, a sigmoid was fit to the truncated smoothed ΔF_{norm}:

$$S(\Delta F_{norm}) = \frac{A}{1 + B \cdot e^{-\lambda \cdot (\Delta F_{norm} - D)} + C} \tag{2.20}$$

Where $S(\Delta F_{norm})$ is the sigmoid fit of the truncated smoothed ΔF_{norm} calcium trace, A, B, λ, C, and D are fitting parameters (Coneva, 2015). Fitting parameters were iteratively optimized using the MATLAB function fminsearch. Next, the frame at which the fit reached the half-maximum was calculated. Fits were excluded if the half-maximum was outside of the response window of 0 to ∼150 ms post stimulation time window. Since each FOV was imaged 5-7 times, averages across the repeats of ΔF_{norm} and the calculated half-maxima were computed.

To determine if the responsiveness of spines can be determined despite the presence of a dendritic calcium spike (flooding all spines with calcium), three computational approaches were used, with the aim to uncover which spines received synaptic input.

First, a set of response criteria, as described earlier (Coneva, 2015) were used to determine spine responsiveness with and without the occurrence of a dendritic calcium spike. In short, $\Delta F/F_0$ traces of dendritic subROIs and spines were smoothed using a 7 point moving average. Subsequently, the responsiveness of each spine and matched dendritic subROI was determined as follows:

$$Response(R) = \begin{cases} 1 & \text{if } M_{peak}(R) > \overline{M_{bsl}}(R) + 3 \cdot \sigma(M_{bsl})(R) \\ 0 & \text{if } M_{peak}(R) < \overline{M_{bsl}}(R) + 3 \cdot \sigma(M_{bsl}(R)) \end{cases}$$

Where Response(R) is the responsiveness of ROI R (spine or dendrite), M is the smoothed $\Delta F/F_0$, peak connotates the peak during the response window, $\overline{M_{bsl}}$ is the mean during baseline, and $\sigma(M_{bsl})$ is the standard deviation during baseline. Subsequently, 3 scenarios (cases) were tested to assess if a spine was responsive.

In Case 1, the spine ROI is responsive, yet its matched dendritic subROI is not. Hence, the spine is deemed responsive. In Case 2, both the spine and matched dendritic subROI are responsive. The smoothed $\Delta F/F_0$ trace is then truncated from the beginning to the temporal location of $Measure_{peak}$ and subsequently normalized (see equation 2.18 with the exception that instead of $\Delta F/F_0$, smoothed $\Delta F/F_0$ was used). A sigmoid (see equation 2.19) is then fit to the truncated and normalized calcium trace. Subsequently, it

is determined which ROI, spine or matched dendrite subROI, reaches 67 % of the maximum first. If the spine reaches this threshold first, it is deemed to be responsive, following Case 2.1.

Some sigmoid fits are not suited for this analysis due to too noisy calcium traces. Fits are excluded if (1) the maximum of the fit is below 75% of the truncated and normalized smoothed $\Delta F/F_0$, (2) the MATLAB function exceeds the maximum number of iterations to find a good fit, (3) and if the 67 % threshold is crossed before the photostimulation onset. If a fit is excluded, the time point (frame) of crossing the half-maximum (50 %) is determined using the truncated and normalized smoothed $\Delta F/F_0$. If the spine ROI crosses this threshold prior to the matched dendritic subROI, the spine was considered to be responsive, following Case 2.2. In the original report by Coneva, the step of identifying bad fits was done manually (2015). The automated approach described here was employed to approach this part of the processing pipeline in a potentially less subjective manner.

The second approach to unmix dendrite and spine signals during dendritic calcium spikes, that was tested in this dissertation was a version of the "robust fit" approach described earlier (Chen et al., 2013; Wilson et al., 2016; Scholl, Wilson, & Fitzpatrick, 2017). In this approach, a scaled version of the dendritic calcium signal is used and subtracted from the spine calcium signal to determine if a spine received synaptic input during the occurrence of the dendritic calcium spike. This was implemented as follows (Wilson et al., 2016): $\Delta F/F_0$ was determined for each spine ROI, as well as the ROI of the entire dendrite of a given movie. Next, a robust linear regression was fit (MATLAB, robustfit), which determined the slope of the fit, α. If the two traces (spine and entire dendrite ROI) fit well, the slope would be large. Hence, α was used to scale the dendritic ROI trace and subsequently subtract it from the spine ROI signal as follows:

$$\Delta F/F_{0 Spinespecific} = \Delta F/F_{0 Spine} - \alpha \cdot \Delta F/F_{0 Dendrite} \tag{2.21}$$

Next, to determine if the subtraction worked, the Spearman correlation of $\Delta F/F_{0\text{Spine specific}}$ and the entire dendrite ROI signal was calculated. Note, that $\Delta F/F_0$ values below 0 (over-subtraction) were omitted from this analysis. If the correlation was 0.5, the spine was excluded from further analysis. Next, responsiveness of $\Delta F/F_{0\text{Spine specific}}$ was determined, by testing whether

consecutive frames of the response window were always above 2 standard deviations above baseline for at least 100 ms (see above).

The second approach to unmix dendrite and spine signals during dendritic calcium spikes, that was tested in this dissertation was previously described by Kerlin and colleagues (2019). In this approach, the electrophysiological signal underlying a dendritic calcium event is estimated and subsequently fitted to each spine signal individually. The resulting fitted signal is then subtracted from the spine signal to identify if a spine received synaptic input during the dendritic calcium spike. This approach was implemented as follows: in short, the entire dendrite ROI $\Delta F/F_0$ signal (i.e. reference) was deconvolved, to estimate the underlying electrophysiological signal. This was done using a constrained deconvolutional spike inference algorithm (Vogelstein et al., 2010; Pnevmatikakis et al., 2016), using a 'fudge factor' of 0.5 and autoregressive order of 1. The $\Delta F/F_0$ signal of each spine was then fit using a differential evolution algorithm that minimizes the L2-norm using a differential:

$$model(t) = a \times reference(t) * e^{\frac{-t}{\tau}} \tag{2.22}$$

Where model(t) is the fitted value as a function of time t, a is an amplitude constant, reference(t) is the deconvolved $\Delta F/F_0$ reference signal as a function of time t. This differential is then fitted using a differntial evolution algorithm using the following criterium:

$$Minimize\ a, \tau = \sum_{t=1}^{N} \sqrt{(model(t) - mask(t))^2} \tag{2.23}$$

Where mask(t) is the $\Delta F/F_0$ signal of the spine ROI as a function of time t, and τ is the single-exponential decay kernel (time constant). The fitted value (model(t)) was then subtracted from the mask:

$$Subtracted(t) = mask(t) - model(t) \tag{2.24}$$

Where Subtracted(t) is the fit-subtracted $\Delta F/F_0$ signal of the spine ROI at time point t. Finally, using Subtracted(t), the responsiveness of each spine ROI was determined,by testing whether consecutive frames of the response window were always above 2 standard deviations above baseline for at least 100 ms (see above).

Structural *in vivo* data

Structural images of basal and apical dendrites of L2/3 pyramidal neurons were processed as follows: pixel intensities were band-pass filtered at mean ± 1 standard deviation and subsequently de-interlaced. Then, within-stack x-z registration was performed using rigid followed by non-rigid registration methods (Lucas, Kanade, et al., 1981). During this step, individual frames per z-level were averaged. Finally, a 2D median filter (2 pixel radius) was applied. All analysis was performed using MATLAB custom-written code.

Point spread functions

Images of point spread functions of the two imaging pathways of the main setup ("regular pathway", "Bessel pathway") were deinterlaced and subsequently manually registered using the ImageJ plugin CoordinateShift (https://signaling.riken.jp/en/en-tools/imagej/635/).

Pseudo-coloring

Pseudo-coloring of images was performed in the ImageJ software (Schindelin et al., 2012). Color-coding of imaging depth in Fig. 2.3A was performed by an open-source plugin in ImageJ (see Katrukha, 2021).

2.11 Deep neural networks

To automatically outline dendritic spines and dendrites in imaging data, custom-generated convolutional neural networks were employed. The devised framework was termed DeepD3 (**Deep** learning framework for **D**etection of **D**endritic Spines and **D**endrites).

2.11.1 Architecture

DeepD3 uses a U-Net architecture (Ronneberger, Fischer, & Brox, 2015) with a single encoder and two decoder pathways, one for spine and one for dendrite prediction. Data is encoded across four fully convolutional layers, each employing two repeated convolutions (3×3 kernel, with zero padding), batch normalization, a swish activation function and 2×2 max pooling with stride 2 for down-sampling. Accordingly, feature channels doubled between

each convolutional layer in the encoder pathway. Latent variable space was calculated using a 1×1 convolution. Upsampling in the decoder pathway was performed using 2×2 "up-convolutions", effectively halving the feature channel dimension. Upsampled data was then concatenated with data of the same convolutional depth as the encoder pathway, which was provided via skip connections, effectively propagating spatial information from the encoder to the decoder pathway across layers. After concatenation, two repeated convolutions (3×3 kernel, with zero padding), batch normalization and a swish activation function were employed per convolutional layer in the decoder pathway. The last layer of both decoder pathways is activated by a logistic function, to limit probabilities in the output images to values between 0 and 1.

$$g(x) = x \cdot f(x) = \frac{x}{1 - e^{-x}} \tag{2.25}$$

$$f(x) = \frac{1}{1 - e^{-x}} \tag{2.26}$$

Optimization of image segmentation is performed via two independent loss structures (decoder pathways), one for each, spine and dendrite prediction. For the former, the mean square error (MSE) is employed, while the latter is optimized via a Dice loss.

$$\mathcal{L}_{Dendrites} = 1 - \frac{2 \sum_i \cdot \hat{y}_i \cdot y_i}{\sum_i \hat{y}_i^2 + \sum_i y_i^2} \tag{2.27}$$

$$\mathcal{L}_{Spines} = \sum_i (y_i - \hat{y}_i)^2 \tag{2.28}$$

Where y is the human-annotated ground truth, and $\hat{y}$ is the prediction of pixel i.

2.11.2 Training data and procedure

The training data for DeepD3 was curated from two-photon image data of CA1 pyramidal neurons from rat organotypic hippocampal slice cultures and confocal image data of cortical neurons from Thy-1-GFP mice (see Table 7). 2D images were generated via average intensity projections of registered calcium imaging movies using the structural channel. 3D images were de-interlaced but otherwise not further processed. Images had intentionally

varied signal-to-noise ratio and scale (pixel size) to generate a heterogeneous training dataset.

Model	**Image type**	**Dimensionality**	**Fluorophore**	**Resolution (XY) in μm**	**Resolution (Z) in μm**	λ
OHSC CA1	2-photon	3D	tdTomato	0.094	0.5	1040
OHSC CA1	2-photon	2D	tdTomato	0.0917	N/A	1000
OHSC CA1	2-photon	2D	tdTomato	0.0917	N/A	940
OHSC CA1	2-photon	3D	Alexa-594	0.1035	0.5	810
OHSC CA1	2-photon	3D	Alexa-594	0.094	0.5	810
OHSC CA1	2-photon	3D	tdTomato	0.0212	0.5	940
OHSC CA1	2-photon	3D	tdTomato	0.0232	0.5	1040
OHSC CA1	2-photon	3D	tdTomato	0.0458	0.5	1040
OHSC CA1	2-photon	3D	tdTomato	0.1245	1	1040
Thy1-GFP mouse Cortex	Confocal	3D	EGFP	0.075	0.5	476
Thy1-GFP mouse Cortex	Confocal	3D	EGFP	0.117	0.5	476
Thy1-GFP mouse Cortex	Confocal	3D	EGFP	0.061	0.5	476

Thy1-GFP mouse Cortex	Confocal	3D	EGFP	0.104	0.5	476
OHSC CA1	2-photon	3D	tdTomato	0.0458	0.5	1040

Table 7. DeepD3 training data
Overview of generated training data, with location and model of cell (n.b, all cells were pyramidal neurons), microscopy type, dimensionality of the dataset, pixel-size (resolution) in xy, and in z, imaging wavelength and the number of generated training data tiles.

Image data from these four sources were subsequently human-annotated: Using a flood-filling-based neuromorphology reconstruction software package (NeuTube; Feng, Zhao, & Kim, 2015), dendrites were traced in a pixel-wise manner. Spines were also hand-annotated, using PiPrA, a pixel precise annotator software similar to a paintbrush tool (Gómez et al., 2020). These two hand-annotations provided the ground truth for DeepD3 training.

Prior to training, image data was linearly rescaled [-1, 1] (minimum and maximum intensity) and subsequently tiled into 128 × 128 pixel tiles. To increase the size of the training dataset, primary data augmentation in the shape of rotation (4 cardinal directions; $p = 0.5$) and reflection (vertical, horizontal; each $p = 0.5$) was performed with a set probability per tile. Similarly, secondary data augmentation was applied via Gaussian blur (kernel size randomly chosen between 3 and 7 pixels; $p = 0.2$), addition of Gaussian noise (mean 0, standard deviation randomly chosen between 10 and 50; $p = 0.5$), adjustment of brightness and contrast (both changed based on a factor randomly chosen between -0.2 and 0.2; $p = 0.25$) to train some models. Secondary data augmentation was performed with the albumentations package (Buslaev et al., 2018).

The total training dataset comprised of ∼80.000 image tiles. 10 % of training data was selected for validation and never utilized in training. Training was performed via backpropagation, optimizing DICE and MSE losses for den-

drite and spine prediction, respectively. During training, mini-batch (batch size: 16 - 64 images; iterations per epoch: 1250 - 5000) gradient descent on the minimization of the sum of both loss functions was performed. Training time was limited to 25 epochs with a learning rate of 0.0005. To optimize spine and dendrite segmentation for various data types, a variety of models using one or more of the above outlined data sources were trained (see Table 8).

Some DeepD3 networks were trained using a different procedure, where image tiles were flexibly streamed during training, thereby exceeding the dataset size of ∼80.000 image tiles. Validation was then performed on a fully annotated dataset that was not used during training, instead of splitting training data into 90/10 (training/validation). Here, the learning rate was set to $0.5 \cdot 10^{-3}$ for 15, after which an exponential decay with a time constant of 0.1 was introduce.

All networks were optimized using the Adam optimizer in the TensorFlow environment using the Keras package (Kingma & Ba, 2014; Abadi et al., 2016).

Model purpose	**Training data**	**Secondary data augmentation**	**Figures**
Calcium imaging	All 2D images of OHSC CA1 neurons	None	3.2.1B, 3.2.5A-E, 3.3.3A-D, 3.3.4, 3.3.5, 3.3.6, 3.3.7E-H, 3.3.8A, B,
Low zoom structural imaging	3D images of OHSC CA1 neurons (Alexa 594, tdTomato) with pixel size 0.094 or 0.1035 μm	None	3.2.2, 3.2.4,

High zoom structural imaging	3D images of OHSC CA1 neurons (tdTomato) with pixel size 0.0212 μm	None	3.2.3, 3.2.5F, G, 3.3.2,
Generalized model	All data	Yes	S3.2.2

Table 8. Overview of trained models
Overview of trained models with intended purpose in this dissertation, used training data, whether or not secondary data augmentation was employed and the figures this a particular model was used in

2.11.3 Features of DeepD3

ROI detection

Raw images were fed into DeepD3 to automatically predict and segment dendritic spines and dendrites within the image. DeepD3 outputs two images of the same size as the input image, one each for spine and dendrite prediction. Output images reflect pixel-wise probabilities for dendrites and spines based on features of the input image and the chosen/trained model. Dendrite ROIs are identified from the dendrite prediction image based on probability (dendrite threshold) and size of the ROI (minimum dendritic ROI size, i.e. 2D or 3D connected components). Spine ROIs are identified from the spine prediction image based on two probability thresholds: first, a stringent threshold was employed, limiting the *number* of considered spine ROIs. Since a strict threshold also limits the area of the spine ROI, a second, more lenient threshold was employed. Taking only the spine ROIs that met the criteria of the stringent threshold into account, the circumference of these spine ROIs was then drawn by the second, lenient threshold. The resulting spine prediction image was then segmented into spine ROIs using 2D or 3D watershed segmentation (Ollion et al., 2013). Spine ROIs were further

cleaned up, depending on user settings of size of the ROI (minimum spine ROI size) and maximum distance to dendrite.

Probability and minimum ROI sizes of spines and dendrites were computed using image thresholding and connected component analyses in Python 3 and Matlab. To determine the distances of spine ROIs to dendrites, image moments (eq. 2.29) were used to compute the center of mass of a given spine ROI (eq. 2.30). Next, a user-determined radius (maximum distance to dendrite) relative to the centroid of the ROI was assessed for pixels with probability values at the dendrite threshold or higher.

$$\mathrm{M}_{pqr} = \sum_i \sum_j \sum_k I_{i,j,k} \cdot x_i^p \cdot y_j^q \cdot z_k^r \tag{2.29}$$

$$c_y = \frac{M_{100}}{M_{000}}, \quad c_x = \frac{M_{010}}{M_{000}}, \quad c_z = \frac{M_{001}}{M_{000}} \tag{2.30}$$

Where i, j and k are pixel coordinates and p, q and r are moments in the three dimensions y, x, and z. The centroid of the spine ROI is determined by calculating the mean (M) of all included pixels along a single dimension (e.g. 100 for the y dimension), resulting in the dimension-specific centroids c^y, c^x, and c^z.

2.11.4 Validation

To validate DeepD3 performance, a number of human-annotated datasets were acquired: *in vitro* structural images of rat CA1 pyramidal neurons in OHSCs expressing tdTomato (see methods, e.g. Fig. 3.2.3, 3.2.5A-D, 3.2.7), *in vitro* structural images of mouse CA1 pyramidal neurons in OHSCs, expressing GFP (see methods, Smirnov, Garrett, & Yasuda, 2018, Fig. 3.2.4A-C), *in vivo* structural images of L2/3 pyramidal neurons of mouse bV1 expressing mRuby2 (see methods, Fig. 3.2.4D-F, 3.2.6A-E). Manual annotations of data were either done pixel-wisely or simply by annotation of a single point near the centroid of the spine head. Hence, several validation methods were devised.

Pixel-wise validation

Pixel-wise validation was performed on data similar to training data (OHSC, CA1 pyramidal cell, two-photon structural stack, imaging tdTomato at 1040

nm). Spine predictions were performed by jointly permuting both spine thresholds (confining the area of the ROI) across 9 values (10 - 90 % spine probability), obtaining a full confusion matrix and measures (precision, recall, F1 score) per threshold (Fig. 3.2.3D). Particular DeepD3 settings: maximal dendrite displacement was 40 pixels, minimum spine ROI size was 30 connected pixels, minimal dendrite size was 1000 connected pixels, dendrite threshold was 0.995, ROIs were generated in 3D, spines ROIs were excluded if they spanned less than 3 planes.

ROI-wise validation

Since most datasets were not annotated on a per-pixel basis but rather via annotation of a single point in the center of the dendritic spine head, DeepD3 performance was also validated per spine ROI. To this end, two measures were employed: first, a distance-based measure, using a nearest-neighbor approach of the annotation points and the centroids of the predicted spine ROIs without replacement (i.e. a centroid could not be matched to multiple annotation points). Nearest-neighbor annotation/prediction points were thresholded at 12 pixels ($\sim$1.12 μm) to uniquely match spine annotations to spine predictions. In Fig. 3.2.3E the manual annotation was done in a pixel-wise manner, hence the annotation points were replaced by the centroids of the spine annotations. To validate this method, a second measure was devised, the area-based measure. Here, it was tested whether each annotation point was part of the area of a DeepD3-generated spine ROI without replacement. Since manual annotations were done in a pixel-wise manner in Fig. 3.2.3F, here, overlap of predicted spine ROI and annotated spine ROI was quantified. An overlap of more than 50 % of the pixels was taken as a correctly identified spine ROI (true positive).

2.11.5 Inter- and intra-rater reliability

To compare DeepD3 performance to human annotation performance, two datasets were manually annotated by several users (Fig. 3.2.5, 3.2.6). Inter-rater reliability was calculated using a slightly modified version of the distance-based ROI-wise validation method. This method was required to establish whether two annotation points of two annotators marked the same dendritic spine. To this end, the nearest neighbor of all annotation points of annotator pairs were established. Neighbors that were outside of a Euclidean

distance of 12 pixel (∼1.12 μm) and not within 5 z steps (2 above, 2 below) were excluded. Additionally, points could only be uniquely matched (no replacement). Annotation points that fulfilled these criteria were regarded as marking the same spine (TP). In this analysis, the annotations of one annotator were compared to the annotations of another (annotators 1 and 2, respectively). FP and FN were computed according to the performance of annotator 2 with regards to annotator 1. Subsequently, recall and precision were computed per rater pair (Fig. 3.2.5D, 3.2.6E). Intra-rater reliability was done similarly, but comparing annotations of the same raters (generated with an inter-rating interval of at least two weeks).

2.11.6 DeepD3 settings

Figure	**Model**	**Max. dendrite displacement**	**Min. spine ROI size**	**Min. dendrite size**	**Dendrite threshold**	**Min. planes**
3.2.2C	Low zoom structural imaging	40	30	1000	0.7	3
3.2.2D-E	Low zoom structural imaging	40	30	1000	0.7	3
3.2.3B-C	High zoom structural imaging	45	30	1000	0.7	3
3.2.3E-F	Low zoom structural imaging	40	30	1000	0.7	3
3.2.4B-D	Low zoom structural imaging	40	30	1000	0.7	3

3.2.4G-I	Low zoom structural imaging	40	30	1000	0.7	3
3.2.5B-C	Calcium imaging	35	30	1000	0.995	N/A
3.2.5.D-E	Low zoom structural imaging	35	30	1000	0.995	N/A
3.2.5F-G	High zoom structural imaging	335	30	1000	0.7	3
Fig S3.2.1A-C	Calcium imaging	35	30	1000	0.995	N/A
Fig S3.2.1D-F	Generalized model	50	30	1000	0.7	3
Fig S3.2.3F	Generalized model	50	30	1000	0.7	3
3.3.2E-H	High zoom structural imaging	30	1000	0.7	0.7	3
3.3.3C-E	Calcium imaging	35	30	1000	0.995	N/A
3.3.4B-F	Calcium imaging	35	30	1000	0.995	N/A
3.3.4G-J	Calcium imaging	35	30	1000	0.995	N/A
3.3.5A-C	Calcium imaging	35	30	1000	0.995	N/A
3.3.6A-C	Calcium imaging	35	30	1000	0.995	N/A
3.3.7G-H	Calcium imaging	35	30	1000	0.995	N/A
3.3.8A-B	Calcium imaging	35	30	1000	0.995	N/A

3.3.8C-D	Calcium imaging	35	30	1000	0.995	N/A

Table 9 DeepD3 settings
Overview of DeepD3 settings used for all figures. For model names, see Table 8. Values are given in pixels. Pixel sizes between images varied slightly but were usually between 73 and 94 nm (see image acquisition)

2.11.7 DeepSpineTool

To qualitatively compare segmentation performance of DeepD3 to a recently published tool for the automated segmentation of dendrites and dendritic spines (Vidaurre-Gallart et al., 2022), this method (DeepSpineTool) was obtained. DeepSpineTool offers three trained networks, which perform image segmentation (Vidaurre-Gallart et al., 2022). The results of all models of the DeepSpineTool are shown in Fig. S3.2.4. Visual inspection suggests that DeepD3 outperforms DeepSpineTool, at least in the data shown in that figure.

2.12 Quality control and data exclusion criteria

2.12.1 Binocular convergence in the dLGN

The dataset comprised of 220 dLGN neurons, for which binocular mapping and subsequent imaging was performed. Data quality was rigorously controlled using semi-automated quality control procedures (see, Bauer et al., 2021). In short, electrophysiological, confocal image (and soma re-identification), transduction, morphology tracing and ACCF alignment quality were separately assessed, such that the assessor was blinded to the other parameters. Electrophysiological data was excluded based on AMPAR responses (38 cells), NMDAR responses (67 cells), and series resistance changes

($\geq$ 50 % between recordings, 14 cells). Data was excluded for AMPAR, NMDAR and AMPAR-to-NMDAR quantifications, respectively. 35 cells were excluded from morphological analysis (34 for having total dendrite length $\leq$ 600 μm, one for having typical dLGN interneuron morphology). 25 cells were excluded from ACCF analyses due to poor confocal image quality. 17 cells were excluded from electrophysiological and fluorescence analyses based on poor local transduction. Cells were excluded from mFD analyses based on protrusion of dendrites (in z: 20 cells with $\geq$ 30 % of the dendritic tree; in x,y 18 cells with $\geq$ 10 % of the dendritic tree outside of dLGN). Exclusion criteria were enforced for relevant quantifications (e.g. cells with poor morphological reconstructions were still used for AMPAR response comparisons).

2.12.2 Automated detection of dendritic spines and dendrites

For inter-rater reliability experiments, data of one spine annotator was excluded, due to insufficiently dense labeling (mean of all annotators: 352 spines annotated, standard deviation 58; excluded annotator: 237 spines annotated). One annotator provided two annotations, one more liberal, one more conservative. For this annotator, after personal communication, it was agreed upon that the liberal annotation best matched the task (count all dendritic spines in the image file). Importantly, this was done blindly (without looking at the performance of that annotator). Hence, the conservative annotation of that annotator was not used in analyses.

2.12.3 Towards establishing wiring rules during LTP-induced synaptogenesis

For tracking spine maturity over several days, 2 imaging regions were excluded on one day based on poor image registration of structural and spine maturity images. For analysis of single-spine responsiveness, dendritic calcium spikes were excluded according to the above mentioned criteria. This concerned calcium-imaging analyses of muscimol wash-in and VGCC blockers (Fig. 3.3.8 and 3.3.9). In electrophysiological recordings that included the subtype-unspecific VGCC blocker D890 in the internal solution, recordings that lasted less than 15 minutes were excluded. Additionally, if the cell was poorly filled with Alexa 594 or Fluo-4 (determined by visual inspection),

it was excluded from analysis.

2.13 Statistics

2.13.1 Binocular convergence in the dLGN

Data are reported as mean ± standard error of the mean (SEM) unless stated otherwise. To analyze some morphology measures in dLGN cells, circular statistics were employed (CircStat, circStatNP; Berens, 2009; Dervinis, 2020). Linear data was tested for normality prior to individual tests. When normality was determined (Kolmogorov-Smirnov Goodness-of-Fit), parametric tests were utilized (two-tailed two-sample unequal-variance, two-way ANOVA, or paired t-tests). On the other hand, when normality assumptions were not met, nonparametric tests (Wilcoxon rank-sum test, Mann-Whitney U test or Kruskal-Wallis) were chosen. In the case of periodic variables, a von Mises distribution was assumed. Correlations between linear variables were calculated using Pearson's and Spearman's correlations (normality assumed and not assumed, respectively). Periodic measures were correlated with other periodic measures and linear data using circular-circular and circular-linear correlations, respectively. Asterisks indicate significance thresholds as follows: $p < 0.05$ (*), $p < 0.01$ (**), $p < 0.001$ (***), unless otherwise stated. Multiple comparison corrections (Bonferroni) were employed when necessary.

2.13.2 Automated detection of dendritic spines and dendrites

To compare DeepD3 performance against inter-annotator reliability a Kruskal-Wallis tests were performed using the distance-based criterion of all annotator pairs and the recall of DeepD3 per annotator (Fig. 3.2.5C, 3.2.6D).

2.13.3 Towards establishing wiring rules during LTP-induced synaptogenesis

To compare spine size to spine maturity levels across imaging days, the Pearson's correlation between spine ROI size (in pixels) and the RSDR value was calculated (Fig. 3.3.2G). To compare release probabilities of spines before

and after wash-in of pharmacological agents (muscimol, VGCC blockers), Pearson's chi-squared tests were performed on the release probability of each spine before and after wash-in (Fig. 3.3.8F, 3.3.9B). To assess the frequency of eliciting dendritic calcium spikes during photostimulation before and after wash-in of pharmacological agents (muscimol, VGCC blockers), McNemar's tests were performed on all available movies of each dendritic region of interest before and after wash-in (Fig. 3.3.8H, 3.3.9C). To assess whether the stimulation power differed in trials in which no dendritic calcium spike was detected before and after the application of muscimol, a McNemar's tests was performed on the recorded peak stimulation power, as measured from the photodiode (Fig. 3.3.8G). To assess whether the maximal normalized inward current was altered by the wash-in of muscimol during patch-clamp experiments, a McNemar's tests was performed (Fig. 3.3.8C). To identify criteria of spine responsivity, Wilcoxon rank-sum tests were performed between values in the baseline and response windows. Values were either $\Delta F/F_0$ or $\Delta F/F_0$ (smoothed) taken from spine ROIs. Significance thresholds were set to α= 0.05, 0.01, 0.001, 0.0001, and 0.00001. An identical approach was utilized to identify criteria for the automated detection of dendritic calcium spikes, this time, however, using values from dendritic sub-ROIs.

Chapter 3

Results

3.1 Binocularity in the dLGN

The dLGN has typically been seen as a relay station between the retinae and the primary visual cortex in adult mice. However, recent evidence suggests otherwise, with structural (Rompani et al., 2017) and functional studies (Jaepel et al., 2017; Sommeijer et al., 2017; Huh et al., 2020) disagreeing on the amount of binocular convergence in the retinogeniculate pathway. Hence, the aims of this part of the dissertation were to: (A) quantify retinogeniculate convergence with optimal signal-to-noise and (B) identify which mechanisms underlie binocular integration on a single-cell level in the dLGN.

3.1.1 A dual-channel input mapping approach for studying crosstalk-free eye-specific retinogeniculate convergence

Rationale

There is high variability in recent reports of the amount of binocular retinogeniculate convergence (Rompani et al., 2017; Jaepel et al., 2017; Sommeijer et al., 2017; Huh et al., 2020). Direct comparisons between these studies are difficult, given the differences in recording methods (calcium imaging, electrophysiological single unit recordings, retrograde rabies tracing), spatial sampling and chosen analyses. Therefore, an *in vitro* approach combining optogenetics and whole-cell patch clamp electrophysiology was devised to map

retinogeniculate inputs of both eyes with optimal signal-to-noise ratio in single dLGN neurons (Fig. 3.1.1A). Critically, to quantitatively assess the input strength of both eyes, their respective axonal afferents needed to be stimulated independently. To this end, it was assessed whether the opsins ChrimsonR and Chronos, given their minimal spectral overlap, could be activated without spectral crosstalk. Since ChrimsonR, the red-shifted (excitation peak = 589 nm Klapoetke et al., 2014) opsin, is also blue-light responsive, a previously established sequential photostimulation approach (Hooks et al., 2015) was utilized and modified. In this approach, ChrimsonR is rendered unresponsive to blue light stimulation immediately after prolonged exposure (tens of ms) to red light. Therefore, using a long red pulse would depolarize only ChrimsonR-expressing axonal terminals, and promptly delivered blue light stimulation would depolarize only Chronos- but not ChrimsonR-expressing boutons.

Proof of principle

To test this, RGCs were transduced monocularly with ChrimsonR-tdTomato via intravitreal injections of AAVs in mice. After sufficient expression time (5+ weeks), acute brain slices were prepared to obtain whole cell patch-clamp recordings of individual dLGN neurons. Di-synaptic feedforward inhibition was blocked (bicuculline, 20 μM) to isolate monosynaptic inputs. As expected, ChrimsonR was found to be blue-light responsive (Fig. 3.1.1B, Fig. S3.1.1A). Importantly however, this crosstalk responsivity was circumvented by using sequential photostimulation as described above: ChrimsonR was rendered non-responsive to blue-light stimulation (50ms, 472 nm) immediately after red light exposure (250ms, 637 nm, 3.1.1B). Hence, by employing sequential photo-stimulation, independent measurements of inputs of both eyes to dLGN neurons were made possible.

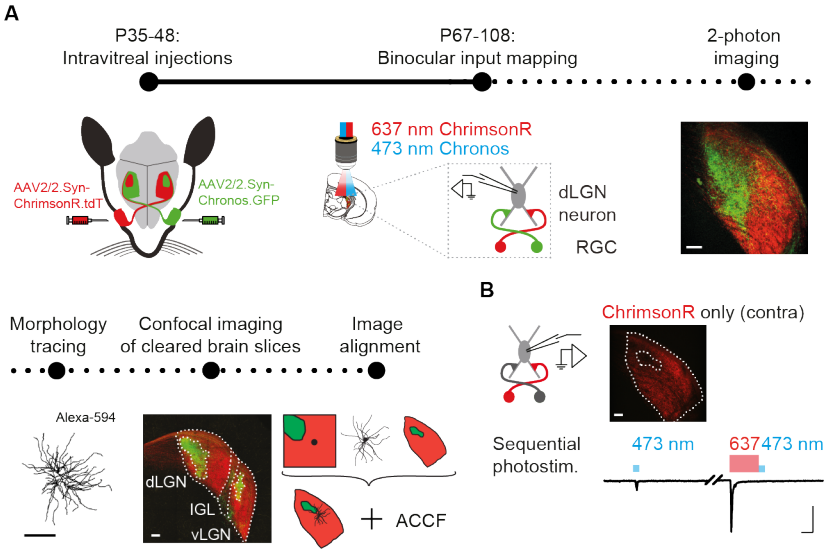

Figure 3.1.1 An assay to map eye-specific functional inputs in the retinogeniculate pathway

A Experimental timeline (from top left to bottom right): The red- and blue-light excitable opsins ChrimsonR/Chronos are introduced to RGCs via intravitreal injections. Whole-cell patch clamp recordings of individual dLGN neurons are performed in acute brain slices using dual-color optogentic stimulation to map binocular inputs. Retinogeniculate input is assessed via optogenetic stimulation of ChrimsonR+/Chronos+ RGC axons using red and blue light (sequential photostimulation). Maximum intensity projection of a two-photon image of an acute slice, showing typical eye-specific projection zone pattern of the two eyes, via ChrimsonR-tdT and Chronos-EGFP in RGC axonal terminals within the dLGN. Alexa-594-reconstructed morphology of representative dLGN neuron. Maximum intensity projection of confocal image of a cleared brain slice. Images are aligned among each other and to the ACCF for further analysis. **B** Suppression of spectral crosstalk using sequential photostimulation: maximum intensity projection of ChrimsonR-tdT expression pattern within dLGN (top). Photoresponses of dLGN neuron (clamped to -70 mV) to 473 nm stimulation (50 ms, trace before the break; irradiance: 5.1 mW/mm^2) and sequential photostimulation using 637 nm (250ms) and 473 nm (50 ms, trace after the break; irradiance 473 nm: 5.1 mW/mm^2; irradiance 637 nm: 3.4 mW/mm^2). Figure modified with permission from Bauer et al. (2021).

Photoproperties of ChrimsonR in the assay

Next, ChrimsonR properties within the sequential photostimulation paradigm were further tested. Even very short red light stimulation (10 ms) was found to be sufficient to prevent blue-light responsivity (Fig. S3.1.1B, C). As expected, long (250 ms) red-light stimulation also proved to work well in preventing spectral crosstalk (Fig. S3.1.1B, C). Hence, to temporally separate the responses to either wavelength stimulation, a long (250 ms) red light stimulation duration was chosen for the final protocol (see below). Surprisingly, it was discovered that repeated and prolonged red-light exposure renders ChrimsonR nearly unresponsive (decrease of > 70 %) to further stimulation (Fig. S3.1.1D, E). Interestingly, blue light stimulation prevents this phenomenon and enables ChrimsonR to be used repeatedly without any loss in photo-responsivity (Fig. S3.1.1D, E). Hence, the use of sequential photostimulation fulfils a second purpose in ensuring reliable responsiveness of ChrimsonR throughout the experiment (Fig. S3.1.2A).

Quantitative binocular input size measurements

To quantitatively assess the contribution of both eyes to a dLGN neuron's input, the maximal input strength of each eye was measured separately. To this end, RGCs of either eye were transduced with ChrimsonR-tdTomato and Chronos-GFP, respectively. After sufficient expression was achieved, whole cell patch-clamp recordings of dLGN neurons were performed in acutely prepared coronal brain slices, while pairing the sequential photostimulation approach with two sequentially performed step protocols: First, the maximal responsivity of a dLGN neuron to increasing amounts of blue light stimulation was established in 11 steps (0 - 100 % laser power). Second, another step protocol was performed, in which red light stimulation was increased in 11 steps (0 - 100 % laser power). In this second protocol, sequential photostimulation was applied, such that each red light stimulation event was immediately followed by blue light stimulation of the intensity that gave the maximal response in the first step protocol. Using this second step protocol, the maximal input strength of both eyes could be measured in single dLGN neurons by taking maximal response values to blue- and red-light stimulation (Fig. 3.1.2A).

Prominent eye-specific retinogeniculate convergence but limited functional binocularity

Both step protocols were applied twice, clamping the cell to -70 and +40 mV to quantify AMPAR- and NMDAR-mediated responses, respectively. Neurons were selected throughout the dLGN, with a slight oversampling in the dorsomedial region to better quantify the amount of binocular retinogeniculate convergence. While all neurons received input from RGC afferents, two main input types were identified based on the observed response patterns: some neurons only received input from the ipsilateral or contralateral eye (monocular neurons), while others were functionally connected to both eyes. A small fraction of these binocular neurons were only responsive to one eye when clamped at +40 mV, indicating a large availability of silent, AMPAR-deficient synapses (Fig. 3.1.2B). Interestingly, the converse, NMDAR-lacking synaptic connectivity, was also observed in a minority of cells. These cells were binocular in their AMPAR-mediated connectivity, but monocularly lacked NMDAR-mediated transmission. Notably, the majority (64 %) of all recorded dLGN neurons were found to receive some input from both eyes (Fig. 3.1.2C). Given the signal-to-noise ratio of whole-cell patch clamp electrophysiological measurements, it is possible to even detect single quanta (Chen, Harata, & Tsien, 2004). As such, whole-cell patch clamp recordings can reveal even weak synaptic connectivity and therefore help in precisely quantifying the amount of eye-specific retinogeniculate convergence.

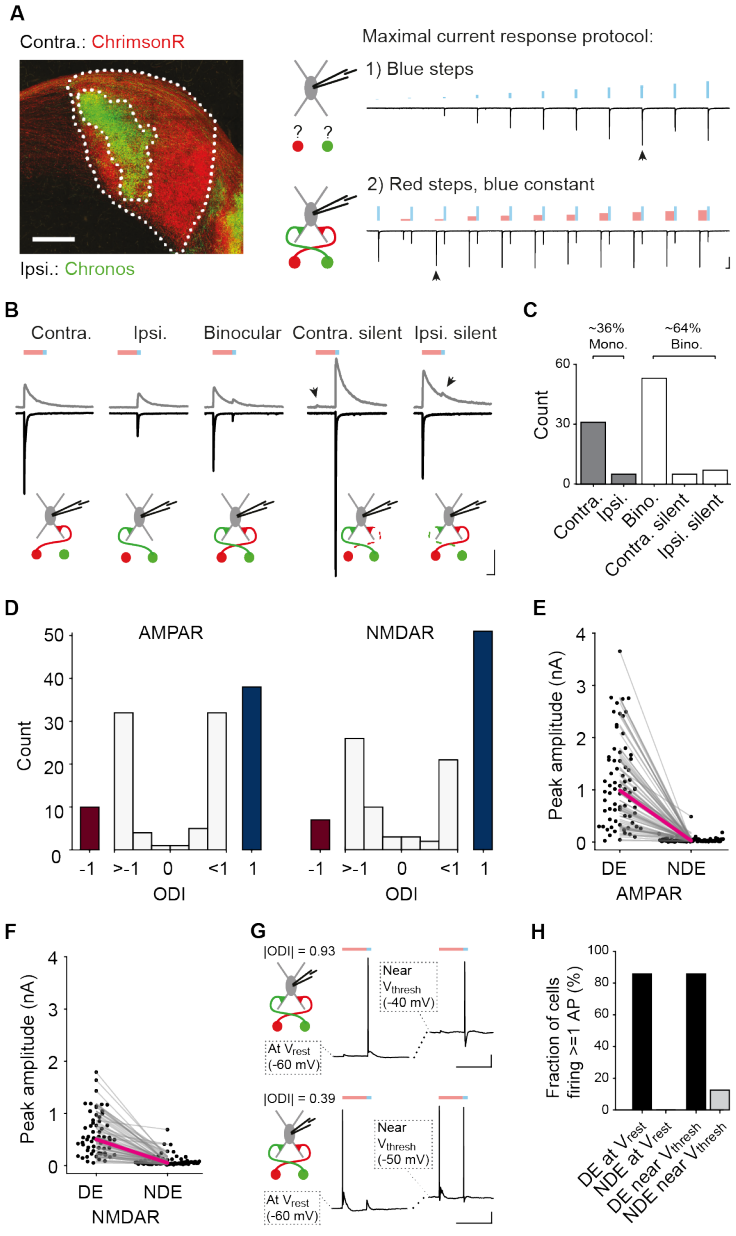

Figure 3.1.2 The retinogeniculate pathway shows robust binocular convergence with limited functional binocularity

A Maximum intensity projection of eye-specific projection zones (ChrimsonR-tdTomato, Chronos-GFP) in dLGN (left). Blue-light-evoked PSCs (473 nm) using increasing irradiances in the 11-step protocol (top). Sequential photostimulation-

evoked PSCs of the same neuron (637 nm for 250 ms, 473 nm for 50 ms, ISI: 10 s) (bottom). Arrowheads indicate maximal response to blue light (top) and successful sequential photostimulation (bottom), respectively. **B** Observed input patterns of eye-specific evoked PSCs for AMPAR- (-70 mV; black) and NMDAR-mediated (+40 mV; gray) responses. AMPA-silent inputs are indicated by arrowheads. **C** Quantification of main input categories, shown in B (n = 101 cells). **D** ODI distributions of AMPA- and NMDAR-mediated currents in dLGN (n = 123 cells). **E** Input strength (peak current amplitude) of dominant and non-dominat eye responses for AMPAR-mediated currents of binocular cells (n = 75 cells) and NMDAR-mediated (right) currents of binocular cells. Gray lines and dots indicate individual cells, medians are indicated in magenta. **F** Same as E but for NMDAR-mediated currents of binocular cells. Gray lines and dots indicate individual cells, medians are indicated in magenta. **G** Representative examples of whole-cell current clamp recordings of dLGN neurons: sequential photostimulation-induced membrane voltage deflections of two binocular dLGN cells. Dominant eye (DE) stimulation evokes an action potential in both, whereas the NDE (non-dominant eye) fails to elicit spiking at resting potential (left). Depolarization via current injection elicits NDE spiking in the more binocular neuron (bottom, right). **H** Quantification of F (n = 8 binocular cells). Electrophysiology trace scale bars in A-B: 100 ms, 250 pA; and in F: 250 ms, 10 mV. Morphology scale bars: 100 μm. Figure modified with permission from Bauer et al. (2021).

But what are the functional implications of the high amount of binocular wiring that was observed? The two step protocol enabled quantification of the maximal input strength of both eyes separately, which could in turn be used to compute the degree of ocular dominance on a single-neuron basis. To this end, the ocular dominance index (ODI) was computed based on the AMPAR- and NMDAR-mediated peak amplitudes. Negative ODI measurements indicate stronger ipsilateral input, while a positive ODI indicates the same for the contralateral input. Maximum (+1) or minimum (-1) ODI values indicate that a cell received only contralateral or ipsilateral input, respectively. Strikingly, only a minority of cells had ODI values near 0, which reflect equisized input strengths from both eyes (Fig. 3.1.2D). The vast majority of cells received a majority of input from one eye (average of AMPAR-based $|\text{ODI}| = 0.91 \pm 0.014$). In fact, on average, the dominant eye (DE) provided 36 times the amount of input as the non-dominant eye (AMPAR-based ODI, Fig. 3.1.2E).

Despite the prominent availability of AMPAR- and NMDAR-deficient synapses in the binocular neuron population, determining dominant eye via AMPAR- or NMDAR-mediated currents provided near-identical results (one cell difference out of 123, Fig. S3.1.3D). The degree of binocularity varied more between the two measures, with NMDAR-based ODI being more binocular on average (Fig. 3.1.2D-F). However, the functional implications of this wiring pattern remained unclear. What is the amount of eye-specific functional convergence between the retinae and the dLGN? Functional connectivity is typically defined as the temporally aligned coordination of neural activity in two regions (Friston, 2011; Engel, Schölvinck, & Lewis, 2021). Hence, neural activity in the shape of action potentials needed to be measured pre- (RGCs) and postsynaptically (dLGN). To this end, whole-cell current-clamp recordings were performed to monitor light-induced voltage deflections in dLGN neurons. Given that the chosen acute slice preparation disconnects RGC cell bodies from the dLGN, optogenetic stimulation of RGC afferents was used as a proxy for neural activity in the retinae. In particular, it was assessed whether inputs from both eyes could independently elicit action potentials in the same dLGN neurons. At resting membrane potential, nearly all dLGN neurons showed spiking activity when stimulated by the dominant eye. Conversely, non-dominant eye stimulation failed to elicit action potentials in all patched dLGN neurons. Surprisingly, even when depolarizing the cell by current injection, only a single cell showed spiking activity in response to stimulation of afferents of the non-dominant eye (Fig. 3.1.2G, H). In conclusion, retinogeniculate wiring seems to be prominently binocular, yet the degree of binocular functional connectivity is very low.

3.1.2 Monocular eye-dominance across dLGN regions and visuotopic space

Binocular retinogeniculate convergence may vary regionally within the dLGN, given that distinct subregions contain RGC afferents of both eyes in varying ratios. To map binocular convergence across dLGN, the location of all recorded cells was registered to the Allen Common Coordinate Framework (ACCF, Fig. 3.1.3A). The contra- and ipsilateral projection zones delineate the expected locations of contra- and ipsilaterally dominated dLGN neurons

(Fig. 3.1.3B).

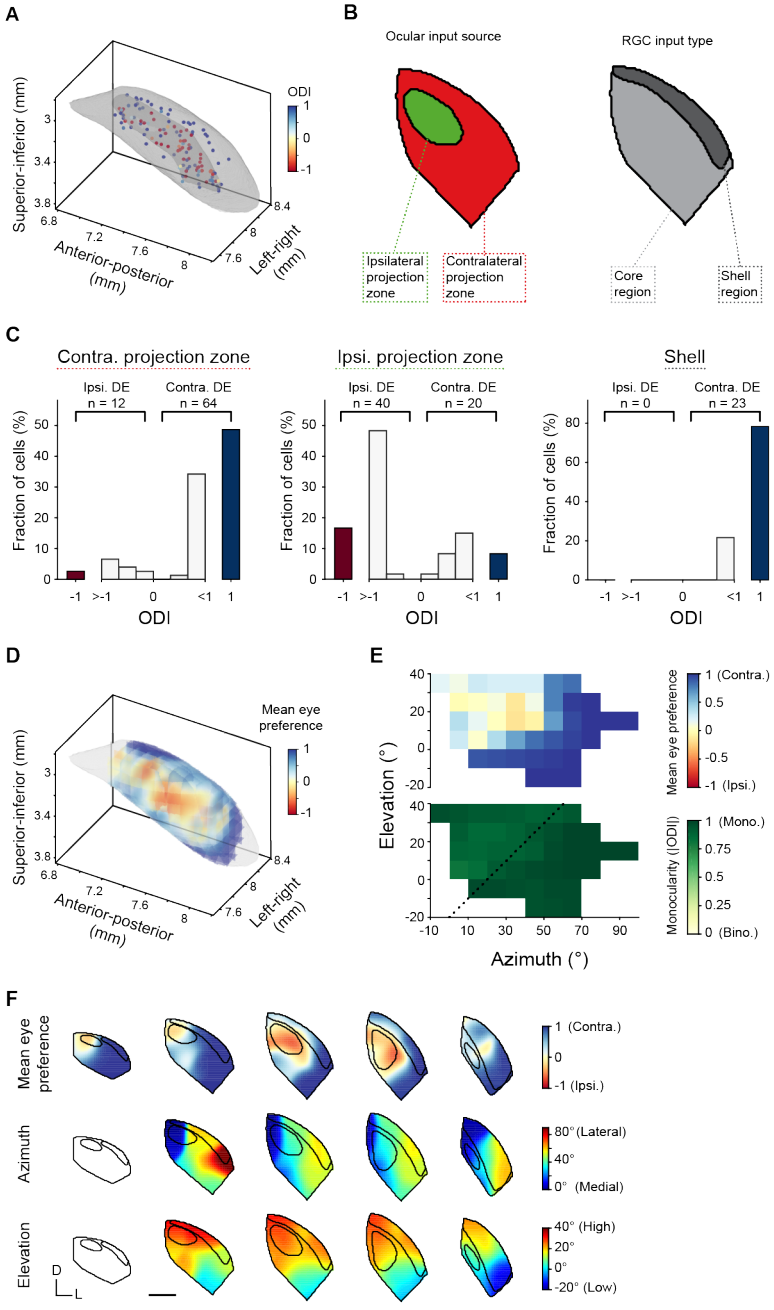
A
Superior-inferior (mm)
Anterior-posterior (mm)
Left-right (mm)
ODI
B
Ocular input source
RGC input type
Ipsilateral projection zone
Contralateral projection zone
Core region
Shell region
C
Contra. projection zone
Ipsi. projection zone
Shell
Ipsi. DE n = 12
Contra. DE n = 64
Ipsi. DE n = 40
Contra. DE n = 20
Ipsi. DE n = 0
Contra. DE n = 23
Fraction of cells (%)
ODI
D
Mean eye preference
E
Elevation (°)
Azimuth (°)
Mean eye preference
Monocularity (|ODI|)
F
Mean eye preference
Azimuth
Elevation

Figure 3.1.3 A map of ocular dominance across dLGN and visuotopic space
A Location of patch-clamped dLGN neurons in the ACCF, color-coded based on ODI (n = 136 cells). Exterior and interior gray hulls are dLGN and ipsilateral projection zone borders, respectively. **B** Schematic of anatomical subdivisions of mouse dLGN. **C** AMPAR-based ODI distributions of neurons inside contra- (n = 76 cells) and ipsilateral (n = 60 cells) projection zone, and the shell region (n = 23 cells). Red, blue and white bars represent monocular ipsilateral, monocular contralateral and binocular cells, respectively. **D** Mean eye dominance map, based on A. **E** Mean eye dominance and mean monocularity (|ODI|) across azimuth and elevation of the visual scene (based on data in F). **F** Coronal sections of dLGN along rostro-caudal axis, color-coded for mean eye dominance (top; based on D), azimuth (middle) and elevation (bottom). Visuotopy interpolations were performed based on data provided by the Niell lab (Piscopo et al., 2013). Scale bar: 200 μm. Figure modified with permission from Bauer et al. (2021).

While for a majority of cells this was found to be true, surprisingly, approximately one quarter of all dLGN neurons (24 %) were situated outside of their expected projection zone, contradicting earlier findings that eye-specific developmental plasticity is thought to be accompanied by a loss in binocular responsiveness (Fig. 3.1.3C; Jaubert-Miazza et al., 2005; Ziburkus & Guido, 2006).

To map how ocular dominance relates to points in the visual scene (visuotopy), a previously published *in vivo* single-unit electrophysiology dataset (Piscopo et al., 2013) was also registered to the ACCF. Using this data, 3D maps of average eye preference (derived from AMPAR-based ODI) and visuotopy were generated and compared (Fig. 3.1.3D, F). Finally, ODI and |ODI| were mapped onto the visual scene (Fig 3.1.3F). Regions representing lateral areas of the visual scene were, as expected, strongly contralaterally tuned (ODI near 1; Fig. 3.1.3E). dLGN regions which process the upper medial field of the visual scene, on the other hand, showed ODI values of near 0, in line with previous reports that this field in the visual scene is repre-

sented by both retinae (Dräger & Olsen, 1980). Importantly, when assessing monocularity via |ODI|, it was found that also this region, just like the rest of the dLGN, contains neurons that are functionally monocular (|ODI| near 1; Fig. 3.1.3E). Thus, the average ODI of near 0 in the upper medial field of the visual scene is a result of a mixed population of functionally monocular neurons, rather than an abundance of binocular neurons in the dLGN.

3.1.3 Three potential mechanisms leading to functional monocularity

The prominent lack of functionally binocular dLGN neurons in the dataset motivated a thorough investigation of which putative mechanisms this bias could be rooted in. In total, three candidate mechanisms were tested: 1) Axon segregation: Given the segregated nature of the eye-specific projection zones, dLGN cell body location could bias sampling from RGC afferents such that most cells receive only monocular input (Fig. 3.1.4A).

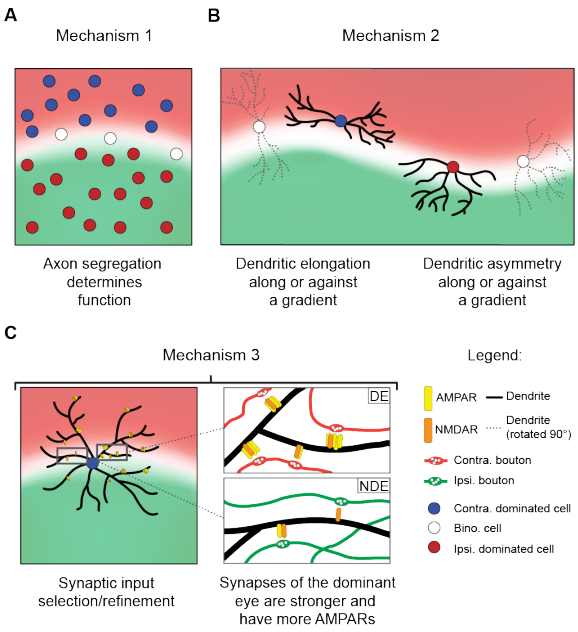

Figure 3.1.4 Potential mechanisms causing functional monocularity in the dLGN Putative mechanisms responsible for the high levels of observed functional monocularity: **A** Axon segregation: the position of neurons determines cells' inputs, causing monocularly biased sampling. **B** Dendritic organization: dLGN neuron dendrites are oriented such that RGC boutons are sampled in a biased manner. **C** Synaptic selection and refinement: despite availability of both eye-specific input sources, dLGN neurons preferentially form synapses with

one of the two bouton populations. Figure reprinted with permission from Bauer et al. (2021).

2) Dendritic orientation: Despite availability of contra- and ipsilateral RGC afferents near the cell body, the dendritic arbor of cells could be situated within the dLGN such that only one eye is effectively being accessed (Fig. 3.1.4B). 3) Input selection and synaptic refinement: Despite availability and connectivity of both ipsi- and contralateral RGC afferents to most cells, dLGN neurons may preferentially form or strengthen synapses with RGC axons from one retina (Fig. 3.1.4C).

3.1.4 Axon segregation does not explain functional monocularity

The segregated nature and geometry of the eye-specific projection zones, coupled with the small dendritic reach of dLGN neurons (average of ∼140 μm), could render dLGN neurons prone to receiving the majority of their input monocularly (Fig. 3.1.4A). Consequently, only some regions in the dLGN should be capable of harboring binocular dLGN cells, based on their availability of contra- and ipsilateral RGC afferents. To explore this putative mechanism, the morphologies of whole-cell recorded dLGN neurons were reconstructed. Next, an average 3-dimensional radial sampling mask was generated based on the average radial histogram of all reconstructed dendrite densities (Fig. 3.1.5A, B). This mask could then be used as a proxy for the average neuronal reach of dLGN neurons. Since ChrimsonR and Chronos had been tagged with fluorophores (tdTomato and EGFP, respectively), RGC axonal innervation was quantified. To this end, brain slices that contained recorded dLGN neurons were cleared and subsequently imaged using confocal microscopy. Here, the fluorescent proteins (tdTomato and EGFP) tagging the two opsins were used to obtain a detailed picture of RGC axon availability. Using the radial sampling mask, the availability of afferents from both eyes at a given location in the dLGN was quantified. In particular, the normalized difference between contra- and ipsilateral voxel counts within the 3D mask was computed, resulting in a measure called the

radial-mask-based fluorescence difference (rFD). Similar to the ODI measurement, negative and positive rFD values indicate higher ipsi- and contralateral axonal innervation, while values near 0 indicate equal availability of both afferents. Using this approach, the distribution of RGC axon availability to dLGN neurons in the dLGN was calculated by sampling rFD values from several equidistant locations across all cleared brain slices (Fig. 3.1.5C-E and Fig. S3.1.4A).

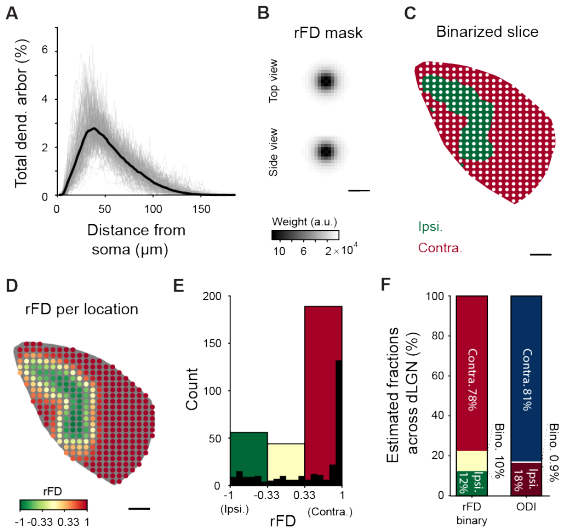

Figure 3.1.5 Mechanism 1: dLGN neuron position
A Dendritic reach in the dLGN is limited: dendritic density as a function of Euclidean distance from soma (average of all cells in black, individual cells in gray). **B** Dendritic sampling (3D radial mask) based on A. **C** Smoothed and binarized confocal image plane shows eye-specific projection zones (red, green) and uniform sampling positions (white; 40 μm spacing). **D** rFD (radial mask-based normalized fluorescence difference) per sampling position, determined by mask shown in B. **E** quantification of D: Ipsilateral (rFD $<$ -0.333; green; 12 %), binocular (rFD within -0.333 and 0.333; yellow; 10 %) and contralateral (rFD $>$ 0.333; red; 78 %) positions sampled. Black bars represent cell-based histogram. **F** Estimated fractions of rFD (left) and ODI (right) across all dLGN slices (see methods, normalized average across 21 slices). ODI classification followed that of rFD (see E; n = 87 cells across same 21 slices). All scale bars: 100 μm. Figure reprinted with permission from Bauer et al. (2021).

Assuming a linear relationship between fluorescence and input strength (for an alternative, see mechanism 3 below), rFD values can be compared to ODI

values since both are normalized measures of two sources. To this end, ODI and rFD values were split into three equisized category bins: contralateral (ODI/rFD >0.33), binocular ($|ODI|/|rFD| \leq 0.33$) and ipsilateral (ODI/rFD <-0.33; Fig. 3.1.5E). Moreover, for this comparison, rFD values were computed using binarized versions of the cleared confocal image stacks. This simulated conditions of perfect eye-specific projection zone segregation. However, even under these optimized conditions axonal innervation patterns were found to be more binocular than the previously observed functional monocularity (rFD, Fig. 3.1.5F). Hence, axon segregation alone cannot explain the observed bias towards functional monocularity in the dLGN.

3.1.5 Dendritic orientation does not account for functional monocularity

As dendritic morphologies of dLGN neurons are not always radially symmetric, sampling within the area of dendritic reach varies considerably between cells. In other words, individual dLGN neurons might sample in a biased fashion along gradients of axonal segregation, effectively resulting in many dLGN neurons only receiving input from one eye and hence rendering them monocularly tuned. To test this, dLGN neuron morphology was further quantified. Three uncorrelated measures - elongation magnitude, asymmetry magnitude and dendritic reach - were determined using morphological reconstructions of recorded neurons (Fig. 3.1.6A, and Fig. S3.1.4A-C). Interestingly, no distinct morphological categories were observed (Fig. S3.1.4D-E), in line with more recent reports (Morgan et al., 2016) but in contrast to others (Krahe et al., 2011; Ling, Hendrickson, & Kalil, 2012). The segregational areas of the eye-specific projection zones were quantified as gradients (see methods) and subsequently compared to the three morphological measures (Fig. 3.1.6A). Only a cell's elongation was found to be correlated with the RGC axon's gradient, indicating that a dLGN neuron's particular dendritic outgrowth might contribute to the observed levels of functional monocularity (Fig. 3.1.6B, C).

To test if a cell's dendritic arbor biases RGC axon sampling, the reconstructed dendritic morphology was used to estimate the amount of eye-specific input. To this end, the morphology-based fluorescence difference (mFD) was computed per cell by utilizing the cell's reconstructed morphology to calculate a 3D histogram of the relative morphological density.

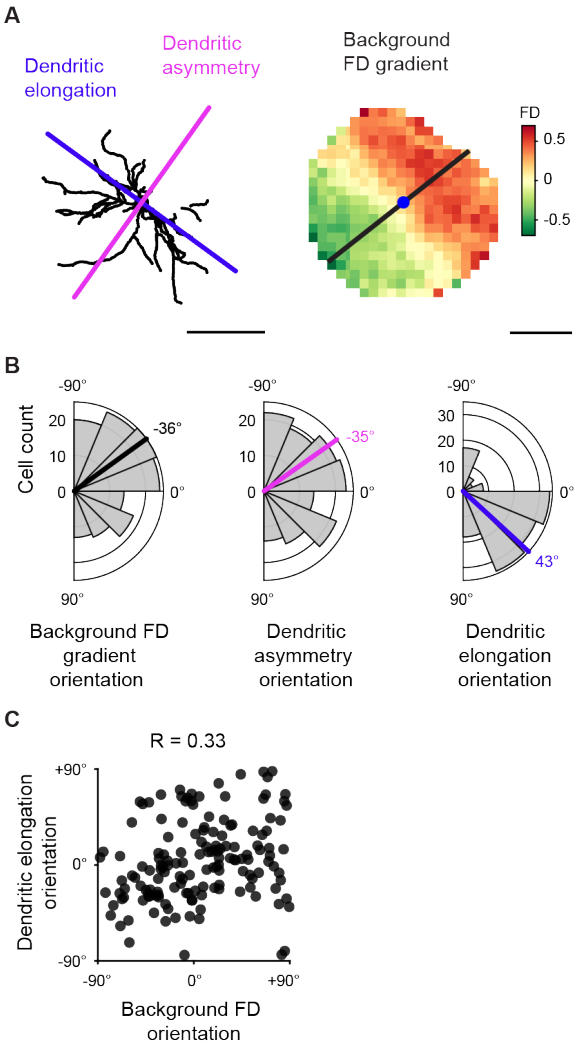

Figure 3.1.6 The relationship between dLGN neuron morphology and local eye-specific RGC axon availability
A Reconstructed morphology of a dLGN cell with its dendritic elongation (blue) and asymmetry (magenta) (left). Maximum intensity projection of the cells normalized background fluorescence difference (FD; 150 μm sphere radius) with the background FD gradient orientation in black and soma location in blue (right). **B** From left to right: polar plots of FD gradient, dendritic asymmetry and elongation orientation of dLGN neurons. Circular averages are displayed in black (-36°), magenta (-35°) and blue (43°), respectively. **C** Dendritic elongation orientation plotted against the average background FD gradient orientation per cell (n = 152 cells, circular-circular Pearson's correlation R = 0.33, p < 0.001). All scale bars: 100 μm. Figure reprinted with permission from Bauer et al. (2021).

This effectively created a 3D mask (mFD mask) per cell that, in conjunction with the cleared confocal image stacks, could be used to calculate axo-dendritic overlap in a similar fashion to the rFD mask (Fig. 3.1.7A). If the detailed dendritic morphologies really biases eye-specific input sampling towards monocularity, rotating the mFD mask but not the confocal image stack should give insight into dendritic orientation with respect to input sampling

(Fig. 3.1.7B): the average of the absolute mFD of all cells should decrease when rotated and be maximal without rotation, effectively implying a correlation between the absolute mFD values and degree of rotation. However, no such effect was found (R = 0.00064, Fig. 3.1.7C, D), indicating that dendritic orientation does not bias axo-dendritic sampling towards monocularity. Consequently, dendritic orientation is unlikely to be the cause for the high observed amounts of functional monocularity.

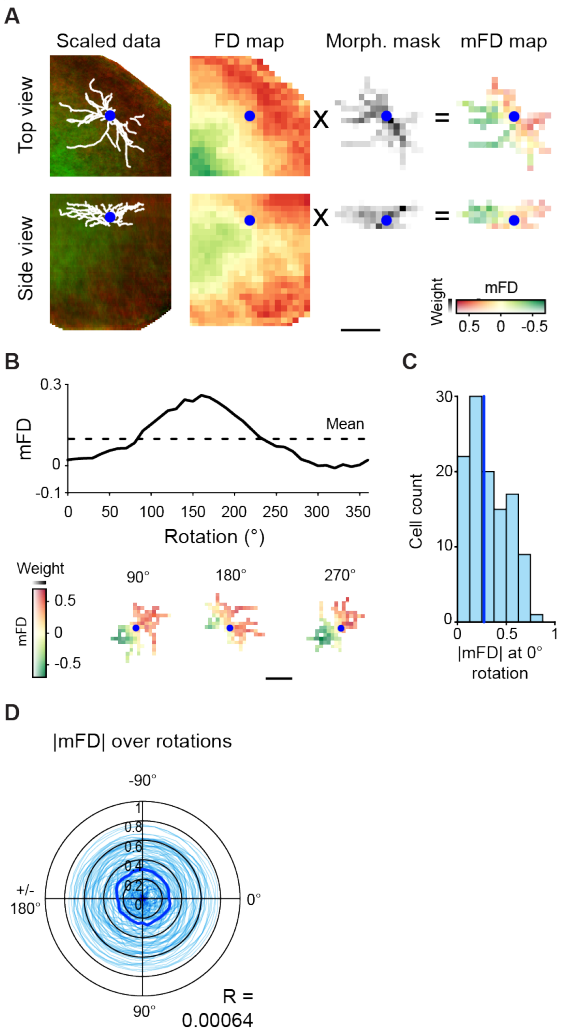

Figure 3.1.7 Mechanism 2: dLGN dendrite orientation
A Morphology-based fluorescence difference (mFD) calculation for an example cell (soma: blue circle) from left to right (z- and x- projections are displayed in the top and bottom rows, respectively): confocal image stack with registered morphology. FD pixel map. Morphology mask of cell. mFD pixel map, based on morphology mask and FD pixel map. **B** mFD as a function of morphology mask rotation (solid line) and mean mFD (dashed line; top). mFD pixel map from cell shown in D at the other three cardinal rotations. **C** Absolute mFD of all cells (light blue; not rotated) and their median absolute mFD (0.27). **D** Absolute mFD of all cells as a function of morphology mask rotation (light blue lines: individual cells, solid blue line: median of all cells). No correlation between rotation and absolute mFD (circular-linear Spearman's corre-

lation = 0.00064, p = 0.28, n = 114 cells) All scale bars: 100 μm. Figure reprinted with permission from Bauer et al. (2021).

3.1.6 Synaptic selection and refinement results in functional monocularity

Neither a cell body's position, nor a bias in axo-dendritic sampling could fully account for the observed levels of functional monocularity. However, mFD values were found to predict eye-dominance (Fig. S3.1.5), and there seems to be a roughly linear relationship between axo-dendritic overlap (mFD) and functional eye-specific input dominance (Fig. 3.1.8C). This suggests that mechanism 1, input availability, plays a significant role in determining a dLGN neuron's functional tuning. However, several deviations from this were found: first, multiple cells were functionally tuned to the eye that had fewer RGC projections in the immediate vicinity of the dendritic arbor (Fig. 3.1.8A). In other words, availability of RGC afferents alone does not fully predict ocular dominance, and also cannot account for the observed levels of functional monocularity in the dLGN. Both of these findings are in line with the results in 3.1.4 (mechanism 1). Second, in some cases, two neurons with near-identical axo-dendritic overlap (mFD) were functionally tuned to opposite eyes (Fig. 3.1.8B). This indicates that beyond mere availability of presynaptic partners, other mechanisms are likely at work, skewing input strength towards one eye. Moreover, these mechanisms seem to differ even between cells that are in close proximity to each other. Third, roughly one quarter of dLGN neurons were situated outside the expected projection zones (see Fig. 3.1.3C). Surprisingly, the rare dLGN neurons with ODIs close to 0 in particular were part of that group, and could be found in areas of the dLGN with an increased availability of axons from the non-dominant eye (Fig. 3.1.8A).

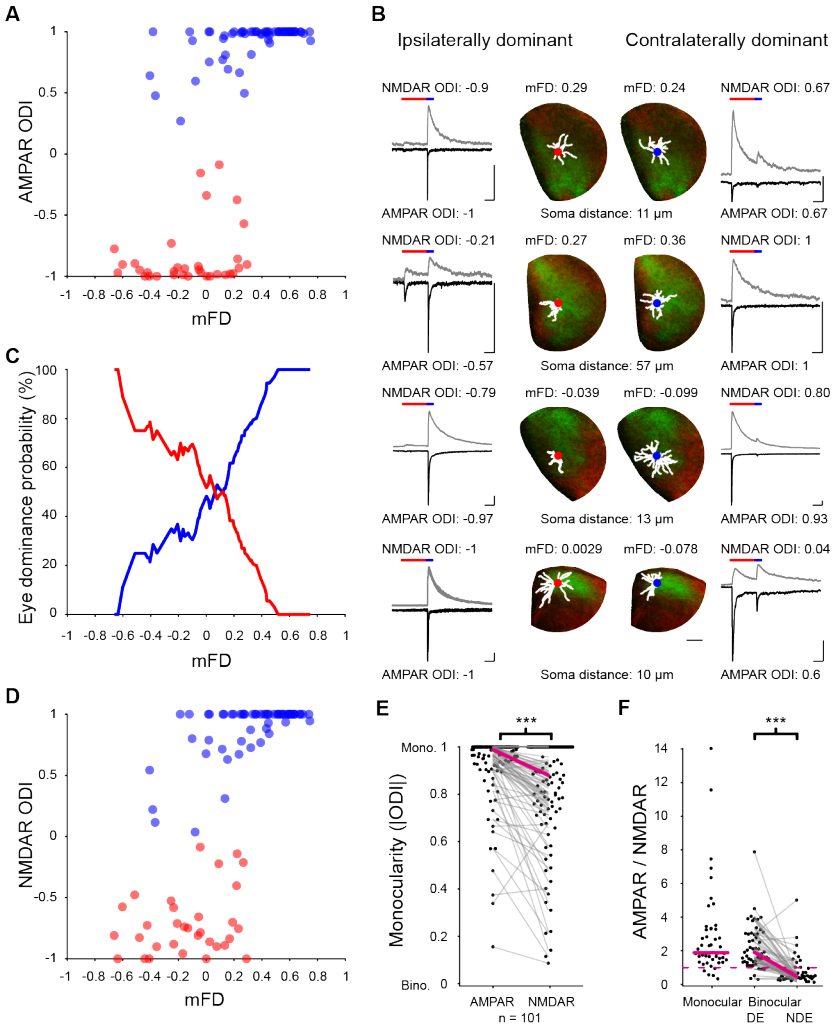

Figure 3.1.7 Mechanism 3: synapse selection and refinement underlie the monocular bias of dLGN neurons

A mFD plotted against AMPAR-based ODI per cell (n = 91 cells; contra- and ipsilaterally dominated cells in blue and red, respectively). **B** Neighboring dLGN neuron pairs with similar axo-dendritic sampling (mFD) but opposite eye preference. Cell morphologies, locations and retinogeniculate projections in middle. Left and right: electrophysiological traces of whole-cell voltage-clamp recordings or AMPAR- (-70 mV, black) and NMDAR-mediated currents (+40 mV, gray) in response to sequential photostimulation (red and blue bar above traces). **C** Probability of eye preference (contralateral: blue, ipsilateral: red) as a function of mFD (sampling: ± 0.2 mFD; n = 91 cells). **D** Same as A but for NMDAR-based

ODI (n = 91 cells). **E** Monocularity (|ODI|) is higher in AMPAR-mediated than in NMDAR-mediated responses (n = 101 cells, Wilcoxon signed-rank test, W = 73, $p < 0.001$). **F** AMPAR-to-NMDAR ratios of monocular cells (n = 48) and the DE of binocular cells (n = 53) are similar (Mann-Whitney U test, U = 2565, p = 0.43). NDE responses have a lower AMPAR-to-NMDAR ratio than their DE counterparts (Wilcoxon signed-rank test, W = 1377, $p < 0.001$). Image and morphology scale bar: 100 μm. Electrophysiology trace scale bars: 100 ms, 200 pA. Figure reprinted with permission from Bauer et al. (2021).

While these deviating cells are noteworthy, on average, dLGN neurons seem to wire more strongly with the eye-specific RGC afferents that are more abundant in their vicinity (Fig. 3.1.8A,C,D). Hence, RGC axon availability (mechanism 1) significantly contributes to the functional tuning of dLGN neurons but cannot explain the observed levels of functional monocularity alone.

Ultimately, fine-scale synaptic selection and/or refinement could be the reason for the high levels of functional monocularity. To investigate how monocularity is manifested, synaptic properties of dLGN neurons were investigated. To this end, AMPAR- and NMDAR-mediated responses of dLGN neurons were further quantified. Interestingly, NMDAR-mediated responses were more binocular than their AMPAR-mediated counterparts (Fig. 3.1.8A, D, E). The ratio of these two receptor-mediated currents, the AMPAR-to-NMDAR ratio, is typically viewed as a measure that positively correlates with synapse stability and maturity (Ripley et al., 2011), despite varying considerably between brain areas (Ji, Saha, and Martin, 2015, but see also Myme et al., 2003). To test if eye-specific differences in AMPAR-to-NMDAR ratio might accentuate sampling of ocular inputs, the AMPAR-to-NMDAR ratio was quantified for monocular cells and the dominant and non-dominant inputs of binocular cells. The AMPAR-to-NMDAR ratio of the dominant eye of binocular cells and monocular cells was found to be similar and in line with earlier reports (Fig. 3.1.8F; Chen & Regehr, 2000; Hooks & Chen, 2006). Strikingly, the AMPAR-to-NMDAR ratio of the non-dominant eye of binocular neurons was more comparable to the ratios of juvenile animals (Fig. 3.1.8F; Chen & Regehr, 2000). This is indicative of a process of synaptic refinement that further tunes the functional ocular dominance of many dLGN neurons towards the dominant eye. Additionally, some synapses are rendered

functionally silent, as they do not contain AMPA receptors and rely on concurrent dendritic depolarization to participate in postsynaptic signalling in a NMDAR-mediated manner. It seems that the inputs of the non-dominant eye remain in a juvenile state long into adulthood. Taken together, while axonal availability predicts ocular dominance in dLGN neurons, synaptic selection and refinement seem to be the main mechanism for rendering the majority of the dLGN neuronal population functionally monocular.

3.2 Automated detection of dendritic spines and dendrites

Dendritic spines are typically identified in microscopy data via human annotation. Usually, this is done to either count single spines by marking their position in an image (for examples, see Hofer et al., 2009; Yang, Pan, & Gan, 2009; Frank et al., 2018; Hernández et al., 2019) or by generating pixel-wise annotations of spines (i.e. marking which pixels in an image are labeled as "spine") (for examples, see Wilson et al., 2016; Iacaruso, Gasler, & Hofer, 2017). The latter method is typically used to then extract fluorescence values, e.g. to quantify the presence of a marker after staining or quantify calcium dynamics during calcium imaging. However, human-annotations are inherently subjective, and biases and user-to-user variability are expected. To automate detection and segmentation of dendritic spines, several attempts have been made in the past (Koh et al., 2002; Fan et al., 2009; Heck et al., 2012; Singh et al., 2017b; Smirnov, Garrett, & Yasuda, 2018). However, these tools for automated spine segmentation have so far not been widely utilized beyond their initial publication. Most likely, their applicability is limited to image data that is similar to the data that has been used to develop these tools. Consequently, a method of identifying dendritic spines that is (1) readily applicable to a diverse range of image qualities and (2) performs similar to or better than the hitherto gold standard, human-annotated data, is still missing. Hence, the aim of this part of the dissertation was to address this long-standing issue of automated detection and segmentation of dendrites and dendritic spines in commonly used light-microscopy image types.

3.2.1 DeepD3: A deep-learning approach for the detection of dendrites and dendritic spines

In the past, deep neural networks have performed well in detecting and segmenting features in image data (for a review see Minaee et al., 2021). Such networks are trained in a supervised manner, typically requiring pixel-wise annotations of images in order to 'learn' which features of the image are to be segmented (Vidaurre-Gallart et al., 2022). These annotations are referred to as ground-truth and together with the original un-annotated image make up the training data. This part of the dissertation deals with the development of DeepD3, a deep-learning framework for the automated detection of

dendrites and dendritic spines.

Generation of training data

To train a deep neural network to identify and segment dendrites and dendritic spines, training data was required. Generally, the quality of training data dictates the performance of the trained network, with homogeneous or poorly annotated data leading to poor performance of networks (e.g. being unable to generalize or providing inaccurate or biased segmentation). To prevent this, particular care was taken to include heterogeneous data from different image modalities, with varying image qualities, annotated by several users. In particular, 2D and 3D images of dendrites and dendritic spines were obtained using two-photon imaging (CA1 pyramidal neurons of rat OHSCs) and confocal microscopy (pyramidal neurons of mouse cortex; for details, see Table 7). Pixel-wise annotations of dendrites and spines were performed using open-source annotation software (see methods). These annotations, the ground truth data of dendrites and spines, shared the same image coordinate system with their respective microscopy images (Fig. 3.2.1B). Images and their annotations were split into 2D image tiles (128 $\times$ 128 pixels) to train the neural network. To increase diversity across training epochs, primary (rotation in multiples of 90°; flipping across both axes) and/or secondary data augmentation (addition of Gaussian noise; application of spatial filters; adjustment of the image contrast) was stochastically performed on some image tiles (see methods; Fig. 3.2.1A).

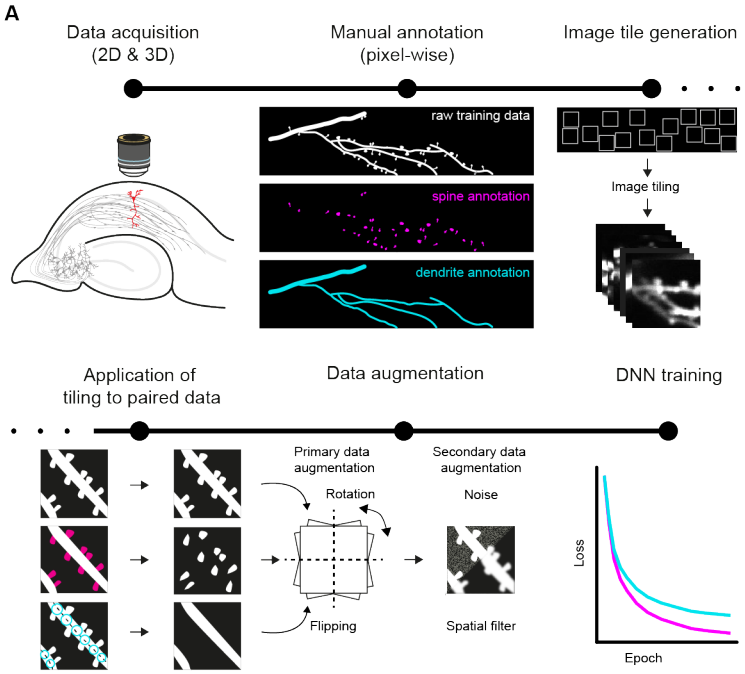
A
Data acquisition
(2D & 3D)
Manual annotation
(pixel-wise)
Image tile generation
raw training data
spine annotation
dendrite annotation
Image tiling
Application of
tiling to paired data
Data augmentation
DNN training
Primary data
augmentation
Rotation
Flipping
Secondary data
augmentation
Noise
Spatial filter
Loss
Epoch

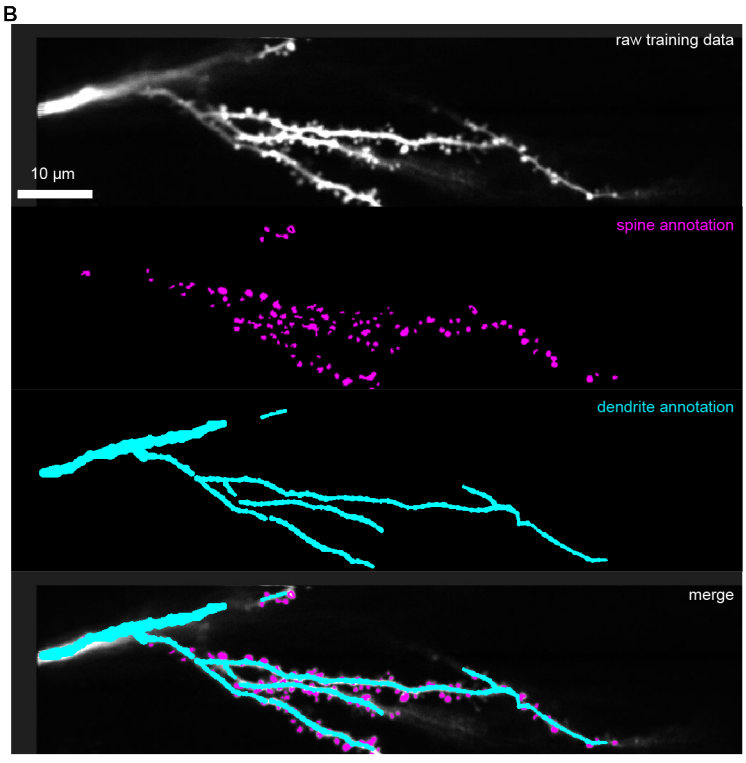
B
raw training data
10 µm
spine annotation
dendrite annotation
merge

Figure 3.2.1 Generation of a training dataset and procedure for the automated detection of dendritic spines
A Workflow of supervised learning (from top left to bottom right): Data acquisition via two-photon morphology imaging of CA1 pyramidal neurons in organotypic hippocampal slice cultures. Pixel-wise human annotations in two-photon images to generate spine and dendrite ground-truth images. Training dataset generation, done via image tiling, application of tiling to paired image data, primary and secondary data augmentation. Deep neural network training on training data. **B** Example of training data quality (from top to bottom): Example of a 2-dimensional two-photon image. Manual, pixel-wise dendritic spine annotations. Manual, pixel-wise dendrite annotation. Merge of all three channels.

Network architecture and training

Given the recent success of the U-Net architecture (Ronneberger, Fischer, & Brox, 2015) in semantically segmenting image data (Çiçek et al., 2016; Oktay et al., 2018; Falk et al., 2019), a custom-variant of this architecture was engineered: encoding of input images occurred across 4 convolutional layers that each employed two repeated applications of convolution, each followed by batch normalization (Ioffe & Szegedy, 2015) and a swish activation function (Ramachandran, Zoph, & Le, 2017). The second application of this process also utilized residual layers (He et al., 2016). Finally, data was down-sampled for the next layer using max pooling (Fig. 3.2.2A; Yamaguchi & Matsumoto, 1990, for details, see methods). The final encoding layer, the latent space, feeds two independent decoding pathways (Fig. 3.2.2A), one for spine and one for dendrite predictions. Both decoding pathways followed the classical U-Net architecture in 4 convolutional layers. Per layer, data of the previous layer was first upsampled and concatenated with input from the encoder pathway (provided via skip connections). These skip connections aided in maintaining spatial features across convolutional layers in the encoder paths. After concatenation, two repeated applications of convolution, each followed by batch normalization and swish activation function, were performed per convolutional layer (Fig. 3.2.2A).

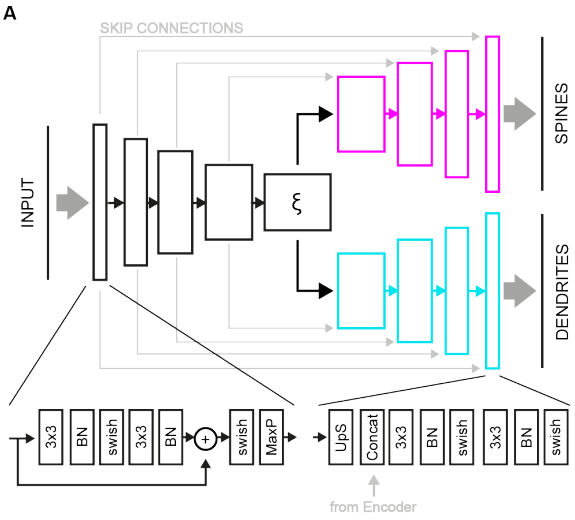

Figure 3.2.2 Architecture of DeepD3, a deep-learning approach for the detection of dendrites and dendritic spines **A** Architecture of DeepD3: Input images pass through 4 convolutional layers (encoder path, black) until they reach the latent space (ξ). Each convolutional layer is comprised of two 3×3 convolutions, followed by batch normalization, which are fed into a swish activation function. Finally, downsampling is done via 2×2 max pooling (bottom left). After encoding, the latent space is decoded in two independent pathways, one each for spines and dendrites, respectively (magenta, turquoise). Each decoder path is comprised of 4 convolutional layers with the same structure: after 2×2 upsampling, skip connections from the encoder path (gray arrows) are concatenated to the image, and subsequently two 3×3 convolutions, followed by batch normalization are each fed into a swish activation function (bottom right). Each decoder path generates a prediction image of the same size as the input image (black lines on the right). Finally, back-propagation-mediated training is done via optimization of DICE and MSE loss for dendrite and spine prediction, respectively.

Backpropagation-aided, supervised training was implemented via DICE and MSE losses for dendrite and spine prediction, respectively. During training, mini-batch gradient descent (Bottou et al., 1998) on minimization of the sum of the loss functions was performed using the training data. Initially, only a part of the training dataset was used, and only primary data augmentation was applied. Despite good performance on the training data, the validation loss did not seem to improve over training epochs (Fig. S3.2.3A), indicative of the network overfitting the data during training. Interestingly, this network still segmented dendrites and dendritic spines well in novel data that was similar to the training data in terms of pixel size and signal-to-

noise ratio (Fig. S3.2.3B). However, the ability of the trained network to generalize was limited, as evidenced by its poor performance on data with different pixel size and signal-to-noise ratio (Fig. S3.2.3C). As mentioned above, when DNNs are trained on homogeneous data, generalizability typically suffers. Microscopy data of dendritic spines can vary considerably in many image features, most prominently pixel size (how many pixels a spine contains), signal-to-noise ratio (defined here as the difference in brightness between spine/dendrite and background pixels), and relative brightness differences within the image (e.g. spines and dendrites). To approach this more systematically, a larger portion of the training dataset was used (spanning a range of pixel sizes) and secondary data augmentation was applied (adding noise, spatial filters and changes to contrast to the training data) to train another network. During training of this network, validation loss decreased over training epochs (Fig. S3.2.3B), indicative of better model generalization. Indeed, this general network performed well on data with different pixel sizes and signal-to-noise ratios (Fig. S3.2.3B, D, E, F).

Despite the better performance of the generalized network, a number of networks were trained to generate an array of options when automatically segmenting qualitatively heterogeneous data. General networks were trained without a premeditated data quality in mind, such that they could be employed more broadly. For these networks, primary and secondary data augmentation was performed and heterogeneous training data was used. Alternatively, networks were trained with a more homogeneous subset of the training dataset that in some cases was not augmented in a second step. This type of training data produced specialized networks, which proved to perform well on test data that was similar to training data in terms of signal-to-noise ratio and pixel size. In this dissertation, both specialized and general networks were utilized (for details, see Table 8).

Workflow and features of DeepD3

DeepD3 performs annotations of dendrites and spines in two steps: prediction and segmentation, which are performed in sequence (see Fig. S3.2.1, S3.2.2). An array of user-defined hyper-parameters aids in both steps to arrive at optimal annotations. During prediction, DeepD3, generates two images that have the same dimensions as the input image, one each for the prediction of dendrites and dendritic spines. The choice of model for prediction, as

outlined above, can greatly influence these output images. Independent of model choice, pixel values in both images range from 0 to 1, indicative of the probability DeepD3 assigns to a certain pixel of being part of a spine or dendrite (Fig. S3.2.2C). These probabilities can then be leveraged to enhance predictions in multiple steps. For example, pixels with weak dendrite prediction values (e.g. $p < 0.3$) can be omitted by application of a threshold to the dendrite prediction images (Fig. S3.2.1B). Moreover, the biological characteristics of dendrites and spines can be utilized to further enhance predictions. Dendrites, for example, tend to be contiguous, tube-like structures that, depending on the pixel size, span hundreds to thousands of pixels. Hence, users can apply a threshold of minimal dendritic length (in connected pixels), which effectively removes all pixels that are not part of a contiguous dendrite arbor (i.e. noise). Spines, on the other hand, are connected to dendrites via a spine neck, and are thus always found in close proximity to dendrites. Consequently, when spine prediction pixels are limited to a user-defined distance to detected dendrites, false positive spine predictions can be effectively removed.

The cleaned prediction image is then further processed during segmentation to generate regions of interest (ROIs) on a spine-by-spine basis. All contiguously connected pixels are treated as individual spine ROIs, which are then further cleaned. ROIs that do not contain high probability pixel values (e.g. > 0.7) are subsequently excluded (Fig. S3.2.2C). Next, the outline of ROIs is determined by high-pass thresholding the image based on spine probability values (n.b. low filter threshold leads to larger ROI sizes). Watershed segmentation is utilized to segment connected or overlapping spine ROIs. As a last step in ROI cleaning, maximum and minimum spine size are exploited to exclude artifacts. After ROI generation and cleaning, the two prediction images, as well as all identified spine ROIs, can be saved. An entire image (size: $\sim$500 GB; containing $\sim$500 spines) can be loaded, segmented, cleaned, and the results saved within four minutes using a standard computer equipped with a 8 GB GPU chip. In comparison, human annotation of such an image would take several hours. In conclusion, DeepD3 provides a toolbox of networks and hyper-parameters to quickly identify and segment dendrites and dendritic spines in image data.

Validation of DeepD3: homogeneous test data

To validate DeepD3 beyond the initial validation data, an independent, pixel-wise annotated dataset was generated. Data quality resembled that of the training dataset, hence this dataset was termed homogeneous validation data. To validate DeepD3 on the homogeneous test data, performance was inspected in three stages: First, DeepD3-generated spine and dendrite predictions were visually compared to ground-truth data annotations. Both predictions seemed to follow annotations closely, with most dendritic spines seemingly being detected (Fig. 3.2.3B, C). Second, to quantify DeepD3 performance, prediction images were assessed by comparing manual annotations to DeepD3 predictions in a pixel-wise manner across a range of user-defined hyper-parameters. Using a confusion matrix, all pixels could be classified into four categories (true positive, false positive, true negative, false negative) by testing DeepD3 performance against manual annotations (see methods). Using these four categories, precision, recall and F1 score were computed. DeepD3 was able to detect roughly 50 % of all spine pixels (Fig. 3.2.3D). False positives (measured in precision) decreased and false negatives increased (measured in recall) as the inclusion criteria for spine ROIs became more stringent (higher spine probability threshold). Third, one of the main applications of DeepD3 is identifying dendritic spines, rather than identifying every pixel of a dendritic spine. Hence, ROI-wise prediction of DeepD3 across a range of user-defined hyper-parameters was assessed. To this end, the same pixel-wise human annotations were compared to DeepD3 predictions (ROI matching) using two methods: based on inter-ROI distance, i.e. whether the Euclidean distance of the DeepD3-predicted and manually annotated ROI centroids was less than 120 μm. Alternatively, ROIs were matched based on their overlap, with a requirement of 50 % overlap between DeepD3- and manually generated ROIs (see methods). ROI-wise spine segmentation was found to be robust across a large range of hyper-parameters (precision $>$ 85 %, with both ROI matching methods being in agreement; Fig. 3.2.3E, F).

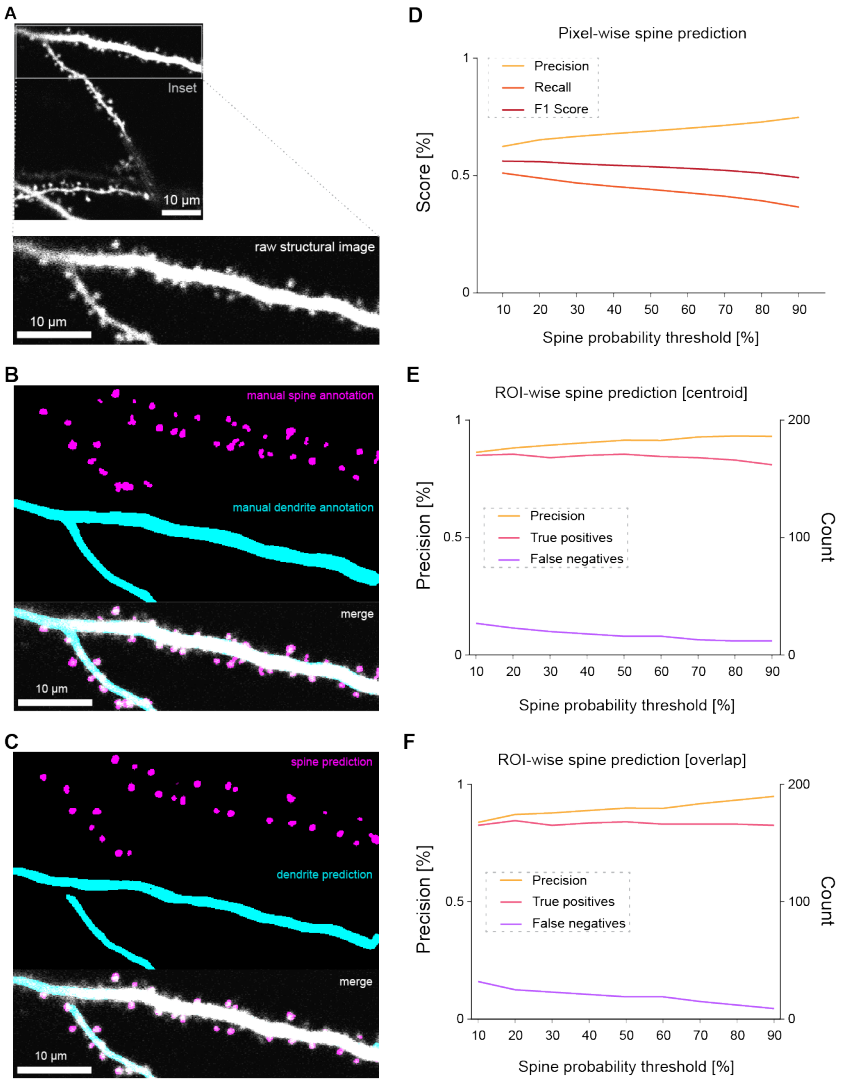

Figure 3.2.3 Validation of DeepD3: homogeneous test data
A Top: Maximum intensity projection of a 3D two-photon image of a dendritic region of a CA1 pyramidal cell. Gray box delineates the inset shown at the bottom. **B** From top to bottom: manual spine annotation, manual dendrite annotation, merge of annotations with raw structural data (inset in A). **C** From top to bottom: DeepD3-generated spine prediction, DeepD3-generated dendrite prediction, merge of predictions with raw structural data (inset in A). **D** DeepD3 performance as a function of spine probability threshold. Pixel-wise performance of true positive rate (recall, orange), positive predictive value (precision, yellow) and their

harmonic mean (F1 score, red). More stringent thresholds tend to perform more poorly. **E** DeepD3 performance as a function of spine probability threshold. Spine ROI-wise precision (yellow) and the number of true positives (magenta) and false negatives (purple). Performance based on centroid-to-centroid distance. Performance is good and stable across spine probability threshold values. **F** Same as E but for performance based on ROI overlap (> 50 %). Performance is good and stable across spine probability threshold values.

3.2.2 Cross-validation of DeepD3 on diverse datasets

To confirm the applicability of DeepD3 on a wide range of data types and qualities, cross-validation on two additional datasets was performed. This step is critical to evaluate whether DeepD3 performs well across images of different qualities. Image quality in this case concerns two aspects, which are critical to the performance of an automated tool: first, the signal-to-noise ratio of the image. In images with a high signal-to-noise ratio, dendrites and dendritic spines can easily be visually distinguished from the background noise, thereby making segmentation easier. The second key aspect of images is the pixel size, i.e. how many pixels are contained in a dendrite or other morphological feature. Typically, automated approaches need to 'learn' how large (in pixels) a feature is to perform well. For simplification, these two aspects of images will be referred to as image quality. Ideally, an automated tool should perform well in a range of signal-to-noise ratios and pixel sizes to allow users to flexibly segment images with different image qualities.

Mouse organotypic hippocampal slice culture *in vitro*

In the first cross-validation test, DeepD3 performance was tested in a publicly available dataset (Smirnov, Garrett, & Yasuda, 2018). This dataset contained images of CA1 neurons of mouse (as opposed to rat in the training data) organotypic hippocampal slice cultures. In particular, spines and dendrites of secondary apical dendrites in the *stratum radiatum* were captured using two-photon imaging, resulting in images with high image quality (see methods; Fig. 3.2.4A, B). DeepD3 reliably found hand-annotated spines in these images (recall = 0.91/0.93; Fig. 3.2.4C). However, a high amount of false positive spine ROIs (precision = 0.46/47) indicated that several potential spine ROIs had been identified by DeepD3 that had not been

hand-annotated. Indeed, upon closer inspection, it seems that several dendritic spines had not been hand-annotated in the publicly available data (Fig. 3.2.4B). Hence, the true precision of DeepD3 on this dataset is likely much higher than 0.46/0.47. DeepD3's performance on the cross-validation data, in conjunction with the performance on the homogeneous validation data, indicates that DeepD3 readily identifies dendritic spines in *in vitro* data.

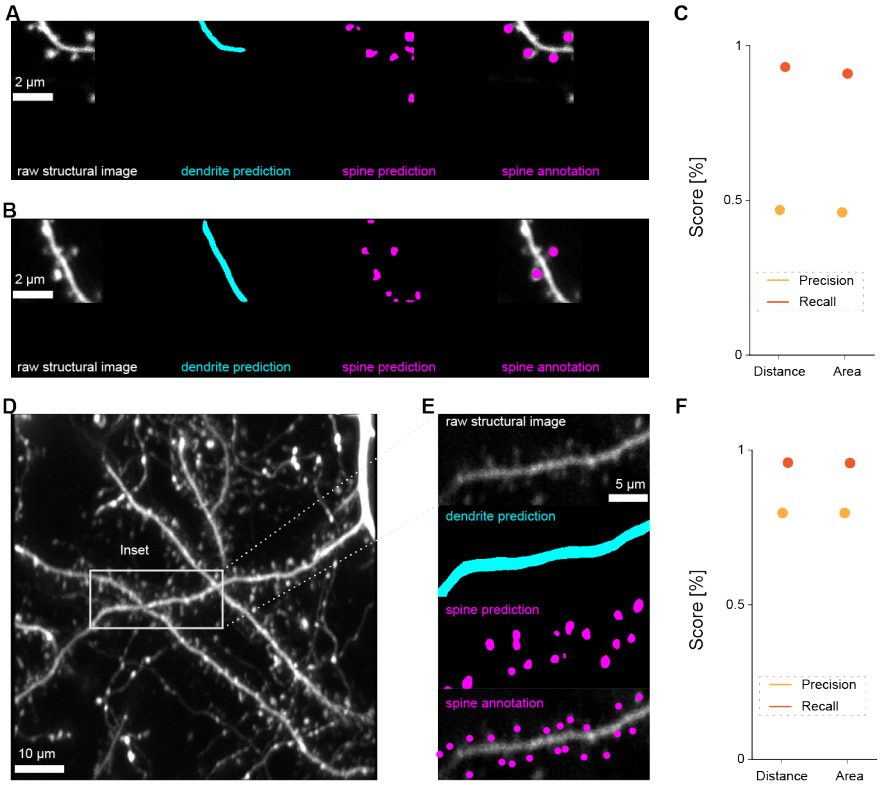

Figure 3.2.4 Cross-validation of DeepD3
A From left to right: raw structural image, DeepD3-generated dendrite prediction (turquoise), DeepD3-generated spine prediction (magenta), manual spine annotation (magenta) (data from Smirnov, Garrett, & Yasuda, 2018). **B** Same as A but different image. Example of incomplete spine annotation. **C** Performance of DeepD3 on a public dataset, obtained from Smirnov et al. 2018. Precision (yellow) is poor, since some dendritic spines were not annotated in the dataset but were found by DeepD3 (see B). DeepD3 identifies most annotated dendritic spines (see recall, orange). Distance-based criterion: Euclidean

distance between the centroid of the prediction ROI and the human annotation is within 1.1 μm. Area-based criterion: prediction ROI contains human annotation. **D** Two-photon structural images of L2/3 pyramidal neurons of mouse bV1 were obtained in vivo (maximum intensity projection). Inset is shown in E. **E** From top to bottom: single frame of inset of raw structural image shown in D, single frame of DeepD3-generated dendrite prediction (turquoise), single frame of DeepD3-generated spine prediction (magenta), all manual spine annotation (magenta). **F** Performance of DeepD3 on data in D, E. Precision (yellow) is still suboptimal, as not all spines on all dendritic stretches were annotated. DeepD3 identifies almost all annotated dendritic spines (see recall, orange).

Layer 2/3 pyramidal cells of mouse binocular visual cortex *in vivo*

DeepD3 was next challenged with *in vivo* image data. This type of data typically suffers from worse optical access and higher density of neurons, making spine identification more difficult. To test DeepD3 on *in vivo* data, structural image stacks of apical and basal dendrites of pyramidal L2/3 neurons of mouse binocular V1 were acquired (see methods; Fig. 3.2.4D). Per image stack, spines along 1-2 dendrites were human-annotated. Strikingly, DeepD3 identified the vast majority of hand-annotated dendritic spines (recall = 0.96), indicating that neither the difference in modality (*in vivo*), nor the more dense labeling posed problems (Fig. 3.2.4E, F). Again, several false-positives were identified when automatically identifying dendritic spines (precision = 0.80). Two factors contribute to this. A) Image data was only annotated for 1-2 dendrites, hence spines on other branches were identified by DeepD3 but not human-annotated. In an effort to compare DeepD3 performance on the same subset of dendritic spines, the area of possible predictions was limited, based on manual annotations (see methods). Nevertheless, some dendritic branches crossed into the area in which DeepD3 performance was quantified. Hence, some dendritic spines that had not been manually annotated contributed to the amount of false positives. B) This dataset was part of a larger dataset, which investigated spine dynamics in L2/3 of mouse bV1 chronically (Bauer et al., unpublished data). Here, annotations were performed with the goal of matching dendritic spines across time. As a consequence, a small fraction of dendritic spines were not annotated, resulting in a similar problem when quantifying DeepD3's precision.

In conclusion, DeepD3 readily identified dendritic spines across multiple, independently generated and annotated datasets, that differ in image quality and characteristics.

3.2.3 DeepD3 performs as well as a human in spine identification

So far, DeepD3 was shown to reproduce human annotations in a variety of datasets and criteria. However, these comparisons were only done with regard to annotations of a single user per dataset. Annotations within a single dataset might, however, vary between different annotators (inter-annotator reliability), given that spine identification in image data is a subjective task: after all, image quality and user biases might contribute to the choice of a user to localize and annotate a dendritic spine. Moreover, when tasked to annotate the same images on two occasions performance of a single annotator might also vary over time (intra-annotator reliability). A thorough search of the relevant literature yielded no articles evaluating this inherent variability within and between annotators. To address this gap, two additional datasets were obtained and manually annotated by multiple experienced users and subsequently compared to DeepD3 performance.

Rat organotypic hippocampal slice culture *in vitro*

A large volume ($\sim$134 $\times$ 34 $\times$ 35 μm^3) of a CA1 pyramidal cell's apical dendrites containing hundreds of dendritic spines was manually annotated by seven experienced users (Fig. 3.2.5A, B). Importantly, in contrast to the previously analyzed datasets (Fig. 3.2.4), where only some dendritic branches had been annotated, here users were instructed to densely annotate the image and identify all dendritic spines in the volume. Mean inter-annotator reliability was high (precision: 0.81) but varied mildly between user pairs (Fig. 3.2.5D). Intra-annotator reliability (n = 2 users, k = 2 repeats) in the same dataset was found to roughly match inter-annotator reliability (mean precision: 0.85, Fig. S3.2.3G). DeepD3 performance was on par with the average performance of human annotations (precision: 0.84/0.81, recall: 0.73/0.73, p = 0.475 and p = 0.2301 for recall and precision, respectively; Fig. 3.2.5C).

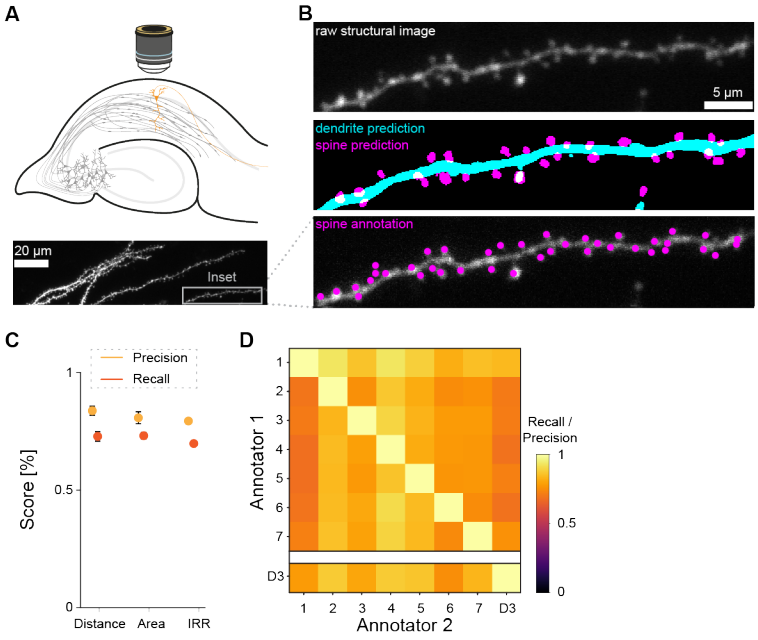

Figure 3.2.5 DeepD3 performs as well as a human in spine identification in *in vitro* data

A Schematic of data generation: two-photon structural images of tdTomato-expressing CA1 pyramidal neurons in organotypic hippocampal slice cultures were obtained (top). Example maximum intensity projection of a dendritic region (bottom) with inset (shown in B). **B** From top to bottom: raw structural image (maximum intensity projection, in gray), DeepD3-generated spine (magenta) and dendrite prediction (turquoise), manual spine annotation of a single annotator (magenta). **C** Mean performance (precision: yellow, recall: orange) of DeepD3 across all annotators. Distance-based criterion: Euclidean distance between the centroid of the prediction ROI and the human annotation is within 1.1 μm. Area-based criterion: prediction ROI contains human annotation. DeepD3 performed as well as human annotators in identifying dendritic spines ($p = 0.2301$, Kruskal-Wallis test of distance-based recall of DeepD3 and all inter-annotator reliability measures; $p = 0.475$ for distance-based precision of DeepD3). **D** Inter-annotator-reliability as a function of recall (top). Agreement of annotator 1 to annotator 2 is quantified. Distance-based criterion is used for DeepD3 performance (denoted as annotator D3). Bottom: DeepD3 performance per annotator as a function of precision.

Layer 2/3 pyramidal cells of mouse binocular visual cortex *in vivo*

Next, DeepD3 performance was assessed in more densely labeled *in vivo* image data (Fig. 3.2.6A-C). To this end, a different image stack of the previously used L2/3 mouse bV1 dataset was annotated by six users. As outlined above, this dataset was sparsely annotated (2 of 5 dendritic branches), and annotators were instructed to match spines across other, not analyzed time points, potentially confounding comparisons of false-positives (precision). The variability between human annotations was higher than in the OHSC *in vitro* dataset (precision: 0.63, recall: 0.61, Fig. 3.2.6D, E). As in the previous analysis on images of this dataset (Fig. 3.2.4D-E), DeepD3 identified additional dendritic spines that were not annotated by the users (precision: 0.56/0.46). However, most dendritic spines found by human annotation could also be detected using DeepD3 segmentation (recall: 0.82/0.67; 3.2.6D, E). Overall, DeepD3 performed better than human annotators in this *in vivo* dataset in terms of recall ($p < 0.001$). However, given that manual annotation was performed with the goal of matching dendritic spines across other, not here analyzed, time points, the generalization that DeepD3 performs better than humans in detecting spines is not warranted. Precision of DeepD3, on the other hand was worse than that of humans ($p < 0.001$), indicating that several dendritic spines were found by DeepD3 that had not been identified by humans (false positives). However, upon closer inspection of the data, it became evident that some dendritic spines had been overlooked by some annotators (see for example upper left part of the dendrite in 3.2.6C), explaining the sudden increase in false positives. Overall, however, it seems that also in *in vivo* image data, DeepD3 performs at least on par with the average performance of human annotations.

In conclusion, DeepD3 is a novel, automated tool for the detection of dendrites and dendritic spines. It performs at least equally well as the hitherto gold standard, human annotations, in terms of intra- and inter-user reliability. Moreover, its applicability has been tested in a variety of datasets *in vitro* and *in vivo* with varying image quality.

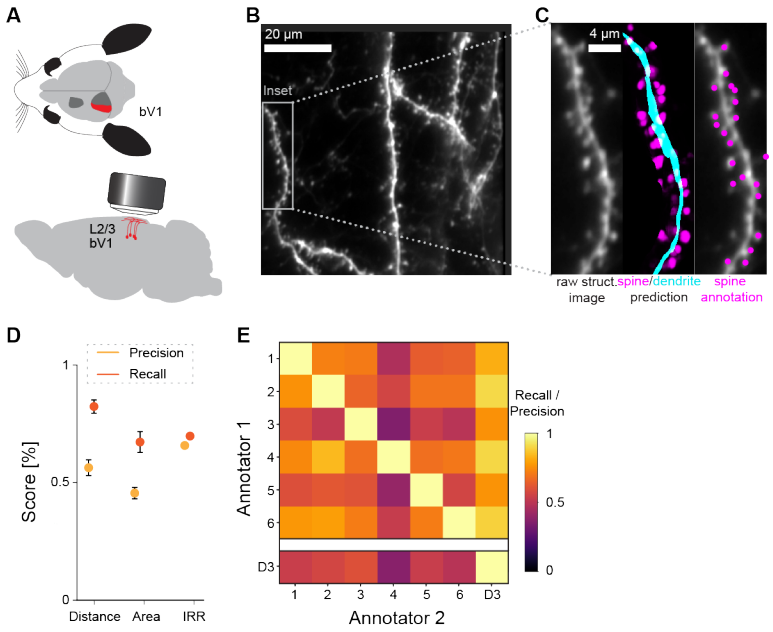

Figure 3.2.6 DeepD3 performs as well as a human in spine identification in *in vivo* data

A Schematic of data generation: two-photon structural images of L2/3 pyramidal neurons of mouse bV1 were obtained in vivo. **B** Raw structural image (maximum intensity projection; left) with a high-resolution inset (right). **C** From left to right: raw structural image (maximum intensity projection, in gray), DeepD3-generated spine (magenta) and dendrite prediction (turquoise), manual spine annotation of a single annotator (magenta). Some spines (e.g. right image, top left) have not been manually annotated but were detected by DeepD3 (middle image), influencing DeepD3 precision (see H, I). **D** Same as C but for in vivo data. DeepD3 performed better than human annotators in identifying dendritic spines ($p < 0.001$, Kruskal-Wallis test of distance-based recall of DeepD3 and all inter-annotator reliability measures; $p < 0.01$, Kruskal-Wallis test for distance-based precision of DeepD3). **E** Same as D but for in vivo data annotations. Distance-based criterion is used for DeepD3 performance (denoted as annotator D3). Bottom: DeepD3 performance per annotator as a function of precision. Error bars are $\pm$ SEM. NB: Some error bars for inter-annotator reliability scores of precision and recall are too small to be displayed.

3.2.4 Proof of concept application of DeepD3 in 3D and time-course data

DeepD3-generated segmentation of dendrites and spines in microscopy data can be utilized beyond counting spines. In particular, DeepD3 outputs can be utilized when analyzing fluorescence measurements of dendritic spines, to extract raw fluorescence values of images. As a proof of concept, DeepD3 was incorporated in data analysis pipelines to extract fluorescence measurements of dendrites and dendritic spines in 3D and in 2D time-course data: first, stimulation-induced calcium transients of dendrites and dendritic spines were quantified. To this end, a single CA1 pyramidal cell culture was transfected with a structural (tdTomato) and a GECI (GCaMP7b; functional marker) via single-cell electroporation (SCE; Fig. 3.2.7A). Presynaptic activity was controlled via AAV-mediated transduction of a population of CA3 cells with ChR2(H134R). DeepD3-generated segmentation of dendrites and dendritic spines was performed to quantify optogenetically induced calcium transients (Fig. 3.2.7B). Dendrite ROIs were further segmented into dendritic sub-ROIs, which in turn were matched to individual spines, opening avenues for commonly used single-spine calcium imaging analysis methods (Scholl, Wilson, & Fitzpatrick, 2017; Kerlin et al., 2019, Fig. 3.2.7B,). Calcium transients of spines and dendritic sub-ROIs were then extracted (Fig. 3.2.7D). As expected, at the time point of ChR2-stimulation, a rapid increase in intracellular calcium was detected in all dendritic sub-ROIs and most dendritic spines (Fig. 3.2.7D).

In addition, using volumetric field-of-depth Bessel-beam imaging (see methods), a much larger dendritic region of a CA1 pyramidal cell was imaged. Unlike the previous example, here calcium transients were not evoked. Rather, spontaneous calcium events in single spines and dendritic calcium spikes were captured. Again, DeepD3 was able to localize dendritic spines in the sample (Fig. 3.2.7C), and calcium transients were extracted using the DeepD3-generated segmentation (Fig. 3.2.7E). Neither the different imaging method nor the difference in image features (i.e. pixel size and signal-to-noise ratio) seemed to pose an issue for DeepD3, and spontaneous calcium events could be captured (Fig. 3.2.7E).

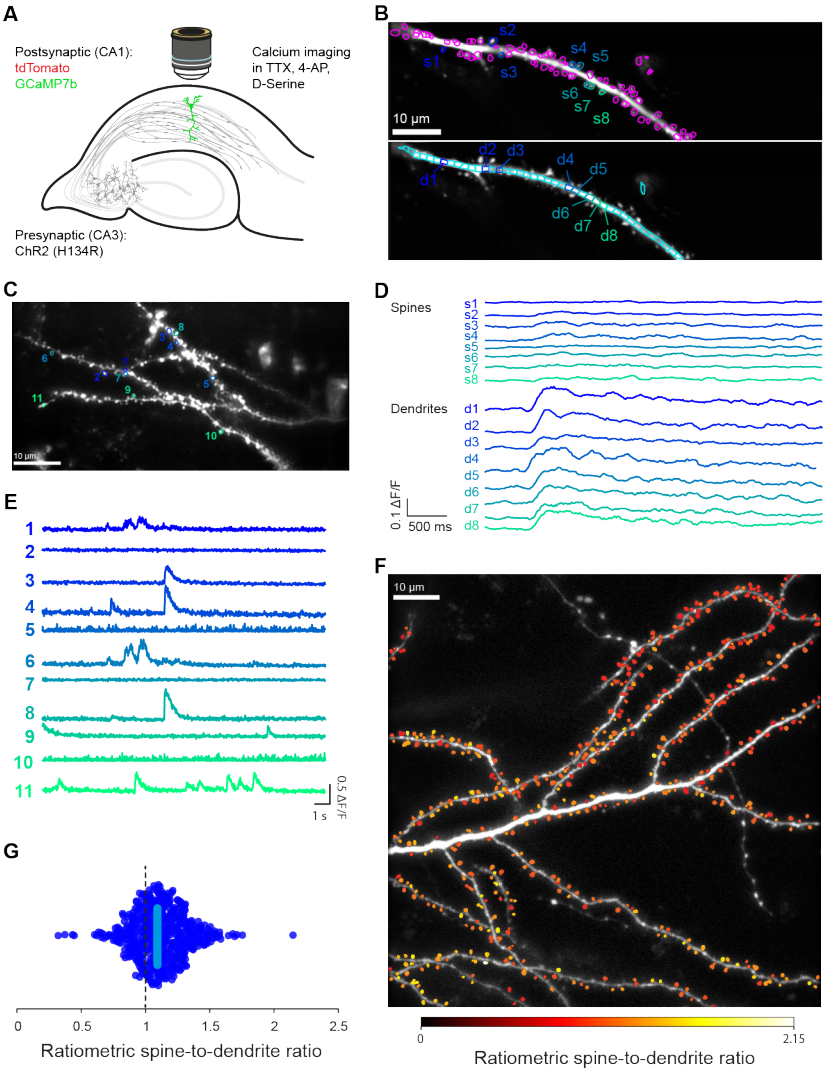

Figure 3.2.7 Application of DeepD3 in 3D and 2D time-course data
A Schematic of data collection. CA1 neurons of organotypic hippocampal slice cultures, expressing tdTomato and GCaMP7b were imaged in the presence of TTX, 4-AP and D-Serine. A subpopulation of CA3 neurons expressed ChR2(H134R). **B** Top: DeepD3-generated spine ROIs (magenta). Corresponding spine segments of the calcium traces in C are color-coded in dark blue to green.

Bottom: DeepD3-generated dendrite sub-ROIs (turquoise). Corresponding dendritic segments of the calcium traces in C are color-coded in dark blue to green. **C** Example dendritic stretch with dendritic spines (average intensity projection of calcium-imaging time series of CA1 pyramidal cell) with DeepD3-generated spine ROIs (green to blue). Image was acquired using extended depth-of-field Bessel beam imaging (see methods). **D** Photostimulation-evoked calcium transients of spine ROIs (s1-8 in color) and their matched dendritic sub-ROIs (d1-8 in matching color), depicted in B. **E** Calcium transients of DeepD3-generated spine ROIs depicted in C. **F** Application of DeepD3 on 3D data: Maximum intensity projection of a 3D structural image (gray). Spine-ROI-wise ratiometric spine-to-dendrite ratio (a measure of preferential spine localization) between a structural marker (tdTomato) and a spine maturity marker (Xph-15-mTurquoise2) is depicted in color. **G** Quantification of ratiometric spine-to-dendrite ratio of F. A RSDR threshold of 1 (black dashed line) and the mean RSDR (cyan line) are indicated.

The DeepD3-generated segmentation was leveraged for fluorescence measurements in three-dimensional data. To this end, single CA1 neurons of rat OHSC were transfected with a structural (tdTomato) marker as well as an indicator of spine maturity (Xph-15-mTurquoise2). The latter preferentially localizes to dendritic spines, as it is a nanobody against PSD-95 (Rimbault et al., 2021), a pivotal postsynaptic scaffolding protein (for more details, see 3.3.2 and methods; Kornau et al., 1995; Tu et al., 1999; El-Husseini et al., 2000; Schnell et al., 2002). To assess the degree of localization preference of Xph-15, the ratiometric spine-to-dendrite ratio (RSDR) was computed: per spine, the ratio of the average intensities of the maturity marker (mTurquoise2) and the structural marker (tdTomato) was quantified and divided by the same ratio for the entire dendritic arbor, resulting in a RSDR per spine. RSDR values >1 are positively correlated with higher preferential localization in the spine, while values of 1 indicate equal expression levels in dendrite and spine. Values below 1 indicate higher expression levels in the dendrite. As expected, most spines had an RSDR of higher than 1 (mean = 1.13, n = 553 spines; 3.2.7F, G), indicating that the nanobody construct preferentially localized to dendritic spines. This demonstrates that DeepD3 can be readily used to extract fluorescence measurements from 3D image data. Manual segmentation, particularly that of 3D data, is very time intensive. For example, manual segmentation of an image stack as shown in

Figure 3.2.7F typically requires 3-5 hours. In contrast, DeepD3 was able to perform this task in less than four minutes using a standard computer, equipped with a 8 GB GPU chip. This difference in segmentation speed should allow researchers to investigate dendritic spines in much larger quantities than previously possible.

In conclusion, DeepD3 is a deep-learning framework that rapidly identifies and segments dendrites and dendritic spines in a wide range of microscopy data. Segmentations can not only be utilized to count dendritic spines, but can also be leveraged to perform fluorescence measurements in dendrites and spines in 2D and 3D data. The speed with which DeepD3 performs segmentation could be critical for future experiments, as results can be rapidly provided and large datasets can be analyzed within much shorter time frames.

3.3 Towards establishing wiring rules during LTP-induced synaptogenesis

New dendritic spines grow in neurons undergoing LTP (Engert & Bonhoeffer, 1999; Maletic-Savatic, Malinow, & Svoboda, 1999; Toni et al., 1999) and subsequently form functional synapses with axons in their vicinity (Nägerl et al., 2007; Roo et al., 2007; Zito et al., 2009; Hill & Zito, 2013; Coneva, 2015). However, it remains unclear how these newly formed, LTP-induced synapses choose their presynaptic partners. There are a number of potential scenarios (Fig. 3.3.1C): *de novo* spines could avoid forming synapses with inputs that were previously active (anti-Hebbian); or merely seek for any pre-synaptic partner in the vicinity (non-Hebbian). Alternatively, *de novo* spines could preferentially, or even exclusively wire in a coordinated fashion to those neurons that previously caused the spines to emerge during LTP (partially Hebbian or Hebbian). This is reminiscent of Hebbian plasticity mechanisms, as originally proposed by Donald Hebb suggested in his book the Organization of Behavior (1949) and frequently observed in various experiments (Bi & Poo, 1998; Magee & Johnston, 1997; Lamsa, Heeroma, & Kullmann, 2005). To investigate these wiring rules, an assay was developed previously (Coneva, 2015). The aim of this part of the dissertation was to further refine this assay, in particular by (1) assessing the role of spine maturity and (2) identifying means to conclusively define functional connectivity of dendritic synapses, which comprised a combination of greatly increased throughput, analysis pipeline development and overall method refinement.

3.3.1 An assay to map functional synaptogenesis during LTP

Organotypic hippocampal slice cultures were chosen as a model for three reasons: first, the stereotyped wiring of the hippocampus permitted reliable definition of pre- and postsynaptic cell populations. Second, OHSCs allow for a multitude of experimental manipulations (e.g. pharmacology) and invasive methodologies (e.g. electrophysiology or single-cell electroporations). Third, OHSCs enable comparisons to previous reports investigating LTP-induced spino- or synaptogenesis, as the majority of these have utilized this model (Engert & Bonhoeffer, 1999; Maletic-Savatic, Malinow, & Svoboda, 1999; Toni et al., 1999; Nägerl et al., 2007; Coneva, 2015). Using OHSCs,

an assay was designed to approach the question of functional connectivity of LTP-induced synaptogenesis (Coneva, 2015). Using the neuronal architecture of the hippocampus, presynaptic (CA3) and postsynaptic (CA1) cells were assigned along the Schaffer collateral pathway.

To obtain optogenetic control over cell activity presynaptically, a sub-population of CA3 pyramidal cells was transduced with ChR2(H134R) via AAV injection (Fig. 3.3.1A, B). This served two purposes: A) it provided means to induce LTP optochemically and in an input-specific manner (Otmakhov et al., 2004; Coneva, 2015). To aid in inducing LTP, cAMP levels were temporarily increased pharmacologically via the addition of forskolin and rolipram. Moreover, by blocking voltage-gated sodium- and potassium channels (VGSCs and VGPCs, respectively), photostimulation-induced neurotransmitter release of CA1-projecting CA3 axons was tightly controlled spatially and temporally (Petreanu et al., 2009). This rendered photoresponsive boutons as the only input source during LTP induction. B) Additionally, optical control over neurotransmission in the Schaffer collateral pathway could be utilized to probe for functional connectivity on a single-spine basis later in the experiment (see below).

To identify pre-existing and LTP-induced spines, as many dendritic spines as possible were tracked over the time course of several hours (the estimated duration needed for functionalization of newly grown dendritic spines, see Nägerl et al., 2007; Zito et al., 2009). In particular, high-resolution chronic two-photon imaging of dendritic spines was performed in dendritic stretches of tdTomato-expressing CA1 neurons, enabling the tracking of several thousand dendritic spines over the time-course of hours.

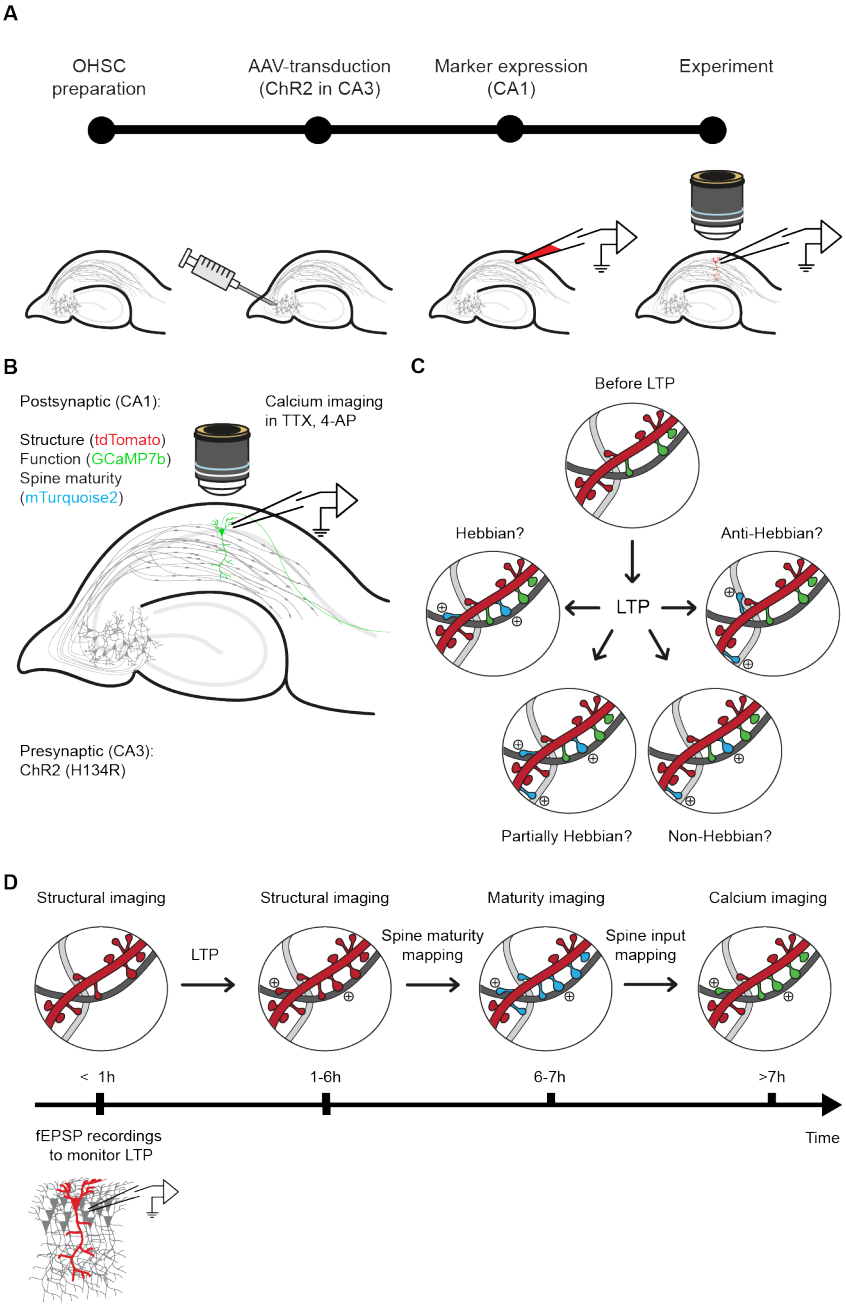
A
OHSC preparation
AAV-transduction (ChR2 in CA3)
Marker expression (CA1)
Experiment
B
Postsynaptic (CA1):
Structure (tdTomato)
Function (GCaMP7b)
Spine maturity (mTurquoise2)
Calcium imaging in TTX, 4-AP
Presynaptic (CA3):
ChR2 (H134R)
C
Before LTP
Hebbian?
Anti-Hebbian?
LTP
Partially Hebbian?
Non-Hebbian?
D
Structural imaging
LTP
Structural imaging
Spine maturity mapping
Maturity imaging
Spine input mapping
Calcium imaging
< 1h
1-6h
6-7h
>7h
Time
fEPSP recordings to monitor LTP

Figure 3.3.1 An assay to map functional synaptogenesis during LTP
A Preparation of experiment. From left to right: organotypic hippocampal slice cultures (OHSC) are prepared, presynaptic inputs (CA3) are transduced with ChR2, postsynaptic markers are expressd in single CA1 cells, experiment is conducted using two-photon imaging and extracellular electrophysiological recordings. **B** Experimental configuration of the model: the CA1 region of an OHSC is two-photon imaged for changes in structure (tdTomato), functional connectivity (GCaMP7b), and spine maturity (Xph-15-mTurquoise2). Simultaneously, extracellular recordings are performed in the direct vicinity of the target cell to quantify LTP. ChR2-expressing boutons of CA1-projecting CA3 neurons are stimulated to induce LTP and map functional connectivity. TTX and 4-AP, blockers of VGSC and VGPC, respectively, are utilized to limit photostimulation spatially. **C** Schematic of potential wiring rules governing LTP-induced synaptogenesis. Dendrites are indicated in red. Two axons are in the vicinity of the dendrite, one inducing LTP (dark gray) and one inactive (light gray). Spines connected to the LTP-inducing axon are indicated in green, others in red. LTP-induced spines are indicated in blue and denoted with a plus symbol. Top: A dendritic stretch with spines before LTP induction. Top left: depiction of input-specific "Hebbian" wiring with newly grown spines only connecting to LTP-inducing axons. Bottom left: same as top left but with less input-specificity ("Partially Hebbian"). Here, some nascent spines also wire to previously inactive inputs (light gray axon). Bottom right: LTP-induced spines form functional synapses randomly with any axon in the vicinity ("Non-Hebbian"). Top right: newly-grown spines exclusively synapse onto previously inactive axons, avoiding LTP-inducing inputs ("Anti-Hebbian"). **D** Experimental timeline. Top, from left to right: A dendritic stretch of interest is identified and structural images are acquired. LTP is induced optochemically. LTP-induced structural changes (spinogenesis) is monitored for 5 hours. Spine maturity is assessed to exclude immature spines from analysis. Functional connectivity is mapped (spine input mapping) via calcium imaging in several regions of interest that lie within the region that has previously been monitored for structural changes. Bottom: before and after the induction of LTP, field excitatory postsynaptic potentials (fEPSP) are monitored to quantify the amount of elicited potentiation.

In addition to the structural marker, a genetically encoded calcium indicator (GCaMP7b) was expressed in the postsynaptic cells to map the functional connectivity of dendritic spines (spine input mapping). Since spontaneous re-

lease events were suppressed (block of VGSCs and VGPCs), photostimulation-induced neurotransmission is the main source of calcium events in postsynaptic compartments (dendritic spines). Thus, using ChR2-stimulation and simultaneous two-photon calcium imaging, the functional connectivity of dendritic spines was mapped to determine which dendritic spines are functionally connected to photostimulation-responsive boutons. Since these boutons also contributed the presynaptic input during LTP inducting, identifying their postsynaptic partners, this effectively effectively quantifies functional connectivity. Moreover, using this same approach, LTP-induced dendritic spines can be functionally characterized, in turn allowing assessment of the rules of functional synaptogenesis after LTP.

One shortcoming of this approach is that it precludes conclusions for unresponsive LTP-induced spines. There are two main reasons for a lack of responsiveness: A) a functional synapse was formed with a photo-insensitive (ChR2-negative) presynaptic partner. B) An immature synapse was formed, which does not have the machinery necessary for synaptic transmission. Such immature synapses per definition cannot be functional, and hence should be excluded when assessing functional synaptogenesis during LTP.

Two means of differentiating between these two scenarios are conceivable. First, the existence of newly grown spines could be assessed at a later time point. In the past, it has been shown that immature dendritic spines rarely survive beyond past 24 hours of their emergence (Cane et al., 2014). Consequently, assessment at a later time point would exclude the majority of immature spines due to their lack of stability. However, a major caveat of this option is that synaptic turnover is extensive in the Schaffer collateral pathway (with up to 40 % turnover in four days, see Pfeiffer et al., 2018) and hence spine stability and connectivity of both pre-existing and LTP-induced spines could be affected over time. This would introduce additional confounding variables and hence limit the conclusions that could be drawn from such an experiment.

Second, spine maturity could be assessed by quantifying the abundance of postsynaptically expressed proteins that are integral for synaptic transmission, such as PSD-95, which is a frequently used marker of spine maturity (Gray et al., 2006; Gross et al., 2013; Cane et al., 2014; Rimbault et al., 2021). This would enable classification of spines into mature and immature,

based on the amount of PSD-95 present. Immature spines could be excluded from analysis, as functionality is not assumed. It is important to note that sufficient time should be given for PSD-95 to accumulate in *de novo* grown spines before spine maturity assessment (e.g. see Lambert et al., 2017).

Finally, to identify the rules governing LTP-induced functional synaptogenesis, a high-throughput data acquisition and analysis are critical. The proposed assay allows for structural tracking of thousands of spines per cell over the course of several hours. A previous approach (Coneva, 2015), mapped functional connectivity throughout the entire experiment in a small area of interest. This limited the number of spines that could be functionally assessed. The photostimulation area, and hence the area in which LTP occurs, can be increased and decoupled from the imaging field of view, e.g. by coupling a blue laser light source to an optic fiber. Consequently, by assessing functional connectivity at the end of the experiment in many dendritic stretches within this photostimulated area, the number of functionally characterized spines can be increased several-fold (Fig. 3.3.1D).

Additionally, recent advances in two-photon microscopy that enable the simultaneous recording of larger areas of neuronal tissue can be employed. As dendritic spines frequently cluster according to their functional connectivity (Wilson et al., 2016; Kerlin et al., 2019), functionally characterizing dendritic spines in close proximity to each other might be critical to determining the rules governing LTP-induced synaptogenesis. Hence, volumetric Bessel beam imaging (Lu et al., 2017, see methods) was established to increase the number of spines that can be functionally characterized per dendritic region of interest. These improvements to the throughput of data acquisition are supplemented by the improvements in speed and accuracy of dendrite and spine segmentation that DeepD3 offers (see Results 3.2).

3.3.2 Development of spine maturity over time

To identify immature dendritic spines, a molecular approach was chosen. A nanobody against PSD-95 called Xph-15 tagged with a blue-shifted fluorophore (mTurquoise2) was utilized to visualize maturity in dendritic spines (Fig. 3.3.2A). Alongside this maturity marker, tdTomato was expressed to visualize dendrites and dendritic spines structurally (Fig. 3.3.2B). Using a ratiometric approach (see results 3.2.4 and methods), the preferred localiza-

tion of mTurquoise2 to spines over dendrites could be quantified in a measure called the ratiometric spine-to-dendrite ratio (RSDR; Fig. D-E). Two characteristics of the approach were tested: First, whether the nanobody preferentially localized to dendritic spines across multiple days, despite overexpression. Second, whether a threshold that lends itself to classify spines as mature and immature is apparent from the distribution of RSDR values.

As overexpression of Xph-15 might render its localization substrate-unspecific, an inhibitory transcriptional auto-control element was implemented (Rimbault et al., 2021). The lower affinity of Xph-15 against the control element compared to its antigen PSD-95 causes the nanobody to only shunt further transcription when little or no untagged PSD-95 is available (Fig. 3.3.2A). To assess the effectiveness of this approach the RSDR was tracked in the same dendritic regions over the course of four days. Throughout all four days, Xph-15 seemed to preferentially target dendritic spines (mean RSDR >1, n = 5010 spines across all days), indicative of effective inhibitory transcriptional auto-control (Fig. 3.3.2F). Surprisingly, and in contrast to previous reports (Knott et al., 2006; Cane et al., 2014; Walker et al., 2017), spine size seemed to only be weakly positively correlated with PSD-95 expression (Fig. 3.3.2G, Pearson's correlation, R = 0.044, p <0.01).

RSDR was unimodally distributed across all days, indicating that PSD-95 expression in spines followed a continuum: No clear threshold between "mature" and "immature" spines was evident. A bimodal distribution of RSDR values would have allowed for a non-arbitrarily defined threshold of spine maturity. However, plasticity-induced, newly grown spines could markedly differ in their RSDR values from this data, which is mainly composed of pre-existing dendritic spines. Hence, further experiments are required to establish whether Xph-15 is a suitable option to identify spines that lack hallmarks of spine maturity.

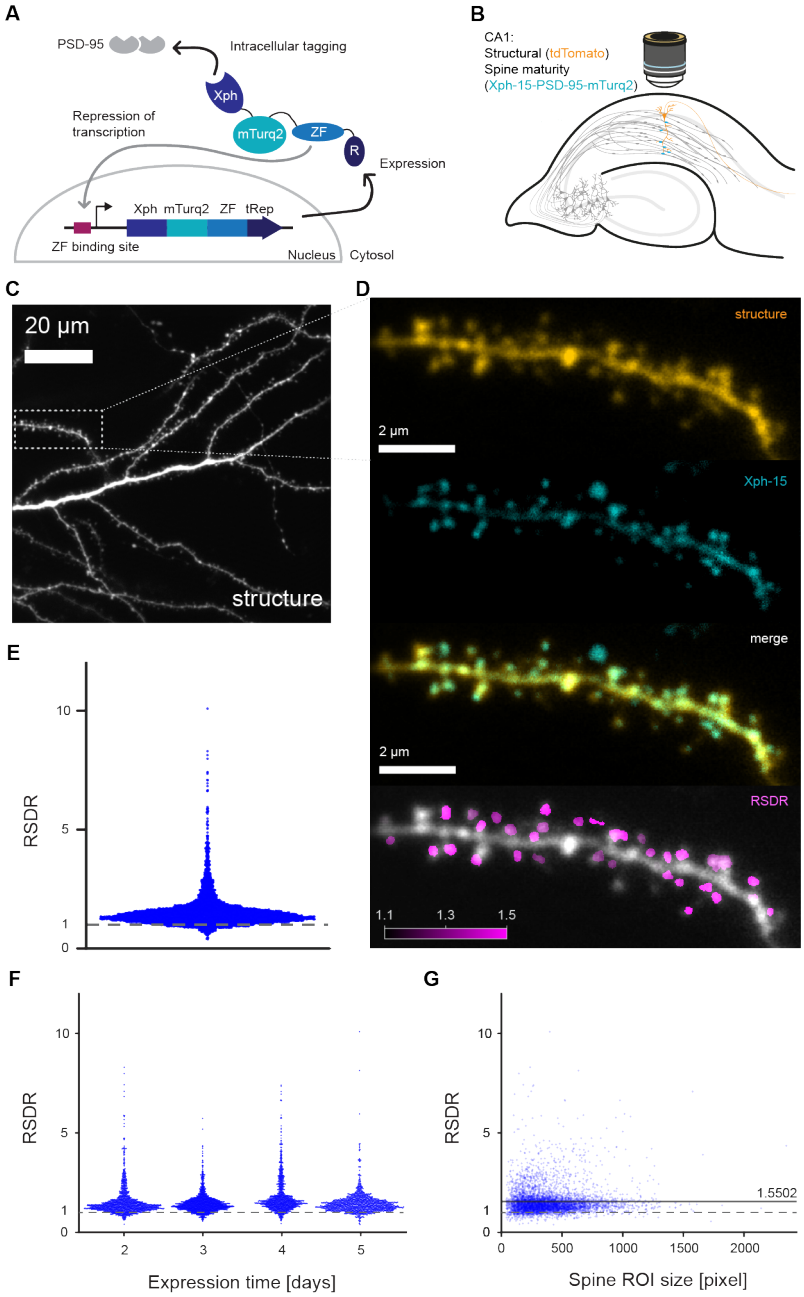

Figure 3.3.2 Development of spine maturity over time

A Schematic of PSD-95 nanobody construct (Rimbault et al., 2021). The Xph element works as a nanobody against PSD-95 (marine blue), it is tagged with the blue fluorophore mTurquoise2 (mTurq2, in turquoise), linked to a zink-finger

sequence (ZF, in light blue). Xph binds to PSD-95, unless no substrate can be tagged, in which case the zink-finger sequence binds to the zink-finger binding site (magenta), shunting expression via a transcription repressor (tREP, R; dark blue). **B** Schematic of the experimental setup. Structural (tdTomato; orange) and spine maturity marker (Xph-15, see A, in turquoise) are co-expressed in single CA1 neurons of OHSCs. **C** Maximum intensity projection of a dendritic region of a CA1 pyramidal cell (bottom left), highlighting a representative area containing dendritic spines (inset). Structure (orange), spine maturity (Xph-15; turquoise) and the merge of the two images are shown (right). **D** Merge of structural (orange) and maturity (turquoise) markers in inset (top). RSDR scores of spines (magenta) over structure (gray). All images are maximum intensity projections. **E** Quantification of RSDR values of all spines across all analyzed images. Most spines show elevated values of PSD-95 (RSDR > 1; gray dashed line). The mean RSDR was 1.5502, the median 1.3864. **F** RSDR scores across days (DIV 2-5). RSDR remains constant, despite overexpression of the Xph-15-mTurquoise2 construct, indicating that the construct's inhibitory transcriptional auto-control element works well and prevents non-specific localization. **G** RSDR scores plotted as a function of spine size (in pixels). Spine size seemed to only be weakly positively correlated with PSD-95 expression (Pearson's correlation, R $= 0.044$, p < 0.01).

3.3.3 Characteristics of dendritic calcium spikes in CA1 pyramidal neurons

To determine functional connectivity of spines in the proposed assay, optogenetic stimulation of ChR2-positive Schaffer collateral boutons is utilized to trigger calcium transients (GCaMP7b) in individual spines of CA1 cells (Fig. 3.3.3A). This is done in the presence of VGSC and VGPC blockers (1μM TTX and 100μM 4-AP, respectively) to spatially confine the area of presynaptic activity. To identify those dendritic spines that are functionally connected to ChR2-expressing boutons, single-spine responses are critically required. These responses are characterized by calcium transients in individual dendritic spines upon presynaptic stimulation. However, the stimulation frequently led to the generation of dendritic calcium spikes, events in which an entire dendritic stretch and all dendritic spines are flooded with calcium.

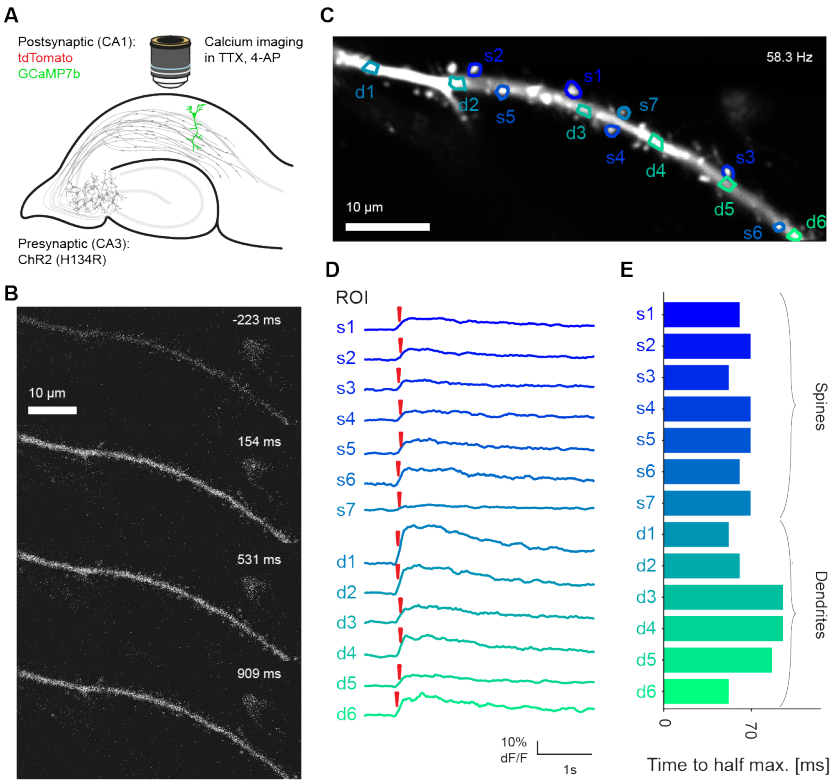

Figure 3.3.3 Time-course of dendritic calcium spikes in CA1 pyramidal cells

A Schematic of the experimental model. Structural (tdTomato; red) and a calcium indicator (GCaMP7b; green) are co-expressed in single CA1 neurons of OHSCs. A population of CA3 neurons is transduced with ChR2(H134R). Two-photon calcium imaging is performed in dendritic regions of the CA1 neuron in conditions preventing the generation of action potentials (TTX, 4-AP). **B** 7-point moving average projections of a dendritic stretch across 4 time points in relation to ChR2 stimulation (white, bottom right corner of each image). After stimulation, the entire dendrite and adjacent dendritic spines seem to be flooded with calcium, indicating a dendritic calcium spike had occurred. **C** Average intensity projection of a calcium movie. Dendritic sub-ROIs and spines outlines are indicated in color. Calcium imaging was performed at 58.3 Hz. **D** Calcium transients in response to blue-light stimulation of movie shown in B with outlines of C. Red arrows indicate time for reaching normalized half-maximal responses. Dendritic segments seem to respond more strongly than spines. Almost all spines seem to show increases in calcium concentration. Traces are representative of

dendritic calcium spikes. **E** Normalized half-maximal response times (red arrows in D) of spines and dendritic regions are plotted in relation to ChR2-stimulation. Spine and dendrite responses happen in rapid succession. Spine responses occur near-simultaneously.

To determine whether dendritic calcium spikes pose a problem in identifying functional connectivity of dendritic spines to ChR2-positive boutons, small dendritic stretches and their accompanying spines were imaged at high temporal resolution (∼58 Hz; Fig. 3.3.3B, C). Despite preventing the generation of APs, sufficiently strong stimulation led to dendritic calcium spikes (Fig. 3.3.3B, D). To further characterize dendritic calcium spikes, the time-course of calcium transients was plotted for spines and dendrites during these events (Fig. 3.3.3C, D). The half-maximal rise time was found to be similar between dendrites and spines (Fig. 3.3.3E), indicating that flooding of both happens faster than can be detected with the temporal resolution utilized during calcium-imaging (∼58 Hz). The spread of calcium across the dendritic arbor happens within milliseconds, as calcium-imaging of an entire CA1 neuron at an even higher temporal resolution (∼280 Hz) showed no differences in half-maximal rise time between image segments (Fig. 3.3.4A-C). Hence, it seems that the observed dendritic calcium transients are not caused by slow calcium-diffusion from the input-receiving spines, and instead seem to be governed by fast voltage- and/or input-dependent mechanisms that span the entire dendritic arbor.

Dendritic calcium spikes mask the calcium response of single dendritic spines, thereby preventing assessment of functional connectivity in the proposed assay. Three potential solutions were considered: A) ChR2 stimulation could be performed below the threshold of dendritic calcium spike generation, circumventing the issue of dendritic calcium spikes all-together. A potential caveat of this approach is that the induction or maintenance of LTP might not be feasible using such low stimulation intensities. Moreover, LTP might increase the input strength of ChR2-positive boutons, and hence, low levels of photostimulation, which elicited single-spine responses before LTP induction, might lead to the generation of dendritic calcium spikes after. Hence, limiting bouton stimulation to intensities such that dendritic calcium spikes are not generated might not be practical in the proposed assay.

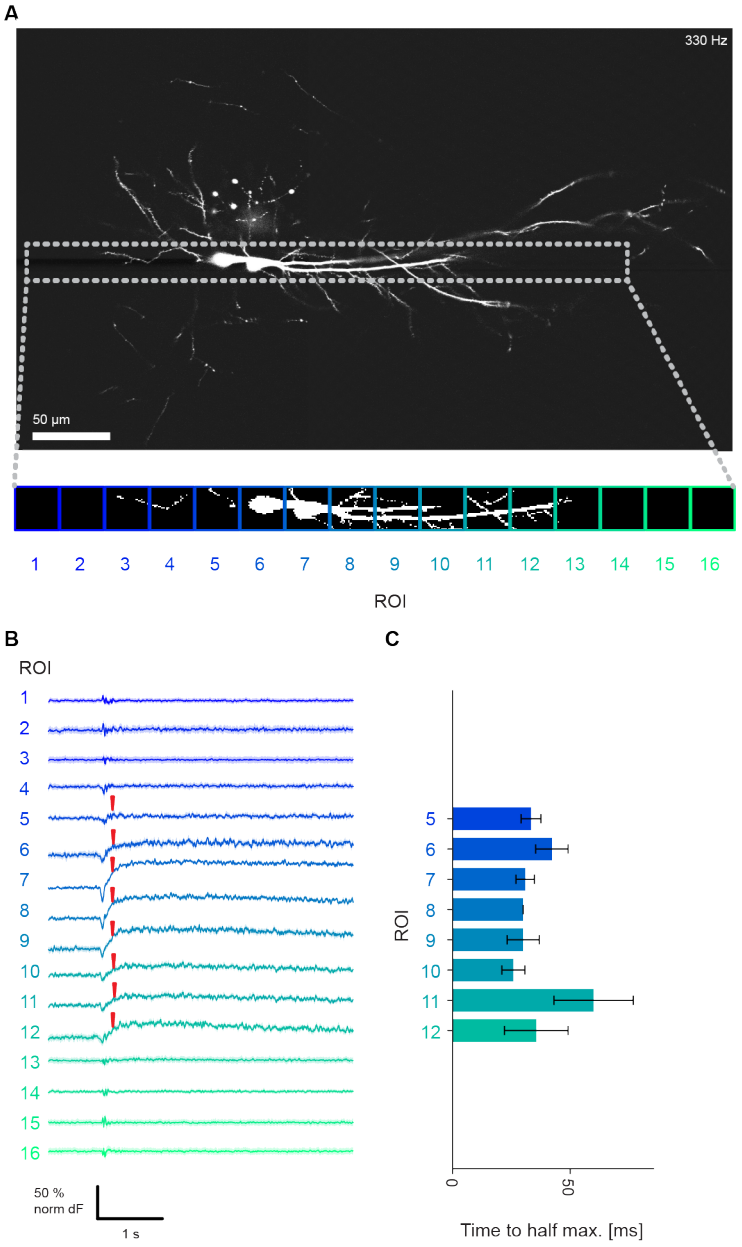

Figure 3.3.4 Time-course of dendritic calcium spikes in CA1 pyramidal cells

A Maximum intensity projection of two CA1 pyramidal neurons. High temporal resolution calcium movies (∼280 Hz) of dendritic calcium spikes were obtained

from the inset region (gray dashed outline). An average intensity projection is shown below, separated into quadratic regions to analyze the spatial spread of dendritic calcium spikes (region/ROIs 1-16 in color). **B** ChR2-stimulation-evoked average calcium transients of ROIs shown in F (1-16 in color). Red arrows indicate time of reaching normalized half-maximal responses. **C** Normalized half-maximal response times (red arrows in G) of ROIs are plotted in relation to ChR2-stimulation. ROIs 3, 13 and 15 show little calcium responsivity and thus large half-maximal response times. Half maximal response times are similar between all other responsive segments, indicating that calcium spread happens rapidly.

B) Computational unmixing of the dendrite and spine signals in calcium-imaging data. This would effectively allow for an assessment of functional connectivity despite the presence of a dendritic calcium spike. This type of analysis is frequently employed when analyzing calcium transients of dendritic spines *in vivo* (Chen et al., 2013; Wilson et al., 2016; Kerlin et al., 2019). Whether unmixing is also possible with calcium transients that occur near simultaneously, as seen here and in contrast to less synchronized events seen in *in vivo* data, is unclear.

C) The generation of dendritic calcium spikes could be prevented by pharmacological means, to ensure single-spine responses. Such an experimental manipulation would be performed at the end of the experiment, which would maintain full flexibility of stimulation intensity throughout the session. Importantly, pharmacological means should be tested on their propensity to affect the responsiveness of dendritic spines, to exclude the possibility of confounding the measurements of functional synaptic connectivity.

3.3.4 Automatic detection of dendritic calcium spikes

Before a solution to the generation of dendritic calcium spikes can be developed, an automated manner of detecting such events is required. To this end, an extensive dataset (64 movies, 9 imaging regions, n = 6 cells) was visually inspected for the presence of dendritic calcium spikes, effectively generating a ground-truth dataset. Next, various approaches were tested for their reliability to detect dendritic calcium spikes in this dataset. The dendrite ROI was segmented into dendritic sub-ROIs (see methods and results 3.2.4), which in turn were individually tested for responsiveness. Ranges of

thresholds and criteria were then tested on their capabilities to detect dendritic calcium spikes in this dataset. In particular, the fraction of responsive dendritic sub-ROIs and the stringency of the responsiveness criterion were permuted to identify optimal detection settings. Ultimately, a set of criteria was found (see methods), for which the vast majority of dendritic calcium spikes were detected with low false-positive and false-negative rates.

3.3.5 Computational approaches to differentiate spine from dendritic calcium events

The presence of dendritic calcium spikes poses the problem of masking the responsiveness of individual dendritic spines to ChR2 stimulation. Calcium imaging of dendritic stretches has long faced this challenge (Sabatini & Svoboda, 2000; Higley & Sabatini, 2008; Chen et al., 2011; Chen et al., 2012; Chen et al., 2013; Iacaruso, Gasler, & Hofer, 2017; El-Boustani et al., 2018). Particularly in *in vivo* recordings, the inconvenience of employing pharmacological means has led to the development of several computational strategies to unmix spine signal from the overriding dendritic calcium spike signal (Chen et al., 2013; Wilson et al., 2016; Kerlin et al., 2019). In the following, three computational approaches were tested to assess whether single-spine responses can be recovered, hence allowing a functional connectivity readout despite the presence of dendritic calcium spikes. To this end, two-photon calcium imaging in CA1 pyramidal neurons of rat OHSCs was performed. In particular, dendritic stretches in the *stratum radiatum* were imaged before and after stimulation of ChR2-positive CA3 Schaffer collaterals to quantify postsynaptic calcium responses. Two types of recordings were obtained per imaging region: data A contained single-spine calcium responses. Data B contained dendritic calcium spikes, typically generated by using stronger blue light stimulation than for data A. Critically, this dataset allowed comparisons of calcium transients of the same dendritic spines with and without the presence of dendritic calcium spikes. Single-spine responses were used as a ground-truth proxy, identifying dendritic spines that should also be classified as responsive when applying computational approaches to the data that contained dendritic calcium spikes (data B). In total $n = 9$ dendritic regions were imaged across $k = 6$ CA1 neurons, capturing 703 dendritic spines. Computational approaches were tested multiple times per dendritic region, as for most regions, dendritic calcium spikes were captured in multiple movies.

While this dataset allows for comparisons of those spines that showed calcium-responsiveness in data A (no dendritic calcium spike), other comparisons are made more difficult by the fact that for the generation of dendritic calcium spikes, frequently stronger stimulation intensities were required. Increased ChR2-stimulation intensity could cause some ChR2-positive boutons to release neurotransmitters, despite being unresponsive previously (during acquisition of data A). Consequently, when comparing responsivity in both data types after computational unmixing, spines that are only responsive in data B could fall into two categories: either the additional stimulation power used caused neurotransmitter release presynaptically, and these spines indeed received input and were correctly classified as responsive spines. Alternatively, the computational method could have wrongly classified the spine as responsive (false positive). It is assumed that previously responsive dendritic spines also faithfully respond in trials using higher ChR-stimulation intensities (data B): given the high amounts of extracellular calcium, release probabilities are high and increased photostimulation has so far not been shown to decrease release probability (Coneva, 2015; Duerst et al., 2020).

Temporal unmixing of dendrite- and spine responses

Calcium transients in dendrites and adjacent dendritic spines can have temporally distinct dynamics in events of synaptically-evoked dendritic calcium spikes (Kerlin et al., 2019). In the previous iteration of the proposed assay (Coneva, 2015), this was leveraged to distinguish those spines that receive synaptic input from those that are flooded with calcium from the dendritic branch via the spine neck. In the following, this unmixing approach was performed on data A and B of the dataset described above (Fig. S3.3.1A-F). In particular, smoothed calcium traces of dendritic spines and a dendritic sub-ROI, located in the immediate vicinity of the spine are compared. Dendritic spines are labeled synaptically connected to stimulated inputs if one of three criteria, termed case 1, case 2.1 and case 2.2, is met. Case 1 corresponds to instances when a spine but not the dendritic sub-ROI was responsive upon photostimulation (Fig. 3.3.5B,C). This is synonymous with the single-spine responses outlined above. If both the dendritic sub-ROI and the spine show a significant increase in calcium (case 2), temporal unmixing is performed.

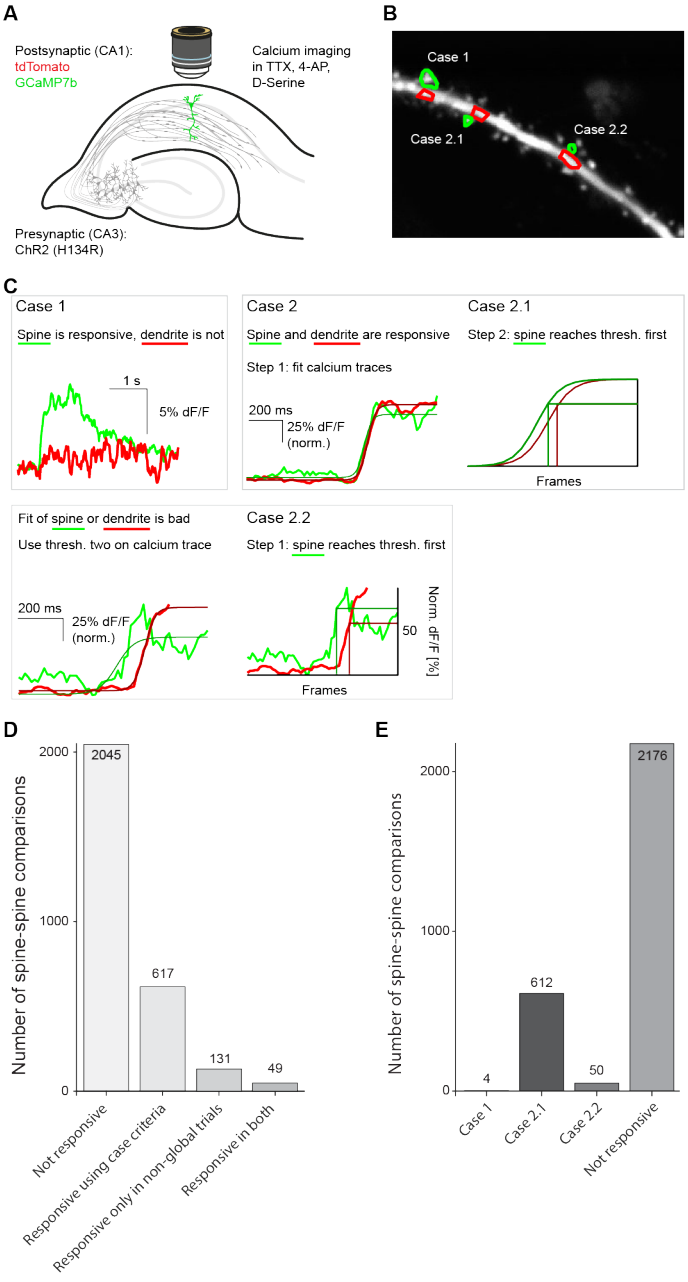
A
Postsynaptic (CA1):
tdTomato
GCaMP7b
Calcium imaging
in TTX, 4-AP,
D-Serine
Presynaptic (CA3):
ChR2 (H134R)
B
Case 1
Case 2.1
Case 2.2
C
Case 1
Spine is responsive, dendrite is not
1 s
5% dF/F
Case 2
Spine and dendrite are responsive
Step 1: fit calcium traces
200 ms
25% dF/F
(norm.)
Case 2.1
Step 2: spine reaches thresh. first
Frames
Fit of spine or dendrite is bad
Use thresh. two on calcium trace
200 ms
25% dF/F
(norm.)
Case 2.2
Step 1: spine reaches thresh. first
50
Norm. dF/F [%]
Frames
D
Number of spine-spine comparisons
2000
1000
0
2045
617
131
49
Not responsive
Responsive using case criteria
Responsive only in non-global trials
Responsive in both
E
Number of spine-spine comparisons
2000
1000
0
4
612
50
2176
Case 1
Case 2.1
Case 2.2
Not responsive

Figure 3.3.5 Temporal unmixing of synaptically-induced spine calcium transients during dendritic calcium spikes
A Schematic of the experimental model. Structural (tdTomato; red) and a calcium indicator (GCaMP7b; green) are co-expressed in single CA1 neurons of OHSCs. A population of CA3 neurons is transduced with ChR2(H134R). Two-photon calcium imaging is performed in dendritic regions of the CA1 neuron in conditions preventing the generation of action potentials (TTX, 4-AP). **B** Average intensity projection of a calcium movie. Some spine outlines are indicated in color. Inset (gray dashed line box) is shown in D, F. Computational unmixing was tested using image data of spines during dendritic calcium spikes and data in which single spines are responsive but the dendrite is not. Movies containing single-spine responses (C, D; data A) and dendritic calcium spikes (E, F; data B). **C** A set of criteria to identify spines that receive synaptic input with or without the occurrence of a dendritic calcium spike. Plotted are calcium traces (7-point moving average of $\Delta F/F_0$) of dendritic spines (green) and dendritic sub-ROIs (red) as well as their respective sigmoid fits (dark green and dark red, respectively). From top left to bottom right: dendritic spine is responsive but matched dendritic sub-ROI is not (Case 1). If spine and dendrite are both responsive, first, sigmoid fits of the smoothed traces are compared to evaluate which of the two reaches the threshold (67 % of normalized maximal response). Only if the spine reaches the threshold before the dendrite, it is considered to have received direct synaptic input (Case 2.1). If the calcium traces of the spine or dendrite cannot be fit well (see methods; here the spine trace), calcium traces of spine and dendrite are compared to evaluate which of the two reaches a threshold (50 % of normalized maximal response) first. Only if the spine reaches the threshold first, it is considered to have received direct synaptic input (Case 2.2). **D** Quantification of effectiveness of criteria to identify synaptically connected dendritic spines in data containing dendritic calcium spikes (data B) and comparing the results to data A. The criteria could not reproduce the results of data A. **E** Results in D by responsiveness type.

In particular, calcium traces are first normalized and subsequently fitted. Then, it is assessed whether the fit of the spine reaches the threshold of 67 % of its maximal response before the dendrite, which would indicate the spine falls into case 2.1 (Fig. 3.3.5C; Coneva, 2015). Should fitting of the traces not be possible due to noisiness of the calcium trace for example, a similar test is performed on the unfitted but normalized data, using a threshold of

50 % of the maximal calcium response. Similar to case 2.1, should the spine reach the threshold before the dendritic sub-ROI, the spine would be labeled as synaptically connected to stimulated inputs, this time satisfying case 2.2 (Fig. 3.3.5C; Coneva, 2015). In all other instances (i.e. spine does not show a significant increase in calcium, dendrite reaches criteria thresholds first or at the same time as the spine) the spine would be classified as not responsive.

To assess whether this approach can accurately identify those dendritic spines that are functionally connected to blue-light-responsive axonal boutons, these criteria were applied to the acquired dataset. In particular, all data containing dendritic calcium spikes (data B) was analyzed using the criteria for cases 1, 2.1 and 2.2 and subsequently compared to responsiveness labeling in single-spine response trials (data A). Using this approach, most dendritic spines in data B were labeled as non-responsive, indicating that despite the occurrence of a dendritic calcium spike, the criteria correctly identify most spines as not synaptically connected to photo-responsive boutons. Moreover, as expected from data B, responsive spines were almost exclusively categorized as cases 2.1 or 2.2 (Fig. 3.3.5E), indicating that the set of criteria correctly identified that dendrites and spines were responsive. However, only a minority (49 of 180) of dendritic spines that were labeled as responsive in data A were also found to be responsive when applying this approach (Fig. 3.3.5D). More importantly, a large amount of spines were found to be responsive using this approach. As outlined above, ChR2-stimulation in data B was stronger than that of data A to elicit dendritic calcium spikes. Hence, it is conceivable that additional axonal boutons were depolarized sufficiently to cause a larger fraction of dendritic spines to receive synaptic input. Nonetheless, given that more than three times as many spines were identified to be responsive in data B, it is likely that a proportion of these spines were false-positively labeled as responsive using this approach. In conclusion, the outlined set of criteria does not seem to accurately identify those dendritic spines that are functionally connected to stimulated presynaptic boutons.

Unmixing of synaptically-induced spine calcium transients during dendritic calcium spikes using robust fit

As calcium transients in dendrites and dendritic spines occur near- simultaneously during dendritic calcium spikes, temporal unmixing is challenging.

However, it is conceivable that signals differ in amplitude when a spine is flooded with calcium during a dendritic calcium spike and when a spine shows increases in calcium due to synaptic input. Consequently, subtraction of the dendritic calcium signal from the spine signals could be a means of differentiating functionally connected spines from those that are flooded by a calcium spike. To test whether this is the case or not, a method, which follows this rationale (Chen et al., 2013; Wilson et al., 2016) was tested on the above mentioned dataset (data A and B): in short, a scaled version of the dendritic calcium signal was subtracted from the spine signal using robust fit (Fig. 3.3.6A, B; see methods; Chen et al., 2013). Subsequently, responsivity of spines was assessed using their dendrite-signal-corrected calcium signals (Fig. 3.3.6B). When applying robust fit analysis to data containing dendritic calcium spikes (data B), most previously responsive spines (data A) could not be re-identified (53 of 192 spines; Fig. 3.3.6C). Moreover, a large proportion of spines was found to be responsive in data B using robust fit (659 spines), indicative of a significant proportion of false positive spine responses when using this method. Thus, robust fit does not seem to reliably identify functional connectivity of individual spines in data containing dendritic calcium spikes in the proposed assay.

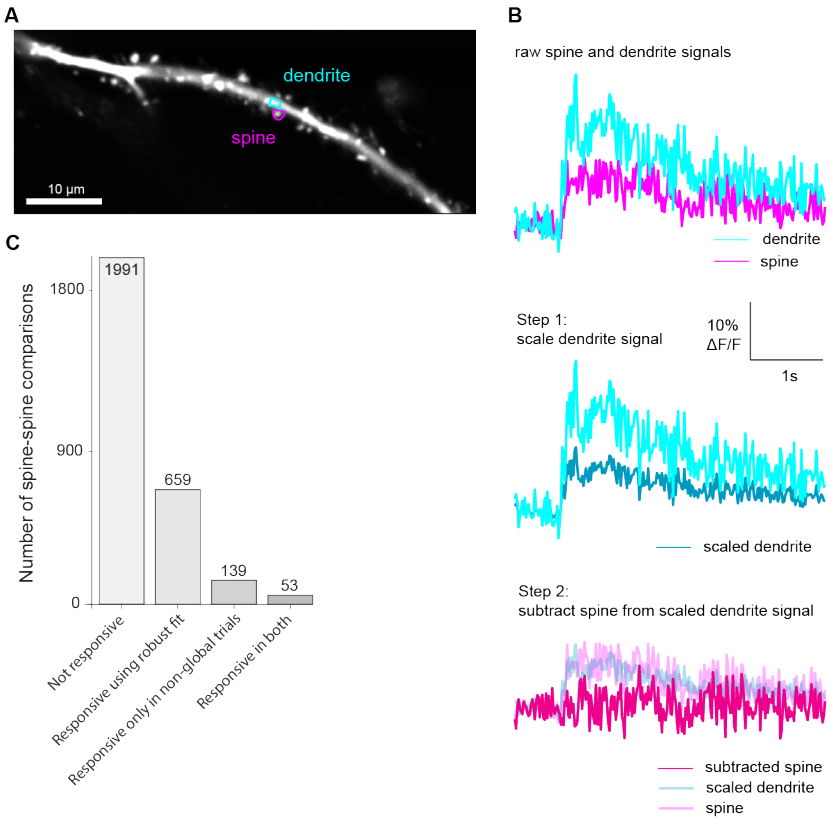

Figure 3.3.6 Unmixing of synaptically-induced spine calcium transients during dendritic calcium spikes using robust fit

A Average intensity projection of a calcium movie containing a dendritic stretch and spines. A spine and dendrite sub-ROI are outlined in magenta and turquoise, respectively. **B** Process of determining which spines receive synaptic inputs during dendritic calcium spikes. Shown are 9-point moving average calcium traces of the spine and its matched dendrite sub-ROI shown in A. From left to right: spine and dendrite show near-identical calcium transients upon photo-stimulation. Dendrite signal (turquoise) is re-scaled (dark blue) according to robust fit of dendrite to spine signals (Step 1). Scaled dendrite signal (faint dark blue) is then subtracted from spine signal (faint magenta) to reveal true synaptic calcium signal in the spine (subtracted spine, magenta; Step 2). **C** Quantification of effectiveness of robust fit analysis to identify synaptically connected dendritic spines in data containing dendritic calcium spikes (data B) and comparing the results to data A. The unmixing approach using robust fit could not reproduce the results of data A.

Subtraction of dendrite from spine signal based on spike inference estimation

In addition to robust-fit subtraction, recently another process of subtracting the dendritic signal from the spine signal was developed (Kerlin et al., 2019). By simultaneously imaging the apical trunk, nearby dendrite or cell soma, a reference signal could be obtained, in addition to a region of interest containing dendrites and dendritic spines. This reference signal was subsequently deconvolved and the underlying electrophysiological signal estimated. The signal of each spine was then individually fit to this spike inference estimation. Lastly, the fit reference signal was subtracted from the spine signal to unmask the synaptically-induced calcium signal of a given dendritic spine (Fig. 3.3.7C; Kerlin et al., 2019). This approach was recreated, although given the limitations of the setup at hand, neither the apical dendrite, nor the cell soma could be imaged simultaneously. Hence, the dendrite was utilized as a reference signal.

Results of this approach on spines of data B were compared to single-spine responses (data A) in the same dataset. In line with the previously tested computational approaches, the majority of dendritic spines was found to be unresponsive (Fig. 3.3.7D). However, again only a fraction of single-responsive spines could be re-identified (17 of 72) as input-receiving during dendritic calcium spikes using this approach. Moreover, and similar to the temporal unmixing approach described above, a large amount of spines (n = 241) were found to receive synaptic input during dendritic calcium spikes (Fig. 3.3.7D). As before, while an increased number of dendritic spines is expected to receive synaptic input, it is likely that a fraction of these spines are falsely labeled as receiving input using this method.

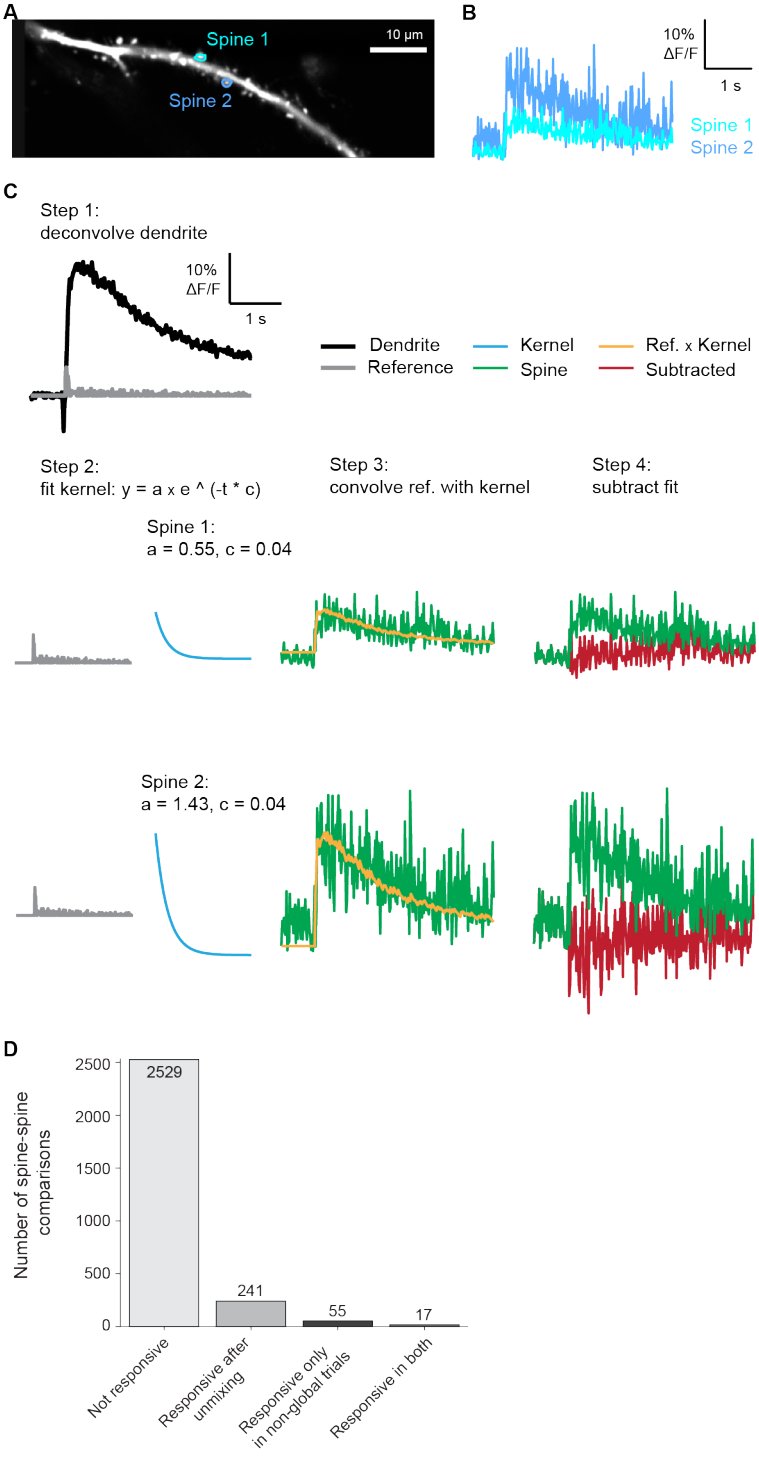
A
Spine 1
Spine 2
10 µm
B
10%
ΔF/F
1 s
Spine 1
Spine 2
C
Step 1:
deconvolve dendrite
10%
ΔF/F
1 s
Dendrite
Reference
Kernel
Spine
Ref. x Kernel
Subtracted
Step 2:
fit kernel: y = a x e ^ (-t * c)
Step 3:
convolve ref. with kernel
Step 4:
subtract fit
Spine 1:
a = 0.55, c = 0.04
Spine 2:
a = 1.43, c = 0.04
D
Number of spine-spine comparisons
2500
2000
1500
1000
500
0
2529
241
55
17
Not responsive
Responsive after unmixing
Responsive only in non-global trials
Responsive in both

Figure 3.3.7 Subtraction of dendrite from spine signal based on spike inference estimation
A Average intensity projection of a registered calcium movie containing a dendritic stretch and spines. Two dendritic spines (teal and blue) are outlined. **B** Process of unmixing dendritic calcium spike signal from neurotransmission-induced calcium signal in dendritic spines (devised after Kerlin et al., 2019). The signal of the entire dendrite (black) is first deconvolved to extract its electrophysiological underpinning and generate a reference signal (gray; Step 1; see methods). Then, per spine, calcium traces are fitted to the reference using differential evolution to generate a kernel (blue; Step 1). The reference signal is then convolved with the kernel (orange) to estimate the proportion of a spine's calcium signal that can be attributed to the dendritic calcium spike (Step 3). This estimate is subsequently subtracted from the raw calcium trace of the spine (green) to estimate the true synaptic calcium signal in the spine (subtracted, red; Step 4). Spine 1 was found to be be photo-responsive in data A, while spine 2 was not found to be photo-responsive in single-spine response data. In both spines, no significant photo-response could be detected after unmixing. **C** Results of the unmixing approach on all data B. Most single-spine-responsive spines could not identified as responsive after unmixing.

In conclusion, this approach seems to not accurately identify those dendritic spines that are functionally connected to stimulated presynaptic boutons. Moreover, none of the computational approaches tested here were able to correctly re-identify those dendritic spines in data of calcium spikes that were previously identified as functionally connected. Hence, it seems that computational approaches are not suited to uncover functional connectivity in the presence of dendritic calcium spikes in the proposed assay.

3.3.6 Pharmacological approaches to differentiate spine from dendritic calcium events

In contrast to managing dendritic calcium spikes computationally, the *in vitro* assay allows for pharmacological interventions, which could prevent such events altogether. Since calcium signaling in dendrites and spines is regulated by many molecular players (for review, see Grienberger & Konnerth, 2012), a large array of options was available. However, localization of the various

receptors and channels is critical, as pharmacological intervention should neither affect presynaptic release, nor calcium processing in dendritic spines. Given these constraints, two potential approaches were identified.

Muscimol

Hyperpolarization of cells has been shown to significantly decrease the frequency of dendritic calcium spikes *in vivo* (Chen et al., 2011). Consequently, chloride-conducting GABA receptors were considered as potential targets of pharmacological manipulation. Particularly the GABA-A receptor, which has been reported to preferentially localize to inhibitory synapses along the dendrite but not at glutamatergic synapses (i.e. on dendritic spines; Serwanski et al., 2006; Magnin et al., 2019) (but also see Chiu et al., 2013), emerged as a primary candidate. Given these reports, sufficient activation of GABA-A receptors should, due to their localization, prevent dendritic calcium spikes without affecting calcium transients in dendritic spines. To test this, two experiments were conducted to quantify the wash-in and -out effects of the potent GABA-A receptor agonist muscimol.

To get an estimate of the effects muscimol has on synaptic transmission, whole-cell patch clamp recordings of CA1 pyramidal cells (n = 5) were performed. Stimulation of ChR2-expressing Schaffer collateral terminals followed an 11-step protocol with increasing stimulation intensities (0-100 % laser power; Fig. 3.3.8A). To mimic the experimental design of the proposed assay, this procedure was performed in conditions preventing the generation of action potentials (1 μM TTX, 100 μM 4-AP Petreanu et al., 2009). The step protocol was performed before and after wash-in of muscimol in the same cells to quantify the effect of muscimol on input strength. Muscimol decreased input strength by $\sim$35 % (Chi square = 2.7931, p = 0.0947, df = 9, Kruskal-Wallis test; Fig. 3.3.8C) and exerted a pronounced effect in inward current size across the majority of the 11 laser intensities used (Fig. 3.3.8B). It remains unclear whether muscimol acts directly, i.e. via bouton hyperpolarization, or indirectly, i.e. via disynaptic changes in release. While muscimol seemed to have a pronounced effect on input strength, neurotransmitter release from Schaffer collaterals remained intact in at least some afferents.

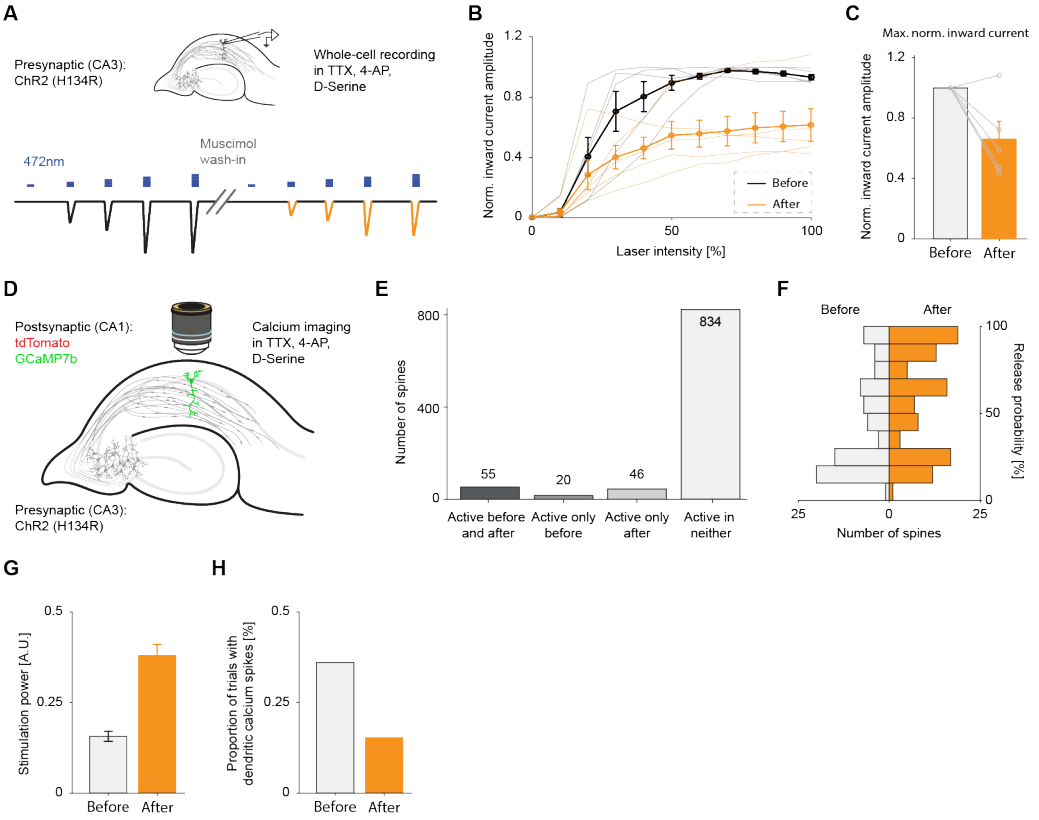

Figure 3.3.8 The effect of the GABA-A agonist muscimol on the generation of dendritic calcium spikes

A Schematic of the experiment: individual CA1 pyramidal cells were recorded using whole-cell patch clamp. A population of CA3 neurons is transduced with ChR2(H134R), recordings were performed in TTX and 4-AP (top). A step protocol with increasing amounts of ChR2-stimulation (472 nm) intensities was employed before and after wash-in of the GABA-A agonist muscimol (bottom). **B** Dose response curve of normalized photo-stimulation-evoked inward current amplitudes as a function of laser intensity before (black) and after (orange) the wash-in of muscimol. Thin lines represent individual cells, thick lines represent the mean of all cells (n = 5). Normalization was performed on the maximal inward current before wash-in. **C** Quantification of B. Application of muscimol seems to lower the normalized inward current amplitude (Chi square = 2.7931, p = 0.0947, df = 9, Kruskal-Wallis test; n = 5 cells). Bars: control in gray, muscimol in orange. Individual cells in gray. **D** Schematic of the experimental model. Structural (tdTomato; red) and a calcium indicator (GCaMP7b; green)

are co-expressed in single CA1 neurons of OHSCs. A population of CA3 neurons is transduced with ChR2(H134R). Two-photon calcium imaging is performed in dendritic regions of the CA1 neuron in conditions preventing the generation of action potentials (TTX, 4-AP). **E** Results of muscimol wash-in on spine responsivity. Many spines seem to be unaffected by muscimol wash-in, however ∼27 % are rendered unresponsive. An additional ∼60 % of spines are responsive after muscimol wash-in. **F** Effect of muscimol on release probability. After muscimol wash-in, higher release probabilities could be achieved (Chi square = 46.208, p <0.001, McNemar's test; n = 185 spines across 236 movies). **G** Stimulation power in trials in which no dendritic calcium spike was triggered is lower before (gray) than after (orange) muscimol wash-in (Chi square = 18.3338, p <0.001, df = 233, Kruskal-Wallis test; 236 movies were analyzed in total). **H** The proportion of trials in which a dendritic calcium spike was triggered before (gray) and after (orange) muscimol wash-in. Error bars are ± SEM.

To further investigate the effect of muscimol on calcium signaling in dendrites and dendritic spines, calcium imaging of CA1 neurons was performed to determine (1) whether the same dendritic spines received synaptic input before and after application of muscimol, and (2) whether muscimol prevented the generation of dendritic calcium spikes. In the proposed assay, the same set of ChR2-expressing boutons are utilized to establish functional connectivity at the end, and induce LTP in the beginning of the experiment. To establish rules of functional connectivity, it is critical to link spine responsiveness to those synapses that contributed to the induction of LTP. Consequently, synaptic transmission at these synapses must remain unaffected by any pharmacological manipulation.

Responsiveness to ChR2 stimulation of individual spines of GCaMP7b-expressing CA1 pyramidal cells was assessed before and after wash-in of muscimol (Fig. 3.3.8D). As expected, the majority of spines were unresponsive irrespective of the presence of muscimol. However, ∼27 % of spines that were responsive before were rendered unresponsive after application of muscimol (Fig. 3.3.8E). Nevertheless, the application of muscimol allowed for stronger ChR2-stimulation before dendritic calcium spikes occurred: the stimulation power was approximately twice as strong after application of muscimol, before dendritic calcium spikes were generated (Chi square = 18.3338, p <0.001, df = 233, Kruskal-Wallis test; Fig. 3.3.8G). Additionally, the proportion of trials

in which a dendritic calcium spike occurred was nearly half after application of muscimol (Fig. 3.3.8H). Moreover, after application of muscimol, higher release probabilities could be observed (Chi square = 46.208, p <0.001, McNemar's test; Fig. 3.3.8F), in line with the additional degrees of freedom of photostimulation power gained by the presence of muscimol. Ultimately, an additional ∼60 % of dendritic spines could be photostimulated by hyperpolarization via muscimol (Z = -2.6498, p <0.01, Wilcoxon rank sum test; Fig. 3.3.8E). In conclusion, muscimol allowed for stronger photostimulation and as a consequence, increased the number of responsive spines before dendritic calcium spikes were generated. However, muscimol also seemed to interfere with synaptic transmission in the Schaffer collateral pathway, rendering some dendritic spines unresponsive. Given the necessity to reliably determine functional connectivity in the proposed assay, muscimol, at least in the concentration used here, seems to not offer the required specificity.

Voltage-gated calcium channel blockers

Dendritic calcium spikes have been shown to be governed by changes in membrane potentials (Grienberger, Chen, & Konnerth, 2014; Harnett et al., 2013), in particular via voltage-gated calcium channels (Magee et al., 1995; Grienberger, Chen, & Konnerth, 2014). Since P/Q- and N-type VGCCs are heavily involved in presynaptic release at the Schaffer collaterals (Wheeler, Randall, & Tsien, 1994; Qian & Noebels, 2000), they were excluded as potential candidates. L-type VGCCs are mostly localized at the soma and the proximal dendrites (Westenbroek, Ahlijanian, & Catterall, 1990; Hell et al., 1993; Obermair et al., 2004) (but see Tippens et al., 2008). Additionally, dendritic spines mostly lack T-type VGCC expression (McKay et al., 2006) (but see Aguado et al., 2016). Hence, it was tested whether subtype-specific blocking of VGCCs could prevent dendritic calcium spikes and unmask functional connectivity of dendritic spines using strong photostimulation. To this end, L-type (nifedipine, 30 μM) and T-Type (mibefradil, 15 μM) VGCC blockers were utilized in wash-in calcium-imaging experiments, similar to the above outlined experiments involving muscimol (Fig. 3.3.8). Most spines that previously showed photostimulation-evoked calcium transients remained responsive after wash-in (48 of 63 spines; Fig. 3.3.9A). However, ∼24 % (n = 15 spines) of previously responsive spines were rendered unresponsive by the presence of nifedipine and mibefradil. In contrast to the muscimol experiments, only a small number of dendritic spines (n = 12) could be additionally

recruited by application of VGCC blockers (Fig. 3.3.9A). As expected, most spines remained unresponsive irrespective of the presence of VGCC blockers (Fig. 3.3.9A). Additionally, release probability remained unchanged after blocking L- and T-type VGCCs (Z = -0.4626, p = 0.6436, Wilcoxon rank sum test; Fig. 3.3.9B). However, similar to the effects of muscimol, the addition of VGCC blockers did not prevent the occurrence of dendritic calcium spikes (Chi square = 46.3133, p <0.001, McNemar's test; Fig. 3.3.9C).

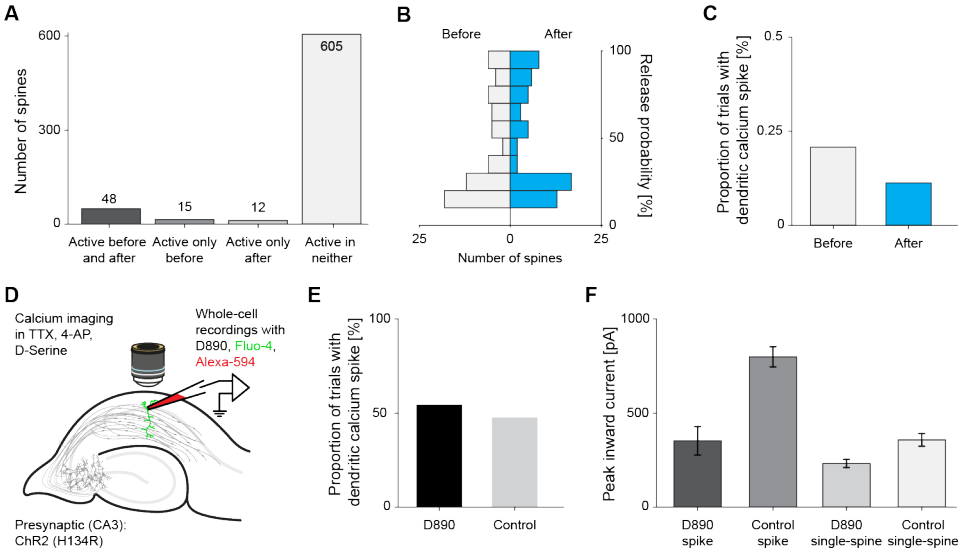

Figure 3.3.9 The effect of VGCC blockers on the generation of dendritic calcium spikes

A Results of L- and T-type VGCC blockers (nifedipine, mibefradil) wash-in on spine responsivity. Most spines seem to be unaffected by wash-in. However, VGCC block leaves the dynamic range of ChR2-stimulation unaffected, given only few additional spines show responsivity after wash-in. **B** No effect of L- and T-type VGCC blockers (nifedipine, mibefradil) wash-in on release probability (Z = -0.4626, p = 0.6436, Wilcoxon rank sum test; n = 681 spines across 182 movies analyzed in total) Release probability is unaffected by L- and T-type VGCC block. **C** Results of L- and T-type VGCC blockers (nifedipine, mibefradil) wash-in on the occurrance of dendritic calcium spikes. Probability of calcium spike occurrence is lower after inclusion of VGCC blockers (Chi square = 46.3133, p <0.001, McNemar's test; 182 movies analyzed in total) . **D** Schematic representation of

the experimental setup involving D890 to block VGCCs. Individual CA1 neurons were patch-clamped and filled with the Alexa-594 and Fluo-4 to reveal structure and calcium transients, respectively. A population of CA3 neurons was transduced to express ChR2(H134R). Calcium imaging of dendrites and spines was performed while stimulating the Schaffer collaterals in the presence of TTX, 4-AP and D-Serine. **E** Probability of calcium spike occurrence after ChR2 simulation with (n = 5 cells) and without (n = 2 cells) inclusion of the subtype-unspecific VGCC blocker D890 in the intracellular solution during whole-cell patch clamp recordings. Probability of calcium spike occurrence seems unaffected by D890 (Chi square = 2, p = 0.1573, Pearson's chi-squared test; 144 movies analyzed in total). **F** Photostimulation-evoked peak inward currents in events of single-spine responsivity and dendritic calcium spikes ("spike") with (n = 5 cells) and without (n = 2 cells) the inclusion of D890 in the intracellular solution during whole-cell patch clamp recordings. D890 decreases inward current irrespective of the presence of dendritic calcium spikes (144 movies analyzed in total).

Since subtype-specific VGCC blockers seemed to not affect the occurrence of dendritic calcium spikes to the desired degree, a recently reported approach was tested: blocking VGCCs subtype-unspecifically in individual pyramidal CA1 neurons *in vivo* prevented the generation of dendritic calcium spikes (Grienberger, Chen, & Konnerth, 2014). This method utilized D-890, a derivative of methoxyverapamil, which has been shown to block VGCCs in a subtype-nonselective manner (Hescheler et al., 1982; Kovalchuk et al., 2000; Grienberger, Chen, & Konnerth, 2014). Of key importance here is that the effects of D890 are confined to individual cells, unlike the wash-in approach outlined above. Two features of D890 restrict its effect to a single postsynaptic cell: first, D890 is rendered membrane impermeable due to its quaternary structure, thereby limiting D890's access. Second, the binding site for D890 is located on the intracellular domain of VGCCs, hence D890 can only exert its effect when supplied intracellularly (Hescheler et al., 1982). As a consequence, when D890 is included in the internal solution during patch-clamp recordings of an individual CA1 neuron, only VGCCs of that neuron were affected and dendritic calcium spikes were prevented (Grienberger, Chen, & Konnerth, 2014). Hence, following this approach, whole-cell patch clamp experiments in voltage-clamp mode were performed with internal solutions containing D890 (1 mM). The addition of a structural (Alexa-694) and a calcium indicator (Fluo-4F) to the internal solution allowed for the simulta-

neous tracking of dendritic and spine calcium responses and EPSCs in the recorded neuron (Fig. 3.3.9D). Likely due to the poor solubility of D890 in aqueous solutions, the series resistance frequently surpassed 40 MΩ within 15 minutes and the experiment had to be terminated. Since the recorded cells could not be visualized (i.e. did not express GECIs or structural markers) before whole-cell recordings, no within-cell comparisons were possible. This is in contrast to the previous pharmacological assessments of muscimol and nifedipine/mibefradil, where responsiveness could be quantified before and after pharmacological manipulation. Hence, the effect of D890 was quantified between cells that were recorded from either with and without the inclusion of D890 in the internal solution. Surprisingly, dendritic calcium spikes were still observed in cells that were patched with D890-containing intracellular solution (Chi square = 2, p = 0.1573, Pearson's chi-squared test; Fig. 3.3.9E). Preliminary evidence suggests that D890 seems to decrease the peak inward current, both during dendritic calcium spikes and stimulation events that elicited single-spine responses, indicating that it does exert an effect on EPSC size (Fig. 3.3.9F). In conclusion, intracellular application of the VGCC blocker D890 does not seem to prevent the occurrence of dendritic calcium spikes.

In conclusion, neither subtype-specific nor -unspecific block of VGCCs seemed to offer the control over dendritic calcium spike generation that is required to establish functional connectivity in the proposed assay. In the future, other approaches should be explored to map functional synaptic connectivity on a single spine basis in the proposed assay and thereby enable investigations into the functional wiring rules that govern LTP-induced synaptogenesis.

Chapter 4

Discussion

4.1 Binocularity in the dLGN

The goal of this section of the thesis was to characterize functional binocular convergence in the dLGN of mature mice. Recent reports on the amount of binocular convergence in the dLGN have provided conflicting results (Howarth, Walmsley, & Brown, 2014; Rompani et al., 2017; Jaepel et al., 2017; Sommeijer et al., 2017; Huh et al., 2020). Hence, a dual-color optogenetic approach was devised to quantify retinogeniculate inputs to single dLGN cells with optimal signal-to-noise ratio *in vitro*. The dataset revealed that, while most dLGN cells receive input from both eyes, the vast majority of all dLGN neurons are functionally monocular. Moreover, the dendritic outgrowth of dLGN cells in relation to the eye-specific projection zones predicted ocular dominance. However, the observed levels of functional monocularity in the dLGN could not be fully explained by dLGN neurons' morphologies and their respective axo-dendritic overlap with eye-specific afferents. Instead, selection and refinement of retinogeniculate wiring seems to be realized via differential expression of AMPA and NMDA receptors, leading to widespread functional monocularity in the dLGN.

4.1.1 Prominent eye-specific retinogeniculate convergence but limited functional binocularity

Until recently, the dLGN has mainly been considered as a relay station, passing information from the retinae on to the visual cortex via independent,

eye-specific processing streams. However, recent work using monosynaptic rabies tracing showed that 40 % of dLGN neurons received structural input from both eyes (Rompani et al., 2017), suggesting that binocular cells might already exist at the level of the visual thalamus. Indeed, using retinogeniculate input mapping - in this dissertation - it could be shown that more than half of dLGN neurons receive input from both eyes. While this suggests that a sizeable proportion of dLGN neurons might be functionally driven by input of either eye, such functional binocularity was not found. In fact, the overwhelming majority (>99 %) of dLGN neurons seem to be functionally monocular. Despite prominent eye-specific convergence, functional binocularity was limited, as the dominant eye provided on average 36 times stronger input than the non-dominant eye. Moreover, stimulation of the non-dominant eye did not lead to the firing of action potentials, further confirming that the dLGN is functionally monocular. This discrepancy between widespread structural convergence and limited functional binocularity indicates that, at least in the retinogeniculate pathway, monosynaptic rabies tracing is not an apt method for evaluating synaptic strength or functional connectivity. In the past, it has been shown that rabies viruses likely label presynaptically connected neurons in a biased manner (Ugolini, 1995; Tang et al., 1999; Feldmeyer et al., 2002; Miyamichi et al., 2011; Callaway & Luo, 2015), while the role of synaptic strength or synapse size, if any, remains unexplored. Hence, as previously suggested (Callaway & Luo, 2015; Luo, Callaway, & Svoboda, 2018), the results here underscore that monosynaptic rabies tracing should be complemented with additional functional experiments in order to quantify functional connectivity. Accordingly, other means of quantifying structural connectivity, such as electron microscopy, are frequently supplemented with functional measurements (Holler et al., 2021; Scholl et al., 2021; Kuan et al., 2022) to enable analyses of functional connectivity.

Deeper insights into the functional convergence of retinal inputs in the dLGN have been provided by two recent electrophysiological studies: despite the availability of many presynaptic inputs, functionally, the majority of input to dLGN neurons is provided by three or fewer RGCs (Hong et al., 2014; Litvina & Chen, 2017). This is well in line with another report, which suggests that dLGN neuron responses *in vivo* can successfully be explained by a combination of few RGC types (Rosón et al., 2019). Taken together, these reports indicate that few RGC inputs dominate neuronal function in the

dLGN. The data presented in the first part of this dissertation provides further evidence in favor of this, as functional binocular convergence of RGCs seems to also be limited.

These findings indicate that it is unlikely that a large proportion of dLGN neurons receive strong binocular input *in vivo*. Functional comparisons between *in vitro* and *in vivo* data are challenging, not only due to differences in connectivity (cortical or tectal inputs are cut off in the assay used here) but also due to different recording techniques, stimulation patterns, analysis methods, and cellular sampling (Rose & Bonhoeffer, 2018). The results here resemble those obtained by previous studies involving calcium imaging of dLGN boutons at the level of V1 *in vivo* (Jaepel et al., 2017; Huh et al., 2020). In these reports, the fraction of binocular dLGN boutons ranged between 6 and 14 %. Recently however, a thorough assessment of mouse thalamocortical binocularity has been conducted, also using two-photon imaging of dLGN boutons *in vivo* (Bauer et al., 2021). It was shown that the fraction of binocular boutons is critically dependent on the stringency of responsiveness and selection criteria that are employed during data analysis. Depending on these criteria between 7 and 21 % of dLGN boutons were found to be binocular. The type and vertical position (elevation) of the stimulus in the visual scene, on the other hand, seemed to affect binocularity only to a minor degree.

Besides two-photon imaging of dLGN afferents, electrophysiological recordings have also been utilized to investigate functional binocularity *in vivo*. Here, much higher levels of binocularity have been reported (Sommeijer et al., 2017), particularly in the dorsomedial tip of the dLGN (Howarth, Walmsley, & Brown, 2014). Here, up to 50 % of dLGN cells in some regions have been found to be functionally binocular (Howarth, Walmsley, & Brown, 2014). Unfortunately, comparisons between electrophysiological and two-photon imaging studies are difficult due to the inherent differences in data types. However, here too, analysis criteria (e.g. threshold criteria used, source separation, smallest detectable response amplitude) likely play a large role and underlie the differences in reported binocularity in the dLGN.

Interestingly, the estimated fraction of binocular dLGN cells found in the *in vitro* mapping results of the first part of this dissertation are even lower than those of recent *in vivo* imaging reports (Jaepel et al., 2017; Bauer et al., 2021). One potential explanation for this might be other sources of poten-

tial activity-driving or -modulating inputs, which are abundant in the dLGN (Howarth, Walmsley, & Brown, 2014; Bickford et al., 2015; Thompson et al., 2016; Born et al., 2021; Spacek et al., 2022). However, it seems unlikely that these inputs render nearly half of the dLGN neurons functionally binocular (see Howarth, Walmsley, & Brown, 2014), when only 1 % of dLGN cells receive sufficient retinogeniculate input to be considered binocular *in vitro* (Bauer et al., 2021). Nevertheless, investigating the role of modulatory inputs in dLGN neurons would provide additional insight in how these cells are functionally tuned. One could envision an extension to the dual-color optogenetic mapping approach, as shown above, that would enable mapping of a third, orthogonal source of presynaptic input. This could be achieved via electrical stimulation or another opsin, which cannot be excited by light in the spectra utilized to stimulate the two opsins used here (blue and red, respectively). Such an approach would allow for simultaneous mapping of binocular inputs, while additionally investigating the modulatory roles of tectal, cortical or thalamic sources.

Besides extending the assay to map inputs of a third source, the type of stimulation pattern used could be changed. One of the shortcomings of the assay as presented here is the artificial nature of the stimulation paradigm. While eliciting maximal input helped in quantifying relative input strength from each eye, this type of neuronal input is unlikely to resemble RGC input patterns during visual stimulation *in vivo*. Hence, in the future, more nuanced stimulation paradigms could be devised to quantify the effect non-dominant inputs have in dLGN cells. Despite their small input strength, these inputs might play a critical modulatory role in shaping the tuning of dLGN neurons

4.1.2 Relating morphological to functional mechanisms of eye-specificity

In the past, dLGN cells have been reported to fall into distinct morphological categories found in particular locations. Due to their localization, it has been hypothesized that these cell types also receive cell type-specific input (Krahe et al., 2011; Bickford et al., 2015). However, the data acquired in the

first part of this dissertation did not reveal such morphological categories, in line with a recent study that assessed dLGN morphology and wiring using electron microscopy (Morgan et al., 2016). Moreover, despite considerable variation in morphological features between cells, most cells were found to be functionally monocular. Additionally, in an effort to elucidate retinogeniculate input sampling of dLGN neurons, the dendritic morphology of recorded cells and the fact that RGC afferents are segregated in the adult animal could be exploited. Using this approach, a cell's ocular dominance could be predicted based on the axo-dendritic overlap with RGC afferents. While eye dominance could be predicted, strikingly, the fact that for almost all cells one eye provided the vast majority of functional input (functional monocular bias) could not be explained by eye-specific input segregation alone, or by dendritic orientation. Even when assuming that retinogeniculate inputs are perfectly segregated, axo-dendritic overlap estimates suggested far higher retinogeniculate binocularity than what was found in the functional, i.e. electrophysiological, data. Moreover, dendrites seemed to not respect eye-specific segregation zones and instead frequently crossed the border between them, a phenomenon seen in other species as well (Sanderson, 1971; Conley, Birecree, & Casagrande, 1985; Krahe et al., 2011).

One methodological shortcoming in this analysis is the resolution limit of the acquired confocal images. Due to the innervation density of RGC axonal afferents in the dLGN, clear identification of axo-dendritic apposition is challenging, despite previous brain clearing. The voxel size utilized (14.6 µm) is far beyond the resolution required for 'true' axo-dendritic apposition used in ultrastructural analyses (average 400 nm Macarico-da-Costa & Martin, 2009). Analyses involving light microscopy, on the other hand, usually involve specific pre- and postsynaptic markers, typically in the form of punctae, and which, when localized in close proximity, suggest the presence of a synapse (Morgan et al., 2011; Velicky et al., 2022). This method has a reported false positive rate of roughly 30 % when detecting functional synaptic connections using common light microscopy methods (Macarico-da-Costa & Martin, 2009). The method utilized in the first part of this dissertation differs in two ways from this: first, no specific synaptic markers were employed. One key feature of such markers is that they generate punctae, signifying the presence of a mature, functional synaptic compartment. In this work, both pre- and postsynaptic compartments were simply labeled by expression of cytosolic or membrane-bound fluorophores. Hence, apposition here indi-

cates proximity, rather than a synaptic compartment. Second, the spatial resolution of the images utilized here is far too low to pinpoint synaptic connectivity between RGC afferents and dLGN cells. Consequently, the results in this dissertation should be interpreted as axonal availability in the vicinity of a cell's dendritic arbor.

While the imaging experiments and analyses here provide an initial insight into binocular retinogeniculate wiring, future studies should investigate how well structural and functional wiring match in this circuit. For example, recent advances in expansion microscopy (M'Saad et al., 2022) might enable analysis of true axo-dendritic apposition in the retinogeniculate pathway. Alternatively, binocular synaptic connectivity could be quantified in the dLGN on a single-cell basis using a recently developed dual-color trans-synaptic mapping approach (Choi et al., 2018). In this approach, two different fluorophores are reconstituted across the synaptic cleft of different populations of pre- and postsynaptic partners, thereby visualizing the location of synapses of two input areas. Precise visualization of synaptic connectivity via such techniques should uncover whether the fine-scale synaptic refinement seen here and previously (Chen & Regehr, 2000; Hong et al., 2014) is also reflected on the synaptic level in the dLGN.

4.1.3 Input selection and synaptic refinement drive functional dLGN monocularity

Synaptic strength varied considerably in dLGN neurons, with retinogeniculate inputs ranging from hundreds to thousands of pA. Despite this variability, one eye typically provided the vast majority (>97 %) of input. Similar to other circuits (Hsia, Malenka, & Nicoll, 1998; Ye et al., 2005), the AMPAR to NMDAR ratio, a measure for synaptic maturity (Crair & Malenka, 1995) increases during development in the retinogeniculate pathway. Moreover, AMPAR-silent synapses become less frequent (Chen & Regehr, 2000), and over time the number of driving dLGN inputs is reduced to three or less (Chen & Regehr, 2000; Litvina & Chen, 2017). Here, a high AMPAR to NMDAR ratio was found for dominant eye inputs, in line with earlier reports (Chen & Regehr, 2000; Hooks & Chen, 2006). The non-dominant eye, on the other hand, not only contributed less absolute input, it also showed a lower AMPAR to NMDAR ratio, reminiscent of retinogeniculate

synapses during development (Chen & Regehr, 2000). The most striking examples of under-developed synapses were the large number of observed AMPAR-silent connections. Typically, such silent synapses are believed to be a dormant plasticity pool that can play a significant role in the induction or maintenance of LTP (Liao, Hessler, & Malinow, 1995; Arendt, Sarti, & Chen, 2013, but see). Theoretically, such synapses could be recruited in an activity-dependent fashion during ocular dominance plasticity. Changes in ocular dominance have been reported in dLGN cells *in vivo* after monocular deprivation during (Sommeijer et al., 2017; Huh et al., 2020) and after (Jaepel et al., 2017) the critical period for ocular dominance plasticity. However, after this sensitive plasticity period, ocular dominance shifts in response to experience-dependent plasticity paradigms tend to diminish in an age-dependent manner (Fischer et al., 2007; Lehmann & Löwel, 2008). Hence, the reservoir of immature, silent synaptic connections found here was surprising given the age of the animals used (>p65). Typically, during development retinogeniculate projections are pruned in an activity-dependent manner (Stevens et al., 2007; Schafer et al., 2012). Our results indicate that, at least in some small inputs, this process does not occur. Which function these silent synapses provide remains entirely unclear. Potentially, together with other inputs, such as tectal or corticothalamic ones, they might contribute to the modulation of inputs and thereby contribute to the functional tuning of dLGN neurons.

4.1.4 Technical considerations

The observed levels of structural binocular convergence exceed previous estimates of structural binocularity in the dLGN (Rompani et al., 2017). However, binocular structural wiring is likely to be even more widespread than found here, due to several technical challenges of the assay. First, some of the recorded cells were more superficially located within the slice than the average dendritic length of a dLGN cell ($\sim$ 70 μm). Consequently, some cells' dendritic arbors might have been severed during the preparation of acute slices, thus compromising the likelihood of binocular wiring. On the other hand, these missing dendritic branches likely did not provide strong retinogeniculate input, as these inputs are typically found near the soma on proximal dendrites (Morgan et al., 2016). Additionally, cells were typically targeted in the upper 100 μm of the acute slice (320 μm thickness), due to the poor transmission light visibility in the dLGN. Unlike other brain ar-

eas, such as cortical regions, cell bodies were not visible and could thus not be precisely targeted for whole-cell electrophysiological recordings. Thinner acute slices should help in achieving better visibility. However, as a consequence, even more dLGN cells would have severed dendritic arbors. Hence, this technical shortcoming is challenging to address in living tissue, despite recent developments in brain clearing techniques (Iijima et al., 2021).

Second, to map functional binocularity in this assay, ideally all retinogeniculate boutons express the optogenetic constructs utilized in this study and can be stimulated effectively. One technical consideration in this matter is the transduction of all RGCs with the utilized opsins following intravitreal injections. To allow for sufficient transduction of the opsins in each eye, *in vitro* experiments were performed ≤ 5 weeks after intravitreal eye injections. Transduction efficiency was estimated to be >90 %, however, the precise efficiency could not be quantified due to signal overlap between RGC cell-bodies. The maximum input strength measured here is well in line with some previous reports using electrical stimulation (Narushima et al., 2016). Others have reported higher maximum RGC input strength in dLGN neurons (Litvina & Chen, 2017), however, this measurement also depends on the type of extracellular solution used (Litvina & Chen, 2017) and the type of acute slice preparation (Chen & Regehr, 2000; Litvina & Chen, 2017), complicating comparisons between studies. Overall, it seems unlikely that RGC transduction levels resulted in an underestimation of the amount of binocular retinogeniculate wiring reported here.

To achieve neurotransmission in all RGC afferents, a large area (>2mm diameter) was optogenetically stimulated. This stimulation spot covered the majority, if not the entire, dLGN and therefore should have been sufficient in stimulating most superficial RGC boutons. However, given the lack of optical accessibility when using transmitted light during patch-clamp recordings, it is feasible that some of the less superficially localized boutons might have received either less or insufficient amounts of photostimulation. However, many cells were already receiving maximal current input, even when only stimulated with 20 % of maximal photostimulation irradiance (Fig. S3.1.1). Hence, while possible, it is unlikely that many retinogeniculate afferents remained unstimulated throughout the two sequentially performed step protocols.

Third, electrical noise levels of the *in vitro* setups exceeded those typical for whole-cell patch clamp recordings (noise amplitude: 8-25 pA). The main reason for this was the requirement for multiple pieces of equipment for each setup in the assay. Both setups required dual-color optogenetic stimulation, two-photon imaging capabilities amongst other features. As a consequence, very small synapses (<10 pA) could have been missed due to the electrical noise that was introduced this way. Despite this, whole-cell patch clamp recordings provide a vastly better signal-to-noise ratio than other techniques (calcium imaging or electrophysiological single unit recordings Jaepel et al., 2017; Sommeijer et al., 2017). Since optical stimulation spanned the majority of the dLGN, it was assumed that the recorded postsynaptic currents represented the sum of all inputs from an eye. It is therefore unlikely that a large proportion of cells received only a single synaptic input from the non-dominant eye, given that up to 91 RGCs are connected to a dLGN neuron (Rompani et al., 2017) with an average single fiber amplitude of several hundred pA (Narushima et al., 2016).

4.1.5 Conclusion and future directions

In conclusion, most cells in the dLGN are structurally connected to both eyes but are rendered functionally monocular via input selection and refinement of the dominant eye. Differential allocation of glutamate receptors seems to be the most prominent factor in this process.

In the future, this assay should be adapted and employed to shed light on input-specific functional convergence in other circuits. For example, functional binocular convergence could be assessed in a similar fashion in other retino-receptive areas, such as the vLGN, IGL, the superior colliculus, nuclei of the pretectum, nuclei of the accessory optic system, or the suprachiasmatic nucleus. This way, the already existing maps of retino-recipient areas from structural tracing studies (Hattar et al., 2006; Morin & Studholme, 2014; Martersteck et al., 2017a) could be supplemented with the functional characterization of eye-specific input patterns. Additionally, other features of visual processing could be investigated with modified versions of this assay. For example, RGC-subtype-specific transduction using transgenic animals (Martersteck et al., 2017b) could be utilized to map input convergence of functional diversity in the dLGN or other retino-receptive areas.

4.2 Automated detection of dendritic spines and dendrites

The second section of this dissertation dealt with the automatic detection of dendritic spines and dendrites in microscopy data. Quantification of dendritic spines is typically done manually, which is an extremely time-consuming task that also introduces user biases. Hence, a deep-learning tool, termed DeepD3, was developed to quickly identify and segment dendrites and dendritic spines in microscopy data with high accuracy. DeepD3 performed robustly across a range of microscopy datasets with different imaging modalities and data qualities. DeepD3 performed as well as experienced spine counters in spine detection in *in vitro* and *in vivo* data. Moreover, the method presented here performed complete spine segmentation orders of magnitude faster than human annotations, the hitherto gold standard. DeepD3-generated segmentations can be utilized beyond spine-counting purposes to extract fluorescence measurements in dendrites and spines in 2D and 3D data. Hence, DeepD3 is a novel tool that automatically, rapidly, and robustly detects and segments dendrites and dendritic spines in light microscopy data.

4.2.1 The accuracy of dendritic spine counting and segmentation

Imaging techniques vary in their ability to capture biological processes. Typically, there is a trade-off between temporal and spatial resolution. Dendritic spines can be visualized using several techniques, such as two-photon imaging, confocal imaging, super-resolution imaging, or electron microscopy. Given their superior spatial resolution (typical voxel size of $\leq 6 \times \leq 6 \times \leq 80$ nm), ultrastructural studies using electron microscopy are currently the gold standard for identifying dendritic spines and their morphological features. However, electron microscopy is constrained to terminal experiments in dead tissue, due to its requirement for heavy metal staining protocols. Therefore, many biological processes cannot be investigated using this imaging method. Light microscopy methods, such as confocal or two-photon microscopy, on the other hand, offer the freedom to visualize living tissue. As such, these methods are frequently utilized for spine visualization, as they allow for repeated imaging with great experimental flexibility *in vivo* and *in vitro*. However, the spatial resolution of the image data might limit the

accuracy of segmentation and/or counting of dendritic spines in images of these microscopy types. In comparison to electron microscopy, the spatial resolution of a standard two-photon microscope is much lower and typically ranges from 325 to 600 nm, depending on the wavelength and objective used. While most dendritic spines are longer than this resolution, spine necks and some types of spines cannot be resolved using this imaging technique (Pfeiffer et al., 2018; Ofer et al., 2021b). As a consequence, branched spines, or those that are in too close proximity to each other, are frequently mistakenly identified as the same spine. Filopodia, spine necks, and branched spines can be particularly thin, with diameters below 100 nm, making them hard to resolve using common light microscopy techniques. In fact, two-photon imaging-based estimates of spine density are typically 30 - 50 % too low (Attardo, Fitzgerald, & Schnitzer, 2015; Pfeiffer et al., 2018). The recent development of super-resolution microscopy has allowed repeated imaging of dendritic spines with a resolution that can capture even fine structures such as spine necks or branched spines (voxel of size $\sim$50 $\times$ $\sim$50 $\times$ $\sim$50 nm Pfeiffer et al., 2018; Velicky et al., 2022). However, super-resolution imaging is not easily employed *in vivo*, and often does not work well in concert with certain other techniques, e.g. some optogenetic constructs (Pfeiffer et al., 2018).

To address the need for automated spine detection in super-resolution image data, in the future, efforts should be made to extend the framework of DeepD3 to data of this image modality as well. Moreover, it could be assessed whether deep-learning allows for detection of dendritic spines beyond the resolution limit of the image. For example, the same region of interest could be imaged with two-photon and super-resolution imaging techniques, similar to a study by Pfeiffer and colleagues (2018). Then, a deep neural network could be trained to segment dendritic spines in two-photon images using the super-resolution images as ground-truth. This particular use of deep learning has recently been utilized to enable ultrastructural studies in living tissue (Velicky et al., 2022). Here, a region of interest was imaged twice, once each with high and low signal-to-noise. The authors then trained a deep neural network to improve image quality using the high signal-to-noise image as the ground truth. This enabled the authors to repeatedly image the same region of interest with relatively low irradiance, thereby preventing phototoxicity within the image region. The resulting images originally had a relatively poor signal-to-noise ratio, but due to the deep neural network, image quality could be improved post hoc. As a consequence, for the first

time, living neuronal tissue could be imaged repeatedly with ultrastructural resolution using super-resolution shadow imaging (Velicky et al., 2022).

Currently, DeepD3 is trained on mostly unprocessed data. On the one hand, this improves applicability, as raw images can simply be fed to DeepD3 without additional steps. On the other hand, it is more challenging to accurately detect dendrites and dendritic spines in unprocessed data. Hence, preprocessing, such as image deconvolution, z-smear correction, spatial and/or more complex filters (Koh et al., 2002; Zhang et al., 2010; Dumitriu, Rodriguez, & Morrison, 2011) could improve signal-to-noise ratio of images, and thus improve DeepD3 performance even further. It is conceivable that preprocessing of input images might also help in detection of dendritic spines beyond the resolution limit of the image. Hence, while necessary preprocessing steps might limit the applicability of DeepD3, such means might be necessary to improve the automated detection beyond the resolution of the two-photon input image. In the future, it should be explored whether preprocessing could improve the performance of DeepD3.

4.2.2 Issues with manual quantification of dendritic spine abundance

In the last two decades, dendritic spines have been at the focus of linking synaptic changes to neuronal functioning and/or behavioral features (Hofer et al., 2009; Kasai et al., 2010; Moczulska et al., 2013; Frank et al., 2018). To quantify changes in synaptic architecture, typically spine density or stability are tracked over time. This is done by manually counting or annotating dendritic spines in a region of interest. However, this method of quantification, which is the current gold standard, shows significant amounts of variability: in the data for this dissertation, average precision was 85% *in vitro* and 63 % *in vivo*, indicating that, depending on the type of data, close to 40 % of dendritic spines were differentially annotated. So far, no comprehensive study investigating spine annotation variability is available. The measurements here were obtained by comparing several annotators (n = 6 and 7 for *in vivo* and *in vitro* data, respectively). However, it is conceivable that using an even higher number of annotators would result in a more precise estimate of inter-annotator spine counting variability. This estimate has so far been lacking, and is critical as a comparison to automated means of quantifying

dendritic spine abundance.

Given the variability reported here, the noise levels introduced by manual annotation of dendritic spines could rival the changes typically seen in spine density (Attardo, Fitzgerald, & Schnitzer, 2015; Pfeiffer et al., 2018) or spine stability measurements (Frank et al., 2018). In some cases, a second annotator was used to independently confirm spine measurements (Frank et al., 2018). While this is good practice, it (A) is rarely done in most reports, and (B) does not eliminate the risk of erroneous spine annotation entirely. One additional factor that could contribute to inter-rater variability is the influence of annotation criteria on users. The results here were obtained by instructing annotators to use the same set of criteria. However, criteria vary between institutions, projects, and laboratories. The most frequent difference is the in- or exclusion of filopodia and dendritic spines that grow orthogonally to the imaging plane. Taking this into account, the variability between annotators could surpass the levels reported here. Interestingly, even the same annotators, tasked to identify dendritic spines in the same image showed considerable (intra-annotator) variability: approximately 15 % of dendritic spines were not identically annotated by the same person weeks later. The small sample size of annotators (n = 2) prevents definitive conclusions concerning intra-annotator variability in this work. Nevertheless, it seems that the outcomes of studies involving quantification of dendritic spine counts might depend not only on who performs the manual annotation, but also on history effects. These biases limit the generalizability and reproducibility of such studies.

4.2.3 Automated approaches of dendritic spine abundance quantification

The above mentioned issues have been discussed in a number of papers over the years (Koh & Lindquist, 2001; Mancuso et al., 2013; Xiao et al., 2018). Accordingly, and to circumvent these shortcomings, automated and semi-automated means of quantifying spine numbers have been attempted. Early approaches relied on image preprocessing and mathematical means to identify spines in images. Typically, the first step was to define a dendritic skeleton or trace using various preprocessing steps (Koh & Lindquist, 2001; Koh et al., 2002; Rodriguez et al., 2008; Shi, Huang, & Hong, 2014). The

second step, the identification of dendritic spines, varies between methods: in some, this is performed in a series of steps, involving estimations of spine length, spine head width, dendrite thickness, and the spine orientation angle (Koh & Lindquist, 2001; Koh et al., 2002). Others have used skeletonization to also identify dendritic spines automatically (Fan et al., 2009). Further image processing (e.g. wavelet transformations or calculation of a Hessian matrix) have also been used to better identify dendritic spines (Fan et al., 2009; Shi, Huang, & Hong, 2014; Singh et al., 2017a). Computationally more intricate methods, such as calculations of vector fields (Zhang et al., 2010) or definition of adaptive local binary fitting energy functions (Fan et al., 2009), have also been reported.

In their respective reports, these automated methods of spine detection typically perform well when compared to manually annotated data (typical sensitivity >85 %). However, several limitations should be kept in mind when evaluating automated methods of spine detection. Most of these methods depend on user-defined parameters (e.g. thresholds or minimal distances). Some parameters, such as the pixel/voxel size, will likely have to be provided by the user, irrespective of the method used. However, thresholds that depend on intensity values of a given image are frequently subjectively chosen and have to be adapted when analyzing different images. Such user intervention means that some approaches automate certain aspects of spine identification but do not provide fully automated spine annotations per se. In an effort to combat erroneous spine identification, most tools allow for manual cleaning of spurious annotations, either between steps of the spine prediction process or at the end. While this is an important and valuable feature of these methods, it should be kept in mind that spine identification then still relies on human annotation, and hence takes away from the automation of spine detection. Typically, manual editing constitutes the bottleneck of image segmentation (Peng et al., 2011). Hence, a trade-off between accuracy and amount of user-involvement is likely unavoidable, and should be chosen based on the experiment at hand.

4.2.4 The lack of a benchmark dataset for dendritic spine detection

The performance of the above mentioned methods for automated spine detection is typically compared to the annotations of a single annotator. As discussed above, manual annotations are inherently subjective, and hence evaluation of methods should be done with annotations of multiple users. Moreover, annotated test data is typically homogeneous, with images sharing identical pixel sizes, similar signal-to-noise ratios, cell types and microscopy types. Moreover, test data usually comprises a few hundred spines at most, raising concerns about generalizability (Koh & Lindquist, 2001; Zhang et al., 2007; Cheng et al., 2007; Fan et al., 2009). After all, spiny neurons typically have at least 1.000, and sometimes > 10.000 dendritic spines. The evaluation on homogenous data is reminiscent of the specialized networks trained here, which work well for certain data types but fail to be applicable in more heterogeneous data. This means that the applicability of many of these previous methods is limited by the image quality of the data. Indeed, many of the above mentioned methods have not seen extensive use in the past, despite being freely available.

A general issue when comparing methods of automated spine detection is the lack of publicly available annotated structural images of dendritic spines - a benchmark dataset. In fact, only two small datasets were found that were publicly available (Ghani et al., 2017; Smirnov, Garrett, & Yasuda, 2018). DeepD3 was tested against one of the two datasets (Smirnov, Garrett, & Yasuda, 2018) and performed well (recall >0.9). However, closer inspection of this dataset revealed that annotation was not complete, with many dendritic spines remaining not manually annotated. Sparse annotations complicate evaluation of automated approaches, as annotations are typically required as ground-truth measurements to evaluate performance of such methods. The other public dataset had several desirable features (Ghani et al., 2017): first, spines were annotated in a pixel-wise manner. This, in principle, allows for more detailed analysis, such as quantification of segmentation performance. Second, the dataset contained images of various pixel sizes, which could be utilized to quantify performance of automated methods in more diverse data. However, this dataset proved to be even more sparsely annotated (only 1 spine per image annotated). Consequently, DeepD3 performance on this data was not evaluated. Despite ever improving methods for structural

spine imaging and the growing number of data storage platforms, raw images of dendritic spines and their annotations are either not available or only available upon request. This seriously hampers the possibility for further development or evaluation of methods for automated spine or dendrite detection. With the publication of DeepD3, all training and test data will be made publicly available, generating - for the first time - an extensive dataset that can be used to improve, test or cross-validate other methods of spine detection. This dataset comprises imaging data of various image qualities, cell types, and imaging modalities.

Along with this dataset, a module is currently being developed that allows users to generate their own models (generalized or specialized) utilizing segmented images from the DeepD3 dataset or their own. It is clear that for some applications, a general method would be advantageous. However, in many experiments, image data is homogeneous in terms of signal-to-noise ratio and pixel size. This is the underlying reason why most approaches so far have not been cross-validated in other datasets. DeepD3 will, in future releases, also allow users to use specialized models that perform according to the user's experimental needs. The generated models can then also be openly shared, growing the options available for users over time.

4.2.5 Quantification of synapses

Only an insignificant proportion of dendritic spines are not structurally connected to a presynaptic bouton (Petrak, Harris, & Kirov, 2005; Wilke et al., 2013) and most excitatory synapses are located at dendritic spines (Berry & Nedivi, 2017). As a consequence, dendritic spines are frequently taken as a proxy for excitatory synapses. Quantifying synapses, their turnover and connectivity this way does not require synapse-specific markers or other tools. Instead, a neuron can simply be intracellularly filled or labeled with a dye and subsequently morphologically visualized. However, attempts have been made to quantify synapses not via identification of dendritic spines, but rather utilizing synaptic markers (Kim et al., 2012; Kuljis et al., 2019; Perez-Alvarez et al., 2020). For example, by reconstituting GFP molecules across the synaptic cleft (mGRASP), individual synapses were visualized as green fluorescent punctae (Kim et al., 2012; Feng, Zhao, & Kim, 2012; Feng et al., 2014). mGRASP images circumvent the requirement to separate spine from dendrite signal, as only the synapse itself is marked. This is exploited in

subsequent data analysis, where synapses are automatically detected using simple thresholding, watershed segmentation, and/or more computationally involved variational Bayesian Gaussian mixture models (Kim et al., 2012; Feng, Zhao, & Kim, 2012). However, spurious fluorescence sources (non-specific trafficking or auto-fluorescence artifacts) can be wrongly labeled as synapses using these methods.

Hence, while mGRASP should in principle constitute an elegant way to identify structural synapses, widespread use is currently lacking, as reports using this approach so far are scarce (Druckmann et al., 2014; Song et al., 2018; Choi et al., 2018; Mukherjee et al., 2021). Others have equipped proteins that are localized postsynaptically with fluorescent tags, thereby visualizing synapses (Kuljis et al., 2019; Perez-Alvarez et al., 2020; Graves et al., 2021). These tags also produce fluorescent punctae, similar to the ones observed when using mGRASP. Accordingly, automated identification methods similar to the mGRASP methods described above were employed, utilizing segmentation based on shape (Kuljis et al., 2019; Perez-Alvarez et al., 2020) and/or a series of criteria (Graves et al., 2021). Interestingly, one of these reports, in which AMPA receptors tagged with a fluorophore were endogenously expressed *in vivo*, also attempted automated signal detection using machine learning (Graves et al., 2021). They, too, compared the congruence of two expert annotators and found that disagreement was large (<75 % of synapses annotated in agreement). Their automated approach performed more reliably compared to human annotation (>80 % of synapses annotated in agreement). However, here, again, auto-fluorescence artifacts might have contributed to the reliability of the method. Moreover, as seen by the high inter-rater variability in this dissertation, two expert annotators might have not been sufficient to identify which punctae were synapses and which not. Despite this large variability, the automated detection outperforms human annotation in terms of reliability. Given that the report is recent, the usefulness of this approach to the field remains to be seen. After all, approximately 20 % of all synapses could not be uniquely identified. This might be a limitation of the molecular approach and consequently the image quality, rather than the machine learning approach employed to automatically detect synapses. Nevertheless, so far, DeepD3 spine detection seems to outperform automated approaches of synapse detection (recall of DeepD3 >85 % in almost all datasets, with recall reaching up to 96 %). In the future, a dataset should be acquired to directly compare DeepD3 to automatic

synapse detection approaches.

4.2.6 Image segmentation of dendritic spines

Approaches of synapse detection employ image segmentation methods, in which individual pixels are assigned to categories, either via outlining synapses or creating a binary mask for them. This is a particularly useful approach, as it allows for measurements beyond just counting synapses, such as synaptic size for example. Similarly, in the past, measurements of dendritic spines apart from spine density and stability have been performed: for example, historically, spines have been stratified into morphological categories according to their shape. Categories included filopodia (long and thin protrusions without a bulbous head), thin spines (spines with a small head), mushroom spines (large protrusions with a large head and thin neck), stubby spines (spines without a spine neck), and branched spines (two or more spine heads that share a common spine neck). Categorization is typically performed by visual inspection. To automate this task and sort spines into categories, mere detection of dendritic spines is not sufficient. Instead, spines are segmented in image data, and according to the shape of the segmentation, assigned to a category. DeepD3's segmentation lends itself for this type of analysis. However, despite widespread use of this type of classification, a recent electron microscopy study has raised concerns about categorization of dendritic spines: morphological features seemed to vary along a unimodal distribution with no identifiable morphological subtypes evident (Ofer et al., 2022).

Nevertheless, segmentation of spines in 2D and 3D light imaging data allows for extraction of other, morphologically relevant features of dendritic spines. For example, the size of the spine head can be estimated, a measurement known to be correlated to synaptic strength (Holler et al., 2021). Moreover, segmentation of dendritic spines allows for fluorescence analyses, such as detection of postsynaptic markers, or measurement of calcium transients. DeepD3 performs full segmentation of dendrites and dendritic spines in input data, and hence enables these types of analyses at large scales. Spine counting is an arduous task, however, manual segmentation of dendritic spines, particularly in 3D, is much more time-intensive. DeepD3 performs this task in an automated fashion on large images rapidly. For example, a $\sim$ 500 MB image is fully processed in under 10 minutes, a process that would require 5 - 7 hours if done manually. In light of this amount of manual work, others

have attempted to automate this process in the past. Some of the above mentioned methods for automatic counting of dendritic spines also provide pixel-wise segmentation (Koh & Lindquist, 2001; Rodriguez et al., 2008; Shi, Huang, & Hong, 2014). Typically, segmentation was then utilized for spine classification, which was generally high (75 - >90 % agreement), but depended on the number of spine subtypes (between 80 and 92 % agreement Shi, Huang, & Hong, 2014). Pixel-wise performance is not reported for these methods.

Commercial products, such as Imaris, Neurolucida 360 or NeuronStudio also offer spine segmentation in image data (Wearne et al., 2005; Swanger et al., 2011). However, the respective companies have not published reports on the accuracy of their tools. Fortunately, performances of NeuronStudio and Neurolucida 360 have been recently compared in a small sample (Xiao et al., 2017), however, both tools had a precision of ≤ 0.5, indicating that up to 50 % of detected spines were false positives. While Imaris currently lacks quantitative assessment of its performance, according to qualitative assessment of one report, it fails to capture dendritic spines accurately (Basu et al., 2018). Imaris offers manual user corrections to more accurately segment dendritic spines, however, this again involves extensive manual time investment from the user.

With the advent of deep learning in image segmentation in the last years, two additional tools have been reported (Xiao et al., 2017; Vidaurre-Gallart et al., 2022). In the first approach, spine segmentation was attempted in two dimensional maximum intensity projections of images (Xiao et al., 2017). This tool proved superior to NeuronStudio and Neurolucida 360 in terms of spine detection. However, again, pixel-wise performance was not quantified. Moreover, this tool is not open source and hence has not been used so far by other groups in the field. Recently, Vidaurre-Gallart and colleages developed another tool, which segments spines in 3D (Vidaurre-Gallart et al., 2022). This tool was trained on a large, homogeneous dataset, acquired via confocal imaging, that had a very high signal-to-noise ratio (Benavides-Piccione et al., 2013; Vidaurre-Gallart et al., 2022). With reported F1 scores between 68 to 77 % the performance of the tool seemed promising. However, DeepD3 seemed to perform better in image data that was obtained via two-photon microscopy (Fig. S3.2.4A-E). Notably, the data DeepD3 was trained on mostly

had lower signal-to-noise ratios than the training data of Vidaurre-Gallart et al. (2022). Hence, DeepD3 might have been better equipped to deal with the relatively low signal-to-noise ratio of the image displayed in Fig. S3.2.4. The networks of Vidaurre-Gallart et al. are reminiscent of the specialized networks that were trained in this dissertation. The performance of these models were still good, but only in data that was similar to the training data in terms of pixel size and signal-to-noise ratio. Hence, the homogeneous training dataset used by Vidaurre-Gallart and colleagues might limit the generalizability of the method to other data. This is not explored in the report, as their method was never cross-validated against other data or data that had been annotated by multiple users. Hence, while this method might achieve segmentation as accurate as, or potentially more accurately than DeepD3 in image data with very high quality, its usability beyond this type of data is questionable.

In summary, DeepD3 was more extensively validated than any other tool available so far. It performs well in identifying dendritic spines in image data with heterogeneous image quality and spines are successfully segmented in the data, enabling further analyses beyond spine count or spine density measurements.

4.2.7 The need for high throughput methods for spines quantification

In order to understand the intricate network dynamics of the brain, ever increasing amounts of neurons are recorded from simultaneously, utilizing modern microscopy or electrophysiological methods such as Neuropixel probes or light beads microscopy (Jun et al., 2017; Demas et al., 2021b; Steinmetz et al., 2021). However, a similar trend in quantifying synaptic dynamics has been missing. Typically, only dozens of dendritic spines are tracked per neuron in most reports (Scholl, Wilson, & Fitzpatrick, 2017; Frank et al., 2018). Given that neurons have between 1.000 and 30.000 synaptic connections (Ichikawa et al., 1993; Megıas et al., 2001), and studies typically characterize 100-300 dendritic spines per neuron (Wilson et al., 2016; Iacaruso, Gasler, & Hofer, 2017), appropriate sampling remains challenging. Moreover, in certain experimental paradigms, not the total number of spines, but rather the emergence or loss of dendritic spines is of critical interest. In these cases, the number

of gained or lost spines is typically below 30 spines per cell (Coneva, 2015; Frank et al., 2018). Recently, it has been argued that some neurons are functionally driven by many small, clustered and functionally similar synapses (Scholl et al., 2021). This re-emphasizes that sufficient sampling of dendritic spines is critical to understand neuronal function. In other words, hotspots of dendritic turnover can only be captured with good sampling, and if certain areas are under-represented, erroneous conclusions are more likely to occur. In this context, DeepD3 should address the current need for high throughput spine analysis methods. While it performs on par with human spine annotation in terms of reliability, the main advantage is its speed in segmenting image data: it is possible to segment dozens of gigabytes of data per day, an undertaking that would require months or years if done manually. This also allows researchers to quantify spines not only in dendritic regions of choice, mostly belonging to individual neurons, but rather agnostically across much larger regions of interest. This should critically improve the number of spines that are quantified per cell/animal.

4.2.8 Biases of DeepD3 and other automated spine detection methods

While automated methods of spine detection provide means of rapidly quantifying large amounts of data, such approaches can also introduce systematic biases to the subsequent analyses. Several of such biases could arise from the imaging data itself. For example, it is likely that large dendritic spines are more reliably detected given the number of pixels and intensities of such spines is typically higher. Small spines can sometimes be hardly resolved by non-super-resolution light microscopy techniques, and therefore should be more difficult to detect. Similarly, spine necks and dendritic spines that grow perpendicular to the imaging plane are typically difficult to resolve, and as a consequence, might be less likely to be segmented accurately. Lastly, spines in close proximity to each other provide lower contrast boundaries and could therefore also be more challenging to segment correctly.

Additional biases might arise from the training data, as deep learning techniques critically depend on the quality of annotations in the training data

(Kim et al., 2019). Although the training data for DeepD3 is extensive, it was generated by annotations of three annotators, with the majority stemming from one. Additionally, all training images were always only annotated once, which could introduce more lingering biases that only occur when segmenting certain types of images. In general, in light of the observed amounts of variability, the question of how reliable manual annotation of few users is and how well an automated approach can perform on a pixel-per-pixel basis remains unclear. It is certainly possible that DeepD3 performs dendrite and spine segmentation in a biased manner. In many deep-learning methods, such as face recognition (Acien et al., 2018; Wang & Deng, 2020), speech classification (Mozafari, Farahbakhsh, & Crespi, 2020), or biomedical applications (Dias & Torkamani, 2019; Cirillo et al., 2020), such biases have been found in the past. In the future, DeepD3 performance should be assessed in additional published datasets that have been manually annotated. Such efforts could give insight into potential biases that might be present in the current version of DeepD3. Further analyses would then be needed to correct for such biases.

4.2.9 Conclusions and outlook

The second section of this dissertation deals with the development of DeepD3, a deep-learning tool for the automated detection and segmentation of dendrites and dendritic spines. Automatically generated image segmentation was utilized to identify dendritic spines across a variety of datasets, showing that DeepD3 performed on par with human annotations, the current gold standard. Critically, DeepD3 performed segmentation orders of magnitude faster than human annotators. Both, fluorescence extraction could be performed reliably in 2D and 3D data.

One feature that is currently lacking in the DeepD3 framework is the option to match spines over time. As a consequence, analyses involving spine turnover can currently not be automated using this tool. Since this is at the core of many investigations involving imaging of dendritic spines, this feature should be incorporated in future versions of DeepD3 or other automated spine detection methods. This is a challenging undertaking for several reasons. First, image-to-image registration of large 3D volumes is essential to match dendritic spines (Fan et al., 2009; Mancuso et al., 2013). However, if annotation and/or matching is done manually, pixel-resolution registration is

not required. Automated methods, however, would require particularly well-registered image volumes - a challenging undertaking of its own (Qu, Long, & Peng, 2014; Haskins, Kruger, & Yan, 2020) - to automatically match dendritic spines across time points. Moreover, even in perfectly registered data, spines cannot be easily matched due to their extensive motility (Dailey & Smith, 1996; Majewska, Tashiro, & Yuste, 2000; Dunaevsky et al., 2001; Bonhoeffer & Yuste, 2002). Spine motility is typically manifested by changes in spine head volume or location (Fischer et al., 1998; Dunaevsky et al., 1999). To circumvent this problem, the base of the spine could be identified. Here again, the resolution limit of two-photon and confocal imaging complicates such an identification, as frequently spine necks or bases are not visible in images stemming from these modalities. However, a DNN could be trained to localize the spine base by complementing such imaging techniques with super-resolution or electron microscopy data. Given a sufficiently accurate network prediction performance, spines could then be matched based on the location of the spine base, not their spine head. Potentially, spine density limits the applicability of this approach, as with increasing density spine bases also lie in closer proximity. Consequently, it is conceivable that there is an upper limit of spine density in which this approach works. Experimental evidence is required to establish whether this is the case, and at which spine density levels such an approach would stop performing reliably. Hence, in the future, a further developed version of DeepD3 could then not only alleviate the time spent on spine annotations, but also perform spine matching to allow neuroscientists to fully automatically and rapidly assess spine dynamics in large datasets.

4.3 Towards establishing wiring rules during LTP-induced synaptogenesis

The goal of this project was to establish an assay to identify the functional connectivity rules governing LTP-induced spinogenesis. This section will present the efforts towards that goal. Neurons undergoing LTP have been shown to grow new dendritic spines (Engert & Bonhoeffer, 1999; Maletic-Savatic, Malinow, & Svoboda, 1999; Toni et al., 1999), which form functional synapses rapidly after formation (Nägerl et al., 2007; Zito et al., 2009; Hill & Zito, 2013). However, the wiring rules these LTP-induced synapses follow, and hence their potential involvement in the maintenance of LTP, remain elusive. The main goal of the research presented here was to improve upon an existing assay to map functional synaptogenesis following LTP *in vitro* (Coneva, 2015). This was achieved in a number of enhancements. In particular, methodological changes boosted the throughput of the assay several-fold, critically enabling functional characterization of hundreds to thousands of dendritic spines. Moreover, a molecular approach to map spine maturity was implemented as a first step towards identifying a sub-population of newly grown dendritic spines that lack the proteomic machinery of a functional synapse. This sub-population of dendritic spines poses a potential confounder when evaluating functional connectivity rules of LTP-induced spines. Lastly, a series of computational and pharmacological approaches to determine synaptic connectivity of single spines in the presence of dendritic calcium spikes were evaluated.

4.3.1 Previous efforts

Since the discovery that new dendritic spines grow during LTP (Engert & Bonhoeffer, 1999), several reports have provided insights into whether, how, and with which cells new synapses are established. The first question was quickly answered: as hypothesized by Engert and Bonhoeffer in 1999, LTP-induced dendritic spines form functional synapses rapidly after outgrowth (Toni et al., 1999; Knott et al., 2006; Nägerl et al., 2007; Coneva, 2015). Accounts on the time-course of functionalization vary, with some reports indicating that establishment of functional synapses happens within minutes of spine outgrowh (Coneva, 2015), while others state that it could take 15 or more hours (Nägerl et al., 2007). Much less is known about *how* den-

dritic spines are functionalized. In the past, it has been shown that the mere presence of elevated glutamate levels near a dendrite can elicit spine outgrowth (Kwon & Sabatini, 2011). However, others have found that AMPA and NMDA receptors localize to the postsynaptic sites during developmental synaptogenesis, even in the absence of glutamatergic receptor activation (Cottrell et al., 2000). Additionally, several molecular players, such as cadherins and neuroligins, have been found to be critical for activity-dependent synaptogenesis (Bozdagi et al., 2000; Garner et al., 2002; Kwon et al., 2012). Others have emphasized the role of local astrocytes in this process (Ullian, Christopherson, & Barres, 2004; Muthukumar, Stork, & Freeman, 2014). Taken together, so far, it is unclear how LTP-induced functional synaptogenesis is organized on a molecular level.

Ultrastructural accounts

Two reports have attempted to shed light on the third question: which presynaptic inputs are chosen when establishing new synapses after LTP? In an electron microscopy study, Toni and colleages provided critical insights (1999): new dendritic spines seemed to grow and rapidly form functional synapses with boutons after LTP (within 45 - 60 min; Toni et al., 1999). Another ultrastructural study later confirmed this discovery (Nägerl et al., 2007), albeit finding that functional synaptogenesis took much longer than previously stated ($\geq$15 h). Interestingly, Toni and colleagues found that axonal boutons were frequently targeted by two dendritic spines originating from the same dendrite after LTP, a phenomenon that is rare under baseline conditions (Toni et al., 1999; reproduced in Knott et al., 2006). Using a marker for calcium entry into spines, it was shown that the majority of these spine pairs seemed to be functionally connected to the axonal bouton. Consequently, LTP seems to lead to the duplication of certain synapses.

While it seems that this already answers the question of functional connectivity rules of synaptogenesis following LTP, there are several shortcomings:

First, due to the low throughput of 3D electron microscopy studies at the time, the number of spines investigated in this report is low. 25 boutons with contacting spine pairs were found, of which 15 had spine pairs originating from the same dendrite. Moreover, only 9 of these 15 spine pairs showed sig-

nificant amounts of calcium precipitate, the proxy for functional connectivity (see below). While this report provides invaluable insights into the structural underpinnings of LTP, such sparse sampling is likely not representative of the functional changes of a hippocampal neuron during LTP.

The second caveat is the method used for assessing functional connectivity. Toni and colleagues employed a protocol using brief but intense presynaptic stimulation just before fixation of the tissue. This should cause calcium to only be present in dendritic spines that are functionally connected to stimulated axonal boutons. During fixation, calcium was then precipitated via a chemical reaction, such that precipitates could be localized in the subsequent electron microscopy imaging (Buchs et al., 1994; Toni et al., 1999). However, given the substantial time between stimulation and fixation (5 minutes), it is possible that this is not a representative measure of functional connectivity. It has been shown in the past that, following presynaptic stimulation, some dendritic spines - in contrast to dendrites - have elevated levels of intracellular calcium (Müller & Connor, 1991). However, regenerative dendritic calcium events are frequently observed in hippocampal neurons (Antic et al., 2010; Sheffield, Adoff, & Dombeck, 2017), and such events can also increase intracellular calcium levels in dendrites and spines up to several minutes (Guthrie, Segal, & Kater, 1991). Such events have been found to occur frequently in response to intense presynaptic stimulation and typically flood all dendritic spines, irrespective of whether synaptic transmission occurred or not (Helmchen et al., 1999; Grienberger, Chen, & Konnerth, 2014; Coneva, 2015). Hence, a proportion of spines in the report by Toni and colleagues 1999 might have been falsely identified as synaptically connected, since the spines' calcium precipitates originated not from previous synaptic input but rather dendritic calcium spikes.

Lastly, screening for boutons contacted by two dendritic spines only 60 minutes after LTP induction represents a selection bias. In particular, dendritic spines that contact axons in places where no axonal bouton has formed would be missed. Moreover, all filopodia and immature dendritic spines were omitted during their analysis. Hence, given that many LTP-induced dendritic spines need more than 60 minutes to form a functional synapse with a presynaptic partner (Nägerl et al., 2007; Coneva, 2015), functional synaptogenesis could not be properly assessed. Consequently, by excluding certain types of LTP-induced spines, the underlying wiring rule cannot be determined. Taken

together, the observation that some newly grown dendritic spines contact previously active axonal boutons should not be seen as evidence for a Hebbian wiring rule, as other newly-grown spines might contact other presynaptic boutons. Consequently, which wiring rule applies to LTP-induced synaptogenesis remains entirely elusive to this day.

Recently, another ultrastructural study investigated a closely related question: how do dendritic spines that grow during learning get functionally integrated into the synaptic network (Hedrick et al., 2022). By combining two-photon imaging of glutamate transients and electron microscopy in the same dendritic spines, Hedrick and colleagues were able to confirm a number of past observations: first, new dendritic spines grow in cortical pyramidal neurons during experience-dependent plasticity paradigms (Hofer et al., 2009; Xu et al., 2009). Second, plasticity at dendritic spines induces local heterosynaptic priming effects for synaptogenesis and future plasticity events (Kwon & Sabatini, 2011; Murakoshi, Wang, & Yasuda, 2011; Hedrick et al., 2016). Third, new spines seem to be grouped in spatially confined functional clusters (Frank et al., 2018; De Roo, Klauser, & Muller, 2008; Fu et al., 2012). Fourth, synaptogenesis seems to happen primarily via filopodial search of boutons in the vicinity (Niell, Meyer, & Smith, 2004; Toni et al., 2007). Interestingly, such synaptogenesis intially is found on multisynaptic boutons, similar to what has been described by Toni and colleagues 1999. Later on, however, such multisynaptic boutons are rarely found, indicating that either one postsynaptic compartment is eliminated or the presynapse is split.

Given the detailed characterization of structure and function of newly-formed dendritic spines, Hedrick and colleagues were also able to investigate a number of new research avenues. Critically, they found that the majority of new dendritic spines seemed to functionally be related to the task, as activity patterns matched those spines that were active during learning of the lever press task (Hedrick et al., 2022). Moreover, the movement required to perform the task was improved when newly-grown dendritic spines were active, indicating that they might contribute to the learned behavior. Lastly, they found an unexpected connectivity rule, namely that newly-formed dendritic spines seemed to preferentially target boutons of those axons that were involved in the task but had no pre-existing functional connection with the postsynaptic neuron (Hedrick et al., 2022). Taken together, this study not

only recapitulates fundamental findings of past efforts, it also shed light on how functional connectivity rules of synaptogenesis work in the motor cortex of mice.

While generally investigating similar biological phenomena, it is necessary to point out several key differences between the study by Hedrick et al. 2022 and the assay proposed in this dissertation. First, while it is believed that experience-dependent plasticity paradigms typically involve LTP, and certain aspects of such paradigms can be reproduced by inducing LTP (Nabavi et al., 2014; Jeong et al., 2021), they are two distinct processes. This is particularly evident as experience-dependent plasticity paradigms are utilized with living animals, where a multitude of complex measureable and non-measureable phenomena occur. One of the technical issues with correlated two-photon microscopy and EM is the low throughput. Hedrick et al. 2022 made a substantial effort in this regard and included imaging regions of four animals in their EM dataset. However, this still only yielded a total of 289 functionally and ultrastructurally analyzed spines, of which 24 grew in during the learning of the motor task. As discussed (see Discussion 4.2.7), throughput is an essential component when describing rules governing functional connectivity. Another issue in the establishment of the connectivity rule by Hedrick et al. 2022 was the volume of the EM sample, reportedly <1mm x <1mm x 150-300 µm . It is likely that some axons in this volume originated from the same cell but could not be identified such in the EM volume. This could confound the wiring rule that Hedrick et al. 2022 found (newly-formed dendritic spines preferentially target axons that were involved in the task but had no pre-existing functional connection with the postsynaptic neuron). Taken together, while the study by Hedrick et al. 2022 provides further invaluable insights into the functional connectivity rules governing learning, the answer to the question of, which wiring rule applies to LTP-induced synaptogenesis remains elusive to this day.

A previous assay to map functional connectivity in LTP-induced spines

In an attempt to investigate the time-course of spine functionalization following LTP and its underlying wiring rule, Coneva developed the original

variant of the proposed assay (Coneva, 2015). Functional synaptogenesis following LTP seemed to occur rapidly, sometimes even within minutes of spine outgrowth. LTP-induced-, in contrast to spontaneously emerged, dendritic spines preferentially formed functional synapses with LTP-driving axonal boutons (64 % vs. 11 % Coneva, 2015), pointing towards an input-specific wiring rule. However, several shortcomings of the original assay required addressing to conclusively establish the wiring rules governing LTP-induced synaptogenesis. The results reported in this dissertation were aimed at improving some of these shortcomings, and to work towards an experimental design that tackles the question driving this project.

One critical step of the assay is the establishment of functional connectivity of all recorded dendritic spines via calcium imaging. Dendritic calcium spikes, large increases in cytosolic calcium levels in response to strong input, occur frequently. Such events mask which spines received synaptic input by flooding all dendritic spines with calcium from the dendrite. In the report by Coneva, functional connectivity of dendritic spines was established using a computational approach that utilizes temporal unmixing of spine and dendrite events (2015). In this dissertation, this approach was thoroughly tested on a dataset in which the same dendritic spines were either flooded with calcium (dendritic calcium spike) or single spines were responsive to presynaptic stimulation. The temporal unmixing approach was unable to identify which spines were synaptically connected to stimulated boutons during dendritic calcium spikes. Moreover, compared to data showing single-spine responsiveness, roughly three times as many dendritic spines were identified as responsive using this approach. Notably, in the report by Coneva, imaging data containing dendritic calcium spikes were not omitted from analysis. Hence, it is feasible that a proportion of spines identified as connected to LTP-inducing boutons were, in fact, not synaptically wired in that way. While there are certain differences, such as a different calcium indicator, between the approach by Coneva and one presented here, it is unlikely that these differences would affect the temporal aspect of dendritic calcium spikes. In fact, the calcium indicator used here (GCaMP7b) has a faster half-rise time than the one utilized by Coneva (GCaMP6s; 2015), which excludes indicator kinematics as a potential confounder (Dana et al., 2019). Additionally, when assessing the spread of calcium through the majority of a CA1 pyramidal neuron's dendritic length, no distinct pattern of calcium wave propagation could be observed, even at very high temporal resolution (∼300 Hz). This

indicates temporal unmixing of spines that receive synaptic input from regenerative dendritic calcium events might not be possible given the imaging frequency used here, or by Coneva (∼60 Hz Coneva, 2015).

Investigations into the time-course of spinogenesis have typically suffered from low throughput (De Roo et al., 2008; Perez-Alvarez et al., 2020). This also applies to the report of Coneva (Coneva, 2015): for example, only 33 LTP-induced dendritic spines across 9 cells could be functionally tracked in all experiments. Moreover, while pre-existing spines could be structurally monitored in much greater quantities (n >1000 spines across 9 cells), the functional connectivity of only a very small fraction of all dendritic spines could be assessed (n ≈11 spines per cell, compared to several thousand spines per CA1 pyramidal neuron). This highlights the critical need for improving the throughput of the assay, as only a fraction of all dendritic spines from each CA1 neuron could be characterized functionally. In this dissertation, it was shown that the throughput of the assay could be improved considerably by employing volumetric Bessel beam imaging, increasing the region of interest tracked throughout the experiment, and utilizing novel methods of automated spine detection (DeepD3; see Results 3.2). This increases the number of dendritic spines that can be functionally characterized per cell to several hundred, and those that can be structurally tracked to over 1000 per cell. Consequently, LTP-induced dendritic spines available for characterization should increase, addressing the low sample size in the previous report.

Occasionally, no dendritic spine grew in response to LTP induction within the imaging field of view in the report by Coneva (2015). In some cases, nearby dendrites were then screened for LTP-induced spines. Critically, the area in which LTP was induced was tethered to the imaging field of view at the time of LTP induction. Due to the limited size of the stimulation area (70 × 70 μm), some of these nearby dendrites resided outside the LTP induction area. Consequently, it is conceivable that some of the observed spinogenesis might not have been LTP-induced, but rather occurred spontaneously. Due to the need to screen nearby dendrites for spinogenesis, sampling from dendritic spines was inhomogenous: some spines were functionally assessed nearly 100 times, others only once (Coneva, 2015). Given the release probability at the Schaffer collateral synapse, at least 5-10 functional measurements should be obtained per spine to definitively characterize functional connectivity. To circumvent the issue of imaging spines outside of the LTP induction area,

and hence ensure homogeneous sampling, two technical improvements could be made: first, increasing the area of presynaptic stimulation during LTP and decoupling it from the imaging area should allow for imaging of several dendritic regions after LTP. This not only guarantees that all functionally characterized dendritic spines are within the LTP induction area, it also boosts throughput as much larger dendritic stretches can be functionally assessed. Second, at the end of the experiment, several dendritic stretches can be functionally assessed multiple times (e.g. 10 times), boosting throughput of the assay and simultaneously ensuring identical repeated recordings of each dendritic spine in all experiments.

Another issue of the previous report is the ambiguity introduced by LTP-induced dendritic spines that remain unresponsive throughout the experiment. Non-responsivity could be interpreted as not being functionally connected to the ChR2-expressing population of boutons that drove LTP induction. Alternatively, an immature, non-functional synapse could have formed between the same or different synaptic partners. While >95 % of pre-existing spines show hallmarks of a mature postsynapse (Arellano et al., 2007a; Nägerl et al., 2007), LTP-induced dendritic spines frequently lack these hallmarks in the first hours after their outgrowth (Nägerl et al., 2007). In the report by Coneva, conflicting results were obtained with respect to determining the wiring rule of LTP-induced dendritic spines: on the one hand, newly grown spines were much more commonly functionally connected to ChR2-expressing boutons when LTP was induced, as opposed to when synaptogenesis happened spontaneously in control conditions (64 % vs. 11 % Coneva, 2015). This could be interpreted as LTP-induced dendritic spines preferentially wiring to LTP-inducing boutons (i.e. a partially Hebbian wiring rule). On the other hand, the wiring of LTP-induced spines was compared to spines that were pre-existing before the induction of LTP. Prior to the onset of optochemical LTP induction, no difference in wiring should exist between boutons that do and those that do not express ChR2. Hence, if the wiring rule LTP-induced dendritic spines follow is partially Hebbian, more LTP-induced spines should be functionally connected to ChR2-expressing boutons than pre-existing spines. However, these two spine populations seemed to be functionally connected to ChR2-expressing boutons at significantly different rates (64 % vs. 55 % Coneva, 2015). A potential explanation for these seemingly conflicting results could be the maturity level of newly grown spines, a critical aspect of the assay that is discussed below.

The importance of spine maturity when assessing functional connectivity in nascent dendritic spines

Whether or not a nascent dendritic spine has the proteomic machinery required for synaptic transmission is critical when assessing functional connectivity. A lack of spine maturity in the original and proposed assays is expressed as the absence of calcium transients in the spine. One possible explanation of the results of Coneva (2015) is that a significant proportion of non-responsive spines was not mature enough to show calcium signaling. This is a potential confounder, as those dendritic spines that have not formed a functional synapse should be omitted from the quantification. With exclusion of immature dendritic spines, the proportion of responsive spines would increase (since the number of non-responsive spines decreased), which could affect both comparisons reported by Coneva (LTP-induced vs. spontaneously grown spines and LTP-induced vs. pre-existing spines; 2015).

In this dissertation, steps were taken to determine spine maturity and consequently address this confounding variable. Using a nanobody against a critical protein in the postsynaptic density, PSD-95, spine maturity could be tracked in thousands of dendritic spines over the course of many days. At the population level, spine maturity was stable. Given that the construct used to visualize spine maturity was over-expressed in single cells, one potential caveat was that over time over-expression artifacts could compromise the localization-specificity of the nanobody. However, an auto-transcriptional control element of the construct ensured that localization occurred at postsynaptic sites across four days.

Spine maturity was distributed unimodally, indicating that using nanobodies against PSD-95 does not allow for a discrete distinction between mature and immature spines. This is in line with previous reports, arguing that spine maturity follows a continuum, rather than separate categories of maturity (Arellano et al., 2007b; Ofer et al., 2021a). Hence, finding a precise cutoff at which spines are mature enough to support synaptically induced postsynaptic calcium transients remains challenging. However, the data analyzed here and previously (Arellano et al., 2007b; Ofer et al., 2021a) mainly consists of pre-existing spines. It is conceivable that LTP-induced spines are more clearly separated in distinct subtypes: previously it has been shown that the presence of PSD-95 stabilizes nascent dendritic spines (Ehrlich et al.,

2007). Moreover, the failure of nascent dendritic spines to acquire sufficient PSD-95 seemingly resulted in spine pruning within 24 hours in most cases (Cane et al., 2014). On the other hand, increased PSD-95 accumulation was positively correlated with spine survival. In the complete version of the proposed assay, the PSD-95 nanobody should be employed to establish whether LTP-induced dendritic spines fall into distinct categories of spine maturity: tracking spines before and after LTP induction and simultaneously quantifying expression levels of the nanobody in LTP-induced dendritic spines should provide insight into how maturity is distributed in this population of spines. Beyond that, spine maturity should be cross-validated by identifying which spine synapses are functional using established tools, such as glutamate uncaging or electron microscopy. These two experiments should clarify whether the nanobody can be used to identify immature LTP-induced dendritic spines and at which nanobody expression level spine maturity can be assumed. As an alternative to the nanobody, other approaches, such as genetic editing of endogenous postsynaptically localized proteins (Willems et al., 2020) could be utilized to assess maturity levels of LTP-induced dendritic spines. Another option would be to use two-photon-guided glutamate uncaging or ultrastructural imaging at the end of the experiment to assess functionality or maturity of synapses.

In conclusion, the assay proposed by Coneva (Coneva, 2015) constitutes the foundation of determining wiring rules of LTP-induced synaptogenesis. In this dissertation, this assay was improved in several ways: Throughput was improved considerably by employing novel microscopy and analysis methods, as well as optimizing the LTP induction area size. Additionally, the previously employed functional connectivity method was evaluated, and shown to be of insufficient accuracy for the determination of functionally connected spines in the shadow of dendritic spikes. Other experimental or computational means are required to precisely determine functional connectivity of all dendritic spines in this assay (see below). Lastly, initial steps were taken to assess spine maturity in order to exclude immature LTP-induced dendritic spines from the analysis.

4.3.2 Computationally determining functional connectivity of dendritic spines in the presence of dendritic calcium spikes

Aside from ultrastructural imaging studies, unambiguous assessments of functional connectivity on a single-spine basis are challenging. The responsiveness criteria used in the original variant of the proposed assay (Coneva, 2015) were shown to not resolve functional responsiveness of individual spines reliably. Therefore, additional computational methods were tested for their ability to discern spines receiving synaptic input from those that are just flooded with calcium during dendritic calcium spikes. Comparing the calcium transients in dendritic spines and nearby dendritic segments was shown to be effective in determining spine responsivity despite the presence of regenerative dendritic calcium events *in vivo* (Chen et al., 2011; Wilson et al., 2016). By subtracting a scaled version of the dendrite's signal from the spine signal, the synaptic input signal could be uncovered. In this dissertation, however, re-identification of previously functionally characterized dendritic spines could not be reliably performed using this approach. This method was originally developed for calcium recordings *in vivo*, where asynchronous inputs are much more frequent. In the experiments performed in this dissertation, it is likely that the absence of action potentials (due to the addition of TTX and 4-AP) and the synchronicity of the calcium responses contributed to the unreliability of the method. In another attempt to resolve single-spine responsiveness in the presence of dendritic calcium spikes, a recently reported deconvolutional approach was tested (Kerlin et al., 2019). In this approach, the electrophysiological underpinning of the dendritic calcium spike is estimated, and subsequently subtracted from the calcium signals of individual spines. However, this method, too, proved unable to reliably determine functional connectivity during dendritic calcium spikes. More advanced/complex methods will be required to determine whether functional connectivity of dendritic spines can be reliably assessed in the proposed assay despite the occurrence of dendritic calcium spikes.

4.3.3 The relevance of dendritic calcium spikes in the proposed assay

The occurrence of dendritic calcium spikes during optogenetic stimulation prevents measurements of synaptic connectivity in spines. Keeping the stimulation power below the threshold of dendritic calcium spike generation throughout the experiment might seem like a possible solution. However, there is evidence that dendritic calcium spikes might be required for the induction of LTP (Golding, Staff, & Spruston, 2002; Kampa, Letzkus, & Stuart, 2006; Brandalise et al., 2016). Additionally, since the input strength increases with LTP, avoidance of such events might not be feasible (Coneva, 2015). In fact, dendritic calcium spikes are frequently observed in CA1 neurons *in vitro* and *in vivo* (Golding et al., 1999; Kovalchuk et al., 2000; Tsay, Dudman, & Siegelbaum, 2007; Grienberger, Chen, & Konnerth, 2014). Nevertheless, it is surprising that these events are so frequently generated in the proposed assay despite the presence of the voltage-gated potassium and sodium channel blockers 4-AP and TTX, as previous findings indicate that blocking other voltage-gated channels should limit the extent of dendritic calcium spread (Jaffe et al., 1992; Regehr & Tank, 1992; Andreasen & Lambert, 1995). One possible explanation is that NMDA receptors might contribute more strongly to the input size in the proposed assay given the low amounts of extracellular magnesium used (0.15 mM, as opposed to 0.89 mM in the cerebrospinal fluid of mice *in vivo*; Sun et al., 2009). This likely renders the majority of NMDARs voltage-independent (Dingledine et al., 1999; Wyllie, Livesey, & Hardingham, 2013), and thus to a large extent, capable of significantly conducting calcium. In the future, it should be investigated whether increasing the concentration of extracellular magnesium could help reduce the probability of dendritic calcium spike generation. Potentially, a balancepoint can be found in which NMDA receptors are still sufficiently activated to trigger LTP, while the occurrence of dendritic calcium spikes is low.

4.3.4 Pharmacological approaches to determine functional connectivity

As mentioned, full suppression of dendritic spikes might interfere with LTP induction. However, an alternative could be to introduce pharmacological

agents at the end of the experiment, long after LTP induction, merely to assess functional connectivity. The potential of this approach was tested in this dissertation. Blocking of voltage-gated calcium channels seemed to not prevent the generation of dendritic calcium spikes, arguing that these events were indeed triggered by NMDA receptor-mediated calcium influx. This is in line with previous accounts of such dendritic calcium events (Schiller et al., 2000; Losonczy & Magee, 2006). Moreover, only very few additional spines were found to be photoresponsive after subtype-specific VGCC block, indicating that the threshold of dendritic calcium spike generation was not shifted to a large extent. This suggests that subtype-specific VGCCs do not seem to contribute much to the generation of dendritic calcium spikes in the proposed assay. This agrees with a previous account, reporting the presence of calcium spikes in the absence of VGCC contribution (Schiller et al., 2000). However, in that report, calcium influx was significantly decreased due to the absence of VGCC opening. In general, VGCCs are thought to play a critical role in the generation of dendritic calcium spikes in pyramidal CA1 neurons (Kovalchuk et al., 2000; Losonczy & Magee, 2006; Grienberger, Chen, & Konnerth, 2014; Wiegert et al., 2018). As mentioned above, the low amount of extracellular magnesium in the experiments of this dissertation might have significantly increased the contribution of NMDA receptors to postsynaptic calcium influx.

In the results deriving from this work, the effects of subtype-unspecifically blocking VGCCs was assessed. In particular D890, a quaternary derivative of methoxy-verapamil (Hescheler et al., 1982) was used. Large amounts of D890 (1 mM) were introduced into single cells via patch-clamp, blocking VGCCs in those cells in a subtype-nonspecific manner (Kovalchuk et al., 2000). This specific localization ensures that presynaptic function remains unaffected, which is not guaranteed with other approaches in which pharmacological agents are provided extracellularly. However, it seemed that dendritic calcium spikes could not be prevented using D890, in contrast to previous reports (Kovalchuk et al., 2000; Grienberger, Chen, & Konnerth, 2014). However, again the composition of the extracellular solution might be responsible for the observed lack of VGCC contribution to dendritic calcium spikes. In the future the viability of D890 in the proposed assay should be further explored. Using higher magnesium concentrations extracellularly in combination with D890 may provide a unique and precise solution to the occurrence of dendritic calcium spikes.

In a separate attempt to pharmacologically disrupt the generation of dendritic calcium spikes, the GABA-A receptor agonist muscimol was used. GABA-A receptor opening decreased the probability of dendritic calcium spike generation as well as the total input strength. This is in line with a report showing that hyperpolarization decreases the occurrence of dendritic calcium spikes (Chen et al., 2011). While the majority of responsive dendritic spines seemed unaffected by the presence of muscimol, ∼30 % became unresponsive after muscimol wash-in. Conversely, many other, previously unresponsive, dendritic spines were rendered photo-responsive upon GABA-A receptor-mediated hyperpolarization, indicating that the threshold of dendritic calcium spike generation had increased. Indeed, after muscimol wash-in, dendritic calcium spikes were observed less frequently, despite increases in photo-stimulation power. This is a desired property of a pharmacological means of blocking dendritic calcium spikes, as more spines can be functionally characterized without the presence of masking dendritic calcium events. However, given the high percentage of unresponsive spines, muscimol either prevented release in boutons via hyperpolarization or shunted calcium transients in some dendritic spines. While some reports indicate that GABA-A receptors might not be involved in calcium signaling in Schaffer collateral boutons (Ruiz et al., 2010), others show that GABA-A receptors are expressed presynaptically (Turecek & Trussell, 2002). Hence, synaptic transmission is likely affected by the muscimol-induced opening of GABA-A receptors. Indeed, here muscimol also decreased the total input strength, indicating that some presynaptic boutons failed to release neurotransmitter in the presence of muscimol. Notwithstanding, both scenarios (altered release threshold or failure of evoking calcium transients in spines) confound the readout of functional connectivity, as these spines/boutons would contribute to the induction of LTP (before the presence of muscimol) but would then remain undetected when assessing functional connectivity. Hence, it seems broad agonism of GABA-A receptors is not a viable approach to preventing dendritic calcium spikes in the proposed assay.

4.3.5 Assessment of functional connectivity with glutamate indicators

A CA1 neuron's propensity to generate dendritic calcium spikes could also prove to be too difficult to solve pharmacologically without affecting other essential biological mechanisms, such as presynaptic neurotransmitter release. Fortunately, other means of visualizing functional synaptic connectivity could be explored. Recently, genetically encoded fluorescent indicators of various neurotransmitters have been developed (Marvin et al., 2013; Sun et al., 2018; Marvin et al., 2018; Wan et al., 2021; Aggarwal et al., 2022; Duffet et al., 2022). Since neurotransmission at the Schaffer collateral synapse is realized via glutamate, iGluSnFRs, a family of fluorescent glutamate indicators, could be employed to quantify functional connectivity. Recently, localization of the sensor to the synaptic cleft has been improved in its latest variant, iGluSnFR3 (Aggarwal et al., 2022). Moreover, artifactual detection of glutamate spillover could be decreased by mutation of the indicator kinetics. Consequently, iGluSnFR3 could be employed to track neurotransmitter release at the Schaffer collateral synapse in the proposed assay, effectively circumventing the challenges of controlling dendritic calcium spikes. Recently, another variant, of the iGluSnFR family was developed (Shindo et al., 2022): by splitting the protein into two separate peptides that are expressed in selected populations of cells, only synapses between these two neuronal populations are equipped with a functional glutamate indicator. This approach should eliminate localization of the indicator to undesired neuronal compartments, reduce background signal and hence aid in visualizing synaptic connectivity more clearly. Similar to iGluSnFR3, this approach should be tested for the proposed assay, as it might constitute an alternative to calcium imaging in identifying functional connectivity between LTP-inducing boutons and dendritic spines.

4.3.6 Reliability of LTP induction

The induction of long-term potentiation in organotypic hippocampal slice cultures, even using well-established protocols, is highly heterogeneous or sometimes impossible (Debanne, Gähwiler, & Thompson, 1999). LTP in the proposed assay is induced optochemically, first by elevating cyclic AMP lev-

els pharmacologically (by delivery of rolipram and forskolin) and then by optogenetically stimulating ChR2-positive Schaffer collateral boutons. However, LTP induction under suppression of voltage-gated sodium channels (via TTX), as attempted in the proposed assay, is challenging, due to their heavy involvement in LTP (Golding, Staff, & Spruston, 2002; Kim et al., 2015). It is conceivable that omitting blockers of voltage gated sodium and potassium channels might help in the induction of LTP. TTX and 4-AP are present to aid in spatial confinement of presynaptic light-stimulation, as action potentials cannot propagate. Severing Schaffer collaterals could constitute another mean of achieving spatially localized optogenetic stimulation, as back-propagating action potentials can no longer reach other axonal branches of CA3 cells (Kuwajima et al., 2020). Since neurotransmitter release remains functional in severed axonal remnants, both LTP induction and probing for functional connectivity can still be performed (Petreanu et al., 2009; Bauer et al., 2021). Moreover, CA1-CA1 inter-connectivity is negligible (Yang et al., 2014), indicating that input to CA1 pyramidal neurons in response to blue-light stimulation will still originate from ChR2-positive boutons. Notably, in the past, LTP could be induced electrically and optogenetically despite severing CA3-CA1 connectivity (Kuwajima et al., 2020). Even considering the disruption of CA3 axonal tracts, omission of TTX and 4-AP arguably constitute a more physiological setting. Hence, it would be worthwhile to explore whether this approach leads to more reliable LTP induction in the assay.

4.3.7 Technical considerations

Recent advances in light microscopy have made it possible to record from ever growing amounts of neurons or neuronal compartments (Lu et al., 2017; Demas et al., 2021b; Yu et al., 2021). Here, it is shown that employing volumetric Bessel beam calcium imaging (Lu et al., 2017) boosts throughput of the assay several-fold at the cost of reduced vertical sectioning. Recently, this technique was further improved to increase the resolution and contrast of volumetric imaging data (Chen et al., 2022). While volumetric imaging improves the amount of dendritic spines that are captured per region of interest, a large part of the imaged regions do not cover dendrites or dendritic spines. These 'blank' areas are still scanned by conventional line-scanning microscopy techniques. However, other approaches have been developed to guide the excitation beam along only those neuronal structures that are of

interest (Botcherby et al., 2008; Nadella et al., 2016). By adding a third optical scanner to the light path, random light paths can be chosen in 3D without sacrificing spatial resolution (Kerlin et al., 2019). Hence, a dendritic branch and all nearby dendritic spines could be scanned without the need to scan all areas of a region of interest that do not contain neuronal compartments of interest. This not only boosts the temporal resolution, it could also be utilized to capture even larger stretches of dendrites for functional characterization.

Finally, a new method called two-photon tomography was described, which could be utilized to increase the amount of dendritic arbor that is functionally characterized per cell in each experiment (Kazemipour et al., 2019). In this method, four light columns are rapidly and independently scanned through the tissue, and the resulting fluorescence signal is utilized to computationally reconstruct the imaging region. As a consequence, arbitrarily chosen, user-defined regions of interest are scanned with frame-rates in the kilohertz range (Kazemipour et al., 2019). Both in terms of space covered in a single region of interest, and temporal resolution, two-photon tomography constitutes a technical improvement over the currently employed Bessel beam volumetric imaging approach. However, the proposed assay allows for functional characterization of hundreds of dendritic spines per cell, even in its present form, satisfying the throughput requirements for addressing functional connectivity rules of LTP-induced dendritic spines.

4.3.8 Alternative approaches

While the current approach has been highly optimized to tackle the question of functional connectivity rules of LTP-induced synaptogenesis, there are also potential, fully orthogonal alternatives. For example, the two mGRASP constructs could be expressed in CA3 neurons and single CA1 neurons, respectively, to identify structural connectivity between these neuronal populations (Feng, Zhao, & Kim, 2012; Kim et al., 2012; Choi et al., 2018). In addition to the presynaptic component of mGRASP, transduced CA3 neurons would also express ChR2 to induce LTP, as is done in the proposed assay. During induction and maintenance of LTP, structural plasticity could be tracked via repeated imaging of CA1 neuron morphology, similar to the way it is done in the proposed assay. Finally, functional connectivity would be established in pre-existing and LTP-induced dendritic spines via gluta-

mate uncaging and recording responsiveness either electrophysiologically or via calcium imaging. Since in such an approach only single dendritic spines would be stimulated, initiation of dendritic calcium spikes in response to glutamate uncaging is unlikely (Bloodgood & Sabatini, 2007). One potential downside of this approach is that mGRASP might artificially stabilize pre- and postsynaptic compartments, thereby increasing the chances of synapse survival in the fraction of LTP-induced dendritic spines that are connected to pre-mGRASP-expressing boutons. This might artificially shift the observed rate of functional connectivity towards this population of presynaptic partners.

A functional connectomics approach would also be feasible: here, the assay would be performed as proposed, with the addition that ChR2-positive CA3 neurons would also express ascorbate peroxidase (Lam et al., 2015; Kuwajima et al., 2020). This enzyme catalyzes a reaction during the EM staining procedure in the tissue, resulting in an electron-dense precipitate in its vicinity. Such electron-dense deposits can be utilized in subsequent electron microscopy, allowing for reidentification of axonal boutons that were involved in the LTP induction (Kuwajima et al., 2020). Consequently, all dendritic spines of the CA1 neurons of interest could be probed for functional synapses via ultrastructural 3D reconstructions. This approach likely constitutes the most thorough methodology to assess the rules of LTP-induced synaptogenesis. However, throughput is a major issue in electron microscopy studies. Hence, it is unlikely that a sufficient number of CA1 cells could be characterized in this manner in a single organotypic hippocampal slice culture. As outlined above, in order to establish fundamental wiring rules of synaptic connectivity, high-throughput approaches are required. Consequently, while an ultrastructural approach would provide unrivaled details on a single-cell basis, generalizability of such an attempt might be compromised given the low total number of cells that can be assessed.

Recently, repeated ultrastructural reconstitution in living tissue was reported for the first time (Velicky et al., 2022). By flooding the extracellular space with a synthetic fluorophore and employing 3D STED, neuronal tissue could be densely reconstructed with sufficient spatial resolution to resolve thin neurites such as dendritic spines or axons (Velicky et al., 2022). Moreover, this technique can be paired with other commonly used light microscopy techniques, such as calcium imaging or live labeling of common pre- or post-

synaptic markers, to identify functional connectivity. Notably, such labeling could also be employed to characterize spine maturity. An advantage of this novel super-resolution microscopy technique is the vastly improved spatial resolution of tracking spine outgrowth in response to LTP. As discussed above, two-photon imaging techniques are limited in their spatial resolution, which makes visualization of certain features of spines challenging. STED has been shown to outperform two-photon imaging in detecting dendritic spines (Pfeiffer et al., 2018). Moreover, in contrast to current 3D ultrastructural studies using electron microscopy, which require months of time for data analysis, this method was also released with an automated saturated segmentation pipeline, which reduces analysis time significantly (Velicky et al., 2022). Overall, this approach would not only enable mapping of LTP-induced spinogenesis with ultrastructural precision, but also provide simultaneous assessments of spine functional connectivity and maturity.

4.3.9 Conclusion and future directions

Here, an effort was made to investigate the functional connectivity rules of nascent, LTP-induced dendritic spines. Since spine growth happens after the initial onset of LTP, it is unlikely that spinogenesis is relevant to the early phase of LTP (Engert & Bonhoeffer, 1999). However, if such spines preferentially form synapses with the axons that triggered LTP, it is likely that this type of wiring aids in maintaining the induced electrophysiological potentiation. Notably, a different set of experiments proposed more than a decade ago, would be required to assess whether this is the case (Hübener & Bonhoeffer, 2010): LTP-induced dendritic spines should be eliminated rapidly after outgrowth to identify whether this affects LTP maintenance *in vitro* and learning/memory *in vivo*. The challenging aspect of this experiment is to generate a tool to selectively eliminate dendritic spines that grow during LTP without affecting other synaptic or dendritic functions. However, such an experiment would give insights into the causal role LTP-induced dendritic spines play in neuronal function. Should spines play a role in LTP maintenance, it is likely that they preferentially wire with LTP-driving presynaptic partners. Such a mechanism would favor a winner-takes-all plasticity rule, as dominant inputs would benefit from additional synaptic connections, rendering them even more dominant. Such wiring rules have been described in the

retinogeniculate pathway of the mouse, where few RGC afferents dominate dLGN neuron input after development (Chen & Regehr, 2000). Downstream, in the mouse visual cortex, however, functional connectivity seems to be much more promiscuous, as cells drift in their functional tuning over time (Marks & Goard, 2021; Deitch, Rubin, & Ziv, 2021; Bauer & Rose, 2021). It seems that different wiring rules are in place in various brain areas.

4.4 Rules governing functional connectivity

Establishing rules of functional connectivity is a major unresolved goal of modern neuroscience. In this dissertation, such rules were investigated in two circuits, the mouse retinogeniculate pathway and the Schaffer collateral pathway of the hippocampus during LTP. Wiring rules, such as these, are critical to our understanding of the brain. After all, how is a system with an estimated 100 billion neurons that share ∼1.000 trillion connections amongst themselves (Zhang, 2019) organized in such a way that everyday behaviors, such as hugging a good friend or reminiscing about a childhood memory, seem effortless?

Despite the development of better imaging and analysis methods, as well as the advent of optical manipulation of neuronal activity via optogenetics, many of the fundamental wiring rules of the brain remain elusive to this day. This also pertains to the functional wiring rule LTP-induced dendritic spines follow. Neither a previous (Coneva, 2015), nor the work of this dissertation managed to successfully determine this fundamental rule of synaptic plasticity. However, arguably, the methodological advances are mounting, such that this and other rules of functional connectivity in the brain can be studied effectively in the future. DeepD3 represents one such advancement, as it allows dendritic spines to be analyzed rapidly and automatically. However, also other recent advances have been made, which allow for investigations into other fundamental wiring rules of the brain. For example, the emergence of functional connectomics - the combination of two-photon calcium imaging and 3D electron microscopy in the same tissue (Reid, 2012) - lends itself to investigate the visual circuit at the thalamocortical synapse. At this synapse, a major transformation occurs in the functional tuning of pre- and postsynaptic cells: while dLGN cells have round receptive fields, pyramidal neurons in the primary visual cortex have elongated receptive fields. The

elongated nature of their receptive fields allows V1 neurons to be direction and/or orientation selective, features which are mostly absent in at the level of the dLGN. In 1962, Hubel and Wiesel proposed that the elongated shape of receptive fields in V1 could originate from the precise arrangement of the receptive fields of afferent dLGN neurons. Computationally, this could be achieved by a simple summation of the correct inputs, likely posing an efficient way of neurally generating these directional properties. While other theories have been developed (Reid & Alonso, 1995; Alonso, Usrey, & Reid, 1996), the prevalent view on the wiring of this circuit is in alignment with the scheme proposed 60 years ago (Hubel & Wiesel, 1962). By employing functional connectomics, receptive fields and direction/orientation selectivity could be mapped simultaneously in dLGN boutons and V1 cells and the ultrastructural wiring later assessed via large-scale 3D electron microscopy.

However, not only techological advances are required to establish rules of functional connectivity. Such work is also done in model organisms with less complex brains than that of the mouse, such as those of the fruit fly *Drosophila melanogaster*. Here, scientists have worked for decades attempting to mathematically understand how the fruit fly brain performs a simple computation: the perception of moving objects - motion detection (Joesch et al., 2010; Maisak et al., 2013; Groschner et al., 2022). Over time, more and more pieces of the puzzle have been uncovered, outlining the specific wiring of direction- and illumination-selective neurons in the fly optic lobe (Dvorak, Bishop, & Eckert, 1975; Maisak et al., 2013; Zheng et al., 2018). However, despite these advances, modeling certain aspects of motion detection in the fly brain remains challenging to this day, indicating that some aspects of the functional connectivity rules in this circuit are still not perfectly understood (Borst, Haag, & Mauss, 2020). While efforts like these are essential to understanding the brain, it should also be kept in mind that full understanding of even a single functional connectivity rule of the brain is equally important as it is technologically challenging and time-intensive.

Chapter 5

Supplementary figures

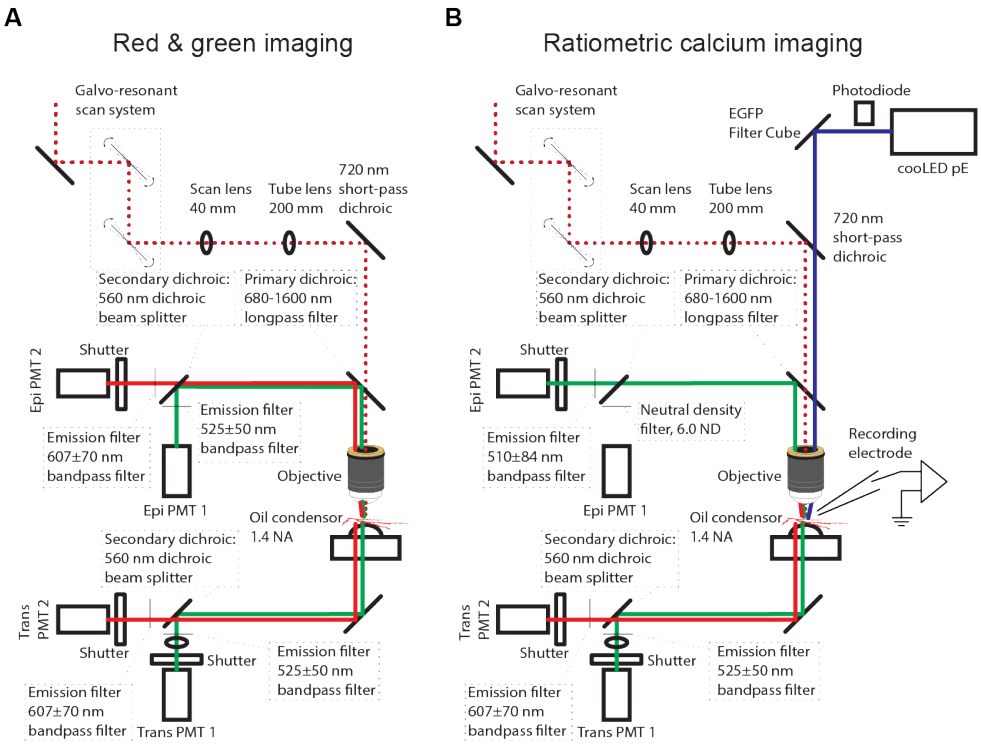

Figure S2.1 Red and green imaging modes of the main setup
The two photon excitation beam is guided through the objective to the sample (dark red dotted line) via a galvo-resonant scan system, the scan and tube lenses, a 720 nm short pass filter and an emission filter. Emitting photons (e.g. red and green lines in A) are captured epi- and transdirectionally via mirrors and subsequently split via an emission filter to guide photons in the green and red spectra to separate PMTs. Different emission filters are employed to image fluorophores of different spectra (see A, B and Fig. S2.2, S2.3) **A** Imaging settings of the main setup to image red and/or green fluorophores. This was employed for imaging overviews of dLGN in acute slices, RGC axonal projection pattern in the vicinity of patched dLGN cells, dLGN cell morphologies and structural imaging of CA1 pyramidal cells in OHSCs. **B** Imaging settings to perform ratiometric calcium imaging using a red structural marker (tdTomato, Alexa 594) and a green calcium indicator (GCaMP7b, Fluo-4). Typically, blue-light stimulation was provided via an LED lamp, and emitted photons of the fluorophores were captured by the three PMTs that were equipped with shutters. Shutters light-shielded PMTs during blue-light stimulation.

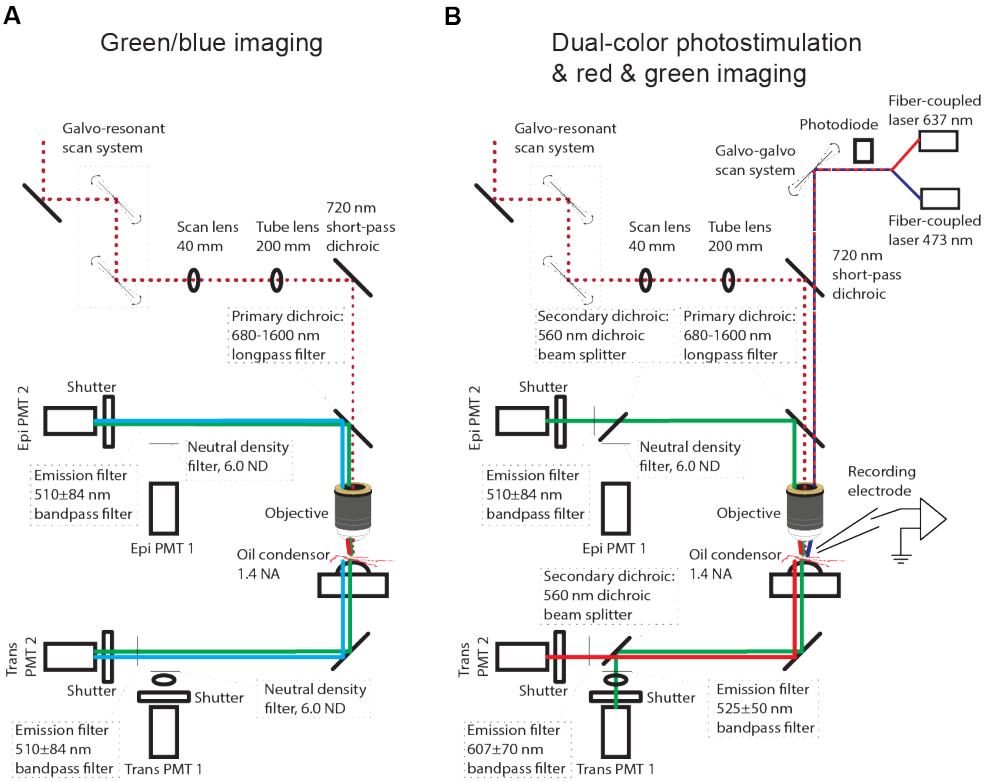

Figure S2.2 Additional imaging and photostimulation modes of the main setup

A Imaging settings to image green or blue fluorophores. This was utilized to image GCaMP7b in the absence of a structural marker, and to image the spine maturity marker Xph-15-mTurquoise2. **B** Imaging settings to perform ratiometric calcium imaging using dual-color optogenetic photostimulation. Two benchtop lasers are used to stimulate blue- and red-shifted opsins. Light is reflected to the sample using a galvo-galvo system. While two-color optogenetic calcium imaging was not performed in this thesis, this setting was used during experiments to map retinogeniculate inputs of single dLGN neurons. In these experiments, the primary dichroic was removed.

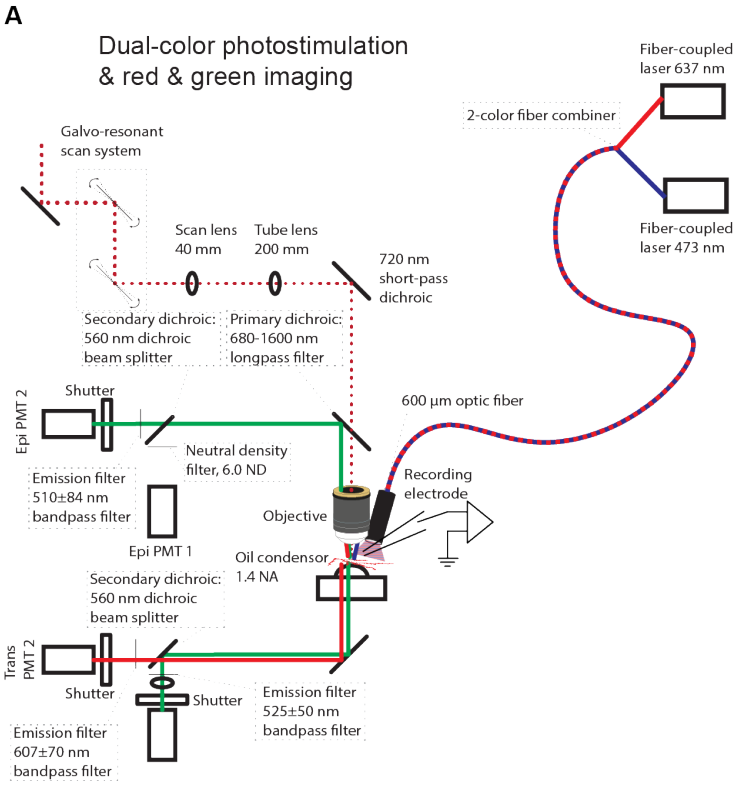

Figure S2.3 Fiber-mediated optogenetic stimulation of the main setup
A Alternative imaging settings to perform ratiometric calcium imaging using dual-color optogenetic photostimulation. Here, instead of utilizing a galvo-galvo scan system to target photostimulation, an optic fiber is placed near the sample to provide spatially confined optogenetic stimulation. This setting was used for patch-clamp experiments involving muscimol wash-in. This setting should be used in the future for experiments to map functional connectivity of LTP-induced spines, as it decouples photostimulation from the two-photon imaging field of view. Hence, several dendritic regions could be investigated using this setting without changing the applied ChR2-stimulation.

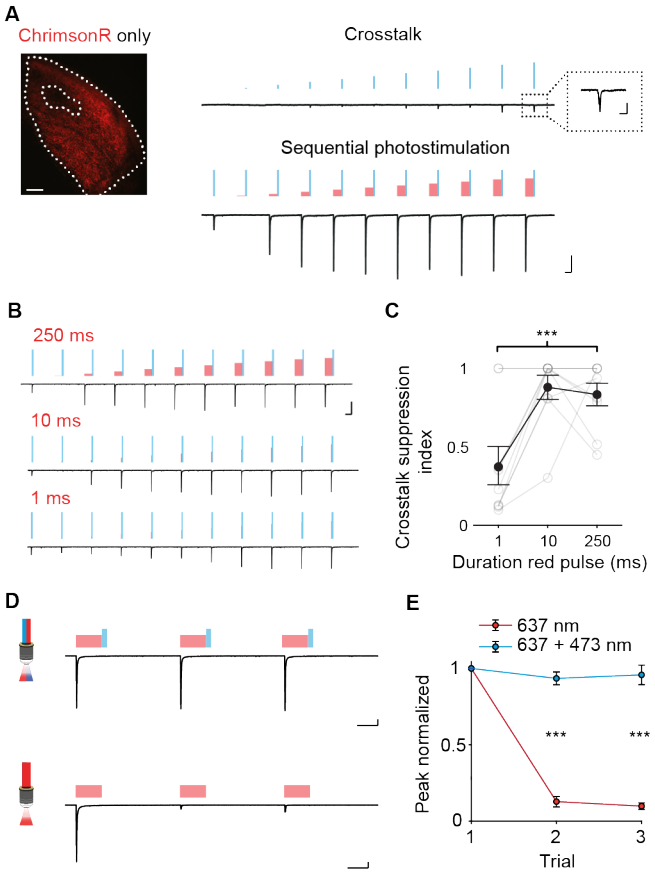

Figure S3.1.1 Photoproperties of ChrimsonR and Chronos during sequential photostimulation

A Maximum intensity projection of ChrimsonR-tdT expression pattern within dLGN (left). Blue-light-evoked PSCs (473 nm) using increasing irradiances in 11-step protocol (top). Inset: close-up of evoked current at highest irradiance. Sequential photostimulation-evoked PSCs of the same neuron (637 nm for 250 ms, 473 nm for 50 ms, ISI: 10 s) (bottom). **B** Sequential photostimulation with varying red-light stimulation durations (250, 10, 1 ms) combined with 50 ms blue-light stimulation. **C** Crosstalk suppression index quantification of B (two-way ANOVA, main effect: $p < 0.01$; post-hoc test: 1 ms vs 10 ms: $p < 0.01$, 1 ms vs 250 ms: $p < 0.01$, 10 ms vs. 250 ms: $p = 0.94$). **D** Photocurrents of dLGN cell in response to sequential photostimulation (top) or repetitive red-light stimulation (bottom). **E** Quantification of D using average peak-normalized responses (two-sample student t-test, sequential photostimulation vs. repetitive red-light stimulation: $p < 0.001$ (stimulation interval 2), $p < 0.001$ (stimulation

interval 3)). Error bars indicate mean ± SEM. Image scale bar: 100 μm. Electrophysiology trace scale bars: 200 ms, 250 pA (zoom in window in A: 50 ms, 75 pA). Figure reprinted with permission from Bauer et al. (2021).

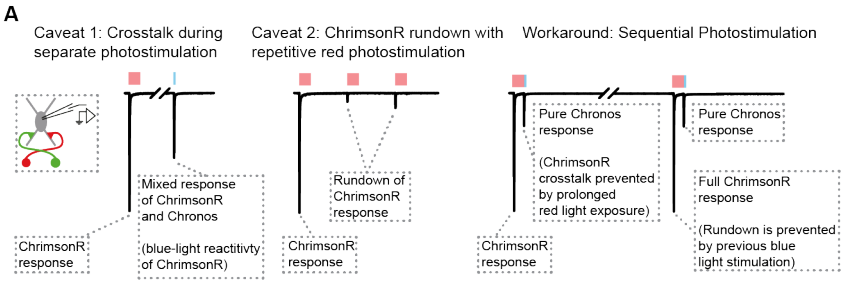

Figure S3.1.2 A quantitative sequential photostimulation paradigm using ChrimsonR and Chronos

A Caveats of pairing ChrimsonR and Chronos for input mapping (from left to right): Caveat 1: blue-light crosstalk of ChrimsonR. Caveat 2: ChrimsonR is rendered minimally photoresponsive after repeated and prolonged red-light exposure. Workaround: Sequential photostimulation. Pairing red- with blue-light stimulation prevents crosstalk (caveat 1) and maintains photoresponsivity of ChrimsonR (caveat 2). Traces serve illustrative purposes, not real data. Figure reprinted with permission from Bauer et al. (2021).

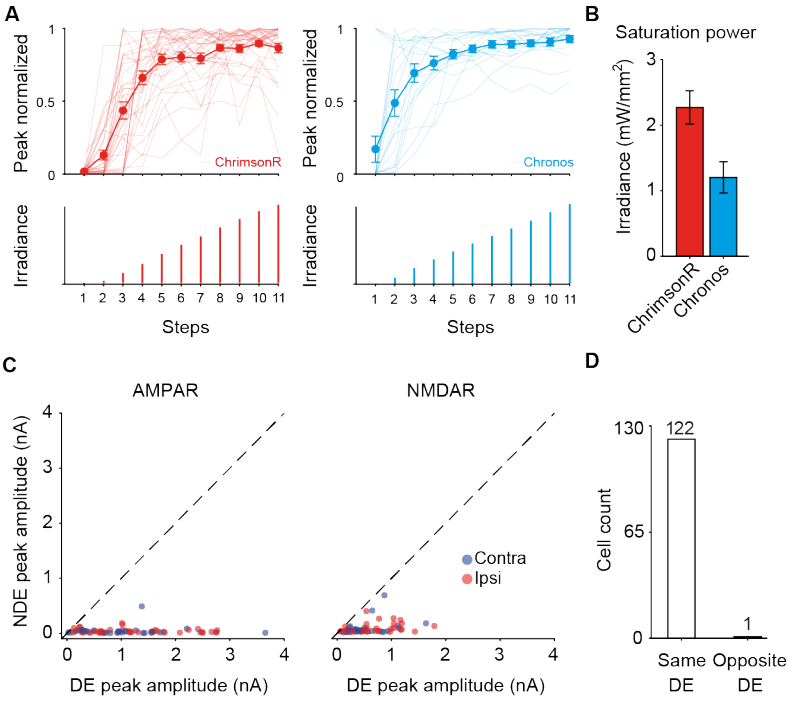

Figure S3.1.3 Photoproperties and -responses during eye-specific mapping in the retinogeniculate pathway

G Left: mean peak-normalized photo-responses of ChrimsonR (637 nm) using 11 step protocol of increasing irradiance. Middle: mean peak-normalized photo-responses of Chronos (473 nm) using 11 step protocol of increasing irradiance. Thin lines represent individual cells, tick lines the mean ± SEM. Right: current-saturating average irradiances used for Chronos and ChrimsonR stimulation. **H** Optically evoked peak PSCs of binocular cells: dominant- (DE) and non-dominant (NDE) eye responses for AMPAR- (left, n = 75 cells) and NMDAR-mediated currents (right, n = 65 cells). Blue and red indicate eye dominance (contra- and ipsilateral, respectively). **I** Agreement between AMPAR- and NMDAR-mediated response quantification of dominant eye preference (n = 123 cells). Most cells share eye dominance between both measures. Figure reprinted with permission from Bauer et al. (2021).

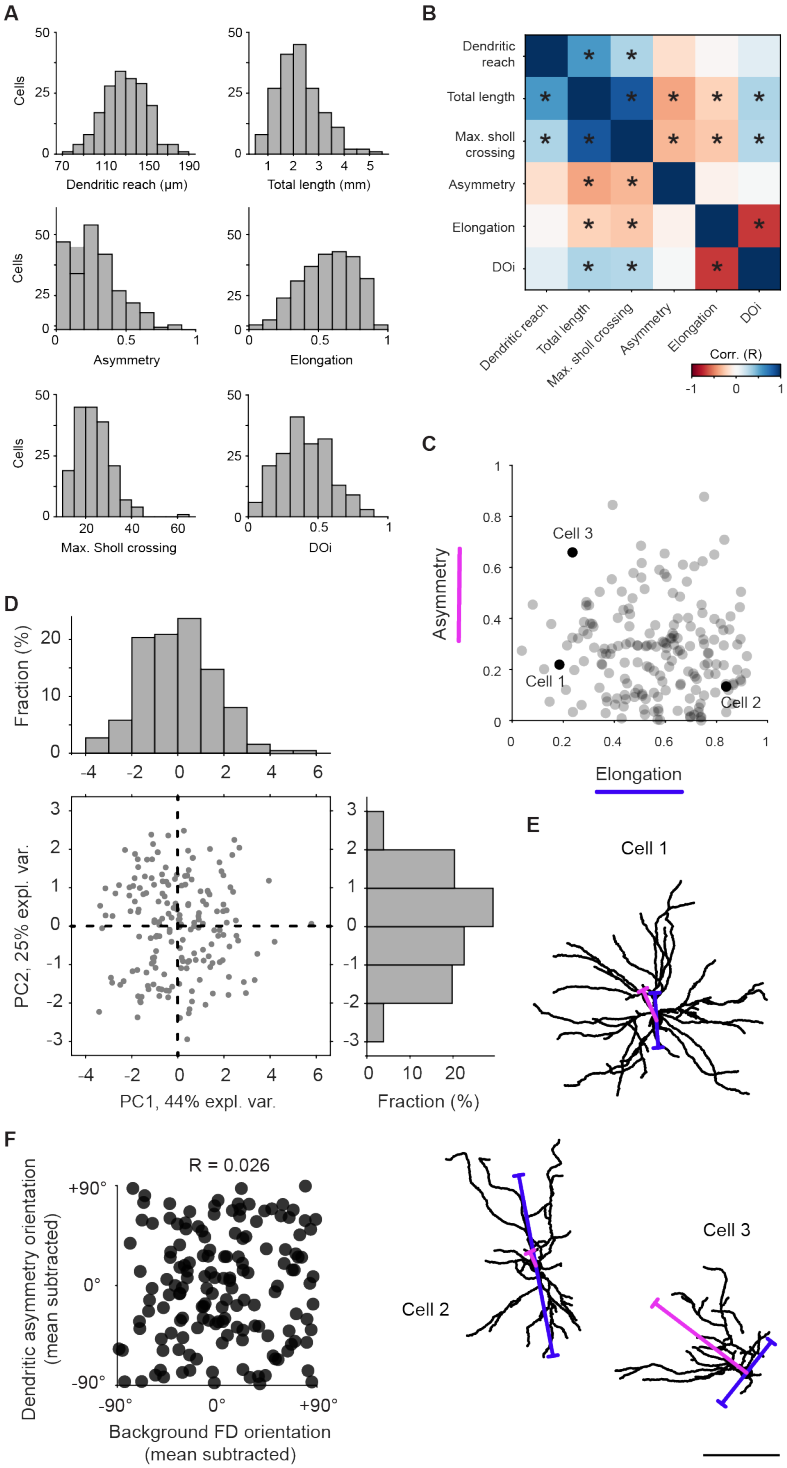
A
Cells
Dendritic reach (µm)
Total length (mm)
Asymmetry
Elongation
Max. Sholl crossing
DOi
B
Dendritic reach
Total length
Max. sholl crossing
Asymmetry
Elongation
DOi
Corr. (R)
C
Cell 3
Cell 1
Cell 2
Asymmetry
Elongation
D
Fraction (%)
PC2, 25% expl. var.
PC1, 44% expl. var.
E
Cell 1
F
R = 0.026
Dendritic asymmetry orientation (mean subtracted)
Background FD orientation (mean subtracted)
Cell 2
Cell 3

Figure S3.1.4 Morphological features of dLGN neurons
A Distributions of morphological features extracted from cell reconstructions (dendritic reach, total dendritic length, max. number of crossings (Sholl analysis), asymmetry magnitude, elongation magnitude, and DOi)(n = 185 cells). **B** Spearman's correlation coefficient matrix of morphological measures of A. * indicates p <0.05 after correction for multiple comparisons (Bonferroni). **C** Scatter plot of asymmetry vs. elongation of all cells (n = 185 cells). Example cells shown in E are highlighted in black. **D** PCA analysis of morphological features. Shown is the distribution of all dLGN neurons along the first two principal components (PC1, PC2). Histograms of PC1 and PC2 are displayed on top and left. Multimodality was not found for either principal component (Hartigan's dip index = 0.023 and 0.019, p = 0.76 and 0.96 for PC1 and PC2, respectively), indicating that no distinct subtypes of neuronal morphologies are expected and cluster analysis is not justified (n = 185 cells). **E** Reconstructed dendritic morphologies of three dLGN neurons (see C). Blue and magenta lines indicate the cells' elongations and asymmetries, respectively. The length of the lines indicate the feature in relationship to the dendritic reach of a cell. **F** Scatter plot of mean-subtracted asymmetry orientation vs mean-subtracted background FD gradient orientation (n = 152 cells). No relationship is evident (circular-circular Pearson's correlation R = 0.026, p = 0.74), indicating that asymmetry does not seem to bias axo-dendritic sampling (rFD) towards monocularity. Figure modified with permission from Bauer et al. (2021).

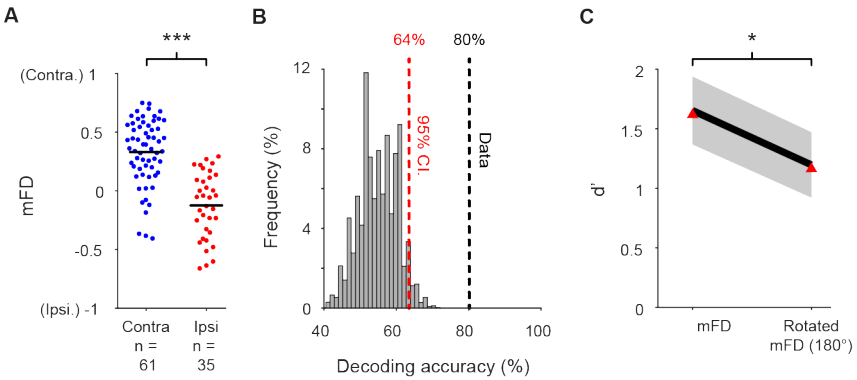

Figure S3.1.5 Decoding eye dominance from local axo-dendritic innervation in the dLGN

A mFD values plotted cell-wise per dominant eye (contralateral in blue, n = 61 cells; ipsilateral in red, n = 35 cells; means in black). Contralateral cells also sample in dLGN regions more densely innervated by contralateral RGC afferents (two-tailed two-sample unequal variance t-test $p < 0.001$, $t = 7.7$). **B** Decoding accuracy of eye preference data from mFD (black dashed line) vs. histogram of decoding accuracies of control data (shuffled eye preference, in gray) with 95 % confidence interval (red dashed line). **C** Eye dominance can be decoded from mFD: comparison of d' values of unrotated mFD and 180° rotated mFD. red triangles: d' based on data, gray: standard deviation of the bootstrapped d' distributions, black: average of bootstrapped d' distributions (n = 82 cells, mFD vs mFD at 180° rotation: two-tailed paired bootstrap p-value of the difference between d' values: $p = 0.0142$). Figure reprinted with permission from Bauer et al. (2021).

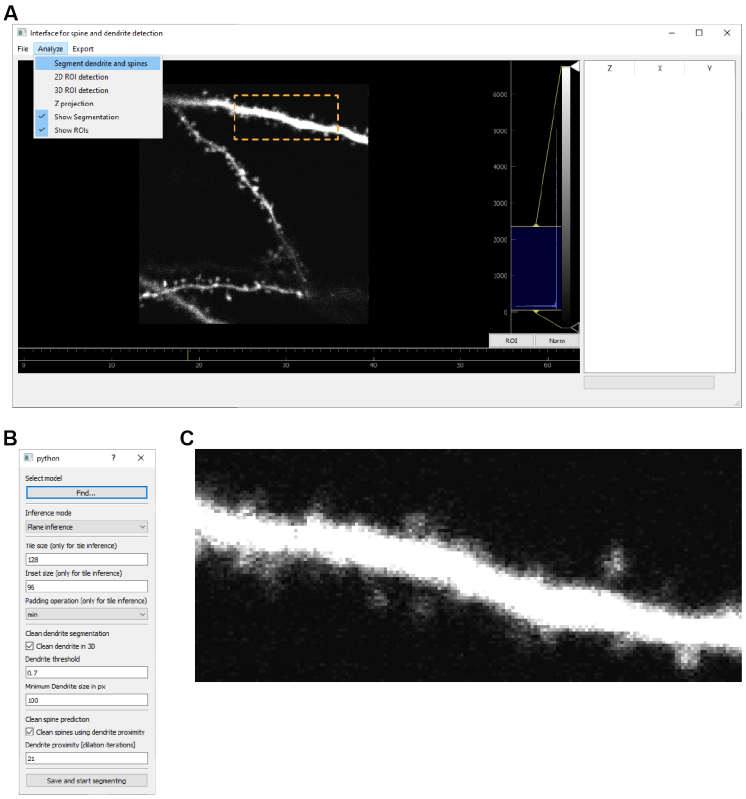

Figure S3.2.1 Graphical user interface of DeepD3
A Graphical user interface of DeepD3. Structure of a dendritic branch is shown in gray scale. Drop-down menus are located in the top left. Image contrast settings are located to the right of the image (gray scale). The area where spine ROIs will be displayed after full segmentation is displayed to the very right. Inset in orange is displayed in panel C. **B** User-defined hyperparameters that can be fine-tuned for image prediction (see methods). **C** Zoom-in of dendrite and spines (orange inset in A).

A

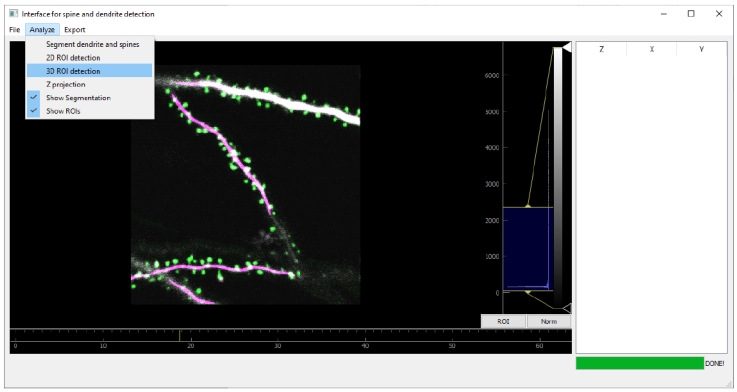
Interface for spine and dendrite detection
File
Analyze
Export
Segment dendrite and spines
2D ROI detection
3D ROI detection
Z projection
Show Segmentation
Show ROIs
Z
X
Y
ROI
Norm
DONE!

B

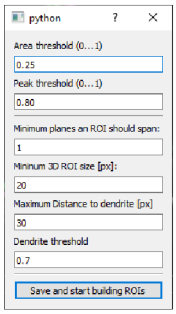
python
Area threshold (0...1)
0.25
Peak threshold (0...1)
0.80
Minimum planes an ROI should span:
1
Mininum 3D ROI size [px]:
20
Maximum Distance to dendrite [px]
30
Dendrite threshold
0.7
Save and start building ROIs

C

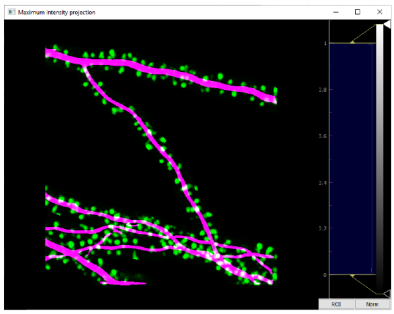
Maximum intensity projection
ROI
None

D

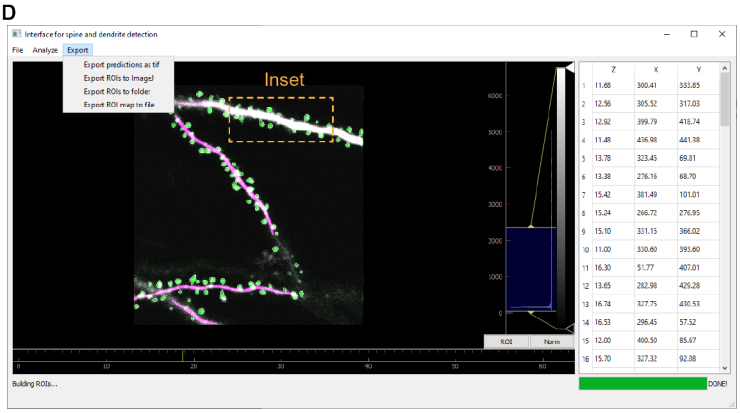
Interface for spine and dendrite detection
File
Analyze
Export
Export predictions as tif
Export ROIs to ImageJ
Export ROIs to folder
Export ROI map to file
Inset
Z
X
Y
ROI
Norm
Building ROIs...
DONE!

E

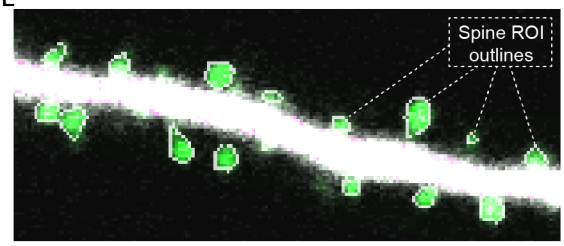
Spine ROI
outlines

Figure S3.2.2 Semantic segmentation of spines and dendrites using the graphical user interface of DeepD3
A Results of spine and dendrite prediction using hyperparameters shown in Fig S3.2.1B. Structure in gray scale, dendrite prediction in magenta, spine prediction in green. **B** User-defined hyperparameters that can be fine-tuned for 3D segmentation of the prediction image. **C** Maximum-intensity projection of the prediction image. Dendrite prediction in magenta, spine prediction in green. **D** Results of image segmentation using hyperparameters shown in B. The number and location of segmented spine ROIs in the current field of view is displayed on the very right. Inset in orange is displayed in panel E. **E** Zoom-in of dendrite and spines (white), their predictions (magenta and green, respectively), as well as the outline of dendritic spines (white, around dendritic spines, predicted in green). A selection of spine ROI outlines is highlighted (dashed lines). Region of the zoom-in is shown in orange in panel D.

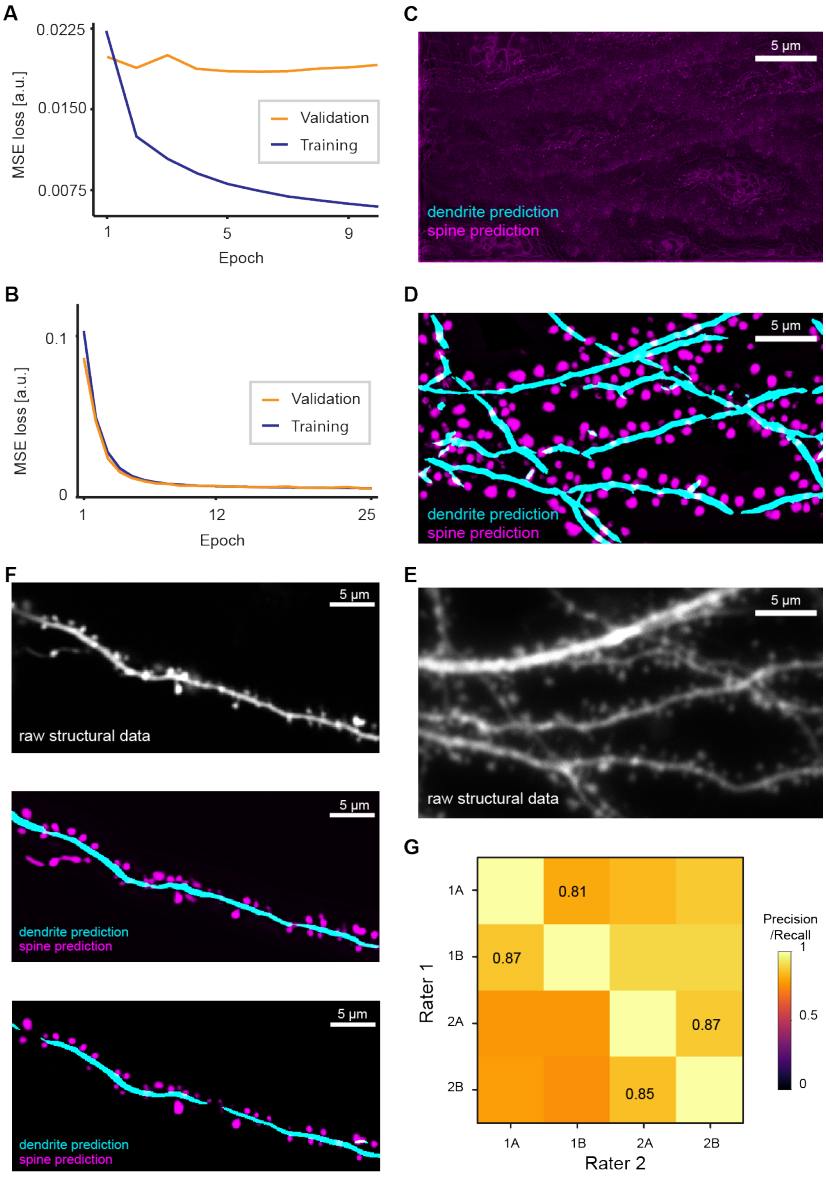

Figure S3.2.3 DeepD3 models and performances

A Performance of a model trained in the DeepD3 framework over training epochs. Performance on training data improved with training epochs. However, performance on validation data did not improve over time, indicating that the model was not able to generalize and potentially overfitted to the training data. No

secondary data augmentation was performed on the training data set generation (see methods). Models without secondary data augmentation are specialized models due to their inability to generalize beyond the training data. **B** Performance of a different model trained in the DeepD3 framework using a training method to produce a generalized model over training epochs. Performance on training data improved with training epochs. Secondary data augmentation was performed on the training data set generation. As a consequence, performance on the validation data seems to improve with training epochs, indicative of the model's ability to generalize beyond the training data set. **C** Performance of the specialized model (see A) on novel data that has a different pixel size and signal-to-noise ratio (see E for raw data) compared to the training data. Using this model DeepD3 fails to detect spines or dendrites. Likely, the model overfitted during training, due to lack of heterogeneous training data. Prediction of spines and dendrites is shown in magenta and turquoise, respectively. **D** Same as C but using a general network (see B) for segmentation. The general network, in contrast to the specialized network could identify dendritic spines reliably, despite a large difference in pixel size between the images in C-E and F (0.0212×0.0212 μm and 0.094×0.094 μm, respectively). **E** Raw, novel structural data that is has a different pixel size than the training data of the specialized model (see A). **F** Top: raw, novel structural data that is similar to the training data of the specialized model (see A). Middle: performance of the specialized model trained in A. Visual inspection of the DeepD-generated segmentation seems to match the locations of dendrites and dendritic spines in the raw data (top image). Prediction of spines and dendrites is shown in magenta and turquoise, respectively. Bottom: performance of the general model trained in B. Visual inspection indicates that spines and dendrites could successfully be segmented. **G** Intra-rater-reliability as a function of precision. Two annotators identified spines in the same image at two timepoints (A, B) with > 2 weeks between annotations. Intra-rater reliability is indicated by numbers in black (average: 85 % precision). Agreement of rater 1 to rater 2 is quantified using a distance-based measure (see methods).

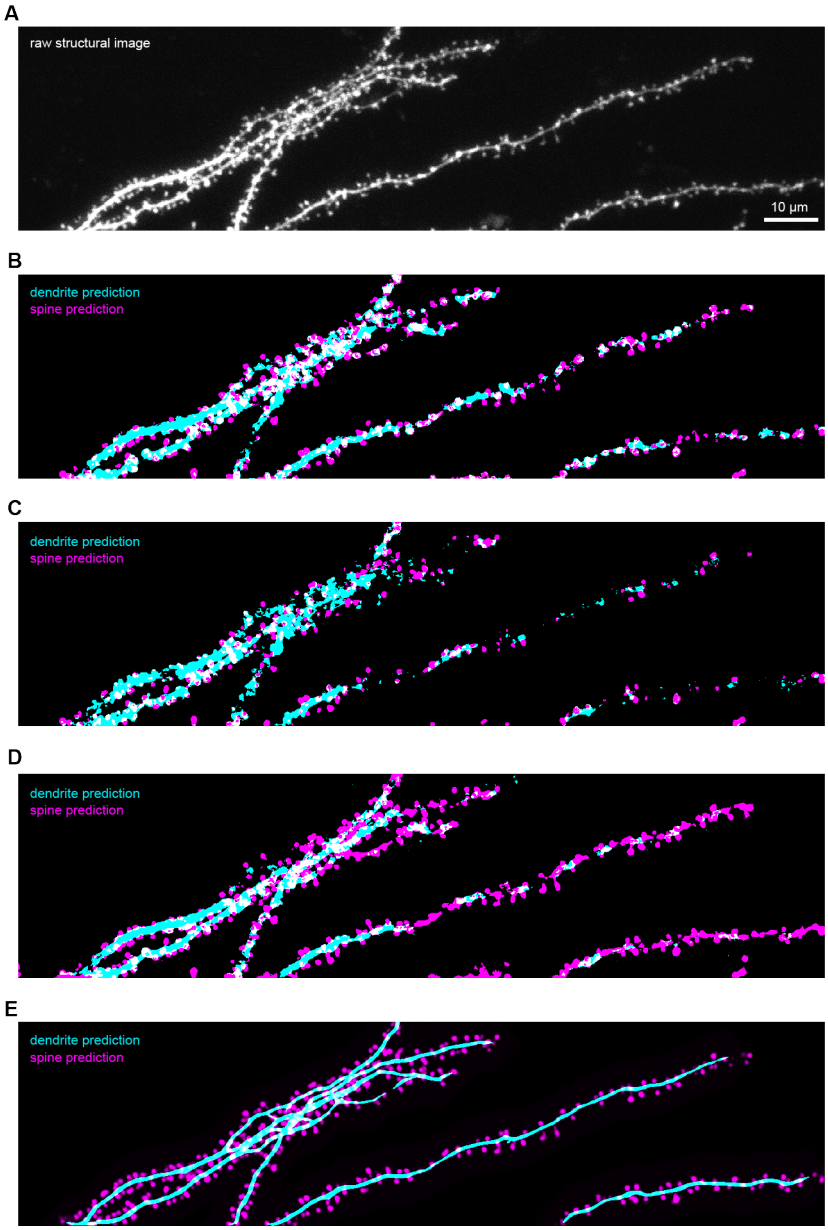

Figure S3.2.4 Performances of DeepD3 and DeepSpineTool
A Maximum intensity projection of an image of a CA1 neuron in a rat OHSC. **B** Segmentation of dendrites (cyan) and dendritic spines (magenta) of the image in panel A of model 1 of DeepSpineTool (Vidaurre-Gallart et al., 2022). Segmen-

tation is displayed as a maximum intensity projection. **C** Same as B but with model 2 of DeepSpineTool. **D** Same as B but with model 3 of DeepSpineTool. **E** Segmentation of dendrites (cyan) and dendritic spines (magenta) of the image in panel A of model 1 using DeepD3. Segmentation is displayed as a maximum intensity projection. All models of the DeepSpineTool fail at segmenting the dendrite well. Some spines are well segmented by the DeepSpineTool. However, qualitatively, DeepD3 outperforms DeepSpineTool.

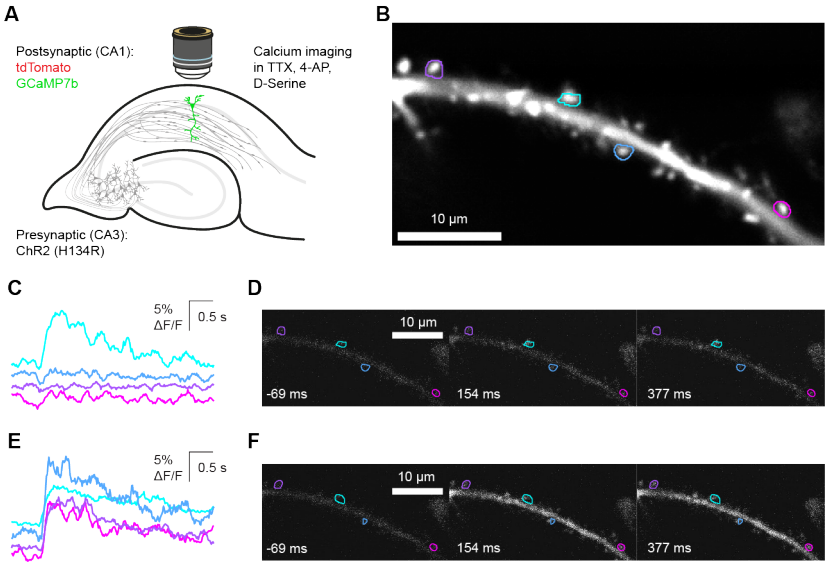

Figure S3.3.1 A dataset for the comparison of single-spine responses and dendritic calcium spikes

A Schematic of the experimental model. Structural (tdTomato; red) and a calcium indicator (GCaMP7b; green) are co-expressed in single CA1 neurons of OHSCs. A population of CA3 neurons is transduced with ChR2(H134R). Two-photon calcium imaging is performed in dendritic regions of the CA1 neuron in conditions preventing the generation of action potentials (TTX, 4-AP). **B** Average intensity projection of a calcium movie. Some spines are outlined in color. Computational unmixing was tested using image data of spines during dendritic calcium spikes and data in which single spines are responsive but the dendrite is not. Movies containing single-spine responses (C, D; data A) and dendritic calcium spikes (E, F; data B). **C** Single-spine responses (data A). An individual spine (turquoise) is responsive to ChR2-stimulation, while all other spines are not. **D** 7-point moving average projections of a dendritic stretch across 3 time points in relation to ChR2 stimulation (white, bottom left corner of each image). Spines (calcium traces shown in C) are outlined in color. After stimulation, only a single spine (turquoise) shows an increase in calcium concentration, while all other spines and the dendrite show no change. **E** Dendritic calcium spike (data B). All dendritic spines are responsive to ChR2 stimulation. Since the dendrite is also flooded with calcium, likely not all spine responses are evoked by direct synaptic transmission at the spine. **F** Same as D but for dendritic calcium spike.

Chapter 6

Appendix

DNA constructs

pAAV-CAG-hChR2(H134R)-WPRE-SV40

ctgcgcgctcgctcgctcactgaggccgcccgggcaaagcccgggcgtcgggcgacctttggtcgcccggc
ctcagtgagcgagcgagcgcgcagagagggagtggccaactccatcactaggggttccttgtagttaatga
ttaacccgccatgctacttatctacgtagccatgctctaggaagagtaccattgacgtcaataatgacgtat
gttcccatagtaacgccaatagggactttccattgacgtcaatgggtggagtatttacggtaaactgcccac
ttggcagtacatcaagtgtatcatatgccaagtacgccccctattgacgtcaatgacggtaaatggcccgcc
tggcattatgcccagtacatgaccttatgggactttcctacttggcagtacatctacgtattagtcatcgcta
ttaccatggtcgaggtgagccccacgttctgcttcactctccccatctcccccccctccccacccccaattttg
tatttatttatttttaattattttgtgcagcgatgggggcgggggggggggggggcgcgcgccaggcgggg
gcggggcggggcgaggggcggggcggggcgaggcggagaggtgcggcggcagccaatcagagcggcgc
gctccgaaagtttccttttatggcgaggcggcggcggcggccctataaaaagcgaagcgcgcggcggg
gcgggagtcgctgcgcgctgccttcgccccgtgccccgctccgccgccgcctcgcgccgcccgccccggctc
tgactgaccgcgttactcccacaggtgagcgggcgggacggcccttctcctccgggctgtaattagcgcttg
gtttaatgacggcttgtttcttttctgtggctgcgtgaaagccttgaggggctccgggagggccctttgtgcg
gggggagcggctcggggctgtccgcgggggggacggctgccttcgggggggacggggcagggcggggttc
ggcttctggcgtgtgaccggcggctctagagcctctgctaaccatgttcatgccttcttcttttttcctacagct
cctgggcaacgtgctggttattgtgctgtctcatcattttggcaaagaattggatcgggatccactagtccag
tgtggtggaattgcccttgctgccaccAtggactatggcggcgctttgtctgccgtcggacgcgaacttttg
ttcgttactaatcctgtggtggtgaacgggtccgtcctggtccctgaggatcaatgttactgtgccggatgga
ttgaatctcgcggcacgaacggcgctcagaccgcgtcaaatgtcctgcagtggcttgcagcaggattcagc
attttgctgctgatgttctatgcctaccaaacctggaaatctacatgcggctgggaggagatctatgtgtgc
gccattgaaatggttaaggtgattctcgagttctttttgagtttaagaatccctctatgctctaccttgccac

aggacaccgggtgcagtggctgcgctatgcagagtggctgctcacttgtcctgtcatccttatccgcctgag
caacctcaccggcctgagcaacgactacagcaggagaaccatgggactccttgtctcagacatcgggacta
tcgtgtgggggctaccagcgccatggcaaccggctatgttaaagtcatcttcttttgtcttggattgtgcta
tggcgcgaacacatttttcacgccgccaaagcatatatcgagggttatcatactgtgccaaagggtcggtg
ccgccaggtcgtgaccggcatggcatggctgtttttcgtgagctggggtatgttcccaattctcttcattttg
gggcccgaaggttttggcgtcctgagcgtctatggctccaccgtaggtcacacgattattgatctgatgagt
aaaaattgttgggggttgttgggacactacctgcgcgtcctgatccacgagcacatattgattcacggagat
atccgcaaaaccaccaaactgaacatcggcggaacggagatcgaggtcgagactctcgtcgaagacgaag
ccgaggccggagccgtgccataAagcggccccggactcgaggccgcaggtaagtatcaaggttacaaga
caggtttaaggagaccaatagaaactgggcttgtcgagacagagaagactcttgcgtttctgataggcacc
tattggtcttactgacatccactttgcctttctctccacaggtgtcgagtggagctcgcgactagtcgattcg
aattcgatatcaagcttatcgataatcaacctctggattacaaaatttgtgaaagattgactggtattcttaa
ctatgttgctccttttacgctatgtggatacgctgctttaatgcctttgtatcatgctattgcttcccgtatggc
tttcattttctcctccttgtataaatcctggttgctgtctctttatgaggagttgtggcccgttgtcaggcaac
gtggcgtggtgtgcactgtgtttgctgacgcaacccccactggttggggcattgccaccacctgtcagctcct
ttccgggactttcgctttccccctccctattgccacggcggaactcatcgccgcctgccttgcccgctgctgga
caggggctcggctgttgggcactgacaattccgtggtgttgtcggggaaatcatcgtcctttccttggctgct
cgcctgtgttgccacctggattctgcgcgggacgtccttctgctacgtcccttcggccctcaatccagcggac
cttccttcccgcggcctgctgccggctctgcggcctcttccgcgtcttcgccttcgccctcagacgagtcgga
tctccctttgggccgcctccccgcatcgataccgtcgacccgggcggccgcttcgagcagacatgataagat
acattgatgagtttggacaaaccacaactagaatgcagtgaaaaaaatgctttatttgtgaaatttgtgatg
ctattgctttatttgtaaccattataagctgcaataaacaagttaacaacaacaattgcattcattttatgttt
caggttcaggggagatgtgggaggtttttaaagcaagtaaaacctctacaaatgtggtaaaatcgataa
ggatcttcctagagcatggctacgtagataagtagcatggcgggttaatcattaactacaaggaacccta
gtgatggagttggccactccctctctgcgcgctcgctcgctcactgaggccgggcgaccaaaggtcgcccga
cgcccgggctttgcccgggcggcctcagtgagcgagcgagcgcgcagccttaattaacctaattcactggcc
gtcgttttacaacgtcgtgactgggaaaaccctggcgttacccaacttaatcgccttgcagcacatccccctt
tcgccagctggcgtaatagcgaagaggcccgcaccgatcgcccttcccaacagttgcgcagcctgaatggc
gaatgggacgcgccctgtagcggcgcattaagcgcggcgggtgtggtggttacgcgcagcgtgaccgctac
acttgccagcgccctagcgcccgctcctttcgctttcttcccttcctttctcgccacgttcgccggctttccccg
tcaagctctaaatcgggggctccctttagggttccgatttagtgctttacggcacctcgaccccaaaaaact
tgattagggtgatggttcacgtagtgggccatcgccctgatagacggtttttcgccctttgacgttggagtcc
acgttctttaatagtggactcttgttccaaactggaacaacactcaaccctatctcggtctattcttttgattt
ataagggattttgccgatttcggcctattggttaaaaaatgagctgatttaacaaaaatttaacgcgaattt
taacaaaatattaacgcttacaatttaggtggcacttttcggggaaatgtgcgcggaacccctatttgtttat
ttttctaaatacattcaaatatgtatccgctcatgagacaataaccctgataaatgcttcaataatattgaaa
aaggaagagtatgagtattcaacatttccgtgtcgcccttattccctttttgcggcattttgccttcctgttt
ttgctcacccagaaacgctggtgaaagtaaaagatgctgaagatcagttgggtgcacgagtgggttacatc

gaactggatctcaacagcggtaagatccttgagagttttcgccccgaagaacgttttccaatgatgagcact
tttaaagttctgctatgtggcgcggtattatcccgtattgacgccgggcaagagcaactcggtcgccgcata
cactattctcagaatgacttggttgagtactcaccagtcacagaaaagcatcttacggatggcatgacagta
agagaattatgcagtgctgccataaccatgagtgataacactgcggccaacttacttctgacaacgatcgg
aggaccgaaggagctaaccgcttttttgcacaacatgggggatcatgtaactcgccttgatcgttgggaacc
ggagctgaatgaagccataccaaacgacgagcgtgacaccacgatgcctgtagcaatggcaacaacgttg
cgcaaactattaactggcgaactacttactctagcttcccggcaacaattaatagactggatggaggcgga
taaagttgcaggaccacttctgcgctcggcccttccggctggctggtttattgctgataaatctggagccggt
gagcgtgggtctcgcggtatcattgcagcactggggccagatggtaagccctcccgtatcgtagttatctac
acgacggggagtcaggcaactatggatgaacgaaatagacagatcgctgagataggtgcctcactgatta
agcattggtaactgtcagaccaagtttactcatatatactttagattgatttaaaacttcatttttaatttaaa
aggatctaggtgaagatccttttgataatctcatgaccaaaatcccttaacgtgagttttcgttccactgag
cgtcagaccccgtagaaaagatcaaaggatcttcttgagatcctttttttctgcgcgtaatctgctgcttgca
aacaaaaaaaccaccgctaccagcggtggtttgtttgccggatcaagagctaccaactctttttccgaaggt
aactggcttcagcagagcgcagataccaaatactgttcttctagtgtagccgtagttaggccaccacttcaa
gaactctgtagcaccgcctacatacctcgctctgctaatcctgttaccagtggctgctgccagtggcgataa
gtcgtgtcttaccgggttggactcaagacgatagttaccggataaggcgcagcggtcgggctgaacggggg
gttcgtgcacacagcccagcttggagcgaacgacctacaccgaactgagatacctacagcgtgagctatga
gaaagcgccacgcttcccgaagggagaaaggcggacaggtatccggtaagcggcagggtcggaacagga
gagcgcacgagggagcttccagggggaaacgcctggtatctttatagtcctgtcgggtttcgccacctctga
cttgagcgtcgatttttgtgatgctcgtcaggggggcggagcctatggaaaaacgccagcaacgcggccttt
ttacggttcctggccttttgctggccttttgctcacatgttctttcctgcgttatcccctgattctgtggataac
cgtattaccgcctttgagtgagctgataccgctcgccgcagccgaacgaccgagcgcagcgagtcagtgag
cgaggaagcggaagagcgcccaatacgcaaaccgcctctccccgcgcgttggccgattcattaatgcagct
ggcacgacaggtttcccgactggaaagcgggcagtgagcgcaacgcaattaatgtgagttagctcactcat
taggcaccccaggctttacactttatgcttccggctcgtatgttgtgtggaattgtgagcggataacaatttc
acacaggaaacagctatgaccatgattacgccagatttaattaagggcaactgttgggaagggcgatcggt
gcgggcctcttcgctattacgccag

pCAG-Xph15-mTurquoise2-CCR5TC

ggtcgacattgattattgactagagtcatcctcatcgtcgacattgattattgactagttattaatagtaatc
aattacggggtcattagttcatagcccatatatggagttccgcgttacataacttacggtaaatggcccgcc
tggctgaccgcccaacgacccccgcccattgacgtcaataatgacgtatgttcccatagtaacgccaatagg
gactttccattgacgtcaatgggtggagtatttacggtaaactgcccacttggcagtacatcaagtgtatca
tatgccaagtacgccccctattgacgtcaatgacggtaaatggcccgcctggcattatgcccagtacatgac
cttatgggactttcctacttggcagtacatctacgtattagtcatcgctattaccatggtcgaggtgagcccc
acgttctgcttcactctcccatctccccccctcccacccccaattttgtatttatttatttttaattatttt

gtgcagcgatgggggcgggggggggggggggcgcgccrgggggggggggggggggggggggggggg
gsggggsgrggcggagaggtgcggcggcagccaatcagagcggcgcgctccgaaagtttccttttatggcg
aggcggcggcggcggcggccctataaaaagcgaagcgcgcggcgggcgggagtcgctgcgcgctgccttc
gccccgtgccccgctccgccgccgcctcgcgccgcccgccccggctctgactgaccgcgttactcccacagg
tgagcgggcgggacggcccttctcctccgggctgtaattagcgcttggtttaatgacggcttgtttcttttct
gtggctgcgtgaaagccttgaggggctccgggagggcccttttgtgcgggggagcggctcgggggtgcg
tgcgtgtgtgtgtgcgtggggagcgccgcgtgcggctccgcgctgcccggcggctgtgagcgctgcgggcg
cggcgcggggctttgtgcgctccgcagtgtgcgcgaggggagcgcggccgggggcggtgccccgcggtgc
gggggggggctgcgaggggaacaaaggctgcgtgcggggtgtgtgcgtgggggggtgagcaggggtgtg
ggcgcgtcggtcgggctgcaacccccccctgcacccccctccccgagttgctgagcacggcccggcttcgggt
gcggggctccgtacggggcgtggcgcggggctcgccgtgccgggcgggggggtggcggcaggtgggggtgc
cgggcggggcggggccgcctcgggccggggagggctcgggggagggggcgcggcggccccggagcgccg
gcggctgtcgaggcgcggcgagccgcagccattgccttttatggtaatcgtgcgagagggcgcagggactt
cctttgtcccaaatctgtgcggagccgaaatctgggaggcgccgccgcaccccctctagcgggcgcggggc
gaagcggtgcggcgccggcaggaaggaaatgggcggggagggccttcgtgcgtcgccgcgccgccgtccc
cttctccctctccagcctcggggctgtccgcgggggacggctgccttcgggggggacggggcagggcggg
gttcggcttctggcgtgtgaccggcggctctagagcctctgctaaccatgttcatgccttcttcttttcctac
agctcctgggcaacgtgctggttattgtgctgtctcatcattttggcaaagaattcggtaccgcgggcccgg
ggccaccatggcgggcagctctgtcagttccgtgccgaccaaactggaagtggttgcggccaccccgacgt
ctctgctgatcagctgggatgcagggcctcgtaatgtcagttattaccgtatcacctatggcgaaacgggcg
gtaactccccggttcaggaattcaccgtcccgggtagttcctcaaccgcaacgatttccggcctgtcaccgg
gtgtcgactataccattacggtttacgcttctggtcatgttagtacgctgatgacgccgatttctatcaatta
ccgtaccggtagcggctccagtagatctggtagcggcgtgagcaagggcgaggagctgttcaccggggtg
gtgcccatcctggtcgagctggacggcgacgtaaacggccacaagttcagcgtgtccggcgagggcgagg
gcgatgccacctacggcaagctgaccctgaagttcatctgcaccaccggcaagctgcccgtgccctggccca
ccctcgtgaccaccctgtcctggggcgtgcagtgcttcgcccgctaccccgaccacatgaagcagcacgact
tcttcaagtccgccatgcccgaaggctacgtccaggagcgcaccatcttcttcaaggacgacggcaactac
aagacccgcgccgaggtgaagttcgagggcgacaccctggtgaaccgcatcgagctgaagggcatcgact
tcaaggaggacggcaacatcctggggcacaagctggagtacaactactttagcgacaacgtctatatcacc
gccgacaagcagaagaacggcatcaaggccaacttcaagatccgccacaacatcgaggacggcggcgtgc
agctcgccgaccactaccagcagaacaccccccatcggcgacggccccgtgctgctgcccgacaaccactac
ctgagcacccagtccaagctgagcaaagaccccaacgagaagcgcgatcacatggtcctgctggagttcgt
gaccgccgccgggatcactctcggcatggacgagctgtacaagggtagcggctcctctgctagcggagctg
gcgctggagcgggtgcaggggctggctctagattccagtgccggatctgcatgcggaacttcagcgaccgg
tccaacctgagcaggcacatcagaacccacaccggagaaaagcccttcgcctgcgacatttgcggccggaa
gttcgccatcagcagcaacctgaacagccacaccaagatccacactggcagccagaaaccctttccagtgca
gaatttgtatgagaaactttagcagaagcgacaacctggccagacacatccggacacatactggtgaaaa
acctttgcctgtgatatctgtggcagaaagtttgccacctccggcaatctgacccggcacacaaagattca

cctgcggggcagccagctatcgattgtcgacgctcctgaacaacgtgaaggtgcttctcaagtttctgtttct
gttacttttgaagatgttgctgttctttttactcgtgatgaatggaaaaaacttgatctttctcaacgttctctt
tatcgtgaagttatgcttgaaaattattctaatcttgcttctatggcttaaacgcgttgtacaagtaaagcgg
ccccggactcgaggccgcaggtaagtatcaaggttacaagacaggtttaaggagaccaatagaaactggg
cttgtcgagacagagaagactcttgcgtttctgataggcacctattggtcttactgacatccactttgcctttc
tctccacaggtgtcgacaatcaacctctggattacaaaatttgtgaaagattgactggtattcttaactatgt
tgctccttttacgctatgtggatacgctgctttaatgcctttgtatcatgctattgcttcccgtatggctttcat
tttctcctccttgtataaatcctggttgctgtctctttatgaggagttgtggcccgttgtcaggcaacgtggcg
tggtgtgcactgtgtttgctgacgcaacccccactggttggggcattgccaccacctgtcagctcctttccgg
gactttcgctttcccctccctattgccacggcggaactcatcgccgcctgccttgcccgctgctggacaggg
gctcggctgttgggcactgacaattccgtggtgttgtcggggaagctgacgtcctttccatggctgctcgcct
gtgttgccacctggattctgcgcgggacgtccttctgctacgtcccttcggccctcaatccagcggaccttcc
ttcccgcggcctgctgccggctctgcggcctcttccgcgtcttcgccttcgccctcagacgagtcggatctccc
tttgggccgcctccccgcctggaattcgagctcggtacgatcagcctcgactgtgccttctagttgccagcca
tctgttgtttgcccctcccccgtgccttccttgaccctggaaggtgccactcccactgtcctttcctaataaaa
tgaggaaattgcatcgcattgtctgagtaggtgtcattctattctgggggggtggggtggggcaggacagca
agggggaggattgggaagacaatagcccagcttttgttccctttagtgagggttaattgcgcgcttggcgta
atcatggtcatmssykwwtycwstsykmarktgcaggctgcctatcagaaggtggtggctggtgtggcc
aatgccctggctcacaaataccactgagatcgatctttttccctctgccaaaaattatggggacatcatgaa
gccccttgagcatctgacttctggctaataaaggaaatttatttttcattgcaatagtgtgttggaatttttgt
gtctctcactcggaaggacatatgggagggcaaatcatttaaaacatcagaatgagtatttggtttagagtt
tggcaacatatgcccatatgctggctgccatgaacaaaggttggctataaagaggtcatcagtatatgaaa
cagccccctgctgtccattccttattccatagaaaagccttgacttgaggttagatttttttatatttgtttt
gtgttatttttttctttaacatccctaaaatttccttacatgttttactagccagatttttcctcctctcctgac
tactcccagtcatagctgtccctcttctcttatggagatccctcgacctgcagcccaagcttggcgtaatcat
ggtcatagctgtttcctgtgtgaaattgttatccgctcacaattccacacaacatacgagccggaagcataa
agtgtaaagcctggggtgcctaatgagtgagctaactcacattaattgcgttgcgctcactgcccgctttcc
agtcgggaaacctgtcgtgccagcggatccgcatctcaattagtcagcaaccatagtcccgcccctaactcc
gcccatcccgcccctaactccgcccagttccgcccattctccgccccatggctgactaatttttttttatttatg
cagaggccgaggccgcctcggcctctgagctattccagaagtagtgaggaggctttttggaggcctaggc
ttttgcaaaaagctaacttgtttattgcagcttataatggttacaaataaagcaatagcatcacaaatttcac
aaataaagcatttttttcactgcattctagttgtggtttgtccaaactcatcaatgtatcttatcatgtctgga
tccgctgcattaatgaatcggccaacgcgcggggagaggcggtttgcgtattgggcgctcttccgcttcctc
gctcactgactcgctgcgctcggtcgttcggctgcggcgagcggtatcagctcactcaaaggcggtaatacg
gttatccacagaatcaggggataacgcaggaaagaacatgtgagcaaaaggccagcaaaaggccaggaa
ccgtaaaaaggccgcgttgctggcgtttttccataggctccgccccctgacgagcatcacaaaaatcgacg
ctcaagtcagaggtggcgaaacccgacaggactataaagataccaggcgtttcccccctggaagctccctcg
tgcgctctcctgttccgaccctgccgcttaccggatacctgtccgcctttctcccttcgggaagcgtggcgctt

tctcatagctcacgctgtaggtatctcagttcggtgtaggtcgttcgctccaagctgggctgtgtgcacgaac
cccccgttcagcccgaccgctgcgccttatccggtaactatcgtcttgagtccaacccggtaagacacgactt
atcgccactggcagcagccactggtaacaggattagcagagcgaggtatgtaggcggtgctacagagttct
tgaagtggtggcctaactacggctacactagaagaacagtatttggtatctgcgctctgctgaagccagtta
ccttcggaaaaagagttggtagctcttgatccggcaaacaaaccaccgctggtagcggtggttttttgtttt
gcaagcagcagattacgcgcagaaaaaaaggatctcaagaagatcctttgatcttttctacggggtctgac
gctcagtggaacgaaaactcacgttaagggattttggtcatgagattatcaaaaaggatcttcacctagatc
cttttaaattaaaaatgaagttttaaatcaatctaaagtatatatgagtaaacttggtctgacagttaccaa
tgcttaatcagtgaggcacctatctcagcgatctgtctatttcgttcatccatagttgcctgactccccgtcgt
gtagataactacgatacgggagggcttaccatctggccccagtgctgcaatgataccgcgagacccacgct
caccggctccagatttatcagcaataaaccagccagccggaagggccgagcgcagaagtggtcctgcaact
ttatccgcctccatccagtctattaattgttgccgggaagctagagtaagtagttcgccagttaatagtttgc
gcaacgttgttgccattgctacaggcatcgtggtgtcacgctcgtcgtttggtatggcttcattcagctccgg
ttcccaacgatcaaggcgagttacatgatcccccatgttgtgcaaaaaagcggttagctccttcggtcctcc
gatcgttgtcagaagtaagttggccgcagtgttatcactcatggttatggcagcactgcataattctcttact
gtcatgccatccgtaagatgcttttctgtgactggtgagtactcaaccaagtcattctgagaatagtgtatgc
ggcgaccgagttgctcttgcccggcgtcaatacgggataataccgcgccacatagcagaactttaaaagtg
ctcatcattggaaaacgttcttcggggcgaaaactctcaaggatcttaccgctgttgagatccagttcgatg
taacccactcgtgcacccaactgatcttcagcatcttttactttcaccagcgtttctgggtgagcaaaaacag
gaaggcaaaatgccgcaaaaaagggaataagggcgacacggaaatgttgaatactcatactcttccttttt
caatattattgaagcatttatcagggttattgtctcatgagcggatacatatttgaatgtatttagaaaaata
aacaaatagggttccgcgcacatttccccgaaaagtgccacctg

pENN.AAV.CAG.tdTomato.WPRE.SV40

ctgcgcgctcgctcgctcactgaggccgcccgggcaaagcccgggcgtcgggcgacctttggtcgcccggc
ctcagtgagcgagcgagcgcgcagagagggagtggccaactccatcactaggggttccttgtagttaatga
ttaacccgccatgctacttatctacgtagccatgctctaggaagagtaccattgacgtcaataatgacgtat
gttcccatagtaacgccaatagggactttccattgacgtcaatgggtggagtatttacggtaaactgcccac
ttggcagtacatcaagtgtatcatatgccaagtacgccccctattgacgtcaatgacggtaaatggcccgcc
tggcattatgcccagtacatgaccttatgggactttcctacttggcagtacatctacgtattagtcatcgcta
ttaccatggtcgaggtgagccccacgttctgcttcactctccccatctccccccccctccccacccccaattttg
tatttatttatttttttaattattttgtgcagcgatgggggcgggggggggggggggcgcgcgccaggcgggg
gcggggcggggcgaggggcggggcggggcgaggcggagaggtgcggcggcagccaatcagagcggcgc
gctccgaaagtttccttttatggcgaggcggcggcggcggccctataaaaagcgaagcgcgcggcggg
gcgggagtcgctgcgcgctgccttcgccccgtgccccgctccgccgccgcctcgcgccgcccgccccggctc
tgactgaccgcgttactcccacaggtgagcgggcgggacggcccttctcctccgggctgtaattagcgcttg
gtttaatgacggcttgtttcttttctgtggctgcgtgaaagccttgaggggctccgggagggccctttgtgcg

ggggggagcggctcggggctgtccgcgggggggacggctgccttcgggggggacggggcagggcggggttc
ggcttctggcgtgtgaccggcggctctagagcctctgctaaccatgttcatgccttcttcttttttcctacagct
cctgggcaacgtgctggttattgtgctgtctcatcattttggcaaagaattggatcccgccaccatggtgagc
aagggcgaggaggtcatcaaagagttcatgcgcttcaaggtgcgcatggagggctccatgaacggccacg
agttcgagatcgagggcgagggcgagggccgcccctacgagggcacccagaccgccaagctgaaggtga
ccaagggcggccccctgcccttcgcctgggacatcctgtccccccagttcatgtacggctccaaggcgtacg
tgaagcaccccgccgacatccccgattacaagaagctgtccttccccgagggcttcaagtgggagcgcgtg
atgaacttcgaggacggcggtctggtgaccgtgacccaggactcctccctgcaggacggcacgctgatcta
caaggtgaagatgcgcggcaccaacttcccccccgacggccccgtaatgcagaagaagaccatgggctgg
gaggcctccaccgagcgcctgtacccccgcgacggcgtgctgaagggcgagatccaccaggccctgaagc
tgaaggacggcggccactacctggtggagttcaagaccatctacatggccaagaagcccgtgcaactgccc
ggctactactacgtggacaccaagctggacatcacctcccacaacgaggactacaccatcgtggaacagta
cgagcgctccgagggccgccaccacctgttcctggggcatggcaccggcagcaccggcagcggcagctccg
gcaccgcctcctccgaggacaacaacatggccgtcatcaaagagttcatgcgcttcaaggtgcgcatggag
ggctccatgaacggccacgagttcgagatcgagggcgagggcgagggccgcccctacgagggcacccaga
ccgccaagctgaaggtgaccaagggcggccccctgcccttcgcctgggacatcctgtccccccagttcatgt
acggctccaaggcgtacgtgaagcaccccgccgacatccccgattacaagaagctgtccttccccgagggc
ttcaagtgggagcgcgtgatgaacttcgaggacggcggtctggtgaccgtgacccaggactcctccctgca
ggacggcacgctgatctacaaggtgaagatgcgcggcaccaacttcccccccgacggccccgtaatgcaga
agaagaccatgggctgggaggcctccaccgagcgcctgtacccccgcgacggcgtgctgaagggcgagat
ccaccaggccctgaagctgaaggacggcggccgctacctggtggagttcaagaccatctacatggccaaga
agcccgtgcaactgcccggctactactacgtggacaccaagctggacatcacctcccacaacgaggactac
accatcgtggaacagtacgagcgctccgagggccgccaccacctgttcctgtacggcatggacgagctgta
caagtaagaattcgaagcttatcgataatcaacctctggattacaaaatttgtgaaagattgactggtattc
ttaactatgttgctccttttacgctatgtggatacgctgctttaatgcctttgtatcatgctattgcttcccgta
tggctttcattttctcctccttgtataaatcctggttgctgtctctttatgaggagttgtggcccgttgtcaggc
aacgtggcgtggtgtgcactgtgtttgctgacgcaacccccactggttggggcattgccaccacctgtcagc
tcctttccgggactttcgctttcccctccctattgccacggcggaactcatcgccgcctgccttgcccgctgc
tggacaggggctcggctgttgggcactgacaattccgtggtgttgtcggggaaatcatcgtcctttccttggg
ctgctcgcctgtgttgccacctggattctgcgcgggacgtccttctgctacgtcccttcggccctcaatccagc
ggaccttccttcccgcggcctgctgccggctctgcggcctcttccgcgtcttcgccttcgccctcagacgagtc
ggatctccctttgggccgcctccccgcatcgataccgtcgacccgggcggccgcttcgagcagacatgataa
gatacattgatgagtttggacaaaccacaactagaatgcagtgaaaaaaatgctttatttgtgaaatttgtg
atgctattgctttatttgtaaccattataagctgcaataaacaagttaacaacaacaattgcattcattttat
gtttcaggttcaggggagatgtgggaggtttttaaagcaagtaaaacctctacaaatgtggtaaaatcg
ataaggatcttcctagagcatggctacgtagataagtagcatggcgggttaatcattaactacaaggaacc
cctagtgatggagttggccactccctctctgcgcgctcgctcgctcactgaggccgggcgaccaaaggtcgc
ccgacgcccgggctttgcccgggcggcctcagtgagcgagcgagcgcgcagctgcattaatgaatcggcca

acgcgcggggagaggcggtttgcgtattgggcgctcttccgcttcctcgctcactgactcgctgcgctcggtc
gttcggctgcggcgagcggtatcagctcactcaaaggcggtaatacggttatccacagaatcaggggataa
cgcaggaaagaacatgtgagcaaaaggccagcaaaaggccaggaaccgtaaaaaggccgcgttgctggc
gtttttccataggctccgccccctgacgagcatcacaaaaatcgacgctcaagtcagaggtggcgaaacc
cgacaggactataaagataccaggcgtttcccccctggaagctccctcgtgcgctctcctgttccgaccctgcc
gcttaccggatacctgtccgcctttctcccttcgggaagcgtggcgctttctcatagctcacgctgtaggtat
ctcagttcggtgtaggtcgttcgctccaagctgggctgtgtgcacgaaccccccgttcagcccgaccgctgc
gccttatccggtaactatcgtcttgagtccaacccggtaagacacgacttatcgccactggcagcagccact
ggtaacaggattagcagagcgaggtatgtaggcggtgctacagagttcttgaagtggtggcctaactacgg
ctacactagaagaacagtatttggtatctgcgctctgctgaagccagttaccttcggaaaaagagttggtag
ctcttgatccggcaaacaaaccaccgctggtagcggtggtttttttgtttgcaagcagcagattacgcgcag
aaaaaaaggatctcaagaagatcctttgatcttttctacggggtctgacgctcagtggaacgaaaactcac
gttaagggattttggtcatgagattatcaaaaaggatcttcacctagatccttttaaattaaaaatgaagtt
ttaaatcaatctaaagtatatatgagtaaacttggtctgacagttaccaatgcttaatcagtgaggcaccta
tctcagcgatctgtctatttcgttcatccatagttgcctgactccccgtcgtgtagataactacgatacggga
gggcttaccatctggccccagtgctgcaatgataccgcgagacccacgctcaccggctccagatttatcagc
aataaaccagccagccggaagggccgagcgcagaagtggtcctgcaactttatccgcctccatccagtcta
ttaattgttgccgggaagctagagtaagtagttcgccagttaatagtttgcgcaacgttgttgccattgctac
aggcatcgtggtgtcacgctcgtcgtttggtatggcttcattcagctccggttcccaacgatcaaggcgagtt
acatgatcccccatgttgtgcaaaaaagcggttagctccttcggtcctccgatcgttgtcagaagtaagttg
gccgcagtgttatcactcatggttatggcagcactgcataattctcttactgtcatgccatccgtaagatgct
tttctgtgactggtgagtactcaaccaagtcattctgagaatagtgtatgcggcgaccgagttgctcttgccc
ggcgtcaatacgggataataccgcgccacatagcagaactttaaaagtgctcatcattggaaaacgttcttc
ggggcgaaaactctcaaggatcttaccgctgttgagatccagttcgatgtaacccactcgtgcacccaactg
atcttcagcatcttttactttcaccagcgtttctgggtgagcaaaaacaggaaggcaaaatgccgcaaaaa
agggaataagggcgacacggaaatgttgaatactcatactcttccttttcaatattattgaagcatttatca
gggttattgtctcatgagcggatacatatttgaatgtatttagaaaaataaacaaataggggttccgcgcac
atttccccgaaaagtgccacctaaattgtaagcgttaatattttgttaaaattcgcgttaaatttttgttaaat
cagctcatttttaaccaataggccgaaatcggcaaaatcccttataaatcaaaagaatagaccgagatag
ggttgagtgttgttccagtttggaacaagagtccactattaaagaacgtggactccaacgtcaaagggcga
aaaaccgtctatcagggcgatggcccactacgtgaaccatcaccctaatcaagttttttggggtcgaggtgc
cgtaaagcactaaatcggaaccctaaagggagcccccgatttagagcttgacggggaaagccggcgaacg
tggcgagaaaggaagggaagaaagcgaaaggagcgggcgctagggcgctggcaagtgtagcggtcacgc
tgcgcgtaaccaccacacccgccgcgcttaatgcgccgctacagggcgcgtcccattcgccattcaggctgc
gcaactgttgggaagggcgatcggtgcgggcctcttcgctattacgccag

pGP-AAV-syn-jGCaMP7b-WPRE

gttgggaagggcgatcggtgcgggcctcttcgctattacgccagctgcgcgctcgctcgctcactgaggccg
cccgggcaaagcccgggcgtcgggcgacctttggtcgcccggcctcagtgagcgagcgagcgcgcagaga
gggagtggccaactccatcactaggggttccttgtagttaatgattaacccgccatgctacttatctacgtag
ccatgctctaggaagatctctgcagagggccctgcgtatgagtgcaagtgggttttaggaccaggatgagg
cggggtgggggtgcctacctgacgaccgaccccgacccactggacaagcacccaaccccattccccaaat
tgcgcatcccctatcagagagggggaggggaaacaggatgcggcgaggcgcgtgcgcactgccagcttca
gcaccgcggacagtgccttcgccccgcctggcggcgcgccaccgccgcctcagcactgaaggcgcgct
gacgtcactcgccggtcccccgcaaactcccctccgggccaccttggtcgcgtccgcgccgccgccggccc
agccggaccgcaccacgcgaggcgcgagataggggggcacgggcgcgaccatctgcgctgcggcgccggc
gactcagcgctgcctcagtctgcggtgggcagcggaggagtcgtgtcgtgcctgagagcgcagtcgaattc
aagctgctagcaaggatccacccgccaccatgggttctcatcatcatcatcatcatggtatggctagcatga
ctggtggacagcaaatgggtcgggatctgtacgacgatgacgataaggatctcgccaccatggtcgactca
tcacgtcgtaagtggaataagacaggtcacgcagtcagagctataggtcggctgagctcactcgagaacgt
ctatatcaaggccgacaagcagaagaacggcatcaaggcgaacttcaagatccgccacaacatcgaggac
ggcggcgtgcagctcgcctaccactaccagcagaacacccccatcggcgacggccccgtgctgctgcccga
caaccactacctgagcgtgcagtccaaactttcgaaagaccccaacgagaagcgcgatcacatggtcctgc
tggagttcgtgaccgccgccgggatcactctcggcatggacgagctgtacaagggcggtaccggagggag
catggtgagcaagggcgaggagctgttcaccggggtggtgcccatcctggtcgagctggacggcgacgta
aacggccacaagttcagcgtgtccggcgagggtgagggcgatgccacctacggcaagctgaccctgaagt
tcatctgcaccaccggcaagctgcccgtgccctggcccaccctcgtgaccaccctgacctacggcgtgcagt
gcttcagccgctaccccgaccacatgaagcagcacgacttcttcaagtccgccatgcccgaaggctacatcc
aggagcgcaccatcttcttcaaggacgacggcaactacaagacccgcgccgaggtgaagttcgagggcga
caccctggtgaaccgcatcgagcttaagggcatcgacttcaaggaggacggcaacatcctggggcacaag
ctggagtacaacccacctgaccaactgactgaagagcagatcgcagaatttaaagagcttttctccctattt
gacaaggacggggatgggacaataacaaccaaggagctggggacggtgatgcggtctctggggcagaac
cccacagaagcagagctgcaggacatgatcaatgaagtagatgccgacggtgacggcacaatcgacttcc
ctgagttcctgacaatgtacgcaagaaaaatgaaatacagggacacggaagaagaaattagagaagcgtt
cggtgtgtttgataaggatggcaatggctacatcagtgcagcagagcttcgccacgtgatgacaaaccttg
gagagaagttaacagatgaagaggttgatgaaatgatcagggaagcagacatcgatggggatggtcagg
taaactacgaagagtttgtacaaatgatgacagcgaagtgaaagcttatcgataatcaacctctggattac
aaaatttgtgaaagattgactggtattcttaactatgttgctccttttacgctatgtggatacgctgctttaat
gcctttgtatcatgctattgcttcccgtatggctttcattttctcctccttgtataaatcctggttgctgtctctt
tatgaggagttgtggcccgttgtcaggcaacgtggcgtggtgtgcactgtgtttgctgacgcaacccccact
ggttggggcattgccaccacctgtcagctcctttccgggactttcgctttcccctccctattgccacggcgg
aactcatcgccgcctgccttgcccgctgctggacaggggctcggctgttgggcactgacaattccgtggtgt
tgtcggggaaatcatcgtcctttccttggctgctcgcctgtgttgccacctggattctgcgcgggacgtcctt

ctgctacgtcccttcggccctcaatccagcggaccttccttcccgcggcctgctgccggctctgcggcctcttc
cgcgtcttcgccttcgccctcagacgagtcggatctccctttgggccgcctccccgcatcgataccgtcgacc
tcgacccgggcggccgcttcgagcagacatgataagatacattgatgagtttggacaaaccacaactagaa
tgcagtgaaaaaaatgctttatttgtgaaatttgtgatgctattgctttatttgtaaccattataagctgcaa
taaacaagttaacaacaacaattgcattcattttatgtttcaggttcaggggagatgtgggaggtttttta
aagcaagtaaaacctctacaaatgtggtaaaatcgataaggatcttcctagagcatggctacgtagataag
tagcatggcgggttaatcattaactacaaggaacccctagtgatggagttggccactccctctctgcgcgct
cgctcgctcactgaggccgggcgaccaaaggtcgcccgacgcccgggctttgcccgggcggcctcagtgag
cgagcgagcgcgcagctgcattaatgaatcggccaacgcgcggggagaggcggtttgcgtattgggcgctc
ttccgcttcctcgctcactgactcgctgcgctcggtcgttcggctgcggcgagcggtatcagctcactcaaag
gcggtaatacggttatccacagaatcaggggataacgcaggaaagaacatgtgagcaaaaggccagcaa
aaggccaggaaccgtaaaaaggccgcgttgctggcgtttttccataggctccgccccctgacgagcatca
caaaaatcgacgctcaagtcagaggtggcgaaacccgacaggactataaagataccaggcgtttcccccctg
gaagctccctcgtgcgctctcctgttccgaccctgccgcttaccggatacctgtccgcctttctcccttcggga
agcgtggcgctttctcatagctcacgctgtaggtatctcagttcggtgtaggtcgttcgctccaagctgggct
gtgtgcacgaacccccgttcagcccgaccgctgcgccttatccggtaactatcgtcttgagtccaacccgg
taagacacgacttatcgccactggcagcagccactggtaacaggattagcagagcgaggtatgtaggcgg
tgctacagagttcttgaagtggtggcctaactacggctacactagaagaacagtatttggtatctgcgctct
gctgaagccagttaccttcggaaaaagagttggtagctcttgatccggcaaacaaaccaccgctggtagcg
gtggtttttttgtttgcaagcagcagattacgcgcagaaaaaaaggatctcaagaagatcctttgatcttttc
tacggggtctgacgctcagtggaacgaaaactcacgttaagggattttggtcatgagattatcaaaaagga
tcttcacctagatccttttaaattaaaaatgaagttttaaatcaatctaaagtatatatgagtaaacttggtc
tgacagttaccaatgcttaatcagtgaggcacctatctcagcgatctgtctatttcgttcatccatagttgcc
tgactccccgtcgtgtagataactacgatacgggagggcttaccatctggccccagtgctgcaatgataccg
cgagacccacgctcaccggctccagatttatcagcaataaaccagccagccggaagggccgagcgcagaa
gtggtcctgcaactttatccgcctccatccagtctattaattgttgccgggaagctagagtaagtagttcgcc
agttaatagtttgcgcaacgttgttgccattgctacaggcatcgtggtgtcacgctcgtcgtttggtatggct
tcattcagctccggttcccaacgatcaaggcgagttacatgatcccccatgttgtgcaaaaaagcggttagc
tccttcggtcctccgatcgttgtcagaagtaagttggccgcagtgttatcactcatggttatggcagcactgc
ataattctcttactgtcatgccatccgtaagatgcttttctgtgactggtgagtactcaaccaagtcattctga
gaatagtgtatgcggcgaccgagttgctcttgcccggcgtcaatacgggataataccgcgccacatagcag
aactttaaaagtgctcatcattggaaaacgttcttcggggcgaaaactctcaaggatcttaccgctgttgag
atccagttcgatgtaacccactcgtgcacccaactgatcttcagcatcttttactttcaccagcgtttctgggt
gagcaaaaacaggaaggcaaaatgccgcaaaaaagggaataagggcgacacggaaatgttgaatactca
tactcttccttttcaatattattgaagcatttatcagggttattgtctcatgagcggatacatatttgaatgt
atttagaaaaataaacaaatagggttccgcgcacatttccccgaaaagtgccacctaaattgtaagcgtt
aatattttgttaaaattcgcgttaaatttttgttaaatcagctcatttttaaccaataggccgaaatcggca
aaatcccttataaatcaaaagaatagaccgagatagggttgagtgttgttccagtttggaacaagagtcca

ctattaaagaacgtggactccaacgtcaaagggcgaaaaaccgtctatcagggcgatggcccactacgtga
accatcaccctaatcaagtttttggggtcgaggtgccgtaaagcactaaatcggaaccctaaagggagcc
cccgatttagagcttgacggggaaagccggcgaacgtggcgagaaaggaagggaagaaagcgaaagga
gcgggcgctagggcgctggcaagtgtagcggtcacgctgcgcgtaaccaccacacccgccgcgcttaatgc
gccgctacagggcgcgtcccattcgccattcaggctgcgcaact

pAAV-Syn-Chronos-GFP

cttccgcttcctcgctcactgactcgctgcgctcggtcgttcggctgcggcgagcggtatcagctcactcaaa
ggcggtaatacggttatccacagaatcaggggataacgcaggaaagaacatgtgagcaaaaggccagca
aaaggccaggaaccgtaaaaaggccgcgttgctggcgtttttccataggctccgccccctgacgagcatc
acaaaaatcgacgctcaagtcagaggtggcgaaacccgacaggactataaagataccaggcgtttccccc
tggaagctccctcgtgcgctctcctgttccgaccctgccgcttaccggatacctgtccgcctttctcccttcgg
gaagcgtggcgctttctcatagctcacgctgtaggtatctcagttcggtgtaggtcgttcgctccaagctggg
ctgtgtgcacgaaccccccgttcagcccgaccgctgcgccttatccggtaactatcgtcttgagtccaacccg
gtaagacacgacttatcgccactggcagcagccactggtaacaggattagcagagcgaggtatgtaggcg
gtgctacagagttcttgaagtggtggcctaactacggctacactagaagaacagtatttggtatctgcgctc
tgctgaagccagttaccttcggaaaaagagttggtagctcttgatccggcaaacaaaccaccgctggtagc
ggtggtttttttgtttgcaagcagcagattacgcgcagaaaaaaaggatctcaagaagatcctttgatcttt
tctacggggtctgacgctcagtggaacgaaaactcacgttaagggattttggtcatgagattatcaaaaag
gatcttcacctagatccttttaaattaaaaatgaagttttaaatcaatctaaagtatatatgagtaaacttgg
tctgacagttaccaatgcttaatcagtgaggcacctatctcagcgatctgtctatttcgttcatccatagttg
cctgactccccgtcgtgtagataactacgatacgggagggcttaccatctggccccagtgctgcaatgatac
cgcgagacccacgctcaccggctccagatttatcagcaataaaccagccagccggaagggccgagcgcag
aagtggtcctgcaactttatccgcctccatccagtctattaattgttgccgggaagctagagtaagtagttcg
ccagttaatagtttgcgcaacgttgttgccattgctacaggcatcgtggtgtcacgctcgtcgtttggtatgg
cttcattcagctccggttcccaacgatcaaggcgagttacatgatcccccatgttgtgcaaaaaagcggtta
gctccttcggtcctccgatcgttgtcagaagtaagttggccgcagtgttatcactcatggttatggcagcact
gcataattctcttactgtcatgccatccgtaagatgcttttctgtgactggtgagtactcaaccaagtcattct
gagaatagtgtatgcggcgaccgagttgctcttgcccggcgtcaatacgggataataccgcgccacatagc
agaactttaaaagtgctcatcattggaaaacgttcttcggggcgaaaactctcaaggatcttaccgctgttg
agatccagttcgatgtaacccactcgtgcacccaactgatcttcagcatcttttactttcaccagcgtttctgg
gtgagcaaaaacaggaaggcaaaatgccgcaaaaaagggaataagggcgacacggaaatgttgaatact
catactcttcctttttcaatattattgaagcatttatcagggttattgtctcatgagcggatacatatttgaat
gtatttagaaaaataaacaaatagggttccgcgcacatttccccgaaaagtgccacctaaattgtaagcg
ttaatattttgttaaaattcgcgttaaatttttgttaaatcagctcatttttaaccaataggccgaaatcggc
aaaatcccttataaatcaaaagaatagaccgagatagggttgagtgttgttccagtttggaacaagagtcc
actattaaagaacgtggactccaacgtcaaagggcgaaaaaccgtctatcagggcgatggcccactacgtg

aaccatcaccctaatcaagttttttggggtcgaggtgccgtaaagcactaaatcggaaccctaaagggagc
ccccgatttagagcttgacggggaaagccggcgaacgtggcgagaaaggaagggaagaaagcgaaagga
gcgggcgctagggcgctggcaagtgtagcggtcacgctgcgcgtaaccaccacacccgccgcgcttaatgc
gccgctacagggcgcgtcccattcgccattcaggctgcgcaactgttgggaagggcgatcggtgcgggcct
cttcgctattacgccagctgcgcgctcgctcgctcactgaggccgcccgggcaaagcccgggcgtcgggcg
acctttggtcgcccggcctcagtgagcgagcgagcgcgcagagagggagtggccaactccatcactaggg
gttccttgtagttaatgattaacccgccatgctacttatctacgtagccatgctctaggaagatcgtaggtta
attaatctagactgcagagggccctgcgtatgagtgcaagtgggttttaggaccaggatgaggcggggtgg
gggtgcctacctgacgaccgaccccgacccactggacaagcacccaacccccattccccaaattgcgcatcc
cctatcagagaggggagggaaacaggatgcggcgaggcgcgtgcgcactgccagcttcagcaccgcgg
acagtgccttcgcccccgcctggcggcgcgcgccaccgccgcctcagcactgaaggcgcgctgacgtcactc
gccggtcccccgcaaactcccctttcccggccaccttggtcgcgtccgcgccgccgccggcccagccggaccg
caccacgcgaggcgcgagataggggggcacgggcgcgaccatctgcgctgcggcgccggcgactcagcgc
tgcctcagtctgcggtgggcagcggaggagtcgtgtcgtgcctgagagcgcagtcgagaggatccgccacc
atggaaacagccgccacaatgacccacgcctttatctcagccgtgcctagcgccgaagccacaattagagg
cctgctgagcgccgcagcagtggtgacaccagcagcagacgctcacggagaaacctctaacgccacaaca
gccggagccgatcacggttgcttcccccacatcaaccacggaaccgagctgcagcacaagatcgcagtggg
actccagtggttcaccgtgatcgtggctatcgtgcagctcatcttctacggttggcacagcttcaaggccaca
accggctgggaggaggtctacgtctgcgtgatcgagctcgtcaagtgcttcatcgagctgttccacgaggtc
gacagcccagccacagtgtaccagaccaacggaggagccgtgatttggctgcggtacagcatgtggctcct
gacttgccccgtgatcctgatccacctgagcaacctgaccggactgcacgaagagtacagcaagcggacca
tgaccatcctggtgaccgacatcggcaacatcgtgtgggggatcacagccgcctttacaaagggccccctg
aagatcctgttcttcatgatcggcctgttctacggcgtgacttgcttcttccagatcgccaaggtgtatatcg
agagctaccacaccctgcccaaaggcgtctgccggaagatttgcaagatcatggcctacgtcttcttctgct
cttggctgatgttccccgtgatgttcatcgccggacacgagggactgggcctgatcacaccttacaccagcg
gaatcggccacctgatcctggatctgatcagcaagaacacttggggcttcctgggccaccacctgagagtg
aagatccacgagcacatcctgatccacggcgacatccggaagacaaccaccatcaacgtggccggcgaga
acatggagatcgagaccttcgtcgacgaggaggaggagggaggagtggcggcaccggtagtagcagtga
gcaagggcgaggagctgttcaccggggtggtgcccatcctggtcgagctggacggcgacgtaaacggcca
caagttcagcgtgtccggcgagggcgagggcgatgccacctacggcaagctgaccctgaagttcatttgca
ccaccggcaagctgcccgtgccctggcccaccctcgtgaccaccctgacctacggcgtgcagtgcttcagcc
gctaccccgaccacatgaagcagcacgacttcttcaagtccgccatgcccgaaggctacgtccaggagcgc
accatcttcttcaaggacgacggcaactacaagacccgcgccgaggtgaagttcgagggcgacaccctggt
gaaccgcatcgagctgaagggcatcgacttcaaggaggacggcaacatcctggggcacaagctggagtac
aactacaacagccacaacgtctatatcatggccgacaagcagaagaacggcatcaaggtgaacttcaaga
tccgccacaacatcgaggacggcagcgtgcagctcgccgaccactaccagcagaacaccccatcggcgac
ggccccgtgctgctgcccgacaaccactacctgagcacccagtccgccctgagcaaagaccccaacgagaa
gcgcgatcacatggtcctgctggagttcgtgaccgccgccgggatcactctcggcatggacgagctgtaca

agtaagaattcgatatcaagcttatcgataatcaacctctggattacaaaatttgtgaaagattgactggta
ttcttaactatgttgctccttttacgctatgtggatacgctgctttaatgcctttgtatcatgctattgcttccc
gtatggctttcattttctcctccttgtataaatcctggttgctgtctctttatgaggagttgtggcccgttgtca
ggcaacgtggcgtggtgtgcactgtgtttgctgacgcaacccccactggttggggcattgccaccacctgtc
agctcctttccgggactttcgctttcccctccctattgccacggcggaactcatcgccgcctgccttgcccgc
tgctggacaggggctcggctgttgggcactgacaattccgtggtgttgtcggggaaatcatcgtcctttcctt
ggctgctcgcctgtgttgccacctggattctgcgcgggacgtccttctgctacgtcccttcggccctcaatcc
agcggaccttccttcccgcggcctgctgccggctctgcggcctcttccgcgtcttcgccttcgccctcagacg
agtcggatctccctttgggccgcctccccgcatcgataccgtcgacccgggcggccgctcataaagctcgac
tgtgccttctagttgccagccatctgttgtttgcccctcccccgtgccttccttgaccctggaaggtgccactc
ccactgtcctttcctaataaaatgaggaaattgcatcgcattgtctgagtaggtgtcattctattctgggggg
tggggtggggcaggacagcaagggggaggattgggaagacaatagcaggcatgctggggatgcggtccg
gactgtacaattgcattcattttatgtttcaggttcaggggggagatgtgggaggtttttaaagcaagtaaa
acctctacaaatgtggtaaaatcgataaggatcttcctagagcatggctacgtagataagtagcatggcgg
gttaatcattaactacaaggaacccctagtgatggagttggccactccctctctgcgcgctcgctcgctcact
gaggccgggcgaccaaaggtcgcccgacgcccgggctttgcccgggcggcctcagtgagcgagcgagcgc
gcagctgcattaatgaatcggccaacgcgcggggagaggcggtttgcgtattgggcgct

pAAV-Syn-ChrimsonR-tdT

gggcgatggcccactacgtgaaccatcaccctaatcaagtttttggggtcgaggtgccgtaaagcactaa
atcggaaccctaaagggagcccccgatttagagcttgacggggaaagccggcgaacgtggcgagaaagg
aagggaagaaagcgaaaggagcgggcgctagggcgctggcaagtgtagcggtcacgctgcgcgtaacca
ccacacccgccgcgcttaatgcgccgctacagggcgcgtcccattcgccattcaggctgcgcaactgttggg
aagggcgatcggtgcgggcctcttcgctattacgccagctgcgcgctcgctcgctcactgaggccgcccggg
caaagcccgggcgtcgggcgacctttggtcgcccggcctcagtgagcgagcgagcgcgcagagagggagt
ggccaactccatcactaggggttccttgtagttaatgattaacccgccatgctacttatctacgtagccatgc
tctaggaagatcgtaggttaattaatctagactgcagagggccctgcgtatgagtgcaagtgggttttagg
accaggatgaggcggggtgggggtgcctacctgacgaccgaccccgacccactggacaagcacccaaccc
ccattccccaaattgcgcatcccctatcagagaggggggaggggaaacaggatgcggcgaggcgcgtgcgc
actgccagcttcagcaccgcggacagtgccttcgcccccgcctggcggcgcgcgccaccgccgcctcagcac
tgaaggcgcgctgacgtcactcgccggtcccccgcaaactcccctttcccggccaccttggtcgcgtccgcgc
cgccgccggcccagccggaccgcaccacgcgaggcgcgagataggggggcacgggcgcgaccatctgcgc
tgcggcgccggcgactcagcgctgcctcagtctgcggtgggcagcggaggagtcgtgtcgtgcctgagagc
gcagtcgagaggatccgccaccatggctgagctgatcagcagcgccaccagatctctgtttgccgccggag
gcatcaacccttggcctaacccctaccaccacgaggacatgggctgtggaggaatgacacctacaggcgag
tgcttcagcaccgagtggtggtgtgacccttcttacggactgagcgacgccggatacggatattgcttcgtg
gaggccacaggcggctacctggtcgtgggagtggagaagaagcaggcttggctgcacagcagaggcacac

caggagaaaagatcggcgcccaggtctgccagtggattgctttcagcatcgccatcgccctgctgacattct
acggcttcagcgcctggaaggccacttgcggttgggaggaggtctacgtctgttgcgtcgaggtgctgttcg
tgaccctggagatcttcaaggagttcagcagccccgccacagtgtacctgtctaccggcaaccacgcctatt
gcctgcgctacttcgagtggctgctgtcttgccccgtgatcctgatcagactgagcaacctgagcggcctga
agaacgactacagcaagcggaccatgggcctgatcgtgtcttgcgtgggaatgatcgtgttcggcatggcc
gcaggactggctaccgattggctcaagtggctgctgtatatcgtgtcttgcatctacggcggctacatgtact
tccaggccgccaagtgctacgtggaagccaaccacagcgtgcctaaaggccattgccgcatggtcgtgaag
ctgatggcctacgcttacttcgcctcttggggcagctacccaatcctctgggcagtgggaccagaaggactg
ctgaagctgagcccttacgccaacagcatcggccacagcatctgcgacatcatcgccaaggagttttggac
cttcctggcccaccacctgaggatcaagatccacgagcacatcctgatccacggcgacatccggaagacca
ccaagatggagatcggaggcgaggaggtggaagtggaagagttcgtggaggaggaggacgaggacaca
gtggcggcaccggtagtagcagtgagtaagggcgaggaagtgatcaaagagttcatgcggtttaaggtga
gaatggaaggaagcatgaacggccacgagttcgaaattgagggagaaggagagggacggccctacgagg
gcacccagacagccaagctgaaagtgacaaagggcgggcctctgccattcgcttgggacatcctgagccca
cagtttatgtacggctccaaggcctatgtgaaacatccagctgacattcccgattataagaaactgagcttc
cccgaggggtttaagtgggaaagagtgatgaacttcgaggacggaggcctggtgactgtgacccaggaca
gctccctgcaggatgggaccctgatctacaaggtgaaaatgagagggacaaattttccccctgatggacct
gtgatgcagaagaaaactatgggatgggaggcctccaccgaaaggctgtatccacgcgacggggtgctga
aaggagaaatccaccaggctctgaagctgaaagatgggggacattacctggtggagttcaagacaatcta
catggccaagaaacctgtgcagctgccaggctactattacgtggacacaaaactggatatcacttcacaca
acgaggactacactattgtggagcagtatgaacggagcgaggggagacaccatctgttcctgggccatgg
gactggaagtaccggctcagggtctagtggaaccgcctcaagcgaggataacaatatggctgtgatcaaa
gagttcatgaggtttaaggtgcgcatggagggcagcatgaatgggcacgaatttgagattgaaggagagg
gcgaagggaggccttacgagggcacacagactgccaagctgaaagtgaccaagggaggaccactgccttt
cgcttgggatatcctgtctcctcagtttatgtacggaagtaaggcctatgtcaagcatcccgctgacattcct
gattacaagaaactgtctttcccagagggctttaagtgggagagagtgatgaattttgaagatggaggcct
ggtgaccgtgacacaggactcctctctgcaggatggcactctgatctacaaagtcaaaatgcgcggcacca
attttccacccgatgggcccgtgatgcagaagaaaacaatggggtgggaggccagcactgaacggctgtat
cctagagacggagtgctgaagggcgaaatccaccaggccctgaagctgaaagacggcggccactacctgg
tggagttcaaaaccatctacatggccaagaaaccagtgcagctgcccggctattactatgtggacaccaag
ctggatatcacatcccacaatgaagactacaccattgtggaacagtatgagaggtctgaaggacgccacca
tctgtttctgtacggcatggatgagctgtataagtaagaattcgatatcaagcttatcgataatcaacctctg
gattacaaaatttgtgaaagattgactggtattcttaactatgttgctccttttacgctatgtggatacgctg
ctttaatgcctttgtatcatgctattgcttcccgtatggctttcattttctcctccttgtataaatcctggttgct
gtctctttatgaggagttgtggcccgttgtcaggcaacgtggcgtggtgtgcactgtgtttgctgacgcaacc
cccactggttggggcattgccaccacctgtcagctcctttccgggactttcgctttcccctccctattgccac
ggcggaactcatcgccgcctgccttgcccgctgctggacaggggctcggctgttgggcactgacaattccgt
ggtgttgtcggggaaatcatcgtcctttccttggctgctcgcctgtgttgccacctggattctgcgcgggacg

tccttctgctacgtcccttcggccctcaatccagcggaccttccttcccgcggcctgctgccggctctgcggcc
tcttccgcgtcttcgccttcgccctcagacgagtcggatctccctttgggccgcctccccgcatcgataccgtc
gacccgggcggccgctcataaagctcgactgtgccttctagttgccagccatctgttgtttgcccctcccccg
tgccttccttgaccctggaaggtgccactcccactgtcctttcctaataaaatgaggaaattgcatcgcattg
tctgagtaggtgtcattctattctgggggggtggggtggggcaggacagcaagggggaggattgggaagac
aatagcaggcatgctggggatgcggtccggactgtacaattgcattcattttatgtttcaggttcagggggga
gatgtgggaggtttttaaagcaagtaaaacctctacaaatgtggtaaaatcgataaggatcttcctagag
catggctacgtagataagtagcatggcgggttaatcattaactacaaggaacccctagtgatggagttggc
cactccctctctgcgcgctcgctcgctcactgaggccgggcgaccaaaggtcgcccgacgcccgggctttgc
ccgggcggcctcagtgagcgagcgagcgcgcagctgcattaatgaatcggccaacgcgcggggagaggcgg
gtttgcgtattgggcgctcttccgcttcctcgctcactgactcgctgcgctcggtcgttcggctgcggcgagc
ggtatcagctcactcaaaggcggtaatacggttatccacagaatcaggggataacgcaggaaagaacatg
tgagcaaaaggccagcaaaaggccaggaaccgtaaaaaggccgcgttgctggcgtttttccataggctccg
ccccccctgacgagcatcacaaaaatcgacgctcaagtcagaggtggcgaaacccgacaggactataaaga
taccaggcgtttcccccctggaagctccctcgtgcgctctcctgttccgaccctgccgcttaccggatacctgtc
cgcctttctcccttcgggaagcgtggcgctttctcatagctcacgctgtaggtatctcagttcggtgtaggtc
gttcgctccaagctgggctgtgtgcacgaaccccccgttcagcccgaccgctgcgccttatccggtaactatc
gtcttgagtccaacccggtaagacacgacttatcgccactggcagcagccactggtaacaggattagcaga
gcgaggtatgtaggcggtgctacagagttcttgaagtggtggcctaactacggctacactagaagaacagt
atttggtatctgcgctctgctgaagccagttaccttcggaaaaagagttggtagctcttgatccggcaaaca
aaccaccgctggtagcggtggtttttttgtttgcaagcagcagattacgcgcagaaaaaaaggatctcaag
aagatcctttgatcttttctacggggtctgacgctcagtggaacgaaaactcacgttaagggattttggtca
tgagattatcaaaaaggatcttcacctagatccttttaaattaaaaatgaagttttaaatcaatctaaagta
tatatgagtaaacttggtctgacagttaccaatgcttaatcagtgaggcacctatctcagcgatctgtctatt
tcgttcatccatagttgcctgactccccgtcgtgtagataactacgatacgggagggcttaccatctggcccc
agtgctgcaatgataccgcgagacccacgctcaccggctccagatttatcagcaataaaccagccagccgg
aagggccgagcgcagaagtggtcctgcaactttatccgcctccatccagtctattaattgttgccgggaagc
tagagtaagtagttcgccagttaatagtttgcgcaacgttgttgccattgctacaggcatcgtggtgtcacg
ctcgtcgtttggtatggcttcattcagctccggttcccaacgatcaaggcgagttacatgatcccccatgttg
tgcaaaaaagcggttagctccttcggtcctccgatcgttgtcagaagtaagttggccgcagtgttatcactc
atggttatggcagcactgcataattctcttactgtcatgccatccgtaagatgcttttctgtgactggtgagt
actcaaccaagtcattctgagaatagtgtatgcggcgaccgagttgctcttgcccggcgtcaatacgggata
ataccgcgccacatagcagaactttaaaagtgctcatcattggaaaacgttcttcggggcgaaaactctca
aggatcttaccgctgttgagatccagttcgatgtaacccactcgtgcacccaactgatcttcagcatctttta
ctttcaccagcgtttctgggtgagcaaaaacaggaaggcaaaatgccgcaaaaaagggaataagggcgac
acggaaatgttgaatactcatactcttcctttttcaatattattgaagcatttatcagggttattgtctcatga
gcggatacatatttgaatgtatttagaaaaataaacaaatagggttccgcgcacatttccccgaaaagtg
ccacctaaattgtaagcgttaatattttgttaaaattcgcgttaaatttttgttaaatcagctcatttttaac

caataggccgaaatcggcaaaatcccttataaatcaaaagaatagaccgagatagggttgagtgttgttcc
agtttggaacaagagtccactattaaagaacgtggactccaacgtcaaagggcgaaaaaccgtctatca

Bibliography

Abadi, Martın et al. (2016). "Tensorflow: A system for large-scale machine learning". In: *12th {USENIX} symposium on operating systems design and implementation ({OSDI} 16)*, pp. 265–283.

Abraham, Wickliffe C and Mark F Bear (1996). "Metaplasticity: the plasticity of synaptic plasticity". In: *Trends in neurosciences* 19.4, pp. 126–130.

Abraham, Wickliffe C and Joanna M Williams (2003). "Properties and mechanisms of LTP maintenance". In: *The Neuroscientist* 9.6, pp. 463–474.

Acien, Alejandro et al. (2018). "Measuring the gender and ethnicity bias in deep models for face recognition". In: *Iberoamerican Congress on Pattern Recognition*. Springer, pp. 584–593.

Adesnik, Hillel and Lamiae Abdeladim (2021). "Probing neural codes with two-photon holographic optogenetics". In: *Nature Neuroscience* 24.10, pp. 1356–1366.

Aggarwal, Abhi et al. (2022). "Glutamate indicators with improved activation kinetics and localization for imaging synaptic transmission". In: *Biorxiv*.

Aguado, Carolina et al. (2016). "Ontogenic changes and differential localization of T-type Ca2+ channel subunits Cav3. 1 and Cav3. 2 in mouse hippocampus and cerebellum". In: *Frontiers in neuroanatomy* 10, p. 83.

Akerboom, Jasper et al. (2012). "Optimization of a GCaMP calcium indicator for neural activity imaging". In: *Journal of neuroscience* 32.40, pp. 13819–13840.

Ali, Farhan et al. (2020). "Ketamine disinhibits dendrites and enhances calcium signals in prefrontal dendritic spines". In: *Nature communications* 11.1, pp. 1–15.

Alonso, Jose-Manuel, W Martin Usrey, and R Clay Reid (1996). "Precisely correlated firing in cells of the lateral geniculate nucleus". In: *Nature* 383.6603, pp. 815–819.

Amaral, David G, Helen E Scharfman, and Pierre Lavenex (2007). "The dentate gyrus: fundamental neuroanatomical organization (dentate gyrus for dummies)". In: *Progress in brain research* 163, pp. 3–790.

Andermann, Mark L et al. (2011). "Functional specialization of mouse higher visual cortical areas". In: *Neuron* 72.6, pp. 1025–1039.

Andersen, Per, TVP Bliss, and K Kr Skrede (1971). "Lamellar organization of hippocampal excitatory pathways". In: *Experimental brain research* 13.2, pp. 222–238.

Andersen, Per et al. (2006). *The hippocampus book*. Oxford university press.

Andrásfalvy, Bertalan K and Jeffrey C Magee (2004). "Changes in AMPA receptor currents following LTP induction on rat CA1 pyramidal neurones". In: *The Journal of physiology* 559.2, pp. 543–554.

Andreasen, Mogens and JD Lambert (1995). "Regenerative properties of pyramidal cell dendrites in area CA1 of the rat hippocampus." In: *The Journal of physiology* 483.2, pp. 421–441.

Annese, Jacopo et al. (2014). "Postmortem examination of patient HM's brain based on histological sectioning and digital 3D reconstruction". In: *Nature communications* 5.1, pp. 1–9.

Antic, Srdjan D et al. (2010). "The decade of the dendritic NMDA spike". In: *Journal of neuroscience research* 88.14, pp. 2991–3001.

Araya, Roberto, Tim P Vogels, and Rafael Yuste (2014). "Activity-dependent dendritic spine neck changes are correlated with synaptic strength". In: *Proceedings of the National Academy of Sciences* 111.28, E2895–E2904.

Arcelli, P et al. (1997). "GABAergic neurons in mammalian thalamus: a marker of thalamic complexity?" In: *Brain research bulletin* 42.1, pp. 27–37.

Arellano, Jon I et al. (2007a). "Non-synaptic dendritic spines in neocortex". In: *Neuroscience* 145.2, pp. 464–469.

Arellano, Jon I et al. (2007b). "Ultrastructure of dendritic spines: correlation between synaptic and spine morphologies". In: *Frontiers in neuroscience* 1, p. 10.

Arendt, K. L., F. Sarti, and L. Chen (Jan. 2013). "Chronic Inactivation of a Neural Circuit Enhances LTP by Inducing Silent Synapse Formation". In: *Journal of Neuroscience* 33.5, pp. 2087–2096. DOI: 10.1523/jneurosci.3880-12.2013. URL: https://doi.org/10.1523/jneurosci.3880-12.2013.

Attardo, Alessio, James E. Fitzgerald, and Mark J. Schnitzer (June 2015). "Impermanence of dendritic spines in live adult CA1 hippocampus". In:

Nature 523.7562, pp. 592–596. DOI: 10.1038/nature14467. URL: https://doi.org/10.1038/nature14467.

Baden, Tom, Thomas Euler, and Philipp Berens (2020). "Understanding the retinal basis of vision across species". In: *Nature Reviews Neuroscience* 21.1, pp. 5–20.

Baden, Tom et al. (2016). "The functional diversity of retinal ganglion cells in the mouse". In: *Nature* 529.7586, pp. 345–350.

Baltaci, Saltuk Bugra, Rasim Mogulkoc, and Abdulkerim Kasim Baltaci (2019). "Molecular mechanisms of early and late LTP". In: *Neurochemical research* 44.2, pp. 281–296.

Banghart, Matthew et al. (Nov. 2004). "Light-activated ion channels for remote control of neuronal firing". In: *Nature Neuroscience* 7.12, pp. 1381–1386. DOI: 10.1038/nn1356. URL: https://doi.org/10.1038/nn1356.

Banke, TG et al. (2001). "Identification of amino acid residues in GluR1 responsible for ligand binding and desensitization". In: *Journal of Neuroscience* 21.9, pp. 3052–3062.

Banker, Gary A and W Maxwell Cowan (1977). "Rat hippocampal neurons in dispersed cell culture". In: *Brain research* 126.3, pp. 397–425.

Barlow, HeB, RM Hill, and WR Levick (1964). "Retinal ganglion cells responding selectively to direction and speed of image motion in the rabbit". In: *The Journal of physiology* 173.3, p. 377.

Basu, Subhadip et al. (2018). "Quantitative 3-D morphometric analysis of individual dendritic spines". In: *Scientific reports* 8.1, pp. 1–13.

Bauer, Elizabeth P, Glenn E Schafe, and Joseph E LeDoux (2002). "NMDA receptors and L-type voltage-gated calcium channels contribute to long-term potentiation and different components of fear memory formation in the lateral amygdala". In: *Journal of Neuroscience* 22.12, pp. 5239–5249.

Bauer, Joel and Tobias Rose (2021). "Mouse vision: Variability and stability across the visual processing hierarchy". In: *Current Biology* 31.19, R1129–R1132.

Bauer, Joel et al. (2021). "Limited functional convergence of eye-specific inputs in the retinogeniculate pathway of the mouse". In: *Neuron*.

Beaulieu, Devin R. et al. (Feb. 2020). "Simultaneous multiplane imaging with reverberation two-photon microscopy". In: *Nature Methods* 17.3, pp. 283–286. DOI: 10.1038/s41592-019-0728-9. URL: https://doi.org/10.1038/s41592-019-0728-9.

Becker, W. et al. (2010). "FLIM and FCS detection in laser-scanning microscopes: Increased efficiency by GaAsP hybrid detectors". In: *Microscopy*

Research and Technique, n/a–n/a. DOI: 10.1002/jemt.20959. URL: https://doi.org/10.1002/jemt.20959.

Béıque, Jean-Claude et al. (2006). "Synapse-specific regulation of AMPA receptor function by PSD-95". In: *Proceedings of the National Academy of Sciences* 103.51, pp. 19535–19540.

Benavides-Piccione, Ruth et al. (2013). "Age-based comparison of human dendritic spine structure using complete three-dimensional reconstructions". In: *Cerebral cortex* 23.8, pp. 1798–1810.

Berens, Philipp (2009). "CircStat: a MATLAB toolbox for circular statistics". In: *Journal of statistical software* 31.1, pp. 1–21.

Berlin, Shai et al. (Mar. 2016). "A family of photoswitchable NMDA receptors". In: *eLife* 5. DOI: 10.7554/elife.12040. URL: https://doi.org/10.7554/elife.12040.

Berndt, André et al. (2011). "High-efficiency channelrhodopsins for fast neuronal stimulation at low light levels". In: *Proceedings of the National Academy of Sciences* 108.18, pp. 7595–7600.

Berry, Kalen P and Elly Nedivi (2017). "Spine dynamics: are they all the same?" In: *Neuron* 96.1, pp. 43–55.

Bhatt, D Harshad, Shengxiang Zhang, and Wen-Biao Gan (2009). "Dendritic spine dynamics". In: *Annual review of physiology* 71, pp. 261–282.

Bi, Guo-qiang and Mu-ming Poo (1998). "Synaptic modifications in cultured hippocampal neurons: dependence on spike timing, synaptic strength, and postsynaptic cell type". In: *Journal of neuroscience* 18.24, pp. 10464–10472.

Bickford, Martha E et al. (2015). "Retinal and tectal "driver-like" inputs converge in the shell of the mouse dorsal lateral geniculate nucleus". In: *Journal of Neuroscience* 35.29, pp. 10523–10534.

Bliss, Tim VP and Terje Lømo (1973). "Long-lasting potentiation of synaptic transmission in the dentate area of the anaesthetized rabbit following stimulation of the perforant path". In: *The Journal of physiology* 232.2, pp. 331–356.

Bloodgood, Brenda L and Bernardo L Sabatini (2007). "Ca2+ signaling in dendritic spines". In: *Current opinion in neurobiology* 17.3, pp. 345–351.

Boccara, Charlotte N et al. (2010). "Grid cells in pre-and parasubiculum". In: *Nature neuroscience* 13.8, pp. 987–994.

Bonhoeffer, T (1999). "Intrinsic signal optical imaging as a tool to visualize the development of functional maps in the mammalian visual cortex". In: *Imaging: A laboratory manual (ed. R. Yuste et al.)*, pp. 46–1.

Bonhoeffer, TAGA (1996). "Optical imaging based on intrinsic signals". In: *Brain mapping: The methods*, pp. 55–97.

Bonhoeffer, Tobias and Rafael Yuste (2002). "Spine motility: phenomenology, mechanisms, and function". In: *Neuron* 35.6, pp. 1019–1027.

Born, Gregory et al. (2021). "Corticothalamic feedback sculpts visual spatial integration in mouse thalamus". In: *Nature neuroscience* 24.12, pp. 1711–1720.

Borst, Alexander, Jürgen Haag, and Alex S Mauss (2020). "How fly neurons compute the direction of visual motion". In: *Journal of Comparative Physiology A* 206.2, pp. 109–124.

Botcherby, E.J. et al. (Feb. 2008). "An optical technique for remote focusing in microscopy". In: *Optics Communications* 281.4, pp. 880–887. DOI: 10.1016/j.optcom.2007.10.007. URL: https://doi.org/10.1016/j.optcom.2007.10.007.

Bottou, Léon et al. (1998). "Online learning and stochastic approximations". In: *On-line learning in neural networks* 17.9, p. 142.

Boulogne, Guillaume-Benjamin Duchenne de (1876). *Mécanisme de la physionomie humaine: ou analyse électro-physilogique de l'expression des passion*. Ballière.

El-Boustani, Sami et al. (2018). "Locally coordinated synaptic plasticity of visual cortex neurons in vivo". In: *Science* 360.6395, pp. 1349–1354.

Boyden, Edward S et al. (2005). "Millisecond-timescale, genetically targeted optical control of neural activity". In: *Nature neuroscience* 8.9, pp. 1263–1268.

Boyle, Patrick M et al. (2013). "A comprehensive multiscale framework for simulating optogenetics in the heart". In: *Nature communications* 4.1, pp. 1–9.

Bozdagi, Ozlem et al. (2000). "Increasing numbers of synaptic puncta during late-phase LTP: N-cadherin is synthesized, recruited to synaptic sites, and required for potentiation". In: *Neuron* 28.1, pp. 245–259.

Brandalise, Federico et al. (2016). "Dendritic NMDA spikes are necessary for timing-dependent associative LTP in CA3 pyramidal cells". In: *Nature communications* 7.1, pp. 1–9.

Briones, Brandy A et al. (2018). "Response learning stimulates dendritic spine growth on dorsal striatal medium spiny neurons". In: *Neurobiology of Learning and Memory* 155, pp. 50–59.

Buchs, P-A et al. (1994). "A new cytochemical method for the ultrastructural localization of calcium in the central nervous system". In: *Journal of neuroscience methods* 54.1, pp. 83–93.

Burnashev, Nail and Pierre Szepetowski (2015). "NMDA receptor subunit mutations in neurodevelopmental disorders". In: *Current opinion in pharmacology* 20, pp. 73–82.

Buslaev, Alexander V. et al. (2018). "Albumentations: fast and flexible image augmentations". In: *CoRR* abs/1809.06839. arXiv: 1809.06839. URL: http://arxiv.org/abs/1809.06839.

Callaway, Edward M and Liqun Luo (2015). "Monosynaptic circuit tracing with glycoprotein-deleted rabies viruses". In: *Journal of Neuroscience* 35.24, pp. 8979–8985.

Cane, Michele et al. (2014). "The relationship between PSD-95 clustering and spine stability in vivo". In: *Journal of Neuroscience* 34.6, pp. 2075–2086.

Carrillo-Reid, Luis et al. (2019). "Controlling visually guided behavior by holographic recalling of cortical ensembles". In: *Cell* 178.2, pp. 447–457.

Cenquizca, Lee A and Larry W Swanson (2007). "Spatial organization of direct hippocampal field CA1 axonal projections to the rest of the cerebral cortex". In: *Brain research reviews* 56.1, pp. 1–26.

Chalfie, Martin et al. (1994). "Green fluorescent protein as a marker for gene expression". In: *Science* 263.5148, pp. 802–805.

Chalifoux, Jason R and Adam G Carter (2011). "GABAB receptor modulation of voltage-sensitive calcium channels in spines and dendrites". In: *Journal of Neuroscience* 31.11, pp. 4221–4232.

Chen, Chinfei and Wade G Regehr (2000). "Developmental remodeling of the retinogeniculate synapse". In: *Neuron* 28.3, pp. 955–966.

Chen, Gong, Nobutoshi C Harata, and Richard W Tsien (2004). "Paired-pulse depression of unitary quantal amplitude at single hippocampal synapses". In: *Proceedings of the National Academy of Sciences* 101.4, pp. 1063–1068.

Chen, Tsai-Wen et al. (July 2013). "Ultrasensitive fluorescent proteins for imaging neuronal activity". In: *Nature* 499.7458, pp. 295–300. DOI: 10.1038/nature12354. URL: https://doi.org/10.1038/nature12354.

Chen, Wei et al. (2022). "Bessel-droplet foci enable high-resolution and high-contrast volumetric imaging of synapses and circulation in the brain in vivo". In: *bioRxiv*.

Chen, Xiaobing et al. (2015). "PSD-95 family MAGUKs are essential for anchoring AMPA and NMDA receptor complexes at the postsynaptic

density". In: *Proceedings of the National Academy of Sciences* 112.50, E6983–E6992.

Chen, Xiaowei et al. (2011). "Functional mapping of single spines in cortical neurons in vivo". In: *Nature* 475.7357, pp. 501–505.

Chen, Xiaowei et al. (2012). "LOTOS-based two-photon calcium imaging of dendritic spines in vivo". In: *Nature protocols* 7.10, pp. 1818–1829.

Cheng, Jie et al. (2007). "A novel computational approach for automatic dendrite spines detection in two-photon laser scan microscopy". In: *Journal of neuroscience methods* 165.1, pp. 122–134.

Ching-Roa, Vincent D. et al. (Apr. 2021). "Publisher Correction: Ultrahigh-speed point scanning two-photon microscopy using high dynamic range silicon photomultipliers". In: *Scientific Reports* 11.1. DOI: 10.1038/s41598-021-88210-x. URL: https://doi.org/10.1038/s41598-021-88210-x.

Chiu, Chiayu Q et al. (2013). "Compartmentalization of GABAergic inhibition by dendritic spines". In: *Science* 340.6133, pp. 759–762.

Choi, Jun-Hyeok et al. (2018). "Interregional synaptic maps among engram cells underlie memory formation". In: *Science* 360.6387, pp. 430–435.

Choquet, Daniel and Patricio Opazo (2022). "The role of AMPAR lateral diffusion in memory". In: *Seminars in Cell & Developmental Biology*. Elsevier.

Çiçek, Özgün et al. (2016). "3D U-Net: learning dense volumetric segmentation from sparse annotation". In: *International conference on medical image computing and computer-assisted intervention*. Springer, pp. 424–432.

Cirillo, Davide et al. (2020). "Sex and gender differences and biases in artificial intelligence for biomedicine and healthcare". In: *NPJ digital medicine* 3.1, pp. 1–11.

Citri, Ami and Robert C Malenka (2008). "Synaptic plasticity: multiple forms, functions, and mechanisms". In: *Neuropsychopharmacology* 33.1, pp. 18–41.

Collingridge, Graham L, SJ Kehl, and H t McLennan (1983). "Excitatory amino acids in synaptic transmission in the Schaffer collateral-commissural pathway of the rat hippocampus." In: *The Journal of physiology* 334.1, pp. 33–46.

Coneva, Cvetalina (Oct. 2015). "Activity-driven formation and stabilization of functional spine synapses". URL: http://nbn-resolving.de/urn:nbn:de:bvb:19-188797.

Conley, Michael, Elizabeth Birecree, and VA Casagrande (1985). "Neuronal classes and their relation to functional and laminar organization of the lateral geniculate nucleus: a Golgi study of the prosimian primate, Galago crassicaudatus". In: *Journal of Comparative Neurology* 242.4, pp. 561–583.

Corkin, Suzanne et al. (1997). "HM's medial temporal lobe lesion: findings from magnetic resonance imaging". In: *Journal of Neuroscience* 17.10, pp. 3964–3979.

Cormack, Brendan P, Raphael H Valdivia, and Stanley Falkow (1996). "FACS-optimized mutants of the green fluorescent protein (GFP)". In: *Gene* 173.1, pp. 33–38.

Cornejo, Victor Hugo, Netanel Ofer, and Rafael Yuste (Nov. 2021). "Voltage compartmentalization in dendritic spines in vivo". In: *Science*. DOI: 10.1126/science.abg0501. URL: https://doi.org/10.1126/science.abg0501.

Cottrell, Jeffrey R et al. (2000). "Distribution, density, and clustering of functional glutamate receptors before and after synaptogenesis in hippocampal neurons". In: *Journal of neurophysiology* 84.3, pp. 1573–1587.

Crair, Michael C and Robert C Malenka (1995). "A critical period for long-term potentiation at thalamocortical synapses". In: *Nature* 375.6529, pp. 325–328.

Cuntz, Hermann et al. (2011). "The TREES toolbox—probing the basis of axonal and dendritic branching". In: *Neuroinformatics* 9.1, pp. 91–96.

Dailey, Michael E and Stephen J Smith (1996). "The dynamics of dendritic structure in developing hippocampal slices". In: *Journal of neuroscience* 16.9, pp. 2983–2994.

Dal Maschio, Marco et al. (2017). "Linking neurons to network function and behavior by two-photon holographic optogenetics and volumetric imaging". In: *Neuron* 94.4, pp. 774–789.

Dan, Yang and Mu-ming Poo (1992). "Hebbian depression of isolated neuromuscular synapses in vitro". In: *Science* 256.5063, pp. 1570–1573.

Dana, Hod et al. (2019). "High-performance calcium sensors for imaging activity in neuronal populations and microcompartments". In: *Nature methods* 16.7, pp. 649–657.

De Robertis, Eduardo DP and H Stanley Bennett (1955). "Some features of the submicroscopic morphology of synapses in frog and earthworm". In: *The Journal of Cell Biology* 1.1, pp. 47–58.

De Roo, Mathias, Paul Klauser, and Dominique Muller (2008). "LTP promotes a selective long-term stabilization and clustering of dendritic spines". In: *PLoS biology* 6.9, e219.

De Roo, Mathias et al. (2008). "Activity-dependent PSD formation and stabilization of newly formed spines in hippocampal slice cultures". In: *Cerebral cortex* 18.1, pp. 151–161.

Debanne, Dominique, Beat H Gähwiler, and Scott M Thompson (1999). "Heterogeneity of synaptic plasticity at unitary CA3–CA1 and CA3–CA3 connections in rat hippocampal slice cultures". In: *Journal of Neuroscience* 19.24, pp. 10664–10671.

Deitch, Daniel, Alon Rubin, and Yaniv Ziv (2021). "Representational drift in the mouse visual cortex". In: *Current Biology* 31.19, pp. 4327–4339.

Demas, Jeffrey et al. (Aug. 2021a). "High-speed, cortex-wide volumetric recording of neuroactivity at cellular resolution using light beads microscopy". In: *Nature Methods* 18.9, pp. 1103–1111. DOI: 10.1038/s41592-021-01239-8. URL: https://doi.org/10.1038/s41592-021-01239-8.

Demas, Jeffrey et al. (2021b). "High-speed, cortex-wide volumetric recording of neuroactivity at cellular resolution using light beads microscopy". In: *Nature Methods* 18.9, pp. 1103–1111.

Denk, Winfried, James H Strickler, and Watt W Webb (1990). "Two-photon laser scanning fluorescence microscopy". In: *Science* 248.4951, pp. 73–76.

Depry, Charlene, Sohum Mehta, and Jin Zhang (2013). "Multiplexed visualization of dynamic signaling networks using genetically encoded fluorescent protein-based biosensors". In: *Pflügers Archiv-European Journal of Physiology* 465.3, pp. 373–381.

Derkach, Victor, Andres Barria, and Thomas R Soderling (1999). "Ca2+/calmodulin-kinase II enhances channel conductance of α-amino-3-hydroxy-5-methyl-4-isoxazolepropionate type glutamate receptors". In: *Proceedings of the National Academy of Sciences* 96.6, pp. 3269–3274.

Dervinis, Martynas (2020). *circStatNP*. https://github.com/dervinism/circStatNP.

Desmond, Nancy L and William B Levy (1986). "Changes in the postsynaptic density with long-term potentiation in the dentate gyrus". In: *Journal of Comparative Neurology* 253.4, pp. 476–482.

Diano, Sabrina et al. (2006). "Ghrelin controls hippocampal spine synapse density and memory performance". In: *Nature neuroscience* 9.3, pp. 381–388.

Dias, Raquel and Ali Torkamani (2019). "Artificial intelligence in clinical and genomic diagnostics". In: *Genome medicine* 11.1, pp. 1–12.

Ding, Jun B., Kevin T. Takasaki, and Bernardo L. Sabatini (Aug. 2009). "Supraresolution Imaging in Brain Slices using Stimulated-Emission Depletion Two-Photon Laser Scanning Microscopy". In: *Neuron* 63.4, pp. 429–437. DOI: 10.1016/j.neuron.2009.07.011. URL: https://doi.org/10.1016/j.neuron.2009.07.011.

Dingledine, Raymond et al. (1999). "The glutamate receptor ion channels". In: *Pharmacological reviews* 51.1, pp. 7–62.

Doeller, Christian F, Caswell Barry, and Neil Burgess (2010). "Evidence for grid cells in a human memory network". In: *Nature* 463.7281, pp. 657–661.

Donthamsetti, Prashant et al. (2021). "Cell specific photoswitchable agonist for reversible control of endogenous dopamine receptors". In: *Nature communications* 12.1, pp. 1–13.

Dosemeci, Ayse et al. (2016). "The postsynaptic density: there is more than meets the eye". In: *Frontiers in synaptic neuroscience* 8, p. 23.

Dräger, Ursula C and John F Olsen (1980). "Origins of crossed and uncrossed retinal projections in pigmented and albino mice". In: *Journal of Comparative Neurology* 191.3, pp. 383–412.

Druckmann, Shaul et al. (2014). "Structured synaptic connectivity between hippocampal regions". In: *Neuron* 81.3, pp. 629–640.

Du Bois-Reymond, Emil (1884). *Untersuchungen über thierische Elektricität*. Vol. 2. G. Reimer.

Duerst, Celine et al. (2020). "The vesicular release probability sets the strength of individual Schaffer collateral synapses". In.

Duffet, Loıc et al. (2022). "A genetically encoded sensor for in vivo imaging of orexin neuropeptides". In: *Nature methods* 19.2, pp. 231–241.

Dumitriu, Dani, Alfredo Rodriguez, and John H Morrison (2011). "High-throughput, detailed, cell-specific neuroanatomy of dendritic spines using microinjection and confocal microscopy". In: *Nature protocols* 6.9, pp. 1391–1411.

Dunaevsky, Anna et al. (1999). "Developmental regulation of spine motility in the mammalian central nervous system". In: *Proceedings of the National Academy of Sciences* 96.23, pp. 13438–13443.

Dunaevsky, Anna et al. (2001). "Spine motility with synaptic contact". In: *Nature neuroscience* 4.7, pp. 685–686.

Dvorak, David R, Lewis G Bishop, and Hendrik E Eckert (1975). "On the identification of movement detectors in the fly optic lobe". In: *Journal of comparative physiology* 100.1, pp. 5–23.

Ehrlich, Ingrid et al. (2007). "PSD-95 is required for activity-driven synapse stabilization". In: *Proceedings of the National Academy of Sciences* 104.10, pp. 4176–4181.

Engel, Tatiana A, Marieke L Schölvinck, and Christopher M Lewis (2021). "The diversity and specificity of functional connectivity across spatial and temporal scales". In: *NeuroImage* 245, p. 118692.

Engert, Florian and Tobias Bonhoeffer (July 1997). "Synapse specificity of long-term potentiation breaks down at short distances". In: *Nature* 388.6639, pp. 279–284. DOI: 10.1038/40870. URL: https://doi.org/10.1038/40870.

Engert, Florian and Tobias Bonhoeffer (1999). "Dendritic spine changes associated with hippocampal long-term synaptic plasticity". In: *Nature* 399.6731, pp. 66–70.

Enoki, Ryosuke et al. (2009). "Expression of long-term plasticity at individual synapses in hippocampus is graded, bidirectional, and mainly presynaptic: optical quantal analysis". In: *Neuron* 62.2, pp. 242–253.

Falk, Thorsten et al. (2019). "U-Net: deep learning for cell counting, detection, and morphometry". In: *Nature methods* 16.1, pp. 67–70.

Falkner, Susanne et al. (2016). "Transplanted embryonic neurons integrate into adult neocortical circuits". In: *Nature* 539.7628, pp. 248–253.

Fan, Jing et al. (2009). "An automated pipeline for dendrite spine detection and tracking of 3D optical microscopy neuron images of in vivo mouse models". In: *Neuroinformatics* 7.2, pp. 113–130.

Fang, Cheng et al. (2021). "Pose estimation and behavior classification of broiler chickens based on deep neural networks". In: *Computers and Electronics in Agriculture* 180, p. 105863.

Farris, Sarah M (2020). "The rise to dominance of genetic model organisms and the decline of curiosity-driven organismal research". In: *Plos one* 15.12, e0243088.

Feldmeyer, Dirk et al. (2002). "Synaptic connections between layer 4 spiny neurone-layer 2/3 pyramidal cell pairs in juvenile rat barrel cortex: physiology and anatomy of interlaminar signalling within a cortical column". In: *The Journal of physiology* 538.3, pp. 803–822.

Feng, Linqing, Ting Zhao, and Jinhyun Kim (2012). "Improved synapse detection for mGRASP-assisted brain connectivity mapping". In: *Bioinformatics* 28.12, pp. i25–i31.

Feng, Linqing, Ting Zhao, and Jinhyun Kim (2015). "neuTube 1.0: a new design for efficient neuron reconstruction software based on the SWC format". In: *eneuro* 2.1.

Feng, Linqing et al. (2014). "Using mammalian GFP reconstitution across synaptic partners (mGRASP) to map synaptic connectivity in the mouse brain". In: *nature protocols* 9.10, pp. 2425–2437.

Fernandez, Diego Carlos et al. (May 2016). "Architecture of retinal projections to the central circadian pacemaker". In: *Proceedings of the National Academy of Sciences* 113.21, pp. 6047–6052. DOI: 10.1073/pnas.1523629113. URL: https://doi.org/10.1073/pnas.1523629113.

Fifková, Eva and Carol L Anderson (1981). "Stimulation-induced changes in dimensions of stalks of dendritic spines in the dentate molecular layer". In: *Experimental neurology* 74.2, pp. 621–627.

Fifková, Eva and A Van Harreveld (1977). "Long-lasting morphological changes in dendritic spines of dentate granular cells following stimulation of the entorhinal area". In: *Journal of neurocytology* 6.2, pp. 211–230.

Finkelstein, Gabriel (2013). *Emil du Bois-Reymond: neuroscience, self, and society in nineteenth-century Germany*. MIT Press.

Fischer, Maria et al. (1998). "Rapid actin-based plasticity in dendritic spines". In: *Neuron* 20.5, pp. 847–854.

Fischer, Quentin S et al. (2007). "Monocular deprivation in adult mice alters visual acuity and single-unit activity". In: *Learning & Memory* 14.4, pp. 277–286.

Frank, Adam C et al. (2018). "Hotspots of dendritic spine turnover facilitate clustered spine addition and learning and memory". In: *Nature communications* 9.1, pp. 1–11.

Frey, Uwe, Y-Y Huang, and ER Kandel (1993). "Effects of cAMP simulate a late stage of LTP in hippocampal CA1 neurons". In: *Science* 260.5114, pp. 1661–1664.

Frey, Uwe et al. (1988). "Anisomycin, an inhibitor of protein synthesis, blocks late phases of LTP phenomena in the hippocampal CA1 region in vitro". In: *Brain research* 452.1-2, pp. 57–65.

Friston, Karl J (2011). "Functional and effective connectivity: a review". In: *Brain connectivity* 1.1, pp. 13–36.

Fu, Min et al. (2012). "Repetitive motor learning induces coordinated formation of clustered dendritic spines in vivo". In: *Nature* 483.7387, pp. 92–95.

Gähwiler, BH (1981). "Organotypic monolayer cultures of nervous tissue". In: *Journal of neuroscience methods* 4.4, pp. 329–342.

Gähwiler, BH (1988). "Organotypic cultures of neural tissue". In: *Trends in neurosciences* 11.11, pp. 484–489.

Gähwiler, BH et al. (1997). "Organotypic slice cultures: a technique has come of age". In: *Trends in neurosciences* 20.10, pp. 471–477.

Galvani, Luigi and Giovanni Aldini (1797). *Memorie sulla elettricità animale di Luigi Galvani... al celebre abate Lazzaro Spallanzani... Aggiunte alcune elettriche esperienze di Gio. Aldini...* Per le stampe del Sassi.

Garner, Craig C et al. (2002). "Molecular mechanisms of CNS synaptogenesis". In: *Trends in neurosciences* 25.5, pp. 243–250.

Ghani, Muhammad Usman et al. (2017). "Dendritic spine classification using shape and appearance features based on two-photon microscopy". In: *Journal of neuroscience methods* 279, pp. 13–21.

Glickfeld, Lindsey L and Shawn R Olsen (2017). "Higher-order areas of the mouse visual cortex". In: *Annual review of vision science* 3, pp. 251–273.

Godement, Pierre, Josselyne Salaün, and Michel Imbert (1984). "Prenatal and postnatal development of retinogeniculate and retinocollicular projections in the mouse". In: *Journal of Comparative Neurology* 230.4, pp. 552–575.

Goebel, Dennis J and Michael S Poosch (1999). "NMDA receptor subunit gene expression in the rat brain: a quantitative analysis of endogenous mRNA levels of NR1Com, NR2A, NR2B, NR2C, NR2D and NR3A". In: *Molecular Brain Research* 69.2, pp. 164–170.

Goedhart, Joachim et al. (Jan. 2012). "Structure-guided evolution of cyan fluorescent proteins towards a quantum yield of 93%". In: *Nature Communications* 3.1. DOI: 10.1038/ncomms1738. URL: https://doi.org/10.1038/ncomms1738.

Gökerküçük, Elif Begüm, Marc Tramier, and Giulia Bertolin (2020). "Imaging mitochondrial functions: from fluorescent dyes to genetically-encoded sensors". In: *Genes* 11.2, p. 125.

Golding, Nace L, Nathan P Staff, and Nelson Spruston (2002). "Dendritic spikes as a mechanism for cooperative long-term potentiation". In: *Nature* 418.6895, pp. 326–331.

Golding, Nace L et al. (1999). "Dendritic calcium spike initiation and repolarization are controlled by distinct potassium channel subtypes in CA1 pyramidal neurons". In: *Journal of Neuroscience* 19.20, pp. 8789–8798.

Golgi, C (1873). "Sulla struttura della sostanza grigia dell cervello', Gazz". In: *Med Lombarda* 33, pp. 224–46.

Golgi, Camillo (1885). *Sulla fina anatomia degli organi centrali del sistema nervoso*. S. Calderini.

Gómez, Pablo et al. (2020). "BAGLS, a multihospital benchmark for automatic glottis segmentation". In: *Scientific data* 7.1, pp. 1–12.

Graves, Austin R et al. (2021). "Visualizing synaptic plasticity in vivo by large-scale imaging of endogenous AMPA receptors". In: *Elife* 10, e66809.

Graving, Jacob M et al. (2019). "DeepPoseKit, a software toolkit for fast and robust animal pose estimation using deep learning". In: *Elife* 8, e47994.

Gray, Edward G (1959a). "Axo-somatic and axo-dendritic synapses of the cerebral cortex: an electron microscope study". In: *Journal of anatomy* 93.Pt 4, p. 420.

Gray, Edward G (1959b). "Electron microscopy of synaptic contacts on dendrite spines of the cerebral cortex". In: *Nature* 183.4675, pp. 1592–1593.

Gray, Noah W et al. (2006). "Rapid redistribution of synaptic PSD-95 in the neocortex in vivo". In: *PLoS biology* 4.11, e370.

Greenwald, Noah F et al. (2022). "Whole-cell segmentation of tissue images with human-level performance using large-scale data annotation and deep learning". In: *Nature biotechnology* 40.4, pp. 555–565.

Grienberger, Christine, Xiaowei Chen, and Arthur Konnerth (2014). "NMDA receptor-dependent multidendrite Ca2+ spikes required for hippocampal burst firing in vivo". In: *Neuron* 81.6, pp. 1274–1281.

Grienberger, Christine and Arthur Konnerth (2012). "Imaging calcium in neurons". In: *Neuron* 73.5, pp. 862–885.

Grinvald, Amiram et al. (1986). "Functional architecture of cortex revealed by optical imaging of intrinsic signals". In: *Nature* 324.6095, pp. 361–364.

Groschner, Lukas N et al. (2022). "A biophysical account of multiplication by a single neuron". In: *Nature* 603.7899, pp. 119–123.

Gross, Garrett G. et al. (June 2013). "Recombinant Probes for Visualizing Endogenous Synaptic Proteins in Living Neurons". In: *Neuron* 78.6, pp. 971–985. DOI: 10.1016/j.neuron.2013.04.017. URL: https://doi.org/10.1016/j.neuron.2013.04.017.

Grubb, Matthew S and Ian D Thompson (2004). "Biochemical and anatomical subdivision of the dorsal lateral geniculate nucleus in normal mice and

in mice lacking the $\beta 2$ subunit of the nicotinic acetylcholine receptor". In: *Vision research* 44.28, pp. 3365–3376.

Gu, JG et al. (1996). "Synaptic strengthening through activation of Ca 2+-permeable AMPA receptors". In: *Nature* 381.6585, pp. 793–796.

Gustafsson, B and H Wigstrom (1986). "Hippocampal long-lasting potentiation produced by pairing single volleys and brief conditioning tetani evoked in separate afferents". In: *Journal of Neuroscience* 6.6, pp. 1575–1582.

Guthrie, Peter B, Menahem Segal, and SB Kater (1991). "Independent regulation of calcium revealed by imaging dendritic spines". In: *Nature* 354.6348, pp. 76–80.

Hafting, Torkel et al. (2005). "Microstructure of a spatial map in the entorhinal cortex". In: *Nature* 436.7052, pp. 801–806.

Hanada, Takahisa (2020). "Ionotropic glutamate receptors in epilepsy: a review focusing on AMPA and NMDA receptors". In: *Biomolecules* 10.3, p. 464.

Hansen, Kasper B et al. (2018). "Structure, function, and allosteric modulation of NMDA receptors". In: *Journal of General Physiology* 150.8, pp. 1081–1105.

Harnett, Mark T et al. (2013). "Potassium channels control the interaction between active dendritic integration compartments in layer 5 cortical pyramidal neurons". In: *Neuron* 79.3, pp. 516–529.

Harris, Eric W, Alan H Ganong, and Carl W Cotman (1984). "Long-term potentiation in the hippocampus involves activation of N-methyl-D-aspartate receptors". In: *Brain research* 323.1, pp. 132–137.

Harris, Kenneth D and Gordon MG Shepherd (2015). "The neocortical circuit: themes and variations". In: *Nature neuroscience* 18.2, pp. 170–181.

Hartigan, John A and Pamela M Hartigan (1985). "The dip test of unimodality". In: *The annals of Statistics*, pp. 70–84.

Hartline, Haldan Keffer (1969). "Visual receptors and retinal interaction". In: *Science* 164.3877, pp. 270–278.

Haskins, Grant, Uwe Kruger, and Pingkun Yan (2020). "Deep learning in medical image registration: a survey". In: *Machine Vision and Applications* 31.1, pp. 1–18.

Hattar, Samer et al. (2006). "Central projections of melanopsin-expressing retinal ganglion cells in the mouse". In: *Journal of Comparative Neurology* 497.3, pp. 326–349.

Häusser, Michael (2014). "Optogenetics: the age of light". In: *Nature methods* 11.10, pp. 1012–1014.

He, Kaiming et al. (2016). "Deep residual learning for image recognition". In: *Proceedings of the IEEE conference on computer vision and pattern recognition*, pp. 770–778.

Hebb, Donald O (1949). "The first stage of perception: growth of the assembly". In: *The Organization of Behavior* 4, pp. 60–78.

Heck, Nicolas et al. (2012). "A deconvolution method to improve automated 3D-analysis of dendritic spines: application to a mouse model of Huntington's disease". In: *Brain Structure and Function* 217.2, pp. 421–434.

Hedrick, Nathan G et al. (2016). "Rho GTPase complementation underlies BDNF-dependent homo-and heterosynaptic plasticity". In: *Nature* 538.7623, pp. 104–108.

Hedrick, Nathan G et al. (2022). "Learning binds new inputs into functional synaptic clusters via spinogenesis". In: *Nature Neuroscience*, pp. 1–12.

Hegemann, Peter, Sabine Ehlenbeck, and Dietrich Gradmann (2005). "Multiple photocycles of channelrhodopsin". In: *Biophysical journal* 89.6, pp. 3911–3918.

Heim, R., D. C. Prasher, and R. Y. Tsien (Dec. 1994). "Wavelength mutations and posttranslational autoxidation of green fluorescent protein." In: *Proceedings of the National Academy of Sciences* 91.26, pp. 12501–12504. DOI: 10.1073/pnas.91.26.12501. URL: https://doi.org/10.1073/pnas.91.26.12501.

Heim, Roger (1995). "Improved green fluorescence". In: *Nature* 373, pp. 663–664.

Hell, Johannes W et al. (1993). "Identification and differential subcellular localization of the neuronal class C and class D L-type calcium channel alpha 1 subunits." In: *The Journal of cell biology* 123.4, pp. 949–962.

Helmchen, Fritjof and Winfried Denk (2005). "Deep tissue two-photon microscopy". In: *Nature methods* 2.12, pp. 932–940.

Helmchen, Fritjof et al. (1999). "In vivo dendritic calcium dynamics in deep-layer cortical pyramidal neurons". In: *Nature neuroscience* 2.11, pp. 989–996.

Henley, Jeremy M and Kevin A Wilkinson (2016). "Synaptic AMPA receptor composition in development, plasticity and disease". In: *Nature Reviews Neuroscience* 17.6, pp. 337–350.

Hernández, CJ et al. (2019). "PINK1 silencing modifies dendritic spine dynamics of mouse hippocampal neurons". In: *Journal of Molecular Neuroscience* 69.4, pp. 570–579.

Hescheler, J et al. (1982). "Does the organic calcium channel blocker D600 act from inside or outside on the cardiac cell membrane?" In: *Pflügers Archiv* 393.4, pp. 287–291.

Higley, Michael J and Bernardo L Sabatini (2008). "Calcium signaling in dendrites and spines: practical and functional considerations". In: *Neuron* 59.6, pp. 902–913.

Hill, Travis C and Karen Zito (2013). "LTP-induced long-term stabilization of individual nascent dendritic spines". In: *Journal of Neuroscience* 33.2, pp. 678–686.

Hofer, Sonja B et al. (2009). "Experience leaves a lasting structural trace in cortical circuits". In: *Nature* 457.7227, pp. 313–317.

Hoffmann, Maximilian et al. (2022). "Brain-wide imaging of an adult vertebrate with image transfer oblique plane microscopy". In: *bioRxiv*. DOI: 10.1101/2022.05.16.492103. URL: https://www.biorxiv.org/content/early/2022/05/17/2022.05.16.492103.

Holler, Simone et al. (2021). "Structure and function of a neocortical synapse". In: *Nature* 591.7848, pp. 111–116.

Holtmaat, Anthony et al. (2006). "Experience-dependent and cell-type-specific spine growth in the neocortex". In: *Nature* 441.7096, pp. 979–983.

Holtmaat, Anthony et al. (2009). "Long-term, high-resolution imaging in the mouse neocortex through a chronic cranial window". In: *Nature protocols* 4.8, pp. 1128–1144.

Holtmaat, Anthony JGD et al. (2005). "Transient and persistent dendritic spines in the neocortex in vivo". In: *Neuron* 45.2, pp. 279–291.

Hong, Y Kate et al. (2014). "Refinement of the retinogeniculate synapse by bouton clustering". In: *Neuron* 84.2, pp. 332–339.

Hooks, Bryan M and Chinfei Chen (2006). "Distinct roles for spontaneous and visual activity in remodeling of the retinogeniculate synapse". In: *Neuron* 52.2, pp. 281–291.

Hooks, Bryan M et al. (2015). "Dual-channel circuit mapping reveals sensorimotor convergence in the primary motor cortex". In: *Journal of Neuroscience* 35.10, pp. 4418–4426.

Hosokawa, Toshiyuki et al. (1995). "Repeated confocal imaging of individual dendritic spines in the living hippocampal slice: evidence for changes

in length and orientation associated with chemically induced LTP". In: *Journal of Neuroscience* 15.8, pp. 5560–5573.

Howarth, Michael, Lauren Walmsley, and Timothy M Brown (2014). "Binocular integration in the mouse lateral geniculate nuclei". In: *Current Biology* 24.11, pp. 1241–1247.

Hruska, Martin, Rachel E Cain, and Matthew B Dalva (2022). "Nanoscale rules governing the organization of glutamate receptors in spine synapses are subunit specific". In: *Nature communications* 13.1, pp. 1–19.

Hruska, Martin et al. (2018). "Synaptic nanomodules underlie the organization and plasticity of spine synapses". In: *Nature neuroscience* 21.5, pp. 671–682.

Hsia, Albert Y, Robert C Malenka, and Roger A Nicoll (1998). "Development of excitatory circuitry in the hippocampus". In: *Journal of neurophysiology* 79.4, pp. 2013–2024.

Huang, Jing et al. (2018). "Circuit dissection of the role of somatostatin in itch and pain". In: *Nature neuroscience* 21.5, pp. 707–716.

Hubel, David H and Torsten N Wiesel (1959). "Receptive fields of single neurones in the cat's striate cortex". In: *The Journal of physiology* 148.3, p. 574.

Hubel, David H and Torsten N Wiesel (1962). "Receptive fields, binocular interaction and functional architecture in the cat's visual cortex". In: *The Journal of physiology* 160.1, pp. 106–154.

Hubel, David H and Torsten N Wiesel (1968). "Receptive fields and functional architecture of monkey striate cortex". In: *The Journal of physiology* 195.1, pp. 215–243.

Hübener, Mark and Tobias Bonhoeffer (2010). "Searching for engrams". In: *Neuron* 67.3, pp. 363–371.

Huh, Carey YL et al. (2020). "Long-term monocular deprivation during juvenile critical period disrupts binocular integration in mouse visual thalamus". In: *Journal of Neuroscience* 40.3, pp. 585–604.

El-Husseini, Alaa El-Din et al. (2000). "PSD-95 involvement in maturation of excitatory synapses". In: *Science* 290.5495, pp. 1364–1368.

Iacaruso, M Florencia, Ioana T Gasler, and Sonja B Hofer (2017). "Synaptic organization of visual space in primary visual cortex". In: *Nature* 547.7664, pp. 449–452.

Ichikawa, Masumi et al. (1993). "Formation and maturation of synapses in primary cultures of rat cerebral cortical cells: an electron microscopic study". In: *Neuroscience research* 16.2, pp. 95–103.

Iijima, Kouichirou et al. (2021). "Optical clearing of living brains with MAGICAL to extend in vivo imaging". In: *Iscience* 24.1, p. 101888.

Inouye, Satoshi and Frederick I Tsuji (1994). "Aequorea green fluorescent protein: Expression of the gene and fluorescence characteristics of the recombinant protein". In: *FEBS letters* 341.2-3, pp. 277–280.

Ioffe, Sergey and Christian Szegedy (2015). "Batch normalization: Accelerating deep network training by reducing internal covariate shift". In: *International conference on machine learning*. PMLR, pp. 448–456.

Ito, Masao, Masaki Sakurai, and Pavich Tongroach (1982). "Climbing fibre induced depression of both mossy fibre responsiveness and glutamate sensitivity of cerebellar Purkinje cells". In: *The Journal of physiology* 324.1, pp. 113–134.

Ivakhnenko, AG and VG Lapa (1965). *Cybernetic predicting devices. Kiev*.

Jaepel, Juliane et al. (2017). "Lateral geniculate neurons projecting to primary visual cortex show ocular dominance plasticity in adult mice". In: *Nature neuroscience* 20.12, pp. 1708–1714.

Jaffe, David B et al. (1992). "The spread of Na+ spikes determines the pattern of dendritic Ca2+ entry into hippocampal neurons". In: *Nature* 357.6375, pp. 244–246.

Jaubert-Miazza, Lisa et al. (2005). "Structural and functional composition of the developing retinogeniculate pathway in the mouse". In: *Visual neuroscience* 22.5, pp. 661–676.

Jeong, Yire et al. (2021). "Synaptic plasticity-dependent competition rule influences memory formation". In: *Nature Communications* 12.1, pp. 1–13.

Ji, Na (Apr. 2017). "Adaptive optical fluorescence microscopy". In: *Nature Methods* 14.4, pp. 374–380. DOI: 10.1038/nmeth.4218. URL: https://doi.org/10.1038/nmeth.4218.

Ji, Xincai, Sucharita Saha, and Gilles E Martin (2015). "The origin of glutamatergic synaptic inputs controls synaptic plasticity and its modulation by alcohol in mice nucleus accumbens". In: *Frontiers in synaptic neuroscience* 7, p. 12.

Jia, Zhengping et al. (1996). "Enhanced LTP in mice deficient in the AMPA receptor GluR2". In: *Neuron* 17.5, pp. 945–956.

Jiao, Shoushu et al. (Apr. 1993). "Particle Bombardment-Mediated Gene Transfer and Expression in Rat Brain Tissues". In: *Nature Biotechnology* 11.4, pp. 497–502. DOI: 10.1038/nbt0493-497. URL: https://doi.org/10.1038/nbt0493-497.

Joesch, Maximilian et al. (2010). "ON and OFF pathways in Drosophila motion vision". In: *Nature* 468.7321, pp. 300–304.

Judkewitz, Benjamin et al. (2009). "Targeted single-cell electroporation of mammalian neurons in vivo". In: *Nature protocols* 4.6, pp. 862–869.

Jun, James J et al. (2017). "Fully integrated silicon probes for high-density recording of neural activity". In: *Nature* 551.7679, pp. 232–236.

Kaech, Stefanie and Gary Banker (2006). "Culturing hippocampal neurons". In: *Nature protocols* 1.5, pp. 2406–2415.

Kampa, Björn M, Johannes J Letzkus, and Greg J Stuart (2006). "Requirement of dendritic calcium spikes for induction of spike-timing-dependent synaptic plasticity". In: *The Journal of physiology* 574.1, pp. 283–290.

Kasai, Haruo et al. (2003). "Structure–stability–function relationships of dendritic spines". In: *Trends in neurosciences* 26.7, pp. 360–368.

Kasai, Haruo et al. (2010). "Structural dynamics of dendritic spines in memory and cognition". In: *Trends in neurosciences* 33.3, pp. 121–129.

Kato, Hideaki E et al. (2012). "Crystal structure of the channelrhodopsin light-gated cation channel". In: *Nature* 482.7385, pp. 369–374.

Katrukha, Eugene (2021). *ZstackDepthColorCode*. `https://github.com/ekatrukha/ZstackDepthColorCode`.

Kazemipour, Abbas et al. (July 2019). "Kilohertz frame-rate two-photon tomography". In: *Nature Methods* 16.8, pp. 778–786. DOI: `10.1038/s41592-019-0493-9`. URL: `https://doi.org/10.1038/s41592-019-0493-9`.

Keck, Tara et al. (2008). "Massive restructuring of neuronal circuits during functional reorganization of adult visual cortex". In: *Nature neuroscience* 11.10, p. 1162.

Kerlin, Aaron et al. (2019). "Functional clustering of dendritic activity during decision-making". In: *Elife* 8, e46966.

Kim, Byungju et al. (2019). "Learning not to learn: Training deep neural networks with biased data". In: *Proceedings of the IEEE/CVF Conference on Computer Vision and Pattern Recognition*, pp. 9012–9020.

Kim, Jinhyun et al. (2012). "mGRASP enables mapping mammalian synaptic connectivity with light microscopy". In: *Nature methods* 9.1, pp. 96–102.

Kim, Yujin et al. (2015). "Dendritic sodium spikes are required for long-term potentiation at distal synapses on hippocampal pyramidal neurons". In: *Elife* 4, e06414.

Kingma, Diederik P and Jimmy Ba (2014). "Adam: A method for stochastic optimization". In: *arXiv preprint arXiv:1412.6980*.

Klapoetke, Nathan C et al. (2014). "Independent optical excitation of distinct neural populations". In: *Nature methods* 11.3, pp. 338–346.

Knott, Graham W et al. (2006). "Spine growth precedes synapse formation in the adult neocortex in vivo". In: *Nature neuroscience* 9.9, pp. 1117–1124.

Al-Kofahi, Yousef et al. (2018). "A deep learning-based algorithm for 2-D cell segmentation in microscopy images". In: *BMC bioinformatics* 19.1, pp. 1–11.

Koh, Ingrid YY and W Brent Lindquist (2001). "Automated 3D dendritic spine detection and analysis from two-photon microscopy". In: *Three-Dimensional and Multidimensional Microscopy: Image Acquisition and Processing VIII*. Vol. 4261. International Society for Optics and Photonics, pp. 48–59.

Koh, Ingrid YY et al. (2002). "An image analysis algorithm for dendritic spines". In: *Neural computation* 14.6, pp. 1283–1310.

Kolb, Helga (1977). "The organization of the outer plexiform layer in the retina of the cat: electron microscopic observations". In: *Journal of neurocytology* 6.2, pp. 131–153.

Kopec, Charles D et al. (2006). "Glutamate receptor exocytosis and spine enlargement during chemically induced long-term potentiation". In: *Journal of Neuroscience* 26.7, pp. 2000–2009.

Kornau, Hans-Christian et al. (1995). "Domain interaction between NMDA receptor subunits and the postsynaptic density protein PSD-95". In: *Science* 269.5231, pp. 1737–1740.

Kovalchuk, Yury et al. (2000). "NMDA receptor-mediated subthreshold Ca2+ signals in spines of hippocampal neurons". In: *Journal of Neuroscience* 20.5, pp. 1791–1799.

Krahe, Thomas E et al. (2011). "Morphologically distinct classes of relay cells exhibit regional preferences in the dorsal lateral geniculate nucleus of the mouse". In: *Journal of Neuroscience* 31.48, pp. 17437–17448.

Krizhevsky, Alex, Ilya Sutskever, and Geoffrey E Hinton (2012). "Imagenet classification with deep convolutional neural networks". In: *Advances in neural information processing systems* 25, pp. 1097–1105.

Kuan, Aaron T. et al. (Apr. 2022). "Synaptic wiring motifs in posterior parietal cortex support decision-making". In: DOI: 10.1101/2022.04.13.488176. URL: https://doi.org/10.1101/2022.04.13.488176.

Kuffler, Stephen W (1953). "Discharge patterns and functional organization of mammalian retina". In: *Journal of neurophysiology* 16.1, pp. 37–68.

Kuhl, Patricia (2013). *Decoding 'the Most Complex Object in the Universe'*. https://www.npr.org/2013/06/14/191614360/decoding-the-most-complex-object-in-the-universe?t=1637584055511. Accessed: 2022-01-21.

Kuljis, Dika A et al. (2019). "Fluorescence-based quantitative synapse analysis for cell type-specific connectomics". In: *Eneuro* 6.5.

Kuwajima, Masaaki et al. (2020). "Ultrastructure of light-activated axons following optogenetic stimulation to produce late-phase long-term potentiation". In: *Plos one* 15.1, e0226797.

Kwon, Hyung-Bae and Bernardo L Sabatini (2011). "Glutamate induces de novo growth of functional spines in developing cortex". In: *Nature* 474.7349, pp. 100–104.

Kwon, Hyung-Bae et al. (2012). "Neuroligin-1–dependent competition regulates cortical synaptogenesis and synapse number". In: *Nature neuroscience* 15.12, pp. 1667–1674.

Lacruz, ME et al. (2010). "Single pulse electrical stimulation of the hippocampus is sufficient to impair human episodic memory". In: *Neuroscience* 170.2, pp. 623–632.

Lam, Stephanie S et al. (2015). "Directed evolution of APEX2 for electron microscopy and proximity labeling". In: *Nature methods* 12.1, pp. 51–54.

Lambert, Jason T et al. (2017). "Protracted and asynchronous accumulation of PSD95-family MAGUKs during maturation of nascent dendritic spines". In: *Developmental neurobiology* 77.10, pp. 1161–1174.

Lamsa, Karri, Joost H Heeroma, and Dimitri M Kullmann (2005). "Hebbian LTP in feed-forward inhibitory interneurons and the temporal fidelity of input discrimination". In: *Nature neuroscience* 8.7, pp. 916–924.

Landhuis, Esther (2017). "Neuroscience: Big brain, big data". In: *Nature* 541.7638, pp. 559–561.

Lauer, Jessy et al. (2021). "Multi-animal pose estimation and tracking with DeepLabCut". In: *BioRxiv*.

LeCun, Y. et al. (Dec. 1989). "Backpropagation Applied to Handwritten Zip Code Recognition". In: *Neural Computation* 1.4, pp. 541–551. DOI: 10.1162/neco.1989.1.4.541. URL: https://doi.org/10.1162/neco.1989.1.4.541.

Lee, Eun-Jae, Su Yeon Choi, and Eunjoon Kim (2015). "NMDA receptor dysfunction in autism spectrum disorders". In: *Current opinion in pharmacology* 20, pp. 8–13.

Lehmann, Konrad and Siegrid Löwel (2008). "Age-dependent ocular dominance plasticity in adult mice". In: *PloS one* 3.9, e3120.

Lein, Ed S et al. (2007). "Genome-wide atlas of gene expression in the adult mouse brain". In: *Nature* 445.7124, pp. 168–176.

Lettvin, Jerome Y et al. (1959). "What the frog's eye tells the frog's brain". In: *Proceedings of the IRE* 47.11, pp. 1940–1951.

Leutgeb, Stefan et al. (2004). "Distinct ensemble codes in hippocampal areas CA3 and CA1". In: *Science* 305.5688, pp. 1295–1298.

Levitz, Joshua et al. (2013). "Optical control of metabotropic glutamate receptors". In: *Nature neuroscience* 16.4, pp. 507–516.

Levy, WB and O Steward (1983). "Temporal contiguity requirements for long-term associative potentiation/depression in the hippocampus". In: *Neuroscience* 8.4, pp. 791–797.

Li, Rongjian et al. (2017). "Deep learning segmentation of optical microscopy images improves 3-D neuron reconstruction". In: *IEEE transactions on medical imaging* 36.7, pp. 1533–1541.

Liao, Dezhi, Neal A. Hessler, and Roberto Malinow (June 1995). "Activation of postsynaptically silent synapses during pairing-induced LTP in CA1 region of hippocampal slice". In: *Nature* 375.6530, pp. 400–404. DOI: 10.1038/375400a0. URL: https://doi.org/10.1038/375400a0.

Lin, Wan-Chen et al. (2014). "Engineering a light-regulated GABAA receptor for optical control of neural inhibition". In: *ACS chemical biology* 9.7, pp. 1414–1419.

Ling, Changying, Michael L Hendrickson, and Ronald E Kalil (2012). "Morphology, classification, and distribution of the projection neurons in the dorsal lateral geniculate nucleus of the rat". In: *PloS one* 7.11, e49161.

Litvina, Elizabeth Y and Chinfei Chen (2017). "Functional convergence at the retinogeniculate synapse". In: *Neuron* 96.2, pp. 330–338.

Liu, XiaoLe et al. (2020). "OptiFlex: video-based animal pose estimation using deep learning enhanced by optical flow". In: *BioRxiv*.

Lo, Donald C., A. Kimberley McAllister, and Lawrence C. Katz (Dec. 1994). "Neuronal transfection in brain slices using particle-mediated gene transfer". In: *Neuron* 13.6, pp. 1263–1268. DOI: 10.1016/0896-6273(94)90412-x. URL: https://doi.org/10.1016/0896-6273(94)90412-x.

Longair, Mark H, Dean A Baker, and J Douglas Armstrong (2011). "Simple Neurite Tracer: open source software for reconstruction, visualization and analysis of neuronal processes". In: *Bioinformatics* 27.17, pp. 2453–2454.

Losonczy, Attila and Jeffrey C Magee (2006). "Integrative properties of radial oblique dendrites in hippocampal CA1 pyramidal neurons". In: *Neuron* 50.2, pp. 291–307.

Losonczy, Attila, Judit K Makara, and Jeffrey C Magee (2008). "Compartmentalized dendritic plasticity and input feature storage in neurons". In: *Nature* 452.7186, pp. 436–441.

Lu, Rongwen et al. (Feb. 2017). "Video-rate volumetric functional imaging of the brain at synaptic resolution". In: *Nature Neuroscience* 20.4, pp. 620–628. DOI: 10.1038/nn.4516. URL: https://doi.org/10.1038/nn.4516.

Lu, Wei-Yang et al. (Jan. 2001a). "Activation of Synaptic NMDA Receptors Induces Membrane Insertion of New AMPA Receptors and LTP in Cultured Hippocampal Neurons". In: *Neuron* 29.1, pp. 243–254. DOI: 10.1016/s0896-6273(01)00194-5. URL: https://doi.org/10.1016/s0896-6273(01)00194-5.

Lu, Wei-Yang et al. (2001b). "Activation of synaptic NMDA receptors induces membrane insertion of new AMPA receptors and LTP in cultured hippocampal neurons". In: *Neuron* 29.1, pp. 243–254.

Lucas, Bruce D, Takeo Kanade, et al. (1981). "An iterative image registration technique with an application to stereo vision". In: Vancouver.

Ludkiewicz, Beata et al. (2002). "Cholinergic innervation of parvalbumin- and calbindin-containing neurones in the hippocampus during postnatal development of the rat brain". In: *Folia morphologica* 61.2, pp. 89–96.

Luo, Liqun, Edward M Callaway, and Karel Svoboda (2018). "Genetic dissection of neural circuits: a decade of progress". In: *Neuron* 98.2, pp. 256–281.

Lütcke, Henry et al. (2013). "Inference of neuronal network spike dynamics and topology from calcium imaging data". In: *Frontiers in Neural Circuits* 7. DOI: 10.3389/fncir.2013.00201. URL: https://doi.org/10.3389/fncir.2013.00201.

Lynch, Gary et al. (1983). "Intracellular injections of EGTA block induction of hippocampal long-term potentiation". In: *Nature* 305.5936, pp. 719–721.

M'Saad, Ons et al. (2022). "All-optical visualization of specific molecules in the ultrastructural context of brain tissue". In: *bioRxiv*.

Macarico-da-Costa, N and KA Martin (2009). "Not every touch is a kiss. Synapses and appositions between dendrites and axons: a correlated light and electron microscopy study". In: *Front. Neurosci. Conference Abstract:*

11th Meeting of the Portuguese Society for Neuroscience. doi: 10.3389/conf. neuro. Vol. 1. 11.005.

MacDonald, Christopher J et al. (2011). "Hippocampal "time cells" bridge the gap in memory for discontiguous events". In: *Neuron* 71.4, pp. 737–749.

Madison, Daniel V, Robert C Malenka, and Roger A Nicoll (1991). "Mechanisms underlying long-term potentiation of synaptic transmission". In: *Annual review of neuroscience* 14.1, pp. 379–397.

Magee, Jeffrey C and Daniel Johnston (1997). "A synaptically controlled, associative signal for Hebbian plasticity in hippocampal neurons". In: *Science* 275.5297, pp. 209–213.

Magee, JEFFREY C et al. (1995). "Subthreshold synaptic activation of voltage-gated Ca2+ channels mediates a localized Ca2+ influx into the dendrites of hippocampal pyramidal neurons". In: *Journal of neurophysiology* 74.3, pp. 1335–1342.

Magnin, Elise et al. (2019). "Input-specific synaptic location and function of the $\alpha 5$ GABAA receptor subunit in the mouse CA1 hippocampal neurons". In: *Journal of Neuroscience* 39.5, pp. 788–801.

Maisak, Matthew S et al. (2013). "A directional tuning map of Drosophila elementary motion detectors". In: *Nature* 500.7461, pp. 212–216.

Majewska, Ania, Ayumu Tashiro, and Rafael Yuste (2000). "Regulation of spine calcium dynamics by rapid spine motility". In: *Journal of Neuroscience* 20.22, pp. 8262–8268.

Malenka, Robert C and Mark F Bear (2004). "LTP and LTD: an embarrassment of riches". In: *Neuron* 44.1, pp. 5–21.

Maletic-Savatic, M, R Malinow, and K Svoboda (1999). "Rapid dendritic morphogenesis in CA1 hippocampal dendrites induced by synaptic activity". In: *Science* 283.5409, pp. 1923–1927.

Malinow, Roberto and Richard W Tsien (1990). "Presynaptic enhancement shown by whole-cell recordings of long-term potentiation in hippocampal slices". In: *Nature* 346.6280, pp. 177–180.

Mancuso, James J et al. (2013). "Methods of dendritic spine detection: from Golgi to high-resolution optical imaging". In: *Neuroscience* 251, pp. 129–140.

Markram, Henry et al. (1997). "Regulation of synaptic efficacy by coincidence of postsynaptic APs and EPSPs". In: *Science* 275.5297, pp. 213–215.

Marks, Tyler D and Michael J Goard (2021). "Stimulus-dependent representational drift in primary visual cortex". In: *Nature communications* 12.1, pp. 1–16.

Marr, D (1971). "Simple memory: a theory for archicortex". In: *Philosophical Transactions of the Royal Society of London. B, Biological Sciences* 262.841, pp. 23–81.

Martersteck, Emily M et al. (2017a). "Diverse central projection patterns of retinal ganglion cells". In: *Cell reports* 18.8, pp. 2058–2072.

Martersteck, Emily M. et al. (Feb. 2017b). "Diverse Central Projection Patterns of Retinal Ganglion Cells". In: *Cell Reports* 18.8, pp. 2058–2072. DOI: 10.1016/j.celrep.2017.01.075. URL: https://doi.org/10.1016/j.celrep.2017.01.075.

Marvin, Jonathan S et al. (2013). "An optimized fluorescent probe for visualizing glutamate neurotransmission". In: *Nature methods* 10.2, pp. 162–170.

Marvin, Jonathan S et al. (2018). "Stability, affinity, and chromatic variants of the glutamate sensor iGluSnFR". In: *Nature methods* 15.11, pp. 936–939.

Mathis, Alexander et al. (2018). "DeepLabCut: markerless pose estimation of user-defined body parts with deep learning". In: *Nature neuroscience* 21.9, pp. 1281–1289.

Matsuzaki, Masanori et al. (June 2004). "Structural basis of long-term potentiation in single dendritic spines". In: *Nature* 429.6993, pp. 761–766. DOI: 10.1038/nature02617. URL: https://doi.org/10.1038/nature02617.

Matteucci, Carlo (1841). *Deuxième mémoire sur le courant électrique propre de la grénouille et sur celui des animaux à sang chaud*. Imprimerie de Bachelier.

Mayer, Mark L, Gary L Westbrook, and Peter B Guthrie (1984). "Voltage-dependent block by Mg 2+ of NMDA responses in spinal cord neurones". In: *Nature* 309.5965, pp. 261–263.

McKay, Bruce E et al. (2006). "CaV3 T-type calcium channel isoforms differentially distribute to somatic and dendritic compartments in rat central neurons". In: *European Journal of Neuroscience* 24.9, pp. 2581–2594.

Megıas, M et al. (2001). "Total number and distribution of inhibitory and excitatory synapses on hippocampal CA1 pyramidal cells". In: *Neuroscience* 102.3, pp. 527–540.

Mellor, J and RA Nicoll (2001). "Hippocampal mossy fiber LTP is independent of postsynaptic calcium". In: *Nature neuroscience* 4.2, pp. 125–126.

Metin, C, P Godement, and M Imbert (1988). "The primary visual cortex in the mouse: receptive field properties and functional organization". In: *Experimental brain research* 69.3, pp. 594–612.

Meyer, Daniel, Tobias Bonhoeffer, and Volker Scheuss (2014). "Balance and stability of synaptic structures during synaptic plasticity". In: *Neuron* 82.2, pp. 430–443.

Minaee, Shervin et al. (2021). "Image segmentation using deep learning: A survey". In: *IEEE transactions on pattern analysis and machine intelligence*.

Miyamichi, Kazunari et al. (2011). "Cortical representations of olfactory input by trans-synaptic tracing". In: *Nature* 472.7342, pp. 191–196.

Moczulska, Kaja Ewa et al. (2013). "Dynamics of dendritic spines in the mouse auditory cortex during memory formation and memory recall". In: *Proceedings of the National Academy of Sciences* 110.45, pp. 18315–18320.

Moneron, Gael and Stefan W. Hell (Aug. 2009). "Two-photon excitation STED microscopy". In: *Optics Express* 17.17, p. 14567. DOI: 10.1364/oe.17.014567. URL: https://doi.org/10.1364/oe.17.014567.

Morgan, Josh Lyskowski et al. (2016). "The fuzzy logic of network connectivity in mouse visual thalamus". In: *Cell* 165.1, pp. 192–206.

Morgan, Joshua L et al. (2011). "Development of cell type-specific connectivity patterns of converging excitatory axons in the retina". In: *Neuron* 71.6, pp. 1014–1021.

Morin, Lawrence P and Keith M Studholme (2014). "Retinofugal projections in the mouse". In: *Journal of Comparative Neurology* 522.16, pp. 3733–3753.

Morris, RGM et al. (1986). "Selective impairment of learning and blockade of long-term potentiation by an N-methyl-D-aspartate receptor antagonist, AP5". In: *Nature* 319.6056, pp. 774–776.

Morris, Richard GM et al. (1982). "Place navigation impaired in rats with hippocampal lesions". In: *Nature* 297.5868, pp. 681–683.

Mosk, Allard P et al. (2012). "Controlling waves in space and time for imaging and focusing in complex media". In: *Nature photonics* 6.5, pp. 283–292.

Mozafari, Marzieh, Reza Farahbakhsh, and Noël Crespi (2020). "Hate speech detection and racial bias mitigation in social media based on BERT model". In: *PloS one* 15.8, e0237861.

Mukherjee, Arghya et al. (2021). "Thalamic circuits for independent control of prefrontal signal and noise". In: *Nature* 600.7887, pp. 100–104.

Mulkey, Rosel M and Robert C Malenka (1992). "Mechanisms underlying induction of homosynaptic long-term depression in area CA1 of the hippocampus". In: *Neuron* 9.5, pp. 967–975.

Müller, Wolfgang and John A Connor (1991). "Dendritic spines as individual neuronal compartments for synaptic Ca2+ responses". In: *Nature* 354.6348, pp. 73–76.

Murakami, Gen et al. (2006). "Comparison between basal and apical dendritic spines in estrogen-induced rapid spinogenesis of CA1 principal neurons in the adult hippocampus". In: *Biochemical and biophysical research communications* 351.2, pp. 553–558.

Murakoshi, Hideji, Hong Wang, and Ryohei Yasuda (2011). "Local, persistent activation of Rho GTPases during plasticity of single dendritic spines". In: *Nature* 472.7341, pp. 100–104.

Muthukumar, Allie K, Tobias Stork, and Marc R Freeman (2014). "Activity-dependent regulation of astrocyte GAT levels during synaptogenesis". In: *Nature neuroscience* 17.10, pp. 1340–1350.

Myme, Chaelon IO et al. (2003). "The NMDA-to-AMPA ratio at synapses onto layer 2/3 pyramidal neurons is conserved across prefrontal and visual cortices". In: *Journal of neurophysiology* 90.2, pp. 771–779.

Nabavi, Sadegh et al. (2014). "Engineering a memory with LTD and LTP". In: *Nature* 511.7509, pp. 348–352.

Nadella, K M Naga Srinivas et al. (Oct. 2016). "Random-access scanning microscopy for 3D imaging in awake behaving animals". In: *Nature Methods* 13.12, pp. 1001–1004. DOI: 10.1038/nmeth.4033. URL: https://doi.org/10.1038/nmeth.4033.

Nagel, Georg et al. (2002). "Channelrhodopsin-1: a light-gated proton channel in green algae". In: *Science* 296.5577, pp. 2395–2398.

Nagel, Georg et al. (2003). "Channelrhodopsin-2, a directly light-gated cation-selective membrane channel". In: *Proceedings of the National Academy of Sciences* 100.24, pp. 13940–13945.

Nagel, Georg et al. (2005). "Light activation of channelrhodopsin-2 in excitable cells of Caenorhabditis elegans triggers rapid behavioral responses". In: *Current Biology* 15.24, pp. 2279–2284.

Nägerl, U Valentin et al. (2007). "Protracted synaptogenesis after activity-dependent spinogenesis in hippocampal neurons". In: *Journal of Neuroscience* 27.30, pp. 8149–8156.

Nakai, Junichi, Masamichi Ohkura, and Keiji Imoto (2001). "A high signal-to-noise Ca 2+ probe composed of a single green fluorescent protein". In: *Nature biotechnology* 19.2, pp. 137–141.

Narushima, Madoka et al. (2016). "The metabotropic glutamate receptor subtype 1 mediates experience-dependent maintenance of mature synaptic connectivity in the visual thalamus". In: *Neuron* 91.5, pp. 1097–1109.

Nayak, Asha et al. (1998). "Maintenance of late-phase LTP is accompanied by PKA-dependent increase in AMPA receptor synthesis". In: *Nature* 394.6694, pp. 680–683.

Nguyen, Peter V, Ted Abel, and Eric R Kandel (1994). "Requirement of a critical period of transcription for induction of a late phase of LTP". In: *Science* 265.5175, pp. 1104–1107.

Nguyen, Q-T. et al. (Dec. 2001). "Construction of a two-photon microscope for video-rate Ca2 imaging". In: *Cell Calcium* 30.6, pp. 383–393. DOI: 10.1054/ceca.2001.0246. URL: https://doi.org/10.1054/ceca.2001.0246.

Niell, Cristopher M (2015). "Cell types, circuits, and receptive fields in the mouse visual cortex". In: *Annual review of neuroscience* 38, pp. 413–431.

Niell, Cristopher M, Martin P Meyer, and Stephen J Smith (2004). "In vivo imaging of synapse formation on a growing dendritic arbor". In: *Nature neuroscience* 7.3, pp. 254–260.

Niell, Cristopher M and Massimo Scanziani (2021). "How cortical circuits implement cortical computations: mouse visual cortex as a model". In: *Annual Review of Neuroscience* 44, pp. 517–546.

Nikolenko, Volodymyr (2008). "SLM microscopy: scanless two-photon imaging and photostimulation using spatial light modulators". In: *Frontiers in Neural Circuits* 2. DOI: 10.3389/neuro.04.005.2008. URL: https://doi.org/10.3389/neuro.04.005.2008.

Nowak, LPPAA et al. (1984). "Magnesium gates glutamate-activated channels in mouse central neurones". In: *Nature* 307.5950, pp. 462–465.

O'Donnell, Cian, Matthew F Nolan, and Mark CW van Rossum (2011). "Dendritic spine dynamics regulate the long-term stability of synaptic plasticity". In: *Journal of Neuroscience* 31.45, pp. 16142–16156.

O'Keefe, John (1976). "Place units in the hippocampus of the freely moving rat". In: *Experimental neurology* 51.1, pp. 78–109.

O'Keefe, John and Jonathan Dostrovsky (1971). "The hippocampus as a spatial map: preliminary evidence from unit activity in the freely-moving rat." In: *Brain research*.

Obermair, Gerald J et al. (2004). "Differential targeting of the L-type Ca2+ channel α1C (CaV1. 2) to synaptic and extrasynaptic compartments in hippocampal neurons". In: *European Journal of Neuroscience* 19.8, pp. 2109–2122.

Ofer, Netanel et al. (2021a). "Ultrastructural analysis of dendritic spine necks reveals a continuum of spine morphologies". In: *Developmental Neurobiology*.

Ofer, Netanel et al. (May 2021b). "Ultrastructural analysis of dendritic spine necks reveals a continuum of spine morphologies". In: *Developmental Neurobiology* 81.5, pp. 746–757. DOI: 10.1002/dneu.22829. URL: https://doi.org/10.1002/dneu.22829.

Ofer, Netanel et al. (2022). "Morphological analysis of human and mouse dendritic spines reveals a morphological continuum and differences across ages and species". In: *bioRxiv*. DOI: 10.1101/2022.01.24.477510. eprint: https://www.biorxiv.org/content/early/2022/01/25/2022.01.24.477510.full.pdf. URL: https://www.biorxiv.org/content/early/2022/01/25/2022.01.24.477510.

Okamoto, Ken-Ichi et al. (2004). "Rapid and persistent modulation of actin dynamics regulates postsynaptic reorganization underlying bidirectional plasticity". In: *Nature neuroscience* 7.10, pp. 1104–1112.

Okamoto, Ken-Ichi et al. (2007). "The role of CaMKII as an F-actin-bundling protein crucial for maintenance of dendritic spine structure". In: *Proceedings of the National Academy of Sciences* 104.15, pp. 6418–6423.

Oktay, Ozan et al. (2018). "Attention u-net: Learning where to look for the pancreas". In: *arXiv preprint arXiv:1804.03999*.

Ollion, Jean et al. (2013). "TANGO: a generic tool for high-throughput 3D image analysis for studying nuclear organization". In: *Bioinformatics* 29.14, pp. 1840–1841.

Omer, David B et al. (2018). "Social place-cells in the bat hippocampus". In: *Science* 359.6372, pp. 218–224.

Opazo, Patricio and Daniel Choquet (2011). "A three-step model for the synaptic recruitment of AMPA receptors". In: *Molecular and Cellular Neuroscience* 46.1, pp. 1–8.

Opazo, Patricio, Matthieu Sainlos, and Daniel Choquet (2012). "Regulation of AMPA receptor surface diffusion by PSD-95 slots". In: *Current opinion in neurobiology* 22.3, pp. 453–460.

Oron, Dan, Eran Tal, and Yaron Silberberg (Mar. 2005). "Scanningless depth-resolved microscopy". In: *Optics Express* 13.5, p. 1468. DOI: 10.1364/opex.13.001468. URL: https://doi.org/10.1364/opex.13.001468.

Osterhout, Jessica A. et al. (Aug. 2011). "Cadherin-6 Mediates Axon-Target Matching in a Non-Image-Forming Visual Circuit". In: *Neuron* 71.4, pp. 632–639. DOI: 10.1016/j.neuron.2011.07.006. URL: https://doi.org/10.1016/j.neuron.2011.07.006.

Ostroff, Linnaea E et al. (2002). "Polyribosomes redistribute from dendritic shafts into spines with enlarged synapses during LTP in developing rat hippocampal slices". In: *Neuron* 35.3, pp. 535–545.

Otmakhov, Nikolai et al. (2004). "Forskolin-induced LTP in the CA1 hippocampal region is NMDA receptor dependent". In: *Journal of neurophysiology* 91.5, pp. 1955–1962.

Peng, Hanchuan et al. (2011). "Proof-editing is the bottleneck of 3D neuron reconstruction: the problem and solutions". In: *Neuroinformatics* 9.2, pp. 103–105.

Pereira, Talmo D et al. (2019). "Fast animal pose estimation using deep neural networks". In: *Nature methods* 16.1, pp. 117–125.

Perez-Alvarez, Alberto et al. (2020). "Freeze-frame imaging of synaptic activity using SynTagMA". In: *Nature communications* 11.1, pp. 1–16.

Peters, Alan and Ita R Kaiserman-Abramof (1970). "The small pyramidal neuron of the rat cerebral cortex. The perikaryon, dendrites and spines". In: *American Journal of Anatomy* 127.4, pp. 321–355.

Petrak, Lara J, Kristen M Harris, and Sergei A Kirov (2005). "Synaptogenesis on mature hippocampal dendrites occurs via filopodia and immature spines during blocked synaptic transmission". In: *Journal of Comparative Neurology* 484.2, pp. 183–190.

Petrantonakis, Panagiotis C and Panayiota Poirazi (2014). "A compressed sensing perspective of hippocampal function". In: *Frontiers in systems neuroscience* 8, p. 141.

Petreanu, Leopoldo et al. (2007). "Channelrhodopsin-2–assisted circuit mapping of long-range callosal projections". In: *Nature neuroscience* 10.5, pp. 663–668.

Petreanu, Leopoldo et al. (2009). "The subcellular organization of neocortical excitatory connections". In: *Nature* 457.7233, pp. 1142–1145.

Pfeiffenberger, Cory et al. (2005). "Ephrin-As and neural activity are required for eye-specific patterning during retinogeniculate mapping". In: *Nature neuroscience* 8.8, pp. 1022–1027.

Pfeiffer, Thomas et al. (2018). "Chronic 2P-STED imaging reveals high turnover of dendritic spines in the hippocampus in vivo". In: *Elife* 7, e34700.

Piscopo, Denise M et al. (2013). "Diverse visual features encoded in mouse lateral geniculate nucleus". In: *Journal of Neuroscience* 33.11, pp. 4642–4656.

Platt, Simon R (2007). "The role of glutamate in central nervous system health and disease–a review". In: *The Veterinary Journal* 173.2, pp. 278–286.

Pnevmatikakis, Eftychios A et al. (2016). "Simultaneous denoising, deconvolution, and demixing of calcium imaging data". In: *Neuron* 89.2, pp. 285–299.

Pologruto, Thomas A, Bernardo L Sabatini, and Karel Svoboda (2003). "ScanImage: flexible software for operating laser scanning microscopes". In: *Biomedical engineering online* 2.1, pp. 1–9.

Prasher, Douglas C et al. (1992). "Primary structure of the Aequorea victoria green-fluorescent protein". In: *Gene* 111.2, pp. 229–233.

Qian, Jing and Jeffrey L Noebels (2000). "Presynaptic Ca2+ influx at a mouse central synapse with Ca2+ channel subunit mutations". In: *Journal of Neuroscience* 20.1, pp. 163–170.

Qu, Lei, Fuhui Long, and Hanchuan Peng (2014). "3-D registration of biological images and models: registration of microscopic images and its uses in segmentation and annotation". In: *IEEE Signal Processing Magazine* 32.1, pp. 70–77.

Ramachandran, Prajit, Barret Zoph, and Quoc V Le (2017). "Searching for activation functions". In: *arXiv preprint arXiv:1710.05941*.

Ramón y Cajal, Santiago (1888). *Estructura de los centros nerviosos de las aves*. Revista Trimestral de Histología Normal y Patológica.

Ramón y Cajal, Santiago (1891). *Sur la structure de l'écorce cérébrale de quelques mammifères*. Typ. de Joseph Van In.

Ranck Jr, James B (1973). "Studies on single neurons in dorsal hippocampal formation and septum in unrestrained rats: Part I. Behavioral correlates and firing repertoires". In: *Experimental neurology* 41.2, pp. 462–531.

Ranck Jr, JB (1984). "Head direction cells in the deep layer of dorsal presubiculum in freely moving rats". In: *Society of Neuroscience Abstract*. Vol. 10, p. 599.

Regehr, Wade G and David W Tank (1992). "Calcium concentration dynamics produced by synaptic activation of CA1 hippocampal pyramidal cells". In: *Journal of Neuroscience* 12.11, pp. 4202–4223.

Reid, R Clay (2012). "From functional architecture to functional connectomics". In: *Neuron* 75.2, pp. 209–217.

Reid, Reid C and Jose-Manuel Alonso (1995). "Specificity of monosynaptic connections from thalamus to visual cortex". In: *Nature* 378.6554, pp. 281–284.

Restivo, Leonardo et al. (2009). "The formation of recent and remote memory is associated with time-dependent formation of dendritic spines in the hippocampus and anterior cingulate cortex". In: *Journal of Neuroscience* 29.25, pp. 8206–8214.

Rimbault, Charlotte et al. (2021). "Engineering paralog-specific PSD-95 synthetic binders as potent and minimally invasive imaging probes". In: *bioRxiv*.

Ripley, Beth et al. (2011). "Regulation of synaptic stability by AMPA receptor reverse signaling". In: *Proceedings of the National Academy of Sciences* 108.1, pp. 367–372.

Roberts, Todd F et al. (2010). "Rapid spine stabilization and synaptic enhancement at the onset of behavioural learning". In: *Nature* 463.7283, pp. 948–952.

Robinson, Nick TM et al. (2020). "Targeted activation of hippocampal place cells drives memory-guided spatial behavior". In: *Cell* 183.6, pp. 1586–1599.

Rochefort, Nathalie L and Arthur Konnerth (2012). "Dendritic spines: from structure to in vivo function". In: *EMBO reports* 13.8, pp. 699–708.

Rodriguez, Alfredo et al. (2008). "Automated three-dimensional detection and shape classification of dendritic spines from fluorescence microscopy images". In: *PloS one* 3.4, e1997.

Rogan, Michael T, Ursula V Stäubli, and Joseph E LeDoux (1997). "Fear conditioning induces associative long-term potentiation in the amygdala". In: *Nature* 390.6660, pp. 604–607.

Rohlfing, Torsten (n.d.). *Computational Morphometry Toolkit (CMTK)*. URL: `https://www.nitrc.org/projects/cmtk/`. (accessed: 11.04.2022).

Rompani, Santiago B et al. (2017). "Different modes of visual integration in the lateral geniculate nucleus revealed by single-cell-initiated transsynaptic tracing". In: *Neuron* 93.4, pp. 767–776.

Ronneberger, Olaf, Philipp Fischer, and Thomas Brox (2015). "U-net: Convolutional networks for biomedical image segmentation". In: *International Conference on Medical image computing and computer-assisted intervention*. Springer, pp. 234–241.

Roo, M. De et al. (May 2007). "Activity-Dependent PSD Formation and Stabilization of Newly Formed Spines in Hippocampal Slice Cultures". In: *Cerebral Cortex* 18.1, pp. 151–161. DOI: 10.1093/cercor/bhm041. URL: https://doi.org/10.1093/cercor/bhm041.

Roome, Christopher J and Bernd Kuhn (2018). "Simultaneous dendritic voltage and calcium imaging and somatic recording from Purkinje neurons in awake mice". In: *Nature communications* 9.1, pp. 1–14.

Rose, Tobias and Tobias Bonhoeffer (2018). "Experience-dependent plasticity in the lateral geniculate nucleus". In: *Current opinion in neurobiology* 53, pp. 22–28.

Rose, Tobias et al. (2016). "Cell-specific restoration of stimulus preference after monocular deprivation in the visual cortex". In: *Science* 352.6291, pp. 1319–1322.

Rosón, Miroslav Román et al. (2019). "Mouse dLGN receives functional input from a diverse population of retinal ganglion cells with limited convergence". In: *Neuron* 102.2, pp. 462–476.

Roth, Morgane M et al. (2016). "Thalamic nuclei convey diverse contextual information to layer 1 of visual cortex". In: *Nature neuroscience* 19.2, pp. 299–307.

Ruiz, Arnaud et al. (2010). "Presynaptic GABA A receptors enhance transmission and LTP induction at hippocampal mossy fiber synapses". In: *Nature neuroscience* 13.4, pp. 431–438.

Ryan, Tomás J et al. (2015). "Engram cells retain memory under retrograde amnesia". In: *Science* 348.6238, pp. 1007–1013.

Sabatini, Bernardo L and Karel Svoboda (2000). "Analysis of calcium channels in single spines using optical fluctuation analysis". In: *Nature* 408.6812, pp. 589–593.

Saberi-Bosari, Sahand, Kevin B Flores, and Adriana San-Miguel (2020). "Deep learning-enabled analysis reveals distinct neuronal phenotypes induced by aging and cold-shock". In: *BMC biology* 18.1, pp. 1–18.

Sahel, José-Alain et al. (2021). "Partial recovery of visual function in a blind patient after optogenetic therapy". In: *Nature Medicine*, pp. 1–7.

Salin, Paul A, Robert C Malenka, and Roger A Nicoll (1996). "Cyclic AMP mediates a presynaptic form of LTP at cerebellar parallel fiber synapses". In: *Neuron* 16.4, pp. 797–803.

Salpietro, Vincenzo et al. (2019). "AMPA receptor GluA2 subunit defects are a cause of neurodevelopmental disorders". In: *Nature communications* 10.1, pp. 1–16.

Sanderson, KJ (1971). "The projection of the visual field to the lateral geniculate and medial interlaminar nuclei in the cat". In: *Journal of Comparative Neurology* 143.1, pp. 101–117.

Schafer, DorothyáP et al. (2012). "Microglia sculpt postnatal neural circuits in an activity and complement-dependent manner". In: *Neuron* 74.4, pp. 691–705.

Schiller, Jackie et al. (Mar. 2000). "NMDA spikes in basal dendrites of cortical pyramidal neurons". In: *Nature* 404.6775, pp. 285–289. DOI: 10.1038/35005094. URL: https://doi.org/10.1038/35005094.

Schindelin, Johannes et al. (2012). "Fiji: an open-source platform for biological-image analysis". In: *Nature methods* 9.7, pp. 676–682.

Schneider, Caroline A, Wayne S Rasband, and Kevin W Eliceiri (2012). "NIH Image to ImageJ: 25 years of image analysis". In: *Nature methods* 9.7, pp. 671–675.

Schnell, Eric et al. (2002). "Direct interactions between PSD-95 and stargazin control synaptic AMPA receptor number". In: *Proceedings of the National Academy of Sciences* 99.21, pp. 13902–13907.

Schoenenberger, Philipp et al. (2008). "Optimizing the spatial resolution of Channelrhodopsin-2 activation". In: *Brain cell biology* 36.1, pp. 119–127.

Scholl, Benjamin, Daniel E Wilson, and David Fitzpatrick (2017). "Local order within global disorder: synaptic architecture of visual space". In: *Neuron* 96.5, pp. 1127–1138.

Scholl, Benjamin et al. (2021). "Cortical response selectivity derives from strength in numbers of synapses". In: *Nature* 590.7844, pp. 111–114.

Schwartzkroin, Philip A (1975). "Characteristics of CA1 neurons recorded intracellularly in the hippocampalin vitro slice preparation". In: *Brain research* 85.3, pp. 423–436.

Scoville, William Beecher and Brenda Milner (1957). "Loss of recent memory after bilateral hippocampal lesions". In: *Journal of neurology, neurosurgery, and psychiatry* 20.1, p. 11.

Seabrook, Tania A et al. (2017). "Architecture, function, and assembly of the mouse visual system". In: *Annual review of neuroscience* 40, pp. 499–538.

Seeburg, Peter H et al. (1995). "The NMDA receptor channel: molecular design of a coincidence detector". In: *Proceedings of the 1993 Laurentian Hormone Conference*. Elsevier, pp. 19–34.

Sellers, Katherine J et al. (2015). "Rapid modulation of synaptogenesis and spinogenesis by 17β-estradiol in primary cortical neurons". In: *Frontiers in cellular neuroscience* 9, p. 137.

Serwanski, David R et al. (2006). "Synaptic and nonsynaptic localization of GABAA receptors containing the $\alpha 5$ subunit in the rat brain". In: *Journal of Comparative Neurology* 499.3, pp. 458–470.

Sheffield, Mark EJ, Michael D Adoff, and Daniel A Dombeck (2017). "Increased prevalence of calcium transients across the dendritic arbor during place field formation". In: *Neuron* 96.2, pp. 490–504.

Shelton, Andrew M et al. (2022). "Single neurons and networks in the claustrum integrate input from widespread cortical sources". In: *bioRxiv*.

Shemiakina, II et al. (2012). "A monomeric red fluorescent protein with low cytotoxicity". In: *Nature communications* 3.1, pp. 1–7.

Shen, Dinggang, Guorong Wu, and Heung-Il Suk (2017). "Deep learning in medical image analysis". In: *Annual review of biomedical engineering* 19, pp. 221–248.

Shen, Kevin and Agenor Limon (2021). "Transcriptomic expression of AMPA receptor subunits and their auxiliary proteins in the human brain". In: *Neuroscience Letters*, p. 135938.

Sheppard, Colin JR and David M Shotton (1997). *Confocal laser scanning microscopy*.

Shi, Peng, Yue Huang, and Jinsheng Hong (2014). "Automated three-dimensional reconstruction and morphological analysis of dendritic spines based on semi-supervised learning". In: *Biomedical optics express* 5.5, pp. 1541–1553.

Shindo, Yutaka et al. (2022). "Genetically encoded sensors for analysing neurotransmission among synaptically-connected neurons". In: *bioRxiv*.

Singh, P. K. et al. (July 2017a). "Automated 3-D Detection of Dendritic Spines from In Vivo Two-Photon Image Stacks". In: *Neuroinformatics* 15.4, pp. 303–319. DOI: 10.1007/s12021-017-9332-2. URL: https://doi.org/10.1007/s12021-017-9332-2.

Singh, Pankaj K et al. (2017b). "Automated 3-D detection of dendritic spines from in vivo two-photon image stacks". In: *Neuroinformatics* 15.4, pp. 303–319.

Smirnov, Michael S, Tavita R Garrett, and Ryohei Yasuda (2018). "An open-source tool for analysis and automatic identification of dendritic spines using machine learning". In: *Plos one* 13.7, e0199589.

Smith, Gordon B et al. (2018). "Distributed network interactions and their emergence in developing neocortex". In: *Nature neuroscience* 21.11, pp. 1600–1608.

Sofroniew, Nicholas James et al. (2016). "A large field of view two-photon mesoscope with subcellular resolution for in vivo imaging". In: *Elife* 5, e14472.

Solstad, Trygve et al. (2008). "Representation of geometric borders in the entorhinal cortex". In: *Science* 322.5909, pp. 1865–1868.

Sommeijer, Jean-Pierre et al. (2017). "Thalamic inhibition regulates critical-period plasticity in visual cortex and thalamus". In: *Nature neuroscience* 20.12, pp. 1715–1721.

Song, Jun Ho et al. (2018). "Combining mGRASP and optogenetics enables high-resolution functional mapping of descending cortical projections". In: *Cell reports* 24.4, pp. 1071–1080.

Spacek, Martin A et al. (2022). "Robust effects of corticothalamic feedback and behavioral state on movie responses in mouse dLGN". In: *Elife* 11, e70469.

Stavis, Robert L and Rona Hirschberg (1973). "Phototaxis in Chlamydomonas reinhardtii". In: *The Journal of cell biology* 59.2, pp. 367–377.

Steinmetz, Nicholas A et al. (2021). "Neuropixels 2.0: A miniaturized high-density probe for stable, long-term brain recordings". In: *Science* 372.6539, eabf4588.

Stevens, Beth et al. (2007). "The classical complement cascade mediates CNS synapse elimination". In: *Cell* 131.6, pp. 1164–1178.

Stoppini, L., P.-A. Buchs, and D. Muller (Apr. 1991a). "A simple method for organotypic cultures of nervous tissue". In: *Journal of Neuroscience Methods* 37.2, pp. 173–182. DOI: 10.1016/0165-0270(91)90128-m. URL: https://doi.org/10.1016/0165-0270(91)90128-m.

Stoppini, Luc, P-A Buchs, and Dominique Muller (1991b). "A simple method for organotypic cultures of nervous tissue". In: *Journal of neuroscience methods* 37.2, pp. 173–182.

Stringer, Carsen et al. (2021). "Cellpose: a generalist algorithm for cellular segmentation". In: *Nature Methods* 18.1, pp. 100–106.

Sun, Fangmiao et al. (2018). "A genetically encoded fluorescent sensor enables rapid and specific detection of dopamine in flies, fish, and mice". In: *Cell* 174.2, pp. 481–496.

Sun, Liyuan et al. (2009). "Magnesium concentration in the cerebrospinal fluid of mice and its response to changes in serum magnesium concentration". In: *Magnesium research* 22.4, pp. 266–272.

Suter, Benjamin A et al. (2010). "Ephus: multipurpose data acquisition software for neuroscience experiments". In: *Frontiers in neural circuits* 4, p. 100.

Suzuki, Junji, Kazunori Kanemaru, and Masamitsu Iino (2016). "Genetically encoded fluorescent indicators for organellar calcium imaging". In: *Biophysical Journal* 111.6, pp. 1119–1131.

Swanger, Sharon A et al. (2011). "Automated 4D analysis of dendritic spine morphology: applications to stimulus-induced spine remodeling and pharmacological rescue in a disease model". In: *Molecular brain* 4.1, pp. 1–14.

Sweeney, N. T., H. Tierney, and D. A. Feldheim (Apr. 2014). "Tbr2 Is Required to Generate a Neural Circuit Mediating the Pupillary Light Reflex". In: *Journal of Neuroscience* 34.16, pp. 5447–5453. DOI: 10.1523/jneurosci.0035-14.2014. URL: https://doi.org/10.1523/jneurosci.0035-14.2014.

Szobota, Stephanie et al. (May 2007). "Remote Control of Neuronal Activity with a Light-Gated Glutamate Receptor". In: *Neuron* 54.4, pp. 535–545. DOI: 10.1016/j.neuron.2007.05.010. URL: https://doi.org/10.1016/j.neuron.2007.05.010.

Tang, Yi et al. (1999). "Spinal and brain circuits to motoneurons of the bulbospongiosus muscle: retrograde transneuronal tracing with rabies virus". In: *Journal of Comparative Neurology* 414.2, pp. 167–192.

Terashima, Akira, Young Ho Suh, and John TR Isaac (2019). "The AMPA receptor subunit GluA1 is required for CA1 hippocampal long-term potentiation but is not essential for synaptic transmission". In: *Neurochemical Research* 44.3, pp. 549–561.

Thompson, Andrew D et al. (2016). "Cortical feedback regulates feedforward retinogeniculate refinement". In: *Neuron* 91.5, pp. 1021–1033.

Tippens, Alyssa L et al. (2008). "Ultrastructural evidence for pre-and postsynaptic localization of Cav1. 2 L-type Ca2+ channels in the rat hippocampus". In: *Journal of Comparative Neurology* 506.4, pp. 569–583.

Toni, Nicolas et al. (1999). "LTP promotes formation of multiple spine synapses between a single axon terminal and a dendrite". In: *Nature* 402.6760, pp. 421–425.

Toni, Nicolas et al. (2007). "Synapse formation on neurons born in the adult hippocampus". In: *Nature neuroscience* 10.6, pp. 727–734.

Trachtenberg, Joshua T. et al. (Dec. 2002). "Long-term in vivo imaging of experience-dependent synaptic plasticity in adult cortex". In: *Nature*

420.6917, pp. 788–794. DOI: 10.1038/nature01273. URL: https://doi.org/10.1038/nature01273.

Treves, Alessandro and Edmund T Rolls (1994). "Computational analysis of the role of the hippocampus in memory". In: *Hippocampus* 4.3, pp. 374–391.

Tsay, David, Joshua T Dudman, and Steven A Siegelbaum (2007). "HCN1 channels constrain synaptically evoked Ca2+ spikes in distal dendrites of CA1 pyramidal neurons". In: *Neuron* 56.6, pp. 1076–1089.

Tsay, David and Rafael Yuste (2004). "On the electrical function of dendritic spines". In: *Trends in neurosciences* 27.2, pp. 77–83.

Tu, Jian Cheng et al. (1999). "Coupling of mGluR/Homer and PSD-95 complexes by the Shank family of postsynaptic density proteins". In: *Neuron* 23.3, pp. 583–592.

Turecek, Rostislav and Laurence O Trussell (2002). "Reciprocal developmental regulation of presynaptic ionotropic receptors". In: *Proceedings of the National Academy of Sciences* 99.21, pp. 13884–13889.

Turrigiano, Gina G and Sacha B Nelson (2004). "Homeostatic plasticity in the developing nervous system". In: *Nature reviews neuroscience* 5.2, pp. 97–107.

Tyson, Adam L et al. (2021). "A deep learning algorithm for 3D cell detection in whole mouse brain image datasets". In: *PLoS computational biology* 17.5, e1009074.

Ugolini, Gabriella (1995). "Specificity of rabies virus as a transneuronal tracer of motor networks: transfer from hypoglossal motoneurons to connected second-order and higher order central nervous system cell groups". In: *Journal of Comparative Neurology* 356.3, pp. 457–480.

Ullian, Erik M, Karen S Christopherson, and Ben A Barres (2004). "Role for glia in synaptogenesis". In: *Glia* 47.3, pp. 209–216.

Van Rossum, Guido and Fred L. Drake (2009). *Python 3 Reference Manual*. Scotts Valley, CA: CreateSpace. ISBN: 1441412697.

Velicky, Philipp et al. (2022). "Saturated reconstruction of living brain tissue". In: *bioRxiv*.

Vetere, Gisella et al. (2011). "Spine growth in the anterior cingulate cortex is necessary for the consolidation of contextual fear memory". In: *Proceedings of the National Academy of Sciences* 108.20, pp. 8456–8460.

Vidaurre-Gallart, Isabel et al. (2022). "A Deep Learning-Based Workflow for Dendritic Spine Segmentation." In: *Frontiers in neuroanatomy* 16, pp. 817903–817903.

Vogelstein, Joshua T et al. (2010). "Fast nonnegative deconvolution for spike train inference from population calcium imaging". In: *Journal of neurophysiology* 104.6, pp. 3691–3704.

Volgraf, Matthew et al. (Dec. 2005). "Allosteric control of an ionotropic glutamate receptor with an optical switch". In: *Nature Chemical Biology* 2.1, pp. 47–52. DOI: 10.1038/nchembio756. URL: https://doi.org/10.1038/nchembio756.

Vries, Saskia EJ de et al. (2020). "A large-scale standardized physiological survey reveals functional organization of the mouse visual cortex". In: *Nature neuroscience* 23.1, pp. 138–151.

Vyas, Kathan et al. (2019). "Recognition of atypical behavior in autism diagnosis from video using pose estimation over time". In: *2019 IEEE 29th International Workshop on Machine Learning for Signal Processing (MLSP)*. IEEE, pp. 1–6.

Wada, Housei (n.d.). *CoordinateShift ImageJ Plugin*. URL: https://signaling.riken.jp/en/en-tools/imagej/635/. (accessed: 11.04.2022).

Walker, Alison S. et al. (Feb. 2017). "Distance-dependent gradient in NMDAR-driven spine calcium signals along tapering dendrites". In: *Proceedings of the National Academy of Sciences* 114.10, E1986–E1995. DOI: 10.1073/pnas.1607462114. URL: https://doi.org/10.1073/pnas.1607462114.

Wan, Jinxia et al. (2021). "A genetically encoded sensor for measuring serotonin dynamics". In: *Nature neuroscience* 24.5, pp. 746–752.

Wang, Mei and Weihong Deng (2020). "Mitigating bias in face recognition using skewness-aware reinforcement learning". In: *Proceedings of the IEEE/CVF conference on computer vision and pattern recognition*, pp. 9322–9331.

Wang, Quanxin et al. (2020). "The Allen mouse brain common coordinate framework: a 3D reference atlas". In: *Cell* 181.4, pp. 936–953.

Wassle, Heinz and BRIAN B Boycott (1991). "Functional architecture of the mammalian retina". In: *Physiological reviews* 71.2, pp. 447–480.

Watkins, JC and RH Evans (1981). "Excitatory amino acid transmitters". In: *Annual review of pharmacology and toxicology* 21.1, pp. 165–204.

Wearne, SL et al. (2005). "New techniques for imaging, digitization and analysis of three-dimensional neural morphology on multiple scales". In: *Neuroscience* 136.3, pp. 661–680.

Weiler, Simon et al. (2018). "High-yield in vitro recordings from neurons functionally characterized in vivo". In: *Nature protocols* 13.6, pp. 1275–1293.

Werblin, Frank S and John E Dowling (1969). "Organization of the retina of the mudpuppy, Necturus maculosus. II. Intracellular recording." In: *Journal of neurophysiology* 32.3, pp. 339–355.

Westenbroek, Ruth E, Michael K Ahlijanian, and William A Catterall (1990). "Clustering of L-type Ca2+ channels at the base of major dendrites in hippocampal pyramidal neurons". In: *Nature* 347.6290, pp. 281–284.

Wheeler, David B, Andrew Randall, and Richard W Tsien (1994). "Roles of N-type and Q-type Ca2+ channels in supporting hippocampal synaptic transmission". In: *Science* 264.5155, pp. 107–111.

White, JG, WB Amos, and M Fordham (1987). "An evaluation of confocal versus conventional imaging of biological structures by fluorescence light microscopy." In: *The Journal of cell biology* 105.1, pp. 41–48.

Wiegert, J Simon and Thomas G Oertner (2013). "Long-term depression triggers the selective elimination of weakly integrated synapses". In: *Proceedings of the National Academy of Sciences* 110.47, E4510–E4519.

Wiegert, J Simon et al. (2018). "The fate of hippocampal synapses depends on the sequence of plasticity-inducing events". In: *Elife* 7, e39151.

Wilke, Scott A et al. (2013). "Deconstructing complexity: serial block-face electron microscopic analysis of the hippocampal mossy fiber synapse". In: *Journal of Neuroscience* 33.2, pp. 507–522.

Willems, Jelmer et al. (2020). "ORANGE: A CRISPR/Cas9-based genome editing toolbox for epitope tagging of endogenous proteins in neurons". In: *PLoS biology* 18.4, e3000665.

Williams, Scott E. et al. (Sept. 2003). "Ephrin-B2 and EphB1 Mediate Retinal Axon Divergence at the Optic Chiasm". In: *Neuron* 39.6, pp. 919–935. DOI: 10.1016/j.neuron.2003.08.017. URL: https://doi.org/10.1016/j.neuron.2003.08.017.

Wilson, Daniel E et al. (2016). "Orientation selectivity and the functional clustering of synaptic inputs in primary visual cortex". In: *Nature neuroscience* 19.8, pp. 1003–1009.

Witter, Menno P and David G Amaral (1991). "Entorhinal cortex of the monkey: V. Projections to the dentate gyrus, hippocampus, and subicular complex". In: *Journal of Comparative Neurology* 307.3, pp. 437–459.

Woolley, Catherine S et al. (1990). "Naturally occurring fluctuation in dendritic spine density on adult hippocampal pyramidal neurons". In: *Journal of neuroscience* 10.12, pp. 4035–4039.

Wu, Weishu, Aaron R. Hawkins, and John E. Bowers (Jan. 1997). "Design of InGaAs/Si avalanche photodetectors for 400-GHz gain-bandwidth prod-

uct". In: *Optoelectronic Integrated Circuits*. Ed. by Yoon-Soo Park and Ramu V. Ramaswamy. SPIE. DOI: 10.1117/12.264251. URL: https://doi.org/10.1117/12.264251.

Wyllie, DJA, MR Livesey, and GE Hardingham (2013). "Influence of GluN2 subunit identity on NMDA receptor function". In: *Neuropharmacology* 74, pp. 4–17.

Xiao, Sa et al. (2017). "Fully automated, deep learning segmentation of oxygen-induced retinopathy images". In: *JCI insight* 2.24.

Xiao, Xuerong et al. (Nov. 2018). "Automated dendritic spine detection using convolutional neural networks on maximum intensity projected microscopic volumes". In: *Journal of Neuroscience Methods* 309, pp. 25–34. DOI: 10.1016/j.jneumeth.2018.08.019. URL: https://doi.org/10.1016/j.jneumeth.2018.08.019.

Xu, Tonghui et al. (2009). "Rapid formation and selective stabilization of synapses for enduring motor memories". In: *Nature* 462.7275, pp. 915–919.

Yamaguchi, Yukiko and Tatsuro Matsumoto (1990). "A neural network approach to multi-language text-to-speech system". In: *Proc. First International Conference on Spoken Language Processing (ICSLP 1990)*, pp. 325–328.

Yang, Guang, Feng Pan, and Wen-Biao Gan (2009). "Stably maintained dendritic spines are associated with lifelong memories". In: *Nature* 462.7275, pp. 920–924.

Yang, Sunggu et al. (2014). "Interlamellar CA1 network in the hippocampus". In: *Proceedings of the National Academy of Sciences* 111.35, pp. 12919–12924.

Yartsev, Michael M, Menno P Witter, and Nachum Ulanovsky (2011). "Grid cells without theta oscillations in the entorhinal cortex of bats". In: *Nature* 479.7371, pp. 103–107.

Ye, Gui-lan et al. (2005). "AMPA and NMDA receptor-mediated currents in developing dentate gyrus granule cells". In: *Developmental brain research* 155.1, pp. 26–32.

Yu, Che-Hang et al. (Nov. 2021). "Diesel2p mesoscope with dual independent scan engines for flexible capture of dynamics in distributed neural circuitry". In: *Nature Communications* 12.1. DOI: 10.1038/s41467-021-26736-4. URL: https://doi.org/10.1038/s41467-021-26736-4.

Yuste, Rafael (2015). "The discovery of dendritic spines by Cajal". In: *Frontiers in neuroanatomy* 9, p. 18.

Yuste, Rafael and Winfried Denk (1995). "Dendritic spines as basic functional units of neuronal integration". In: *Nature* 375.6533, pp. 682–684.

Yuste, Rafael et al. (Mar. 1999). "Mechanisms of Calcium Influx into Hippocampal Spines: Heterogeneity among Spines, Coincidence Detection by NMDA Receptors, and Optical Quantal Analysis". In: *The Journal of Neuroscience* 19.6, pp. 1976–1987. DOI: 10.1523/jneurosci.19-06-01976.1999. URL: https://doi.org/10.1523/jneurosci.19-06-01976.1999.

Zalutsky, Robert A and Roger A Nicoll (1990). "Comparison of two forms of long-term potentiation in single hippocampal neurons". In: *Science* 248.4963, pp. 1619–1624.

Zemelman, Boris V et al. (2002). "Selective photostimulation of genetically chARGed neurons". In: *Neuron* 33.1, pp. 15–22.

Zhang, Jiawei (2019). "Basic neural units of the brain: neurons, synapses and action potential". In: *arXiv preprint arXiv:1906.01703*.

Zhang, Yan et al. (2020). "jGCaMP8 Fast Genetically Encoded Calcium Indicators". In: DOI: 10.25378/JANELIA.13148243. URL: https://janelia.figshare.com/articles/online_resource/jGCaMP8_Fast_Genetically_Encoded_Calcium_Indicators/13148243.

Zhang, Yong et al. (2007). "Dendritic spine detection using curvilinear structure detector and LDA classifier". In: *Neuroimage* 36.2, pp. 346–360.

Zhang, Yong et al. (2010). "A neurocomputational method for fully automated 3D dendritic spine detection and segmentation of medium-sized spiny neurons". In: *Neuroimage* 50.4, pp. 1472–1484.

Zheng, Zhihao et al. (2018). "A complete electron microscopy volume of the brain of adult Drosophila melanogaster". In: *Cell* 174.3, pp. 730–743.

Zhou, Qiang, Koichi J Homma, and Mu-ming Poo (2004). "Shrinkage of dendritic spines associated with long-term depression of hippocampal synapses". In: *Neuron* 44.5, pp. 749–757.

Zhou, Zhi et al. (2018). "DeepNeuron: an open deep learning toolbox for neuron tracing". In: *Brain informatics* 5.2, pp. 1–9.

Zhu, Guanghao et al. (2005). "Simultaneous spatial and temporal focusing of femtosecond pulses". In: *Optics Express* 13.6, p. 2153. DOI: 10.1364/opex.13.002153. URL: https://doi.org/10.1364/opex.13.002153.

Zhu, J Julius et al. (2002). "Ras and Rap control AMPA receptor trafficking during synaptic plasticity". In: *Cell* 110.4, pp. 443–455.

Ziburkus, Jokubas and William Guido (2006). "Loss of binocular responses and reduced retinal convergence during the period of retinogeniculate axon segregation". In: *Journal of neurophysiology* 96.5, pp. 2775–2784.

Zito, Karen et al. (2009). "Rapid functional maturation of nascent dendritic spines". In: *Neuron* 61.2, pp. 247–258.

Zuo, Yi et al. (2005). "Long-term sensory deprivation prevents dendritic spine loss in primary somatosensory cortex". In: *Nature* 436.7048, pp. 261–265.

Declaration of author contribution

Setups

Tobias Rose and Cvetalina Coneva designed the main *in vitro* setup. I made additional modifications and added the "Bessel module" to enable volumetric two-photon imaging. The *in vivo* two photon setup was designed and built by Tobias Rose. The other *in vitro* setup was designed and built by Simon Weiler, Volker Schuess and Michael Myoga. I performed maintenance on that setup.

Binocularity in the dLGN

The project was conceived of by Simon Weiler, Tobias Rose, Joel Bauer and myself. Joel Bauer established and performed intravitreal eye injections. The *in vitro* acute slice approach was developed by Simon Weiler. The two-part step protocols were devised by Simon Weiler and myself. Electrophysiological recordings were performed by Simon Weiler and myself. Brain clearing and immunohistochemistry was performed by Volker Staiger. Confocal imaging was performed by myself with help from Volker Staiger and Robert Kasper. I performed re-identification of cells in confocal data. Volker Staiger, Meike Hack and Ursula Weber reconstructed dLGN cell morphologies. Quality control of the data was performed by Joel Bauer and myself. Joel Bauer and Simon Weiler performed the majority of data analysis for this project.

Automated detection of dendritic spines and dendrites

Andreas Kist and myself conceived of the project. I acquired all *in vitro* training data. Manual, pixel-wise annotations of training data was performed

by Volker Staiger, Claudia Huber and myself. Joel Bauer acquired *in vivo* validation data. I acquired *in vitro* validation data. Manual, single-point spine annotations were performed by Dominik Lindner, Hiranmay Joag, Joel Bauer, Danielle Paynter, Volker Staiger, Adrianna Zgraj, Sascha-Alexander Heye, Simon Weiler, and myself. Andreas Kist built the pipeline to tile training data data. Andreas Kist devised the architecture of DeepD3, as well as the GUI and batch-processing scripts. Andreas Kist trained all models. Quality control and all data analyses were done by me.

Working towards establishing wiring rules during LTP-induced synaptogenesis

Tobias Rose, Tobias Bonhoeffer, Cvetalina Coneva, Drago Guggiana Nilo, and myself conceived of the project and individual experiments. Rat organotypic hippocampal slice cultures were prepared and maintained by Volker Staiger. DNA constructs were designed by myself, Tobias Rose and Claudia Huber. Claudia Huber generated genetic constructs. I performed virus injections, single-cell electroporations and biolistic transfections. Cvetalina Coneva and Tobias Rose established the original variant of the assay. I performed all *in vitro* data acquisition (two-photon imaging, electrophysiology). I performed all quality control. Drago Guggiana Nilo and Andreas Kist helped with maturity to structure image registration. I performed all data analysis.

Eidesstattliche Versicherung/Affidavit

Hiermit versichere ich, Martin Hans Peter Fernholz, an Eides statt, dass ich die vorliegende Dissertation *A search for functional connectivity rules in the visual thalamus and hippocampus* selbstständig angefertigt habe, mich außer der angegebenen keiner weiteren Hilfsmittel bedient und alle Erkenntnisse, die aus dem Schrifttum ganz oder annähernd übernommen sind, als solche kenntlich gemacht und nach ihrer Herkunft unter Bezeichnung der Fundstelle einzeln nachgewiesen habe.

I hereby confirm that the dissertation *A search for functional connectivity rules in the visual thalamus and hippocampus* is the result of my own work and that I have only used sources or materials listed and specified in the dissertation.

Ort und Datum (date and location): München, 19. Oktober 2022

Unterschrift (signature):

Martin Hans Peter Fernholz
München, Oktober 2022